

# *Biofabrication using fibrous shape- morphing materials*

## DISSERTATION

zur Erlangung des akademischen Grades einer Doktorin der Naturwissenschaften

(Dr. rer. nat.)

in der Bayreuther Graduiertenschule für Mathematik und Naturwissenschaften

(BayNAT)

der Universität Bayreuth

vorgelegt von

***Indra Apsite***

*Aus Gulbene, Latvia*

Bayreuth, 2020



The preparation of this doctoral thesis was started in January 2016 at the College of Family and Consumer Sciences, Department of Polymer Fiber and Textile Sciences at the University of Georgia (Athens, USA) under the supervision of Prof. Leonid Ionov. It has been continued in the Biofabrication group at the University of Bayreuth from June 2017 till December 2019 under the supervision of Prof. Leonid Ionov.

This is a full reprint of the thesis submitted to obtain the academic degree of Doctor of Natural Sciences (Dr. rer. nat.) and approved by the Bayreuth Graduate School of Mathematical and Natural Sciences (BayNAT) of the University of Bayreuth.

Date of submission: 13.03.2020

Date of defence: 16.11.2020

Acting director: Prof. Dr. Markus Lippitz

Doctoral committee:

Prof. Dr. Leonid Ionov (reviewer)

Prof. Dr. Seema Agarwal (reviewer)

Prof. Dr. Stephan Gekle (chairman)

Prof. Dr. Andreas Fery

(additional reviewer: Prof. Dr. Mukundan Thelakkat)



## Table of contents

Summary .....	1
Zusammenfassung .....	3
1. Introduction .....	5
1.1. Biofabrication .....	5
1.2. Biofabrication of the tubular structure .....	6
1.2.1. Methods for fabrication of tubular constructs .....	7
1.2.2. Natural tubular tissues with cell alignment .....	9
1.3 Nano- and microfiber formation for cell guidance .....	11
1.3.1. Fiber formation techniques .....	11
1.3.2. Aligned and random fiber spinning .....	15
1.3.3. Parameters in electrospinning .....	18
1.4. Self-folding materials .....	23
1.4.1. Self-folding bilayers: materials & design .....	23
1.4.2. Fiber-based and reinforced self-folding .....	26
1.5 Conclusion .....	28
2. Aim .....	30
3. Synopsis .....	31
3.1. Porous Stimuli-Responsive Self-Folding Electrospun Mats for 4D Biofabrication .....	31
3.2. 4D Biofabrication of skeletal muscle microtissues .....	33
3.3 4D Biofabrication of fibrous artificial nerve grafts for neuron regeneration .....	34
3.3. Conclusion and outlook .....	35
4. References .....	36
5. Publication list .....	41

6. Individual contribution to publications and manuscripts .....	42
Publications .....	45
Part 1. Porous Stimuli-Responsive Self-Folding Electrospun Mats for 4D Biofabrication .....	45
Part 2. 4D biofabrication of skeletal muscle microtissues .....	55
Part 3. 4D Biofabrication of fibrous artificial nerve graft for neuron regeneration .....	81
Part 4. Microfabrication Using Shape-Transforming Soft Materials .....	106
Supporting Information .....	130
Polymer synthesis and product characterization .....	130
Synthesis of benzophenone acrylate (BPA) .....	130
Synthesis of poly(N-isopropylacrylamide)-benzophenone acrylate (P(NIPAM-BPA) .....	131
Synthesis of methacrylated alginate and hyaluronic acid .....	133
Acknowledgments .....	136
(Eidesstattliche) Versicherungen und Erklärungen .....	138



## Summary

Even though the field of medicine is constantly growing and advancing, organ and tissue transplantation remains the standard treatment for life-threatening organ damage. As human life expectancy is constantly increasing, organ demand is greater than the supply of donated organs. Another serious issue with organ transplantation is immune rejection of donor organs. Nowadays, scientists consider tissue engineering as a possible solution to these problems. Even though tissue engineering has promise, fabrication of highly complex tissue with specific/ uniaxial cell alignment remains a significant problem. Another field in close contact with tissue engineering is biofabrication. Biofabrication can be defined as “the production of complex living and non-living biological products from raw materials such as living cells, molecules, extracellular matrices, and biomaterials”<sup>1</sup>. That is, biofabrication deals with fabrication of complex objects with biological functions. A novel biofabrication technique is 4D biofabrication, which assumes fabrication of complex 3D objects by shape-transformation of 2D and 3D objects in response to a specific stimulus. One of major advantage of this approach is that it allows high-resolution fabrication of hollow tubular structures with no use of sacrificial material and easy cell encapsulation.

The aim of this work is development of methods for fabrication of fibrous shape-morphing structures, which shall allow 4D biofabrication of muscle and neural tissues. It is envisioned that fibrous shape-morphing materials will be able to provide high permeability needed for diffusion of oxygen and nutrition as well as structured topography that can be used for improved cell alignment and growth. The novelty of this work is the investigation of the biocompatibility, degradability and cell-material interactions with the fibrous shape-morphing materials.

Three different designs of biocompatible and degradable fibrous shape-morphing materials were prepared and investigated throughout this work. Different folding scenarios of the bilayer and multilayer fibrous shape-morphing materials have been discussed and explained based on various parameters: each layer thickness, the overall thickness of the bilayer/multilayer, number of the layers, environment temperature, choice of media, fiber alignment and shape of the material. Fibrous shape-morphing material interaction with three different cell types (fibroblasts, skeletal muscle cells, and neuron cells) has been described. High degradability has been achieved by the design of a fibrous bilayer system, that was able to achieve 70 % mass loss during a month of degradation without losing the stability of the self-rolled construct.

Overall, through this work, it was shown that designed materials can be used for engineering of tissue with uniaxial cell alignment as skeletal muscle and neuron tissue. It was demonstrated fibrous shape-morphing material potential for functional muscle microtissue formation, that can be further developed by self-assembly into muscle bundles. Electrospinning of conductive fibers could improve both muscle and neuron cell differentiation.

## Zusammenfassung

Auch wenn der Bereich der Medizin ständig wächst und sich weiterentwickelt, bleibt die Organ- und Gewebetransplantation die Standardbehandlung für lebensbedrohliche Organschäden. Da die Lebenserwartung der Menschen ständig steigt, ist die Nachfrage nach Organen größer als das Angebot von Spenderorganen. Ein weiteres ernstes Problem bei der Organtransplantation ist die Immunabstoßung von Spenderorganen. Heutzutage betrachten Wissenschaftler das Tissue Engineering als mögliche Lösung für diese Probleme. Auch wenn das Tissue Engineering vielversprechend ist, bleibt die Herstellung von hochkomplexen Geweben mit spezifischer/ einachsiger Zellausrichtung ein erhebliches Problem. Ein weiterer Bereich, der in engem Kontakt mit dem Tissue Engineering steht, ist die Biofabrikation. Die Biofabrikation kann definiert werden als "die Herstellung komplexer lebender und nicht lebender biologischer Produkte aus Rohmaterialien wie lebenden Zellen, Molekülen, extrazellulären Matrizen und Biomaterialien ". Das heißt, die Biofabrikation befasst sich mit der Herstellung komplexer Objekte mit biologischen Funktionen. Eine neue Biofabrikationstechnik ist die 4D-Biofabrikation, die die Herstellung komplexer 3D-Objekte durch Formtransformation von 2D- und 3D-Objekten als Reaktion auf einen bestimmten Stimulus übernimmt. Einer der Hauptvorteile dieses Ansatzes ist, dass er die hochauflösende Herstellung von hohlen röhrenförmigen Strukturen ohne Verwendung von unterstützenden Materialien und eine einfache Zellkapselung ermöglicht.

Das Ziel dieser Arbeit ist die Entwicklung von Methoden zur Herstellung faserförmiger, formmodellierender Strukturen, die eine 4D-Biofabrikation von Muskel- und Nervengewebe ermöglichen sollen. Es ist vorgesehen, dass faserige formmodellierende Materialien eine hohe Permeabilität, die für die Diffusion von Sauerstoff und Nährstoffen benötigt wird, sowie eine strukturierte Topographie bieten können, die für eine verbesserte Zellausrichtung und ein verbessertes Zellwachstum genutzt werden kann. Die Neuheit dieser Arbeit besteht in der Untersuchung der Biokompatibilität, der biologischen Abbaubarkeit und der Zell-Material-Wechselwirkungen mit den faserförmigen formmodellierenden Materialien.

Drei verschiedene Designs von biokompatiblen und biologisch abbaubaren faserförmigen, formverändernden Materialien wurden im Laufe dieser Arbeit vorbereitet und untersucht. Verschiedene Faltungsszenarien der zweischichtigen und mehrschichtigen faserigen formverändernden Materialien wurden erforscht und anhand verschiedener Parameter erläutert:

Schichtdicke von jeder Schicht, die Gesamtdicke der zweischichtigen/mehrschichtigen Materialien, die Anzahl der Schichten, die Umgebungstemperatur, die Wahl der Medien, die Faserausrichtung und die Form des Materials. Die Wechselwirkung zwischen faserartigem formveränderndem Material und drei verschiedenen Zelltypen (Fibroblasten, Myozyten und Neuronen) wurde beschrieben. Eine hohe biologische Abbaubarkeit wurde durch das Design eines faserigen Doppelschichtsystems erreicht, das in der Lage war, während eines Monats des Abbaus einen Massenverlust von 70 % zu erreichen, ohne die Stabilität des selbstgewickelten Konstrukts zu verlieren.

Insgesamt haben wir durch diese Arbeit jedoch gezeigt, dass die entworfenen Materialien für die Konstruktion von Gewebe mit einachsiger Zellausrichtung als Skelettmuskel- und Nervengewebe verwendet werden können. Wir haben gezeigt, dass faserige, formmodellierende Materialien ein Potenzial für die Bildung von funktionellem Muskelmikrogewebe haben, das durch Selbstmontage zu Muskelbündeln weiterentwickelt werden kann. Das Elektrosplennen von leitfähigen Fasern könnte sowohl die Differenzierung von Muskel- als auch von Nervenzellen verbessern.

# 1. Introduction

## 1.1. Biofabrication

While life expectancy continues to increase globally, the medical and biomedical industries seek to improve the healthcare system with new methods and techniques. Similar to the continual improvement of medicaments and vaccines, scientists are able to design and engineer new approaches for the operating theater. The organ-donor supply is unable to meet current demand for organs for transplantation. Tissue engineering (TE) is considered a possible alternative to the use of organ-donors. In tissue engineering – cells, engineered materials, bio- and physiochemical factors are used in combination to improve, maintain or replace biological tissues. With the help of TE, it is possible to design and obtain tissues or organs that can be matured *in vitro* or *in vivo* and afterward implanted in the human body. Another rapidly advancing field related to TE is biofabrication.

Field of biofabrication focus on microfabrication of defined product with biological function<sup>1</sup>. Biofabrication covers a wide variety of natural and technological processes in diverse disciplines as sensing, catalysis, synthetic biology, biotechnology, regenerative medicine (RM), and tissue engineering (Figure 1). Many methods are used in biofabrication, but most advanced biofabrication approaches that are used for TE are bioprinting and bio-assembly. Bio-assembly is defined as the fabrication of highly ordered constructs with a guided 2D or 3D organization through an automated assembly of previously formed cell-contained building blocks, which can be engineered by cell-driven self-organization or through the development of hybrid cell-material. In this method typically enabling technologies are applied as micro-fabricated molds or microfluidics. Bioprinting is an additive manufacturing method where complex 3D cell-laden hydrogel constructs can be formed using a layer-by-layer deposition. Bioprinting has several advantages as high cell viability, direct and precise deposition, high resolution and complex 3D constructs. Numerous complex tissues, including multilayered skin, tracheal splints, vascular grafts, bone, heart tissue, and cartilaginous structures, have been fabricated and transplanted using 3D bioprinting<sup>2</sup>.

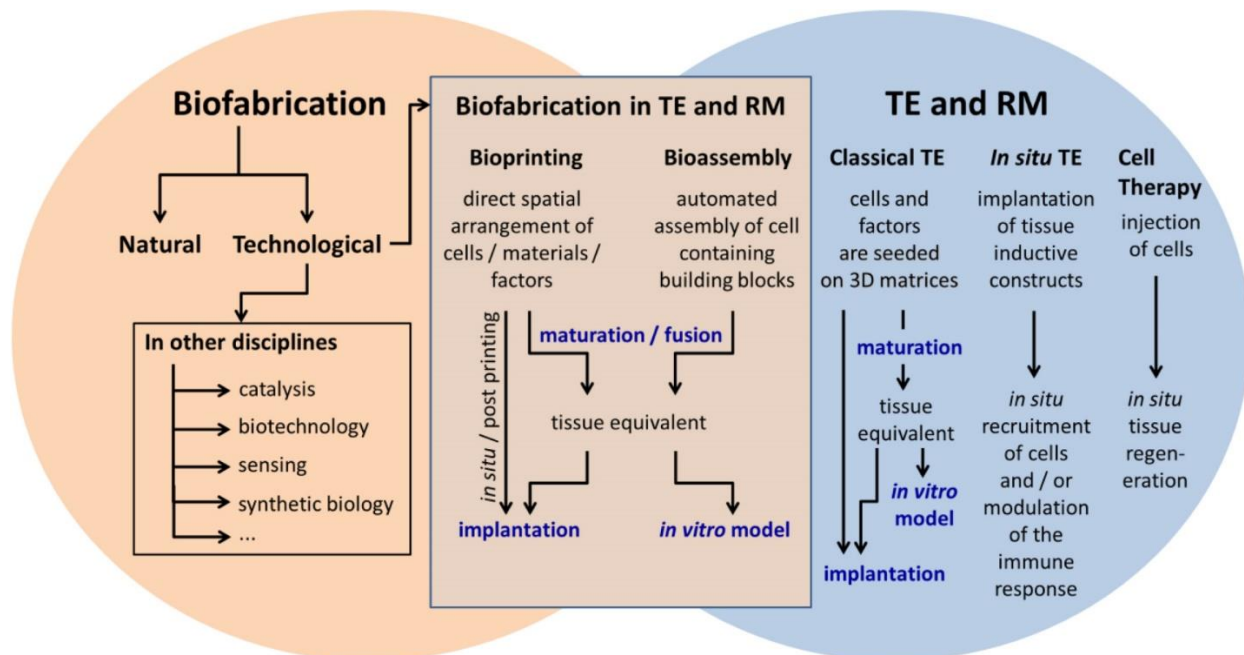


Figure 1. Biofabrication in relation to TE and RM. Reproduced with permission<sup>1</sup>. Copyright 2016, IOP Publishing.

Even though 3D bioprinting has shown good outcomes, it is still challenging to obtain the suitable structural and biochemical support for the cells. Naturally, cells are surrounded by extracellular matrix that provides suitable environment for their growth, differentiation and maintain their function<sup>3</sup>. Extracellular matrix (ECM) consists of a biomacromolecule network, which includes collagen fibers, proteoglycan complexes, fibronectin, laminin, hyaluronic acid, etc. It has been proven that any changes in ECM topography or architecture can lead to alteration of cellular response<sup>4</sup>. For example, collagen fibers in ECM are approximately 1-3  $\mu\text{m}$  thick and aligned, which helps cells to orientate and gives clues to attach. Whereas in bioprinting of cell-laden hydrogels, hydrogel formed mesh size is not always efficient for nutrient and waste product exchange. Likewise, to make the system more like the natural one, hydrogel structures should be reinforced by fibers.

## 1.2. Biofabrication of the tubular structure

Similar to mimicking ECM, another challenging task is to mimic hollow natural tubular structures in the human body like arteries in vasculature system, osteons in the skeletal system, muscle fibers in the muscular system, neurons in the nervous system, etc. These structures are highly ordered and

composed by different cell types, proteins, and signaling molecules<sup>5</sup>, likewise their diameter can be in micrometer as well as millimeter range.

### 1.2.1. Methods for fabrication of tubular constructs

Even though 3D bioprinting offers many advantages like a local deposition, possibility to extrude various materials, automatization, and individual adjustment, there are still some disadvantages. These include insufficient resolution, difficulties of hollow structure formation, no cues for cell orientation, no mechanical anisotropy and disturbed oxygen diffusion that make 3D bioprinting less suitable for tubular structure design<sup>6</sup>. Hollow tubular constructs can be made by the bioprinting of centric ring that involves high shear force formation thus significantly decrease cell viability<sup>7-9</sup>. Another method assumes the printing of sacrificial material that later needs to be removed using high pressure. This makes this method less suitable for cell encapsulation while printing<sup>10-14</sup>. Rod support printing can be as well used for tubular structure formation, but in this case, diameter of tubular structure is defined by on rod diameter, and as rod needs to be durable, the smallest diameter of the rod is usually in millimeters<sup>15</sup>. Overall, there are several models for tubular structure formation using 3D biofabrication. However, there is still a lack of high resolution, high cell viability and narrow tubular construct formation (<300  $\mu\text{m}$ ).

4D biofabrication has shown great potential for the fabrication of tubular structures<sup>16-19</sup>. 4D biofabrication includes a variety of fabrication technologies (3D printing, e-spinning, solvent casting, etc.) that produces 3D elements that can be externally stimulated in a controlled manner to promote shape transformation that lead to the desired structure/shape/morphology<sup>6, 16</sup>. A certain time is required for shape transformation to happen; thus, the fourth dimension (time) contributes to this fabrication method. Using this technology, it is possible to create sophisticated dynamic structures with high resolution, that we are not able to achieve using other biofabrication techniques. There are three general approaches to obtain cell-laden 4D biofabricated constructs (Figure 2). In the first approach, the 3D structure is first fabricated, then the stimulus is added and after shape change cells filled in the scaffold. This approach has a disadvantage that cells need to fill from the sides, which does not ensure good cell distribution in the middle of the construct. In the second approach, cells are seeded on the 3D structure before shape transformation, which produces a uniform cell layer in all structures. In the third approach, the 3D structure is fabricated with the cells, and then shape transformation is performed. For this approach, it is important to use biocompatible materials from the first step of fabrication.

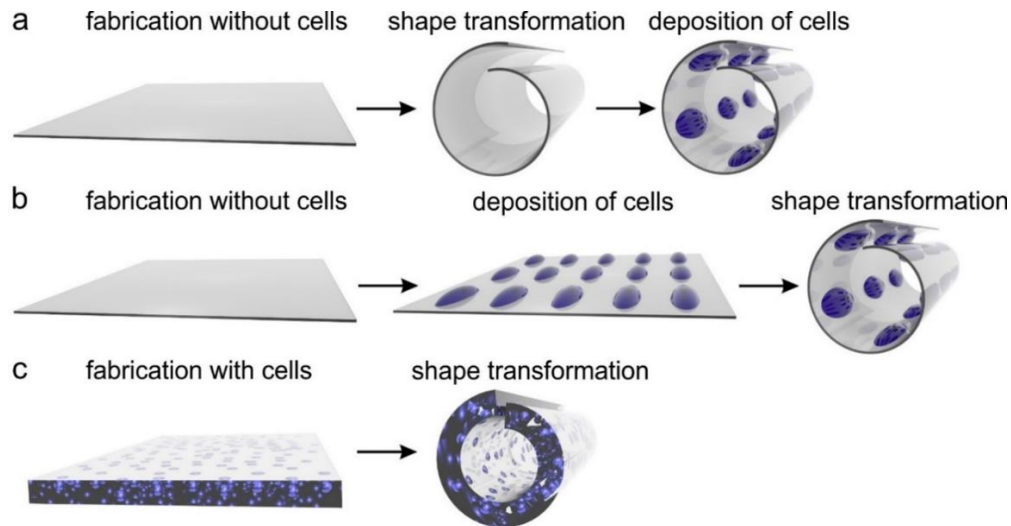


Figure 2. Fabrication of 3D cellular constructs using shape transformation: a) fabrication of nonvital construct, its shape transformation, and cell deposition in construct (blue); b) fabrication of nonvital construct, cell seeding and shape transformation of the cell-filled construct; and c) fabrication of vital construct filled with cells and its shape transformation. Reproduced with permission<sup>6</sup>. Copyright 2018, Wiley-VCH.

Another important feature of 4D biofabrication is the ability to form a wide variety of hollow shapes and sizes<sup>20-21</sup>. This allows us to fabricate not only tubular structures but also sphere-like structures. For example, that could be crucial for lung and gland design where both structures are present. As already showed, tubular structures can be formed upon shape change using rectangular 3D structures<sup>22</sup> (Figure 3a). To form sphere-like structures, the star-shaped 3D structure should be fabricated for shape-changing<sup>23</sup>(Figure 3b). A combination of various tubular and half star-like structures are proposed to form glands<sup>24</sup>(Figure 3c,d). This makes 4D biofabrication promising for a big tubular network, multiple tissue and organ fabrication.

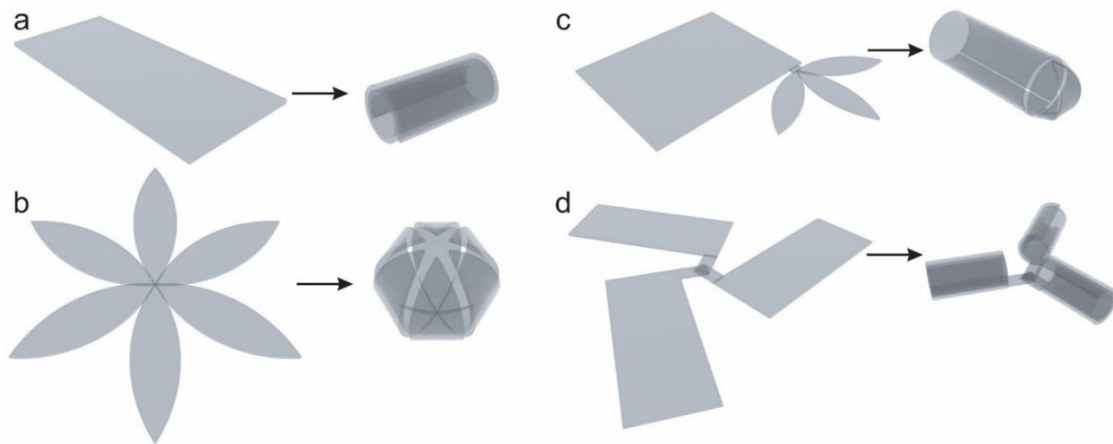


Figure 3. 4D biofabrication of various shapes: a) folding of the rectangular film forms tube; b) folding of the star-like film results in capsule formation; c,d) complex alveolar and branched structures can be formed using combination of rectangular and star-like elements. Reproduced with permission <sup>6</sup>. Copyright 2018, Wiley-VCH.

### 1.2.2. Natural tubular tissues with cell alignment

Our bodies consist of various tissues/organs; some of the tissues have a tubular structure with high cell alignment. Cell alignment is crucial for different cell types like muscle cells in striated muscle tissues, endothelial cells and smooth muscle cells in blood vessels and Schwann cells in neurons<sup>25</sup> (Figure 4). In blood vessels, smooth muscle cells (SMCs) are in the outer layer, and they are circumferentially aligned to provide resilience and tensile strength<sup>26</sup>. In this way, continuous fibrous helix from collagen fibers and elastin bands within vascular media is formed that provides necessary tension resistance for blood vessels to support maximal vessel contraction and dilation (Figure 4a). In comparison to SMCs, endothelial cells (ECs) in blood vessels are oriented along the direction of the vessel longitudinal axis. In blood vessels, ECs maintain the environment with different chemical clues and biophysical stimuli that are promoted by blood flow. Laminar fluid flow shear stress (FSS) evoke alignment of ECs intracellular cytoskeletal components causing cell elongation and polarization parallel to blood flow<sup>27</sup>. Any changes or misalignment of SMCs or ECs in blood vessels can cause changes in vascular behavior and further result in a pathological condition, e.g., atherosclerosis.

For a striated muscle to contract, stretch or beat, it is crucial to have highly aligned intracellular myofilaments – actin and myosin. Muscle cells during myogenesis align and fuse, forming striated

multinucleated myotubes that later are assembled in aligned muscle fibers across the muscle (Figure 4b). When there is any distribution of this orientation, musculoskeletal disorders occur, which can be caused by accidents, tumor excision, or muscular dystrophy<sup>28</sup>. This highly oriented and complex 3D muscle structure with considerable volume is still a challenge for the scientist in biofabrication and TE fields. Furthermore, innervating tissue adds yet another layer of difficulty, as nerve cells grow slowly and also need to be aligned in bundles in order to form proper functioning nerves.

During axonal regeneration, neural cells spontaneously orient parallel to aligned Schwann cells (SCs) in the case of peripheral nerve injury<sup>29</sup> (Figure 4c). SCs can differentiate to form myelin, which is a fatty substance that wraps around nerve cells and protect them. When SCs proliferate during regeneration they are forming longitudinal cell strands called Büngner bands, therefore the injured nerve is restructured by hundreds of microchannels formed along the major axis of the nerve<sup>25</sup>.

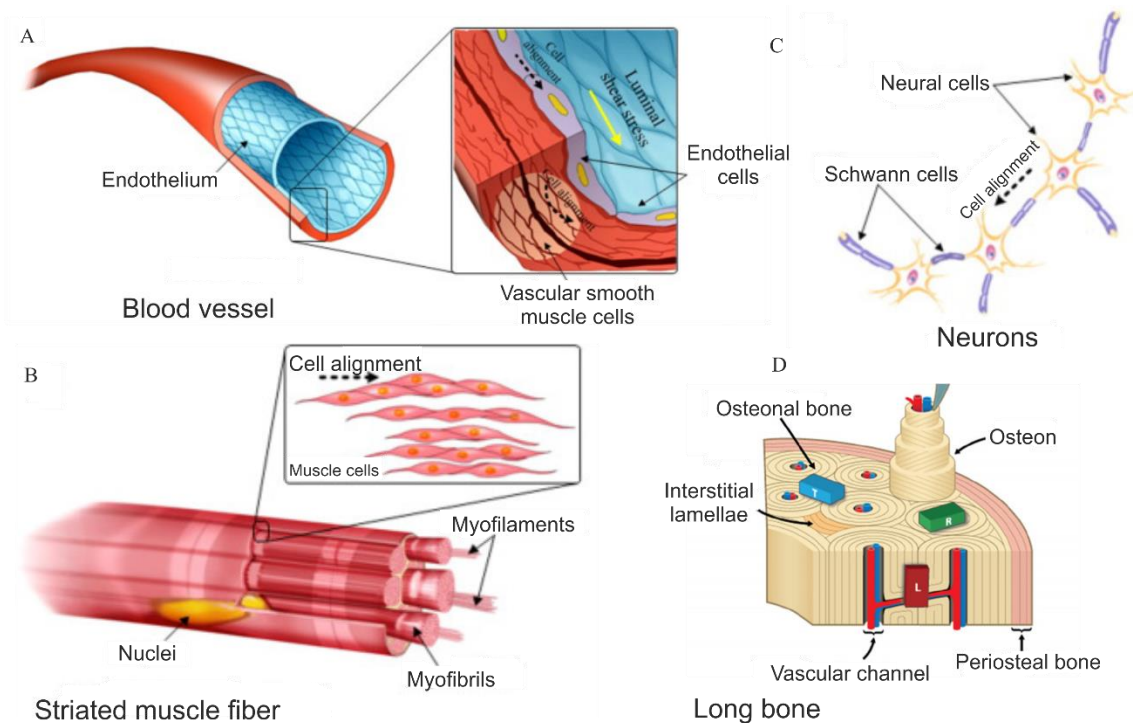


Figure 4. Cell alignment in various native tissues: a) smooth muscle cells in blood vessels; b) muscle cells in striated muscle tissue; c) Schwann cells in neurons. Reproduced with permission<sup>25</sup>. Copyright 2014, Elsevier.; d) Structure and components of long bone. Reproduced with permission<sup>30</sup>. Copyright 2011, Elsevier.

To promote neuron regeneration and other aligned tissue formation, various types of scaffolds with patterned topography like groove, pillar, pit, wrinkle, and fibrous scaffolds can be fabricated<sup>31-33</sup>. Further, various stimuli can be used to improve aligned tissue formation such as mechanical loading, chemical treatment, and electrical stimulation. Mechanical loading can be added to cell tissue or scaffolds with cells and with stretch, fluid flow shear stress or compression loading, it is possible to improve cell alignment. For example, electrical stimulation is used for muscle and neuron cells to promote their growth and differentiation, using electrical stimulation it is possible to achieve an elongation of cells and alignment perpendicular to applied direct current (DC) electrical field. However, stimuli-induced alignment is often difficult to optimize and often results in inconsistent cell alignment. Surface chemical treatment is another method to align cells in the scaffold, that can be done by adding motifs of ECM like Arginylglycylaspartic acid (RGD) peptide to surface where cells should adhere<sup>32</sup>.

### 1.3 Nano- and microfiber formation for cell guidance

As mentioned before, fibrous scaffolds can be used to guide cell alignment. Fibrous scaffolds not only have cell attractive topography but as well offers high porosity and mechanical resistance. Various fiber fabrication techniques can be used to form nano- and microsize fibers that would mimic the fibrous structure of ECM.

#### 1.3.1. Fiber formation techniques

Polymer fiber formation process, in other words, spinning can be divided into various types: wet, dry, melt, gel and electrospinning. Wet spinning is one of the oldest techniques used to produce a polymer fiber. In wet spinning, the syringe is filled with a polymer solution, and fiber is drawn from a chemical bath that causes precipitation and solidification of the polymer. Though wet spinning is an easy method and still holds its position between most used fiber formation techniques, this method requires a high amount of solvents, especially for mass production. In dry spinning hot air is used to solidify polymer fiber. Dry spinning produces less waste as there is less solvent used, but it is dangerous when flammable solvents are used for polymer solution preparation. In comparison to these two methods, melt spinning does not require solvent; molted polymer solidifies right after extrusion. Even though there is less waste, sometimes extremely high temperatures are necessary to melt the polymer. Besides, the choice of polymers is more restricted

in melt spinning as the difference between melting and degradation temperature should be substantial. Gel spinning is used to prepare high-strength fibers; in this case, a gel is cooled by air or solvent and then afterward stretched into fiber<sup>34</sup>. Similar to other previously mentioned methods, it requires a considerable amount of solvent. Electrospinning is a fiber production method where electric force is used to draw charged fibers from a polymer solution or melt. During electrospinning, high voltage is applied to the polymer solution in the needle, at the capillary tip of the needle, due to stress formed by electric field cone-like shape is formed called Taylor cone<sup>35</sup> (Figure 5). Then a polymer jet is drawn from needle tip to collector. While the jet is drawn and polymer fiber is formed charge removal by electrospaying, and solvent evaporation is taking place. Electrospinning is commonly used for biofabrication due to high scaffold surface area in relation to the electrospun volume.

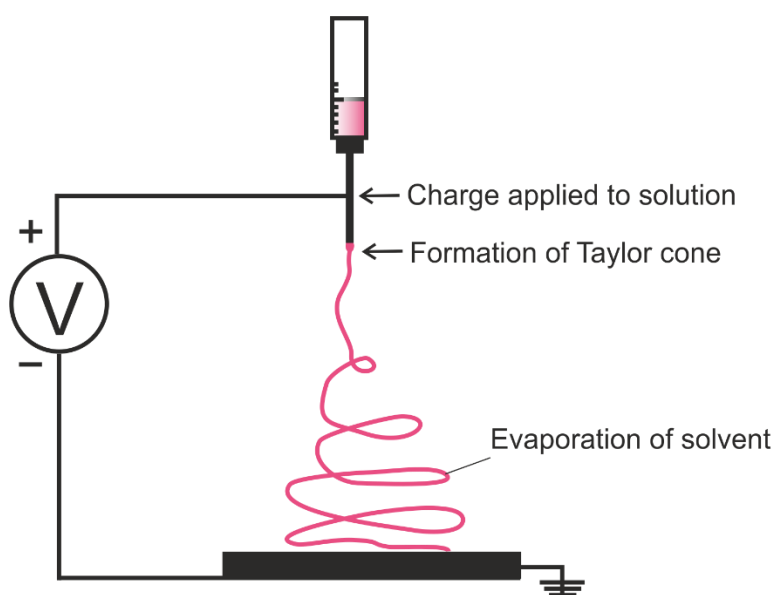


Figure 5. Schematic of electrospinning

From all types of fiber spinning, in TE most commonly used methods are electrospinning, wet spinning (including microfluidics), artificial biospinning and melt spinning (Figure 6)<sup>32</sup>. In biospinning natural silk formed by insects is used for fiber fabrication; due to this, there are several disadvantages of this method: 1) scale-up could be challenging as it depends on resources; 2) preprocessing of natural fibers required, that is time-consuming and expensive; 3) hard to control formed fiber size (Figure 6)<sup>32</sup>. The specific type of wet-spinning called microfluidic spinning is often used for TE. In microfluidic spinning, the crosslinking agent is added by coaxial flow directly,

allowing coded fiber formation (Figure 6). Even though this method is good for tunable fiber preparation, the challenge of this method is to obtain mechanically stable fibers. Another attractive dry spinning based approach is interfacial complexation, where two oppositely charged polyelectrolyte solutions are nearby, and with the needle, the polymer solution is drawn upward to the speed-controlled mechanical roller (Figure 6). This method, as well as some challenges as limited scale-up possibilities, limited material choice, a small range of fiber diameters (10-20  $\mu\text{m}$ )<sup>32</sup>. Therefore, this work primarily considers three of the fiber spinning methods: wet spinning, melt spinning, and electrospinning. For melt spinning, expensive equipment is required based on high temperature and pressure necessary to push polymer to the spinneret. Wet spinning, on the other hand, is more designed for large fiber production  $\sim 250\text{-}500\ \mu\text{m}$ <sup>32</sup>, which can be used for cell alignment if fiber is not smooth and has grooves additionally in its morphology. E-spinning is used for smaller range fibers that are widely used for cell alignment<sup>36-37</sup>.

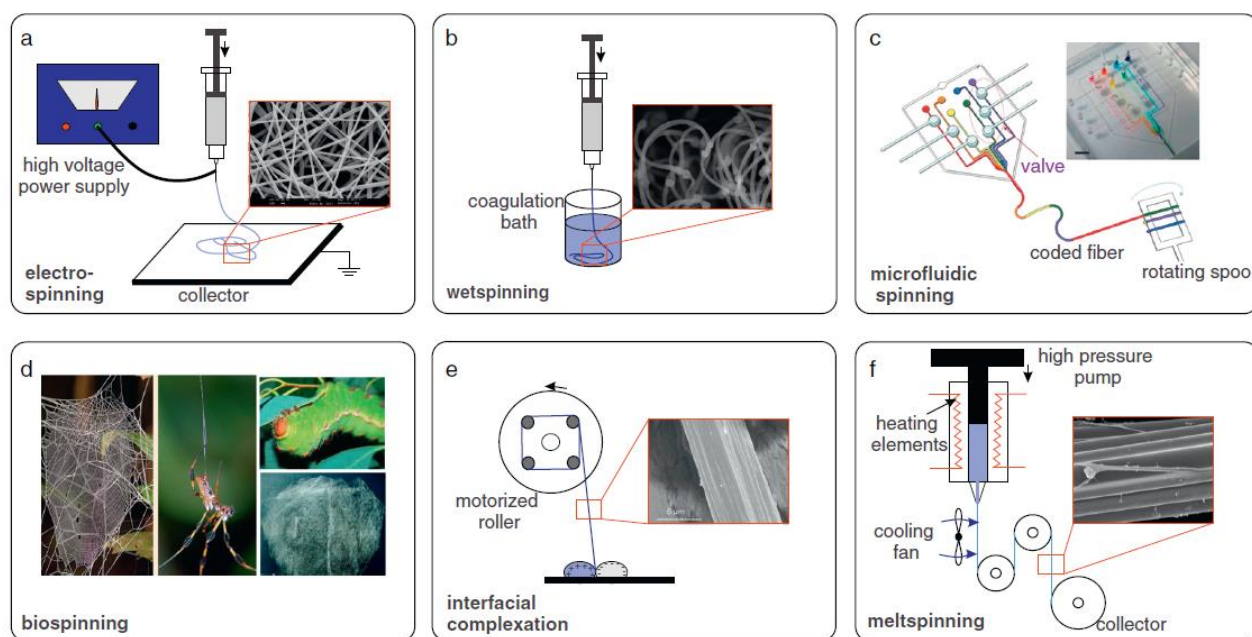


Figure 6. Methods for fiber fabrication in TE: (a) electrospinning – fibers are formed by the flow of a polymer exposed to an electric field; (b) fibers in wet spinning are made by injection of a polymer solution into a coagulation bath; (c) microfluidic platforms fabricate fibers by coaxial flow of a pre-polymer and a crosslinking agent; (d) biospinning – fiber fabrication by insects (silkworms and spiders); (e) interfacial complexation – fiber formation at the interface of two oppositely charged polyelectrolyte solutions; (f) the melt spinning – melted polymer is extruded through a spinneret. Reproduced with permission<sup>32</sup>. Copyright 2013, Elsevier.

Another advancing electrospinning-based technology of fiber production is melt electrospinning writing. This method is a combination of melt electrospinning and 3D printing. As in electrospinning cooled jet is whipping, it is hard to get controlled deposition of electrospun fibers. On the other hand, in the melt electrospinning writing technique, movement in x,y, and z-axis are possible (similar to 3D printing), which allows direct fiber deposition. When the speed of the collector matches the formed jet – critical translation speed (CTS), linear fibers can be produced<sup>38</sup>. Even though it is possible to obtain a good resolution of fibers and controlled deposition, fiber diameter is higher (2-50  $\mu\text{m}$ ) than for melt spinning due to lower voltages and shorter distance between needle and collector used in melt electrospinning writing<sup>39-40</sup> (Figure 7). This is necessary due to the more complex electronic setup of the device. Nevertheless, melt electrospinning writing in comparison to electrospinning takes more time for fiber production.

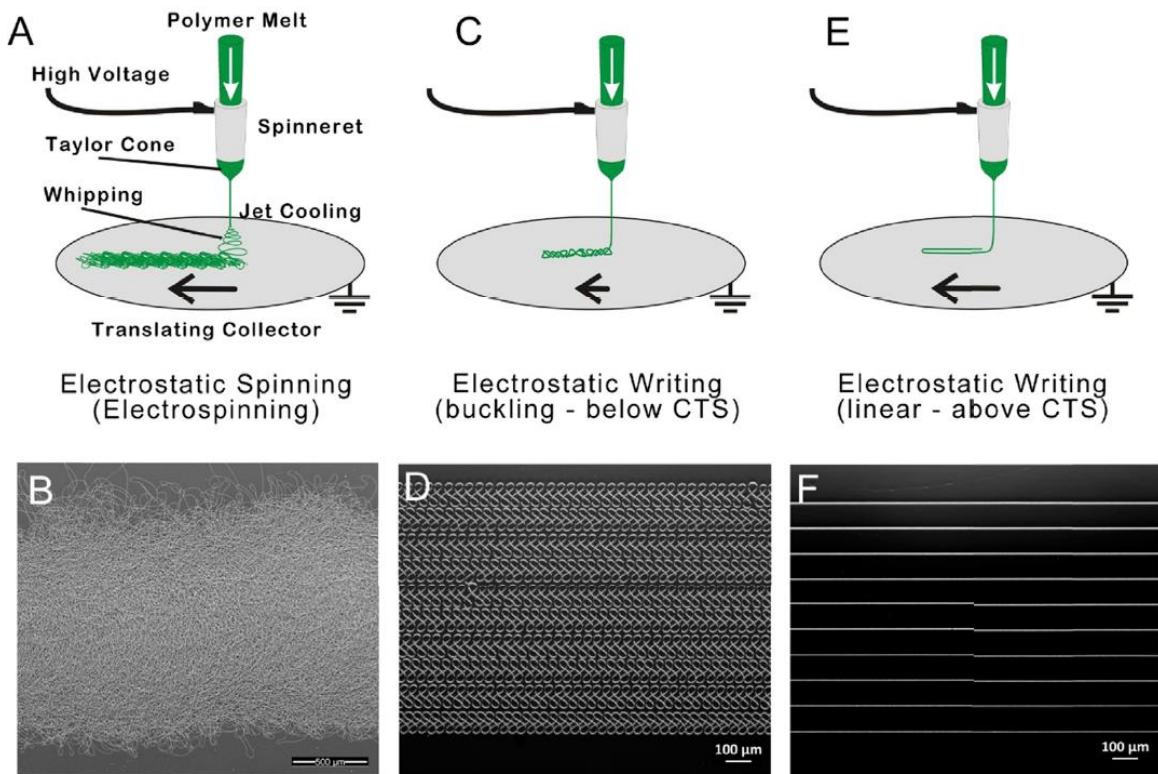


Figure 7. Electrospinning vs electrostatic writing: a) electrospinning set up, polymer jet whipping; b) melt electrospinning formed fibers; c) electrostatic writing below CTS, fiber buckling; d) electrostatic writing fibers below CTS; e) electrostatic writing above CTS, linear fiber formation; f) electrostatic writing fibers above CTS. Reproduced with permission<sup>38</sup>. Copyright 2017, Elsevier.

### 1.3.2. Aligned and random fiber spinning

Based on the choice of the collector and its arrangement while electrospinning, it is possible to obtain random and aligned fibers. A grounded stationary collector is used (flat plate) to obtain random fibers. Usually, the flat electrospun mat is formed using this method (2D). However, with proper adjustment of the collector, it is possible to obtain 3D sponge-like structures. For example, different transient electrical forces when fibers hit the collector can lead to a 3D structure<sup>41</sup>. In this case, first negatively charged fibers are attracted to the positively charged collector, then charge-transfer from collector to fiber is induced, and repulsive force is made leading to one point attached freestanding fiber, whereas for regular electrospinning no charge transfer is formed and attractive force is kept during electrospinning fully attaching fiber parallel to the collector. Another method to obtain a high porosity sponge-like structure is based on the use of a nonconductive spherical disk collector embedded with an array of metal probes<sup>42</sup>. To control fiber alignment, it is possible to use three different forces: electrostatic, mechanical, and magnetic<sup>43</sup>.

A rotating mandrel is used to obtain fiber alignment via mechanical forces (Figure 8a). In this case, the fiber alignment degree depends on the speed of rotation; the higher is the speed of rotation, the higher is the degree of fiber alignment. This is a simple technique to obtain aligned fibers, but it requires extremely high rotation rates for good alignment. Using this method, it is possible to obtain a thick fibrous mat. It is suggested to use a rotating disk with a sharp edge for the improvement of fiber alignment<sup>44</sup>(Figure 8b). Though using the disk as collector gives a small surface area for fiber collection. Another method to improve alignment is adding the wire on the rotating drum collector; on this wire, highly aligned fibers will be formed (Figure 8c). The addition of extra electrodes beneath and on top of the collector could improve alignment, like a negative charge knife-edge blade electrode under small diameter rotating mandrel or spinneret with knife-edged blade and opposite to that negatively charged knife-edge electrode surrounding rotating mandrel (Figure 8d,e)<sup>45</sup>.

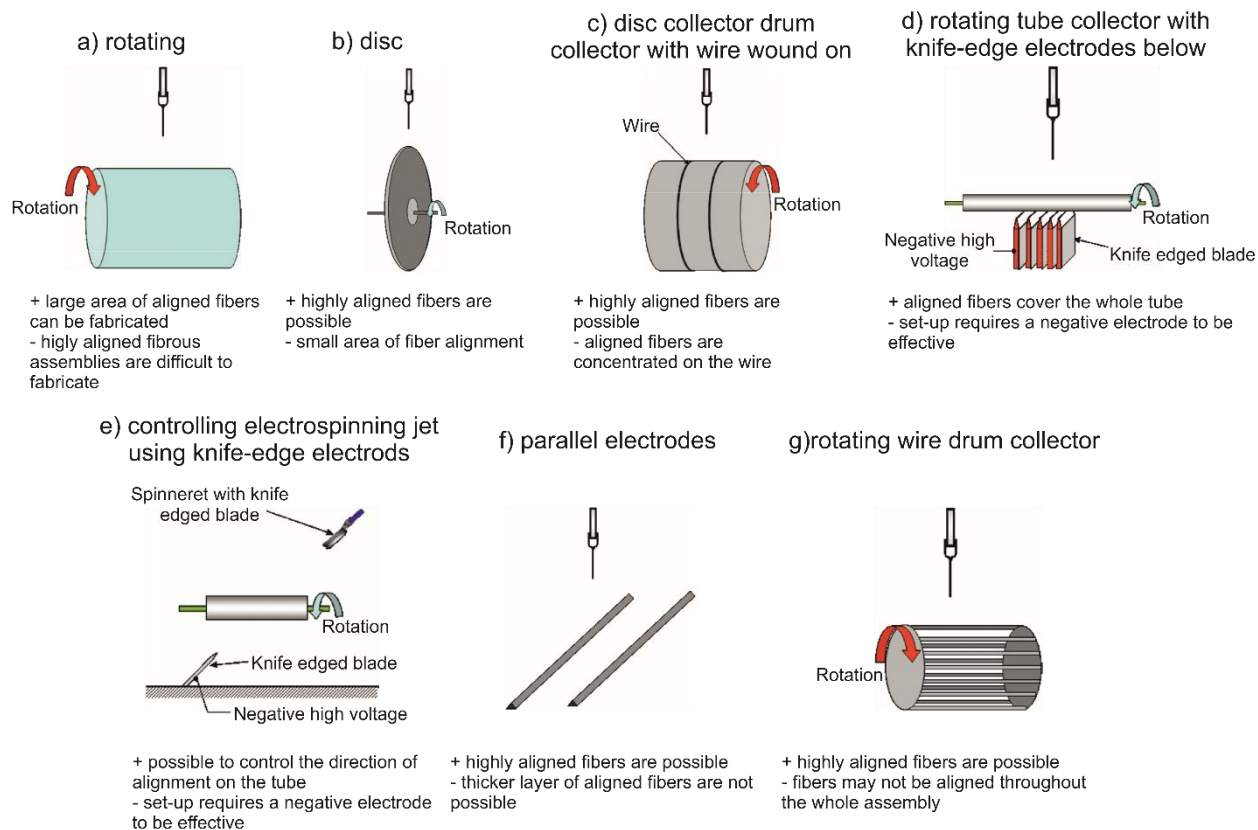
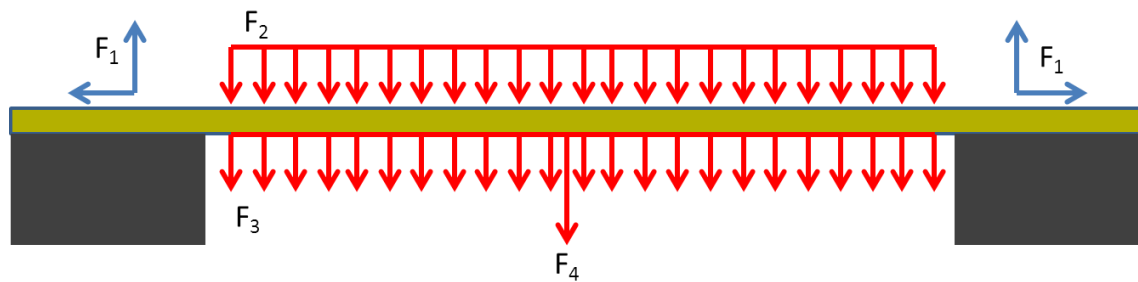


Figure 8. Different electrospinning set-ups for aligned fiber preparation with advantages and disadvantages. Adapted with permission<sup>45</sup>. Copyright 1990, IOP Publishing.

Due to electrostatic charges distributed along the electrospinning jet, it is possible to control fiber alignment using an external electric field. A most known method is to use two conductive parallel substrates with the void gap; across the gap, highly aligned fibers are collected (Figure 8f). Using this method fibers are experiencing electrostatic forces acting in orthogonal directions<sup>43</sup>. The first force is formed while the electrical field is split into two electric fields lined pointing to two electrodes/collectors<sup>46</sup>. While force is pulling fibers to the electrodes, opposite charges are induced on the surface of the electrodes when fiber travels to their proximity. As a result, this forms the second force that stretches the nanofibers across the gap and distributes fibers perpendicularly to edges of the electrodes. Several parameters influence fiber alignment, mat thickness, and length (Figure 9)<sup>47-48</sup>. Three forces act on electrospun fibers: repulsive force from incoming fibers and from charged electrode above, an attractive force from the ground below and weight of the fiber itself, that could lead to breakage of fiber if polymer fiber is not resistant enough. Due to this, there is a limited amount of polymer that could be used for this type of spinning.



- $F_1$ : Anchorage/Adhesion force
- $F_2$ : Repulsive force from incoming fibers and from charged electrode above
- $F_3$ : Attractive force from ground below
- $F_4$ : Weight of fiber

Figure 9. Forces acting on uniaxially aligned fibers. Reproduced under the terms and conditions of the Creative Commons, CC BY 3.0<sup>48</sup>. Copyright 2015, ElectrospinTech.

Fiber alignment highly depends on gap distance; with an increase in gap distance, electric field component increases in the horizontal direction leading to higher fiber alignment<sup>49</sup>. The thickness of fiber mats can be increased by using sharpened electrodes. Sharp edge collectors can gather the charges and induce attractive force on the electrospinning jet<sup>50</sup>.

Similarly, to mechanical force (rotating) collectors, the deposition of fibers and arrangement can be designed according to the shape and arrangement of the collector. For example, using for perpendicularly arranged bar electrodes, we are able to obtain a plaid polymer mesh. Unfortunately, this method has a fiber deposition limitation and low productivity. Additional electrodes and incorporation of other forces like mechanical or magnetic can improve fiber formation and deposition. For example, the design of a drum-like rotating electrode with multiple bars combines advantages from rotating mechanical and electrostatic collectors. These electrodes result in the improvement of fiber alignment for the first deposited layers and increment of polymer mat thickness due to rotation (Figure 8g). Another interesting type of collector is to use automated conductive tracks, that can rotate and stretch uniaxially aligned fibers while they are collected<sup>51</sup>. In this way, it is possible to create higher alignment and increase fiber length via fiber-stretching.

Alignment can also be controlled by magnetic forces, though this method is rather new for aligned fiber formation and more investigation should be made; for example, it is still unclear if polymer solution should contain magnetic particles or not<sup>43</sup>. In this method, two parallel magnets are used

to aligned fibers formed from slightly magnetized (0.5 wt%) or non-magnetized solutions<sup>52-53</sup>. Magnetic field-assisted electrospinning is rather a simple method as it requires just the addition of two magnets to a conventional setup (Figure 10). As well, fiber deposition can be easily manipulated with rearrangement of magnets, and a higher volume of the fibrous mat can be achieved than with electrostatic forces. Though with higher flow rates uniaxially aligned fiber pattern change to wavy<sup>53</sup>. Based on the lack of explanation for aligned fiber production phenomenon by magnetic field-assisted electrospinning, it is less used than the other two forces.

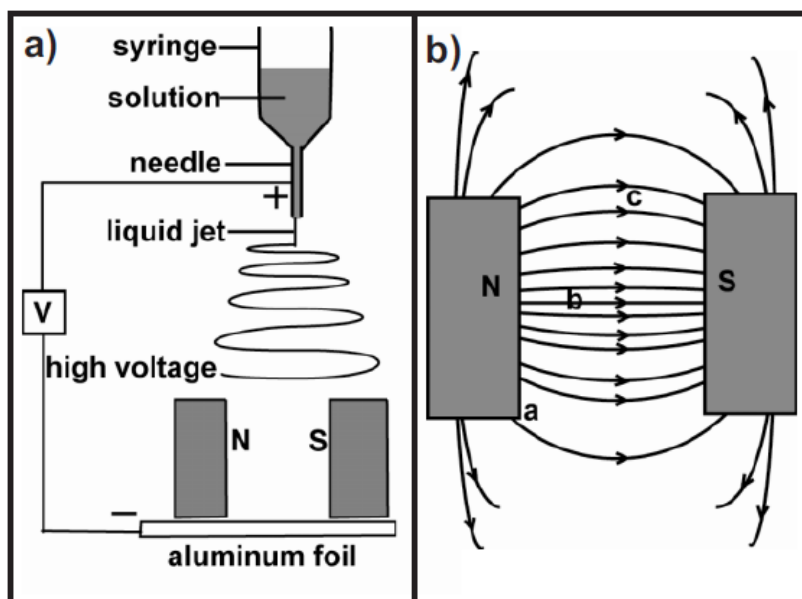


Figure 10. a) Magnetic electrospinning(MES) setup. The key component – magnetic field generated by two parallel-positioned magnets; b) Calculated magnetic field strength vectors between the two magnets. The arrows show magnetic field line directions. a, b, c- represents magnetic field strength (120, 32, 25 mT). Reproduced with permission<sup>52</sup>. Copyright 2007, Wiley-VCH.

### 1.3.3. Parameters in electrospinning

There are several working parameters to consider while electrospinning; they can be divided into three groups: process, solution, and ambient parameters. One of the solution parameters is concentration, usually low concentration polymer solutions would form small particles while electrospinning, in this case, more correct word for this process is electrospraying (Figure 11). When concentration is slightly increased beaded fibers are forming. In optimal solution

concentration, we can obtain bead free nano- and micro-sized fibers. When solution concentration is too high, helix-shaped micro-ribbons are achieved<sup>54</sup>. Another solution based parameter is polymer molecular weight, that similar to concentration would influence beaded and bead free fiber formation. Polymer molecular weight directly influence polymer chain entanglement, when polymer chains are too short, no entanglement can be formed leading to electrospinning, this can be solved by incorporation of polymers that can be used as template polymers like PEO or increasing of molecular weight<sup>55</sup>. Another closely related parameter to concentration and molecular weight is viscosity. There is an optimal concentration of viscosity that needs to be achieved during electrospinning; when viscosity is too low, we would get beaded fibers, but when it is too high it can clog the needle. Another important solution parameter that needs to be considered is surface tension. When solvent with high surface tension (for example, water) is used for electrospinning, beaded fibers are formed. Polymer concentration, solvent mixtures with various mass ratios, and surfactants can be modified to reduce surface tension and obtain bead-less fibers<sup>56-57</sup>. The last solution related parameter that influences electrospinning is conductivity. It has been described that by adding ionic salts that can improve solution conductivity it is possible to obtain thinner and bead-less fibers<sup>58</sup>.

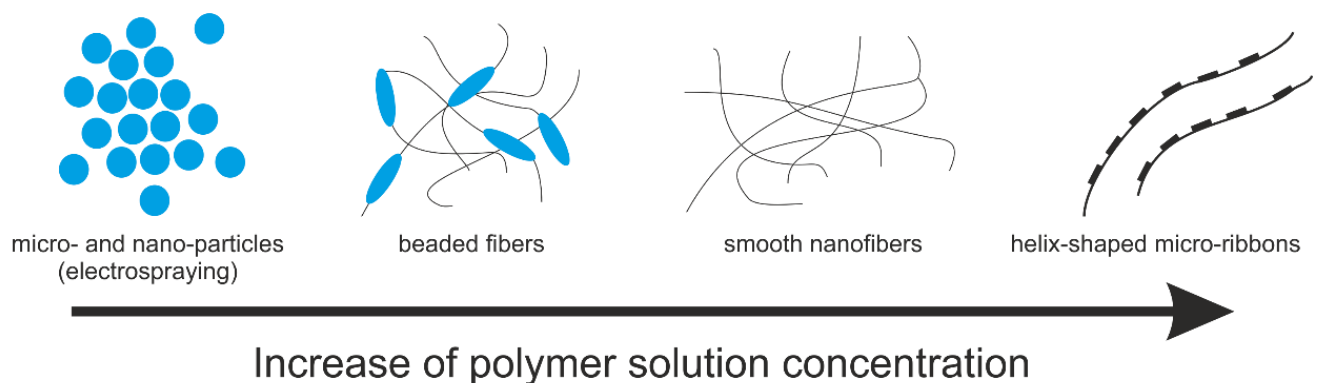


Figure 11. Solution concentration influence on fiber formation during electrospinning

Further, it is important to consider processing parameters, which include flow rate, voltage, collectors and distance between the collector and the tip of the needle. The applied voltage is an essential parameter of electrospinning. Nevertheless, the effect of voltage on electrospun fibers is controversial. Several groups have suggested that there is no effect on fiber diameter. Some others suggest that fiber diameter increased with the increase of electrospinning voltage. Others suggest

that fibers formed thinner, based on an increase of electrostatic repulsive force on the charged jet<sup>54, 59</sup>. To summarize, the voltage influences fiber diameter and bead-free fiber formation, but it highly depends on the polymer solution chosen for electrospinning and distance between the tip of the needle and collector. A clear effect of voltage on electrospinning is that higher voltage added to the electrospinning jet gives a greater volume of solution drawn from the needle tip. Moreover, by constant flow rate, this would mean more unstable Taylor cone formation and even Taylor cone formation inside of the needle that leads to multijet formation. Figure 12 summarizes possible theories on how voltage could influence fiber diameter based on the increase of volume drawn from the needle. Similarly, in a recent paper from Schubert et al., instabilities caused by voltage directly influence the final fiber diameter of the fiber, theory described by Schubert shows that three main regimes influence fiber diameter: flow dominated, potential jet splitting and drying dominated regime<sup>60</sup>. Especially the second regime highly depends on the voltage used. Following equation is proposed for the prediction of electrospun fiber diameter:

$$d_{split\_dry} \sim \eta^{4/9} \cdot c^{1/2} \cdot \gamma^{1/3} \cdot p_V^{2/9} \cdot U^{-14/9} \quad (1)$$

Where  $\eta$  – solution viscosity;  $c$  – solution concentration;  $\gamma$  – surface tension;  $p_V$  – vapor pressure that defines evaporation rate for electrospinning;  $U$  – applied voltage.

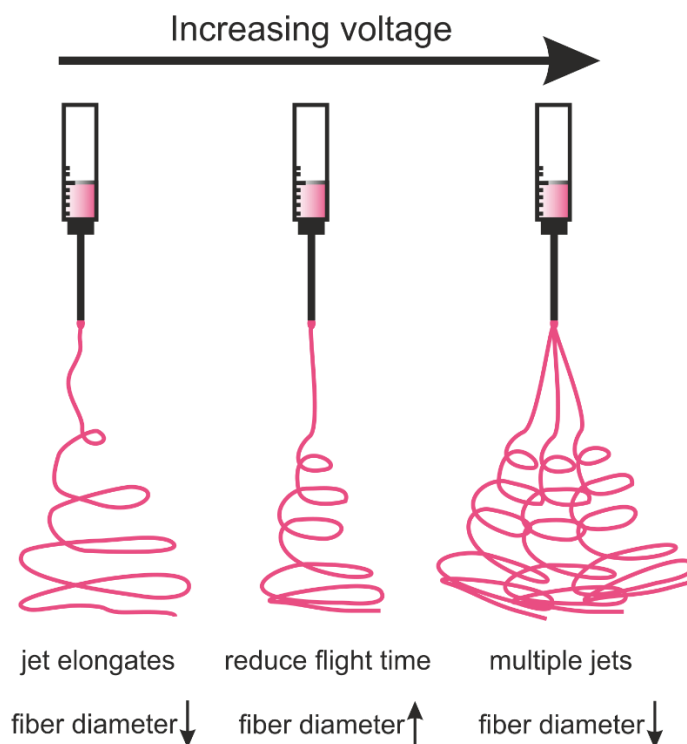


Figure 12. Voltage effect on electrospinning

On another hand, flowrate has a definite influence on fiber diameter and bead formation. Usually, lower flow rates are recommended so that polymer solutions have enough time for polarization, and thinner fibers without beads can be formed<sup>54</sup>. When the flow rate increases, fiber diameter due to more material extruded increases, and it leads to the higher formation of beads. As previously mentioned, collector selection has a strong influence over the directionality of the fibers, e.g., aligned, random, free-standing fibrous mat formation. The last processing parameter is the distance between the collector and the tip of the needle. This is an important parameter due to that it directly affects the electrical field area. When the distance between the tip of the needle and collector is too short, there is not enough time for the polymer to solidify, and beaded fibers can be formed. Usually, it is possible to obtain thinner fibers when the distance between the tip of the needle and the collector is greater.

The last set of working parameters that can influence electrospinning is ambient parameters. The increase of temperature favors thinner fiber formation, as a polymer can faster solidify<sup>61</sup>. However, higher humidity leads to the formation of thicker fibers as it is harder for a polymer solution to solidify in these conditions. Nevertheless, higher humidity influence fiber morphology from smooth fibers to fibers pores on the fiber surface<sup>62</sup>.

Since electrospinning is a method where a high amount of fibers is formed in less than a minute, the direct deposition of fibers is quite complicated. Based on changes in the electrical field and airflow, fibers can accumulate in indefinite places on the collector. There are several ways suggested for controlled deposition. One of the methods is to use near-field electrospinning. It is a technique where electrospinning is done from a close distance ( $\leq 3$  mm) and with a lower voltage than for regular electrospinning (600 V)<sup>63</sup>. Even though using this method it is possible to control area of deposition, it is hard to obtain straight and aligned fibers with this method as well it is important to find correct voltage and distance as there are higher chances of electrical short circuit. Another method is to use ring electrodes around the electrospinning jet, which has the same polarity as the one applied to the needle<sup>64</sup>. These electrodes allow controlling electric field line distribution from macroscopic to uniform straight field line direction until the collector leading to controlled and central deposition of fibers on the grounded collector (Figure 13).

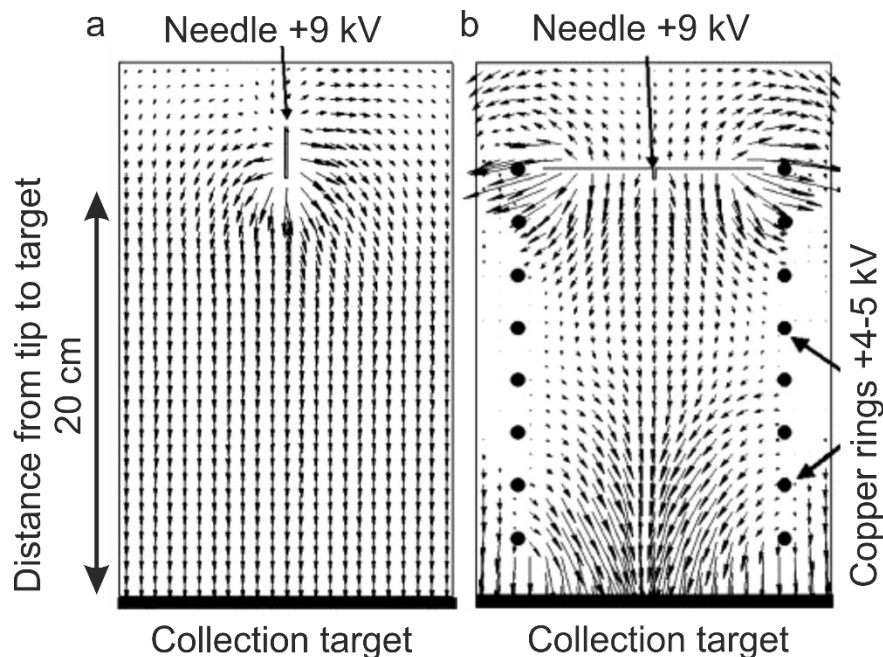


Figure 13. Electric field lines calculated for conventional electrospinning setup (a) and electrospinning setup with ring electrodes for jet focusing (b). Reproduced with permission<sup>64</sup>. Copyrights 2001, Elsevier.

## 1.4. Self-folding materials

Self-folding materials are able to change their properties and shape in response to the change of mild external stimuli like temperature, pH, humidity etc. The ability to react to mild conditions and to be fabricated into micrometer-scale makes them suitable for various biomedical applications. Different kinds of materials demonstrate these properties – hydrogels with low and upper critical solution temperature behavior, polyelectrolyte hydrogel, liquid crystalline elastomers, shape-memory polymers. Self-folding or smart materials can actuate in various ways based on their structure and composition, based on smart material programming obtained 3D structures can be more complex or simple, with reversible or irreversible actuation<sup>16, 21-23</sup>.

### 1.4.1. Self-folding bilayers: materials & design

Initially, the self-folding of bimetal beams was described by Timoshenko in 1925. It described bilayer system bending, where bilayer is formed by two welded metals with different thermal expansion coefficients<sup>65</sup>. The final curvature of formed bilayers can be expressed using the following equation:

$$\frac{1}{\rho} = \frac{6(\alpha_1 - \alpha_2)(t_1 - t_0)(1+m)^2}{h\left(3(1+m)^2 + (1+mn)\left(m^2 + \frac{1}{mn}\right)\right)}, n = \frac{E_1}{E_2}, m = \frac{a_1}{a_2} \quad (2)$$

Where E is elastic modulus, a – thickness of each metal layer, h – thickness of bilayer,  $\alpha$  is the thermal expansion coefficient of the material and  $\rho$  is the radius of the curvature. It was discovered that greater is the difference between each material thermal coefficient; smaller will be the radius of curvature. Further, layer thickness greatly influences the final radius of curvature. Some limitations make Timoshenko equation not applicable to all bilayer systems: derived for small-angle deformations, cannot predict the folding direction, and applicable for reversible elastic deformations.

Similarly, bilayer systems polymer-based polymer systems have different expansion coefficients. Timoshenko equation can be used to characterize polymer-based bilayers, when expansion coefficients are replaced with, for example, swelling degree of the hydrogel. In comparison to metals, polymers can be triggered by a variety of external stimuli and volume change is more significant. Polymer bilayer systems are usually made from active and passive layer. The active layer reacts to external stimuli by the change in its physical-chemical properties. The passive layer, on the other hand, controls and directs active layer response in bending movement. For this design

suitable passive layer is hydrophobic polymers or block copolymers like polyesters or styrenes and as active layer various highly hydrophilic hydrogels.

Hydrogels are crosslinked polymer networks that can absorb an extremely high amount of water content, that can even reach up to 99 wt.% of total hydrogel mass. Hydrogels are able to swell and shrink more than ten times in its volume, which makes them well-suited for bilayer polymer systems<sup>66</sup>. Not only hydrogels can absorb high amounts of water, hydrogel mechanical properties are similar to properties of natural tissues, which makes them appropriate for biomedical applications. Transport of solvent mass (water) in hydrogel determines the actuation of the bilayer system, where hydrogel is an active layer. For hydrogel-based polymer bilayer system temperature, light, pH, ionic strength, magnetic field, etc. can be used as external stimuli to vary water content inside of the hydrogel and change the self-folding behavior of polymer bilayer systems.<sup>67</sup>

Hydrogels resemble swollen elastomers in terms of their structure, and the behavior of hydrogels is similar to rubbers. Hydrogels differentiate from other polymers in that polymer chains are diluted by solvent molecules, which reduce crosslinking point volume density. The swelling degree of hydrogels depends on the correlation between polymer chain elastic deformation (similar to rubbers) and mixing energy that consists of enthalpic and entropic components (Flory theory). Polymer volume fraction in the swollen rubber ( $V_r$ ) is inversely proportional to the swelling degree and molecular weight of polymer chains between crosslinking points ( $M_c$ ). Where crosslinking points proportional to crosslinking degree according to Flory–Rehner equation:

$$M_c = \frac{-\rho V_s (V_r^{1/3} - V_r/2)}{\ln(1 - V_r) + V_r + \chi V_r^2} \quad (3)$$

$\rho$  is rubber density,  $V_s$  is the molar volume of solvent,  $\chi$  is the interaction parameter between the rubber and solvent<sup>68</sup>. Flory Huggins  $\chi$  parameter describes the interactions between solvent molecules and polymer segments. The use of this equation is restricted to small swelling degrees, where polymer chain lengths have Gaussian distribution. Hydrogels are able to demonstrate responsive properties when Flory Huggins parameter alternate, and the molecular weight of polymer chains between crosslinking points directly influence hydrogel swelling degree  $Q_{eq} \sim M_c^{3/5}$  (as predicted by Flory) or  $Q_{eq} \sim M_c^{4/5}$  (as predicted by Khohlov)<sup>68-69</sup>. Like rubbers, hydrogel mechanical properties in theta solvents directly depend on hydrogel crosslinking density, and shear modulus of the hydrogel can be expressed as shear modulus of dry elastomer divided by cubic root of swelling degree.

$$G = \frac{\rho RT}{M_c} Q^{-1/3} = G_{dry\ elastomer} Q^{-1/3} \quad (4)$$

In non-theta conditions, the Elastic modulus (E) also depends on the swelling degree of hydrogel (Q). Elastic modulus can be compared to a multiplication of swelling degree and average molecular weight of a strand as follows:  $E \sim Q^{-b} M_c^{-1}$ , where b is 1/3 for theta solvent, 7/12 for slightly swollen crosslinked hydrogels in good solvent, 5/6 for slightly swollen highly crosslinked hydrogels and 1/6 for strongly stretched strands. From this, we can conclude that interactions between polymer chains and solvent strongly affect swelling of the hydrogel and hydrogel mechanical properties.

Using polymer-based bilayers it is possible to obtain various simple and more complex shapes. The simplest shape that can be obtained by the actuation of polymer-based bilayers is a tube. Though concept and design can seem straightforward, tubular structures perform different folding based on the width/length ratio and relative thickness of the rectangular bilayer film (Figure 14)<sup>70</sup>. For example, long-side folding dominates at high aspect ratios, when the width or the length of the film is comparable to the circumference of the formed tube, requiring low actuation strain. For high actuation strains folding from all sides can be observed. In this case, both width and length highly exceed the circumference of the folded tube. Diagonal folding can be achieved by moderate actuation, where width and length are comparable to the deformed circumference.

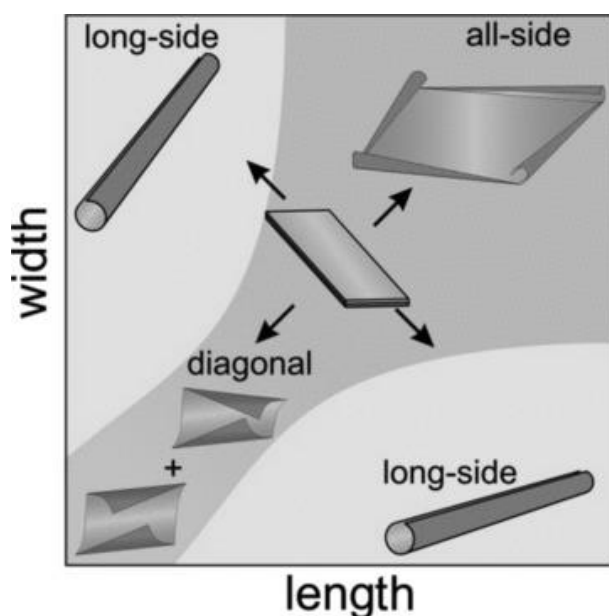


Figure 14. Self-folding rectangular shape bilayer folding scenarios based on width and length ratio. Reproduced with permission<sup>70</sup>. Copyright 2013, Wiley-VCH.

As discussed before different geometries, leads to more complex shapes like a four-arm star with rounded edges leads to the formation of the pyramid. Nevertheless, it is possible to play as well with swelling ratios and crosslinking density. Using strips with high and low-swelling regions, it is possible to form a 3D shape consisting of two cylindrical regions connected by transition neck (Figure 15)<sup>71</sup>.

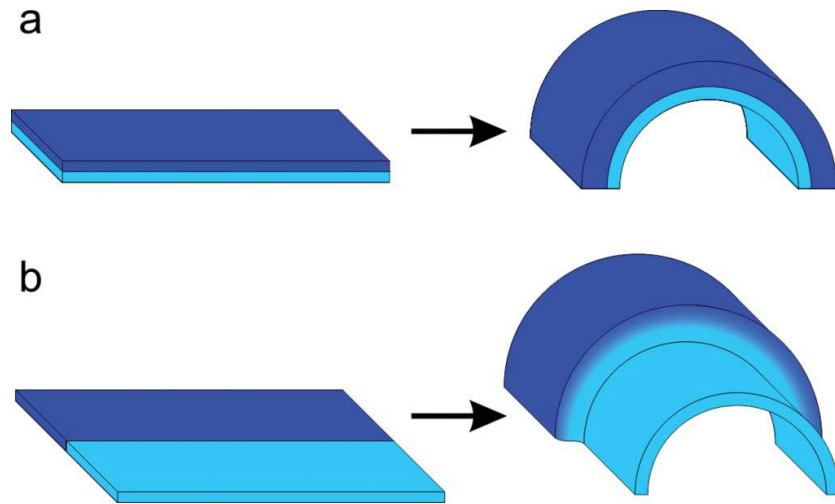


Figure 15. Bending of bilayer rectangular strips divided into high and low-swelling regions. Reproduced with permission<sup>71</sup>. Copyright 2013, Taylor & Francis.

#### 1.4.2. Fiber-based and reinforced self-folding

As already mentioned before actuation of the bilayer system highly depends on the composition and structure of bilayer. Bilayer actuation is caused by stress difference in the plane, which is achieved by strain gradients and various shapes. Depending on the actuation type, we can divide obtained shapes into three categories – basic shape change, complex shape change and combination of shape changes<sup>72</sup>. With basic shapes, simple actuation with one bending motion is described, whereas complex shapes are obtained using multiple folding, rolling, helixing, etc. Complex shapes can be easily obtained by embedding fibrous microstructures in rectangular film. After actuation, these composite films are able to form tubes or spiral-like structures<sup>73-74</sup>. Aligned, reinforced fibers in the film restrict swelling of the film along the long axis of the sample and promote swelling perpendicular to fiber alignment due to more free volume, where water can be absorbed<sup>73</sup>. Randomly aligned reinforced fibers promote swelling in all directions equally. As the film is made

by a bilayer of two different fiber-reinforced layers (aligned and random) with different swelling properties, both layers try to reach minimal energy configuration for bilayer to bend or helix<sup>75</sup>. Bending or helixing can be programmed based on fiber alignment angle, each layer thickness, and the shape of the sample (wide samples promote cylindrical helix formation, whereas narrow strips promote more twisted helix formation).

Alternatively, self-folding, bilayer systems can also be prepared using only fibers. Using electrospinning it is possible to achieve simple and complex shape changes based on fiber alignment and cutting angle of fibrous polymer mats<sup>76-77</sup> (Figure 16). Similar to the already described sample for fiber-reinforced films self-folded bilayer electrospun mats consisting of aligned and random fiber layer shows similar properties and can be programmed for simple and complex actuation<sup>77</sup>.

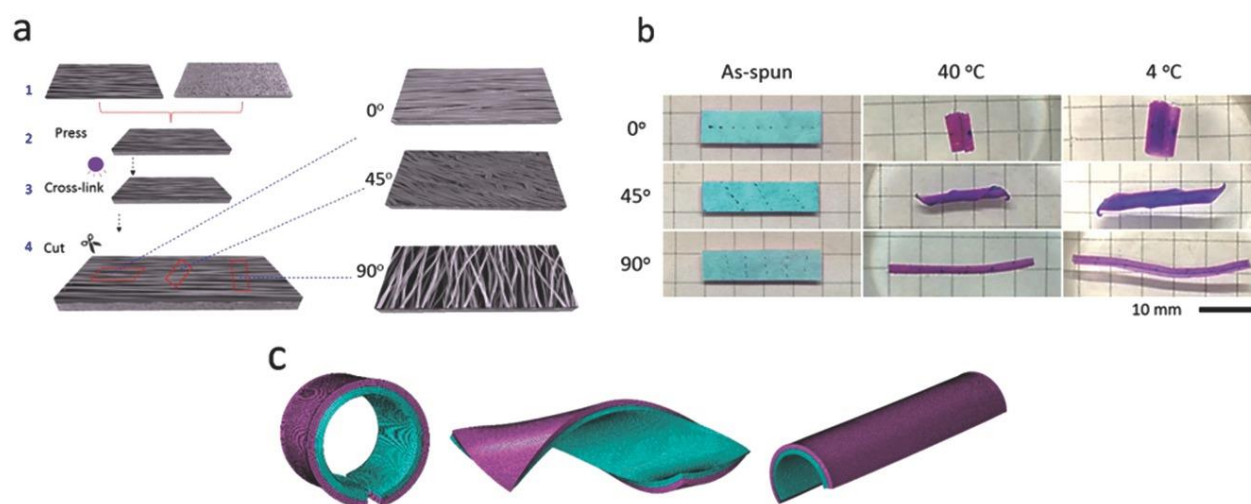


Figure 16. a) Preparation of poly(N-isopropylacrylamide) (Bi-PNIPAM-0°), Bi-PNIPAM-45°, Bi-PNIPAM-90° actuator by electrospinning of random and aligned layer; b) one component poly(NIPAM) directionally controlled actuation of Bi-PNIPAM-0°, Bi-PNIPAM-45°, Bi-PNIPAM-90° mat (random (pink)aligned (blue)); c) equilibrium shapes of bilayer in 40 °C water. Reproduced with permission<sup>77</sup>. Copyright 2016, Wiley-VCH.

In addition, multicompartment fibers have shown great potential for programmed simple or complex actuation<sup>66</sup>. Two polymers with different volume expansion properties are used for multicompartment fiber actuation, which is like bilayer actuation. Based on each component

distribution, it is possible to achieve bending, polypeptide type twisting, and DNA type twisting (Figure 17)<sup>78</sup>. Bending is achieved using fiber with two equal layers of polymer (same as for bilayer). Twisting is achieved by gradient distribution of both layers, whereas DNA twisting is based on gradient trilayer distribution. As multicompartment fiber actuation is based on a similar concept as bilayer actuation, the same design could be used for multilayer electrospun mat actuation.

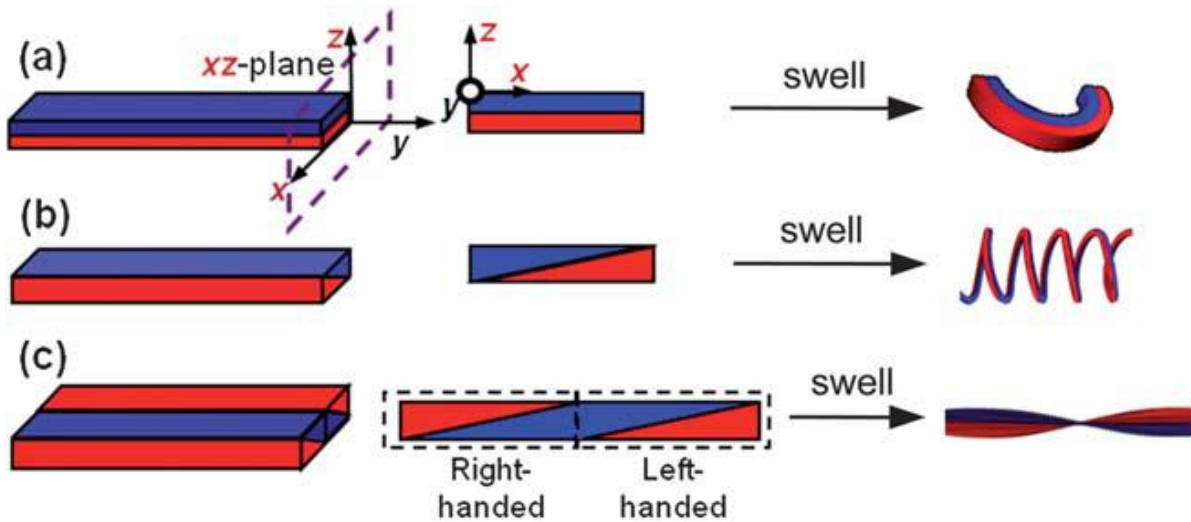


Figure 17. Schematic illustrations of deformation of multicompartment fibers (the “blue” and “red” parts with different swelling properties): (a) bending, (b) polypeptide -type twisting, (c) DNA-type twisting actuators. Reproduced with permission<sup>78</sup>. Copyright 1991, Royal Society of Chemistry.

## 1.5 Conclusion

To summarize, the self-folding approach shows great potential for the formation of complex hollow tubular and sphere-like structures that are able to mimic tissues in our body. Due to the relatively simple preparation of the initial shape of the self-folded scaffold, this technique is more cell-friendly as less stress is added to cells. There are various ways how to include cell alignment cues into the self-folded scaffold: surface topographical patterning, chemical treatment, mechanical loading and electrical stimulation. Nano- and microsized electrospun fibers have been used to obtain cell alignment for the last couple of decades and have shown good cell adhesion due to the ability to mimic fibrous ECM. Self-folding fibrous based materials have shown various advantages in comparison to other self-folded materials: extra-fast actuation rate, high permeability, and fiber guided shape transformation. Though for the use of fibrous self-folding materials for tissue

formation and regeneration biocompatible and degradable fibrous materials need to be further investigated and designed. There is as well lack of understanding of how these materials would interact with cells.

## 2. Aim

The aim of this thesis was to use the electrospinning technique to create uniaxially aligned self-folded tubular constructs for 4D biofabrication applications.

The 4D biofabrication using self-folding electrospun layers shall offer the following set of advantages, which are not available when other biofabrication techniques are used:

1. controllable, reversible 2D to 3D transformation
2. uniaxial aligned fibers for cell guidance
3. high porosity and permeability

Thus, the aim of this project can be divided into three objectives:

Objective (1) is to develop fibrous self-folding multi-layer scaffolds based on thermo-responsive polymers polycaprolactone (PCL) and poly(N-isopropylacrylamide) and determine the leading mechanism for scaffold folding behaviors under different conditions by analyzing each layer properties separately. The final task of this objective is to design the multi-layer system, which folds at 37 °C setting PCL as an inner layer for better cell adhesion.

Objective (2) is to develop a fibrous scroll-like tubular self-folding scaffold containing uniaxially aligned polycaprolactone (PCL) and anisotropic methacrylated alginate (AA-MA) fibers for muscle cell encapsulation and muscle tissue formation.

Objective (3) is to develop a degradable and biocompatible self-folding bilayer scaffold containing uniaxially aligned poly(glycerol sebacate) (PGS-PCL) and randomly aligned methacrylated hyaluronic acid (HA-MA) fibers for the fabrication of artificial nerve graft.

### 3. Synopsis

The results summarized in this dissertation are published in three first author research publications ([publication 1](#), [publication 2](#) and [publication 3](#)), and in one first author review article ([publication 4](#)). The publication list can be found in [section 5](#), and my contribution to each publication is described in [section 6](#).

The 4D biofabrication approach has been used for the research presented in this thesis. 4D biofabrication approach and use of shape-morphing materials for cell encapsulation have been developed and grown significantly over the last decade. Various smart shape-morphing materials can be used for 4D biofabrication as reviewed in [publication 4](#). In comparison to other widely used biofabrication techniques, 4D biofabrication allows reversible formation of hollow tubular shape with low shear stress and no sacrificial material<sup>6</sup>.

The aim of this work was to use the electrospinning technique to fabricate fibrous shape-morphing polymers to use for 4D biofabrication applications. The electrospinning technique was chosen for preparation of shape-morphing materials to as closely mimic native fibrous ECM by its topography and provide high permeability for designed scaffolds. Even though fibrous shape-morphing materials have been designed previously<sup>74, 76-77, 79-80</sup>, biocompatibility and degradability of these materials still need to be improved. Another important problem that needs to be further investigated is the lack of understanding of cell interaction with fibrous shape-morphing material. The first step towards improved biocompatibility for shape morphing materials is to choose an external stimulus that is biocompatible, human body temperature (37 °C) and aqueous environment can be considered as biocompatible external stimuli shown in [publication 1](#). The next step towards higher biocompatibility and degradability is to mimic certain structure, shape and morphology as well as the use of degradable materials described in [publication 2](#). Finally, cell interaction and biocompatibility can be improved as well by adjusting the mechanical properties of shape-morphing materials to a target tissue illustrated in [publication 3](#).

#### 3.1. Porous Stimuli-Responsive Self-Folding Electrospun Mats for 4D Biofabrication

Temperature-sensitive self-folding bilayer films consisting of polycaprolactone (PCL) and poly(N-isopropylacrylamide) (PNIPAM) has been previously used for yeast cell encapsulation and their folding behavior has been extensively explained<sup>23, 81-83</sup>. Electrospinning technique allows fabrication of high porosity fibers in nano- and micro-range that promotes cell adhesion, proliferation, and differentiation<sup>84</sup>. The self-folding of electrospun polymers mats differs from dip-

coated and spin-coated polymer films<sup>76</sup>. In this study, temperature-responsive bilayer mats consisting of polycaprolactone (PCL) and poly(N-isopropylacrylamide) were used to fabricate a multi-layer system that would fold in physiological conditions. Both polymer layers showed thermo-responsive properties leading to the difference of bilayer folding scenario at 20 °C and 37 °C (Figure 18). To investigate bilayer folding properties each layer thermo-responsive properties were described. As a conclusion bilayer folding properties at 20 °C is guided by slight shrinking and strong folding of poly(N-isopropylacrylamide)-benzophenone acrylate (P(NIPAM-BPA)), whereas folding behavior of bilayer in 37 °C is guided by slight contraction of PCL fibers in fiber length and strong shrinking of P(NIPAM-BPA) that sets P(NIPAM-BPA) in the middle of folded construct.

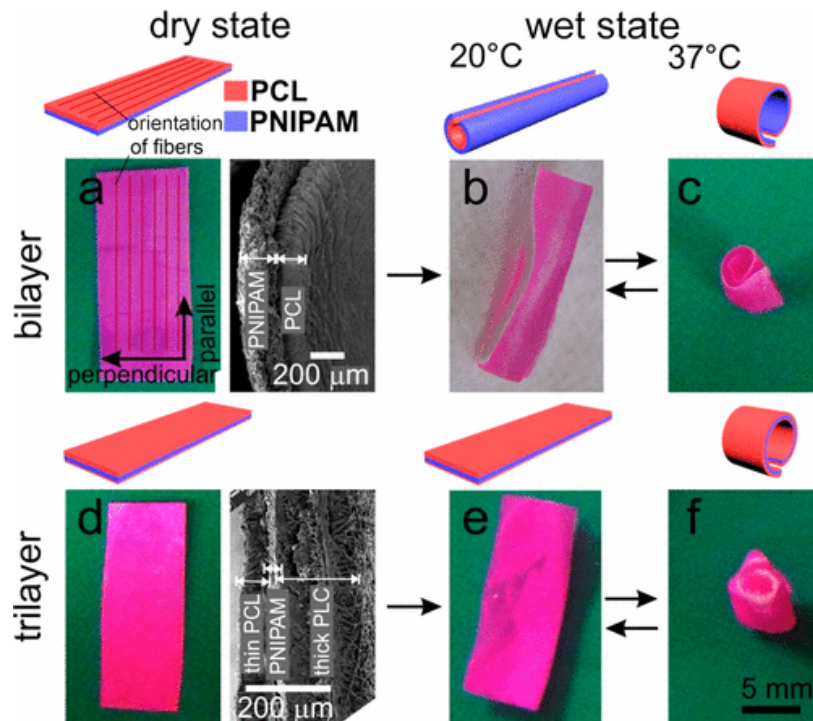


Figure 18. Responsive properties of electrospun P(NIPAM-BPA)-PCL bilayer and PCL-P(NIPAM-BPA)-PCL trilayer mats: (a) left, no folding is observed for the bilayer in air at room temperature; right, representative SEM image of a cross-section of the bilayer used to determine the layer thickness; (b) long-side rolling of the bilayer in water at 20 °C; (c) short-side rolling of the bilayer in water at 37 °C; (d) left, PCL-P(NIPAM-BPA)-PCL trilayer mat in air at room temperature–no folding; right, representative SEM image of a cross-section of the trilayer used to determine the layer thickness; (e) trilayer in water at 20 °C, no folding; (f) trilayer in water at 37 °C, short-side rolling.

To form a multi-layer system that would fold in physiological condition, an additional thin layer of PCL on top of P(NIPAM-BPA) layer was added in the bilayer system, that limited actuation of P(NIPAM-BPA) layer at 20 °C and supported cell adhesion at 37 °C as PCL is a biocompatible polymer. We improved fibroblast cell adhesion on these multi-layer substrates with collagen coating.

### 3.2. 4D Biofabrication of skeletal muscle microtissues

Skeletal muscle tissue is formed by multiple bundles consisting of parallel packed and highly aligned muscle fibers<sup>25</sup>. Various attempts have been made to mimic skeletal muscle tissue in 2D<sup>31, 85-88</sup>, though it is still challenging to use these approaches for 3D skeletal muscle modeling. Various electrospinning approaches can be to achieve high fiber alignment<sup>43, 49</sup>. In this study, biocompatible and degradable polycaprolactone (PCL) and methacrylated alginate (AA-MA) electrospun bilayer systems that can support muscle tissue growth were fabricated. Drum and parallel bar collectors were used to fabricate bilayer consisting of uniaxially aligned PCL and random AA-MA fibers. The self-folding bilayer system was designed to fold by the addition of aqueous media as external stimuli and folding reversibility was achieved by reversible crosslinking of Ca<sup>2+</sup> ions. Various folding scenarios were described based on fibrous mat geometry, each layer thickness and overall thickness of bilayer. Uniaxially aligned PCL fibers were able to guide myoblasts during cell growth and differentiation, forming aligned muscle tissue that showed contractility during electrical stimulation (Figure 19).

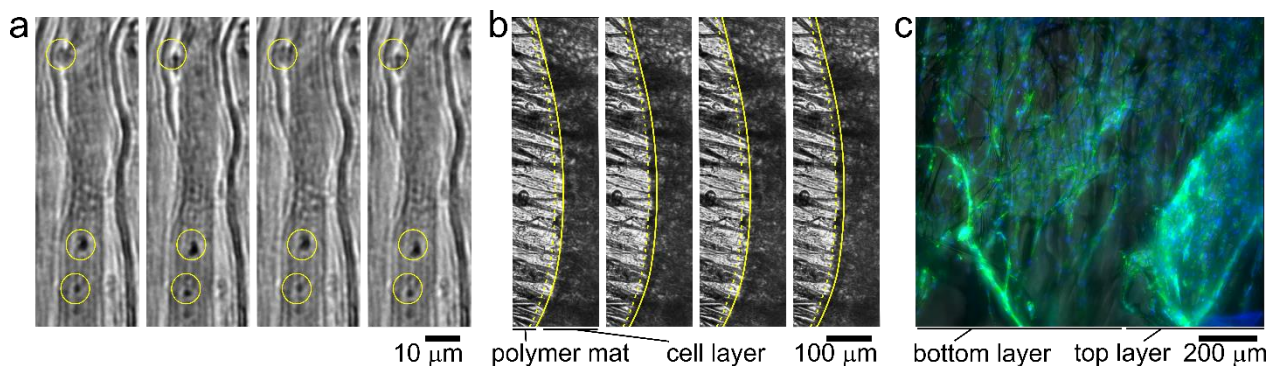


Figure 19. Contractility of the muscle fibers layer under electrical stimulation (4–5 V, frequency: 1 Hz, duration: 1 ms): functional contracting myotubes that are observed by cyclical displacement of features inside yellow circles (a); contracting cell monolayer, solid and yellow dashed lines show edge of contracted and relaxed myotubes layer, respectively (b). The time between images is 1 s;

3D projection of myoblast muscle cells on self-folded bilayer (c). Actin filament and nuclei staining using DAPI (blue) and Phalloidin (green) to evaluate the cell alignment on bilayer mats.

### 3.3 4D Biofabrication of fibrous artificial nerve grafts for neuron regeneration

Self-folding electrospun bilayers can also be used as nerve guide conduits (NGCs) for neuron regeneration. Polycaprolactone is a degradable and biocompatible material, but PCL stiffness makes it less suitable for soft tissue engineering<sup>89</sup>. Hyaluronic acid is a hydrogel that can be found in native ECM and is widely distributed in neural tissues<sup>90</sup>. Therefore, we designed a bilayer system that would consist of methacrylated hyaluronic acid (HA-MA) and polycaprolactone-poly(glycerol sebacate) (PCL-PGS) fibers making self-folding scaffold more mechanical compatible for soft tissue formation and degradable. Stiffness of PCL fibers significantly decreases after the addition of PGS to the blend, resulting in lower stiffness as well for the bilayer system. Degradation of each layer separately and bilayer was investigated, due to use of more biocompatible and degradable materials 70 % of weight loss of bilayer could be achieved during month of real-time degradation (Figure 20). Neuron cells showed high proliferation and viability on designed scaffolds.

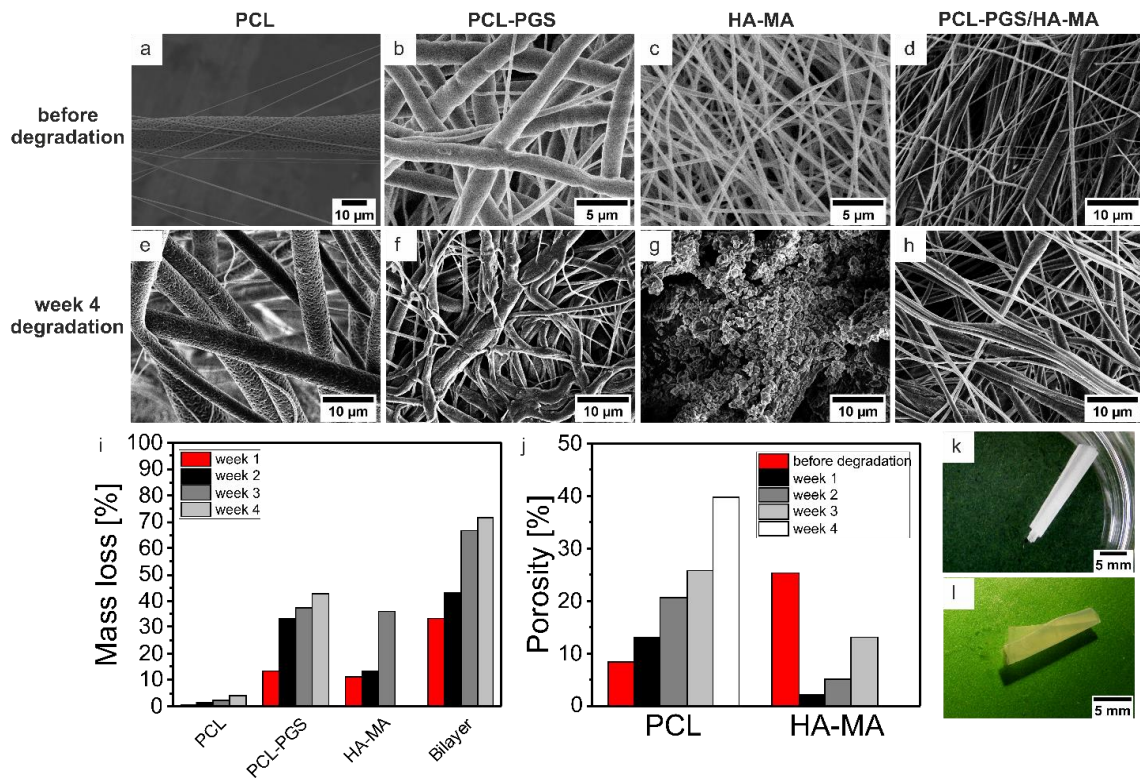


Figure 20. Degradation of electrospun fibers and bilayer scaffold: a-h) morphology of electrospun fiber PCL, PCL-PGS, HA-MA mats and PCL-PGS/HA-MA bilayer before and four weeks after

degradation; i) Mass loss of fibrous mats and bilayer scaffold during four weeks of degradation; j) Porosity change of PCL fibers and HA-MA fibrous mat during four weeks of degradation; k) Self-folded PCL-PGS/HA-MA tube before degradation; l) Self-folded PCL-PGS/HA-MA tube after four weeks of degradation

### 3.3. Conclusion and outlook

These studies have shown that fibrous shape-morphing materials can be used for hollow tubular structure formation with cell alignment for various tissues. All fabricated systems were able to fold in physiological conditions; we have shown reversible and adjustable scroll-like tubular structure formation. The highlight of this work is the formation of the functional muscle tissue layer, which can be further developed for the formation of vascularized tissue. In the future, multiple fibrous shape-morphing scaffolds can be assembled next to each other forming muscle bundles. Additionally, future experiments should involve further investigation of bilayer system application for neuron tissue regeneration and vascular network formation. Conductive fiber adoption in fibrous shape-morphing materials could improve neuron and muscle cell differentiation.

## 4. References

1. Groll, J.; Boland, T.; Blunk, T.; Burdick, J. A.; Cho, D.-W.; Dalton, P. D.; Derby, B.; Forgacs, G.; Li, Q.; Mironov, V. A.; Moroni, L.; Nakamura, M.; Shu, W.; Takeuchi, S.; Vozzi, G.; Woodfield, T. B. F.; Xu, T.; Yoo, J. J.; Malda, J., Biofabrication: reappraising the definition of an evolving field. *Biofabrication* **2016**, *8* (1), 013001.
2. Murphy, S. V.; Atala, A., 3D bioprinting of tissues and organs. *Nat. Biotechnol.* **2014**, *32*, 773.
3. Rosso, F.; Giordano, A.; Barbarisi, M.; Barbarisi, A., From Cell–ECM interactions to tissue engineering. *J. Cell. Physiol.* **2004**, *199* (2), 174-180.
4. Keely, P.; Nain, A., Capturing relevant extracellular matrices for investigating cell migration. *F1000Res* **2015**, *4*, F1000 Faculty Rev-1408.
5. Moroni, L.; Burdick, J. A.; Highley, C.; Lee, S. J.; Morimoto, Y.; Takeuchi, S.; Yoo, J. J., Biofabrication strategies for 3D in vitro models and regenerative medicine. *Nature Reviews Materials* **2018**, *3* (5), 21-37.
6. Ionov, L., 4D Biofabrication: Materials, Methods, and Applications. *Advanced Healthcare Materials* **2018**, *7* (17), 1800412.
7. Ding, H. C., R.C. , Printability Study of Bioprinted Tubular Structures Using Liquid Hydrogel Precursors in a Support Bath. *Applied Sciences* **2018**, *8* (3), 16.
8. Sarker, M. D.; Naghieh, S.; Sharma, N. K.; Chen, X., 3D biofabrication of vascular networks for tissue regeneration: A report on recent advances. *Journal of Pharmaceutical Analysis* **2018**, *8* (5), 277-296.
9. Gao, Q.; He, Y.; Fu, J.-z.; Liu, A.; Ma, L., Coaxial nozzle-assisted 3D bioprinting with built-in microchannels for nutrients delivery. *Biomaterials* **2015**, *61*, 203-215.
10. Jia, W.; Gungor-Ozkerim, P. S.; Zhang, Y. S.; Yue, K.; Zhu, K.; Liu, W.; Pi, Q.; Byambaa, B.; Dokmeci, M. R.; Shin, S. R.; Khademhosseini, A., Direct 3D bioprinting of perfusable vascular constructs using a blend bioink. *Biomaterials* **2016**, *106*, 58-68.
11. Kolesky, D. B.; Truby, R. L.; Gladman, A. S.; Busbee, T. A.; Homan, K. A.; Lewis, J. A., 3D Bioprinting of Vascularized, Heterogeneous Cell-Laden Tissue Constructs. *Adv. Mater.* **2014**, *26* (19), 3124-3130.
12. Kolesky, D. B.; Homan, K. A.; Skylar-Scott, M. A.; Lewis, J. A., Three-dimensional bioprinting of thick vascularized tissues. *Proceedings of the National Academy of Sciences* **2016**, *113* (12), 3179.
13. Wu, W.; DeConinck, A.; Lewis, J. A., Omnidirectional Printing of 3D Microvascular Networks. *Adv. Mater.* **2011**, *23* (24), H178-H183.
14. Miller, J. S.; Stevens, K. R.; Yang, M. T.; Baker, B. M.; Nguyen, D.-H. T.; Cohen, D. M.; Toro, E.; Chen, A. A.; Galie, P. A.; Yu, X.; Chaturvedi, R.; Bhatia, S. N.; Chen, C. S., Rapid casting of patterned vascular networks for perfusable engineered three-dimensional tissues. *Nature Materials* **2012**, *11* (9), 768-774.
15. Holland, I.; Logan, J.; Shi, J.; McCormick, C.; Liu, D.; Shu, W., 3D biofabrication for tubular tissue engineering. *Bio-Design and Manufacturing* **2018**, *1* (2), 89-100.
16. Kirillova, A.; Maxson, R.; Stoychev, G.; Gomillion, C. T.; Ionov, L., 4D Biofabrication Using Shape-Morphing Hydrogels. *Adv. Mater.* **2017**, *29* (46), 1703443.
17. Miao, S.; Zhu, W.; Castro, N. J.; Nowicki, M.; Zhou, X.; Cui, H.; Fisher, J. P.; Zhang, L. G., 4D printing smart biomedical scaffolds with novel soybean oil epoxidized acrylate. *Sci. Rep.* **2016**, *6*, 27226.

18. Stroganov, V.; Pant, J.; Stoychev, G.; Janke, A.; Jehnichen, D.; Fery, A.; Handa, H.; Ionov, L., 4D Biofabrication: 3D Cell Patterning Using Shape-Changing Films. *Adv. Funct. Mater.* **2018**, *28* (11), 1706248.
19. Li, Y.-C.; Zhang, Y. S.; Akpek, A.; Shin, S. R.; Khademhosseini, A., 4D bioprinting: the next-generation technology for biofabrication enabled by stimuli-responsive materials. *Biofabrication* **2016**, *9* (1), 012001.
20. Na, J.-H.; Evans, A. A.; Bae, J.; Chiappelli, M. C.; Santangelo, C. D.; Lang, R. J.; Hull, T. C.; Hayward, R. C., Programming Reversibly Self-Folding Origami with Micropatterned Photo-Crosslinkable Polymer Trilayers. *Adv. Mater.* **2015**, *27* (1), 79-85.
21. Stoychev, G.; Guiducci, L.; Turcaud, S.; Dunlop, J. W. C.; Ionov, L., Hole-Programmed Superfast Multistep Folding of Hydrogel Bilayers. *Adv. Funct. Mater.* **2016**, *26* (42), 7733-7739.
22. Zakharchenko, S.; Puretskiy, N.; Stoychev, G.; Stamm, M.; Ionov, L., Temperature controlled encapsulation and release using partially biodegradable thermo-magneto-sensitive self-rolling tubes. *Soft Matter* **2010**, *6* (12), 2633-2636.
23. Stoychev, G.; Puretskiy, N.; Ionov, L., Self-folding all-polymer thermoresponsive microcapsules. *Soft Matter* **2011**, *7* (7), 3277-3279.
24. A Self-Folding Hydrogel In Vitro Model for Ductal Carcinoma. *Tissue Engineering Part C: Methods* **2016**, *22* (4), 398-407.
25. Li, Y.; Huang, G.; Zhang, X.; Wang, L.; Du, Y.; Lu, T. J.; Xu, F., Engineering cell alignment in vitro. *Biotechnol. Adv.* **2014**, *32* (2), 347-365.
26. Zhu, M.; Wang, Z.; Zhang, J.; Wang, L.; Yang, X.; Chen, J.; Fan, G.; Ji, S.; Xing, C.; Wang, K.; Zhao, Q.; Zhu, Y.; Kong, D.; Wang, L., Circumferentially aligned fibers guided functional neovessel regeneration in vivo. *Biomaterials* **2015**, *61*, 85-94.
27. Duan, Y.; Gotoh, N.; Yan, Q.; Du, Z.; Weinstein, A. M.; Wang, T.; Weinbaum, S., Shear-induced reorganization of renal proximal tubule cell actin cytoskeleton and apical junctional complexes. *Proceedings of the National Academy of Sciences* **2008**, *105* (32), 11418-11423.
28. Bartels, E. M.; Danneskiold-Samsøe, B., HISTOLOGICAL ABNORMALITIES IN MUSCLE FROM PATIENTS WITH CERTAIN TYPES OF FIBROSITIS. *The Lancet* **1986**, *327* (8484), 755-757.
29. Guénard, V.; Kleitman, N.; Morrissey, T. K.; Bunge, R. P.; Aebischer, P., Syngeneic Schwann cells derived from adult nerves seeded in semipermeable guidance channels enhance peripheral nerve regeneration. *The Journal of neuroscience : the official journal of the Society for Neuroscience* **1992**, *12* (9), 3310-3320.
30. Novitskaya, E.; Chen, P.-Y.; Lee, S.; Castro-Ceseña, A.; Hirata, G.; Lubarda, V. A.; McKittrick, J., Anisotropy in the compressive mechanical properties of bovine cortical bone and the mineral and protein constituents. *Acta Biomater.* **2011**, *7* (8), 3170-3177.
31. Hosseini, V.; Ahadian, S.; Ostrovidov, S.; Camci-Unal, G.; Chen, S.; Kaji, H.; Ramalingam, M.; Khademhosseini, A., Engineered contractile skeletal muscle tissue on a microgrooved methacrylated gelatin substrate. *Tissue Eng Part A* **2012**, *18* (23-24), 2453-2465.
32. Tamayol, A.; Akbari, M.; Annabi, N.; Paul, A.; Khademhosseini, A.; Juncker, D., Fiber-based tissue engineering: Progress, challenges, and opportunities. *Biotechnol. Adv.* **2013**, *31* (5), 669-687.
33. Fujie, T.; Shi, X.; Ostrovidov, S.; Liang, X.; Nakajima, K.; Chen, Y.; Wu, H.; Khademhosseini, A., Spatial coordination of cell orientation directed by nanoribbon sheets. *Biomaterials* **2015**, *53*, 86-94.
34. Kuo, C. J.; Lan, W. L., 5 - Gel spinning of synthetic polymer fibres. In *Advances in Filament Yarn Spinning of Textiles and Polymers*, Zhang, D., Ed. Woodhead Publishing: 2014; pp 100-112.

35. Collins, G.; Federici, J.; Imura, Y.; Catalani, L. H., Charge generation, charge transport, and residual charge in the electrospinning of polymers: A review of issues and complications. *J. Appl. Phys.* **2012**, *111* (4), 044701.
36. Li, X.; Wang, X.; Yao, D.; Jiang, J.; Guo, X.; Gao, Y.; Li, Q.; Shen, C., Effects of aligned and random fibers with different diameter on cell behaviors. *Colloids Surf. B. Biointerfaces* **2018**, *171*, 461-467.
37. Liu, C.; Zhu, C.; Li, J.; Zhou, P.; Chen, M.; Yang, H.; Li, B., The effect of the fibre orientation of electrospun scaffolds on the matrix production of rabbit annulus fibrosus-derived stem cells. *Bone Research* **2015**, *3*, 15012.
38. Dalton, P. D., Melt electrowriting with additive manufacturing principles. *Current Opinion in Biomedical Engineering* **2017**, *2*, 49-57.
39. Hrynevich, A.; Elçi, B. Ş.; Haigh, J. N.; McMaster, R.; Youssef, A.; Blum, C.; Blunk, T.; Hochleitner, G.; Groll, J.; Dalton, P. D., Dimension-Based Design of Melt Electrowritten Scaffolds. *Small* **2018**, *14* (22), 1800232.
40. Dalton, P. D.; Klinkhammer, K.; Salber, J.; Klee, D.; Möller, M., Direct in Vitro Electrospinning with Polymer Melts. *Biomacromolecules* **2006**, *7* (3), 686-690.
41. Cai, S.; Xu, H.; Jiang, Q.; Yang, Y., Novel 3D Electrospun Scaffolds with Fibers Oriented Randomly and Evenly in Three Dimensions to Closely Mimic the Unique Architectures of Extracellular Matrices in Soft Tissues: Fabrication and Mechanism Study. *Langmuir* **2013**, *29* (7), 2311-2318.
42. Rnjak-Kovacina, J.; Weiss, A., Increasing the Pore Size of Electrospun Scaffolds. *Tissue engineering. Part B, Reviews* **2011**, *17*, 365-72.
43. Liu, W.; Thomopoulos, S.; Xia, Y., Electrospun Nanofibers for Regenerative Medicine. *Advanced Healthcare Materials* **2012**, *1* (1), 10-25.
44. Yawen Li, T. B. A., Electrospinning in Tissue Engineering. In *Electrospinning - Material, Techniques, and Biomedical Applications*, Haider, S. H. a. A., Ed. IntechOpen: 2016.
45. Teo, W. E.; Ramakrishna, S., A review on electrospinning design and nanofibre assemblies. *Nanotechnology* **2006**, *17* (14), R89-R106.
46. Li, D.; Wang, Y.; Xia, Y., Electrospinning of Polymeric and Ceramic Nanofibers as Uniaxially Aligned Arrays. *Nano Lett.* **2003**, *3* (8), 1167-1171.
47. Beachley, V.; Wen, X., Effect of electrospinning parameters on the nanofiber diameter and length. *Materials Science and Engineering: C* **2009**, *29* (3), 663-668.
48. Teo, W.-E., *Order from Chaos in Electrospinning*. ElectrospinTech: 2015; p 64.
49. Liu, L.; A Dzenis, Y., *Analysis of the Effects of the Residual Charge and Gap Size on Electrospun Nanofiber Alignment in a Gap Method*. 2008; Vol. 19, p 355307.
50. Secasanu, V. P.; Giardina, C. K.; Wang, Y., A novel electrospinning target to improve the yield of uniaxially aligned fibers. *Biotechnol. Progr.* **2009**, *25* (4), 1169-1175.
51. Brennan, D. A.; Jao, D.; Siracusa, M. C.; Wilkinson, A. R.; Hu, X.; Beachley, V. Z., Concurrent collection and post-drawing of individual electrospun polymer nanofibers to enhance macromolecular alignment and mechanical properties. *Polymer* **2016**, *103*, 243-250.
52. Yang, D.; Lu, B.; Zhao, Y.; Jiang, X., Fabrication of Aligned Fibrous Arrays by Magnetic Electrospinning. *Adv. Mater.* **2007**, *19* (21), 3702-3706.
53. Liu, Y.; Zhang, X.; Xia, Y.; Yang, H., Magnetic-Field-Assisted Electrospinning of Aligned Straight and Wavy Polymeric Nanofibers. *Adv. Mater.* **2010**, *22* (22), 2454-2457.
54. Li, Z.; Wang, C., Effects of Working Parameters on Electrospinning. In *One-Dimensional nanostructures: Electrospinning Technique and Unique Nanofibers*, Li, Z.; Wang, C., Eds. Springer Berlin Heidelberg: Berlin, Heidelberg, 2013; pp 15-28.

55. Bonino, C. A.; Krebs, M. D.; Saquing, C. D.; Jeong, S. I.; Shearer, K. L.; Alsberg, E.; Khan, S. A., Electrospinning alginate-based nanofibers: From blends to crosslinked low molecular weight alginate-only systems. *Carbohydr. Polym.* **2011**, *85* (1), 111-119.
56. Yang, Q.; Li, Z.; Hong, Y.; Zhao, Y.; Qiu, S.; Wang, C.; Wei, Y., Influence of solvents on the formation of ultrathin uniform poly(vinyl pyrrolidone) nanofibers with electrospinning. *J. Polym. Sci., Part B: Polym. Phys.* **2004**, *42* (20), 3721-3726.
57. Fang, D.; Liu, Y.; Jiang, S.; Nie, J.; Ma, G., Effect of intermolecular interaction on electrospinning of sodium alginate. *Carbohydr. Polym.* **2011**, *85* (1), 276-279.
58. Huang, C.; Chen, S.; Lai, C.; Reneker, D. H.; Qiu, H.; Ye, Y.; Hou, H., Electrospun polymer nanofibres with small diameters. *Nanotechnology* **2006**, *17* (6), 1558-1563.
59. Teo, W.-E., *Introduction to Electrospinning Parameters and Fiber Control* ElectrospinTech: 2015; p 41.
60. Schubert, D. W., Revealing Novel Power Laws and Quantization in Electrospinning Considering Jet Splitting—Toward Predicting Fiber Diameter and Its Distribution. *Macromol. Theory Simul.* **2019**, *28* (4), 1900006.
61. Ki, C. S.; Kim, J. W.; Hyun, J. H.; Lee, K. H.; Hattori, M.; Rah, D. K.; Park, Y. H., Electrospun three-dimensional silk fibroin nanofibrous scaffold. *J. Appl. Polym. Sci.* **2007**, *106* (6), 3922-3928.
62. Casper, C. L.; Stephens, J. S.; Tassi, N. G.; Chase, D. B.; Rabolt, J. F., Controlling Surface Morphology of Electrospun Polystyrene Fibers: Effect of Humidity and Molecular Weight in the Electrospinning Process. *Macromolecules* **2004**, *37* (2), 573-578.
63. Sun, D.; Chang, C.; Li, S.; Lin, L., Near-Field Electrospinning. *Nano Lett.* **2006**, *6* (4), 839-842.
64. Deitzel, J. M.; Kleinmeyer, J. D.; Hirvonen, J. K.; Beck Tan, N. C., Controlled deposition of electrospun poly(ethylene oxide) fibers. *Polymer* **2001**, *42* (19), 8163-8170.
65. Timoshenko, S., Analysis of Bi-Metal Thermostats. *J. Opt. Soc. Am.* **1925**, *11* (3), 233-255.
66. Stoychev, G. V.; Ionov, L., Actuating Fibers: Design and Applications. *ACS Applied Materials & Interfaces* **2016**, *8* (37), 24281-24294.
67. Mohamed, M. A.; Fallahi, A.; El-sokkary, A. M. A.; Salehi, S.; Akl, M. A.; Jafari, A.; Tamayol, A.; Fenniri, H.; Khademhosseini, A.; Andreadis, S. T.; Cheng, C., Stimuli-Responsive Hydrogels for Manipulation of Cell Microenvironment: From Chemistry to Biofabrication Technology. *Prog. Polym. Sci.* **2019**, 101147.
68. Flory, P. J., Thermodynamics of High Polymer Solutions. *The Journal of Chemical Physics* **1941**, *9* (8), 660-660.
69. Khokhlov, A. R.; Khalatur, P. G., Conformation-Dependent Sequence Design (Engineering) of  $\{AB\}$  Copolymers. *Phys. Rev. Lett.* **1999**, *82* (17), 3456-3459.
70. Ionov, L., Biomimetic Hydrogel-Based Actuating Systems. *Adv. Funct. Mater.* **2013**, *23* (36), 4555-4570.
71. Ionov, L., 3D Microfabrication using Stimuli-Responsive Self-Folding Polymer Films. *Polymer Reviews* **2013**, *53* (1), 92-107.
72. Nam, S.; Pei, E., A taxonomy of shape-changing behavior for 4D printed parts using shape-memory polymers. *Progress in Additive Manufacturing* **2019**, *4* (2), 167-184.
73. Erb, R. M.; Sander, J. S.; Grisch, R.; Studart, A. R., Self-shaping composites with programmable bioinspired microstructures. *Nature Communications* **2013**, *4*, 1712.
74. Liu, L.; Bakhshi, H.; Jiang, S.; Schmalz, H.; Agarwal, S., Composite Polymeric Membranes with Directionally Embedded Fibers for Controlled Dual Actuation. *Macromol. Rapid Commun.* **2018**, *39* (10), 1800082.

75. Armon, S.; Efrati, E.; Kupferman, R.; Sharon, E., Geometry and Mechanics in the Opening of Chiral Seed Pods. *Science* **2011**, 333 (6050), 1726-1730.
76. Jiang, S.; Liu, F.; Lerch, A.; Ionov, L.; Agarwal, S., Unusual and Superfast Temperature-Triggered Actuators. *Adv. Mater.* **2015**, 27 (33), 4865-4870.
77. Liu, L.; Ghaemi, A.; Gekle, S.; Agarwal, S., One-Component Dual Actuation: Poly(NIPAM) Can Actuate to Stable 3D Forms with Reversible Size Change. *Adv. Mater.* **2016**, 28 (44), 9792-9796.
78. Jeong, K.-U.; Jang, J.-H.; Kim, D.-Y.; Nah, C.; Lee, J. H.; Lee, M.-H.; Sun, H.-J.; Wang, C.-L.; Cheng, S. Z. D.; Thomas, E. L., Three-dimensional actuators transformed from the programmed two-dimensional structures via bending, twisting and folding mechanisms. *J. Mater. Chem.* **2011**, 21 (19), 6824-6830.
79. Chen, T.; Bakhshi, H.; Liu, L.; Ji, J.; Agarwal, S., Combining 3D Printing with Electrospinning for Rapid Response and Enhanced Designability of Hydrogel Actuators. *Adv. Funct. Mater.* **2018**, 28 (19), 1800514.
80. Sydney Gladman, A.; Matsumoto, E. A.; Nuzzo, R. G.; Mahadevan, L.; Lewis, J. A., Biomimetic 4D printing. *Nature Materials* **2016**, 15, 413.
81. Zakharchenko, S.; Ionov, L., Anisotropic Liquid Microcapsules from Biomimetic Self-Folding Polymer Films. *ACS Applied Materials & Interfaces* **2015**, 7 (23), 12367-12372.
82. Zakharchenko, S.; Puretskiy, N.; Stoychev, G.; Waurisch, C.; Hickey, S. G.; Eychmüller, A.; Sommer, J.-U.; Ionov, L., Stimuli-responsive hierarchically self-assembled 3D porous polymer-based structures with aligned pores. *Journal of Materials Chemistry B* **2013**, 1 (13), 1786-1793.
83. Stoychev, G.; Zakharchenko, S.; Turcaud, S.; Dunlop, J. W. C.; Ionov, L., Shape-Programmed Folding of Stimuli-Responsive Polymer Bilayers. *ACS Nano* **2012**, 6 (5), 3925-3934.
84. Tan, G. Z.; Zhou, Y., Tunable 3D Nanofiber Architecture of Polycaprolactone by Divergence Electrospinning for Potential Tissue Engineering Applications. *Nano-Micro Letters* **2018**, 10 (4), 73.
85. Bajaj, P.; Reddy, B., Jr.; Millet, L.; Wei, C.; Zorlutuna, P.; Bao, G.; Bashir, R., Patterning the differentiation of C2C12 skeletal myoblasts. *Integrative Biology* **2011**, 3 (9), 897-909.
86. Ebrahimi, M.; Ostrovidov, S.; Salehi, S.; Kim, S. B.; Bae, H.; Khademhosseini, A., Enhanced skeletal muscle formation on microfluidic spun gelatin methacryloyl (GelMA) fibres using surface patterning and agrin treatment. *J. Tissue Eng. Regen. Med.* **2018**, 12 (11), 2151-2163.
87. Ku, S. H.; Lee, S. H.; Park, C. B., Synergic effects of nanofiber alignment and electroactivity on myoblast differentiation. *Biomaterials* **2012**, 33 (26), 6098-6104.
88. Sun, Y.; Duffy, R.; Lee, A.; Feinberg, A. W., Optimizing the structure and contractility of engineered skeletal muscle thin films. *Acta Biomater.* **2013**, 9 (8), 7885-7894.
89. Tan, P. S.; Teoh, S. H., Effect of stiffness of polycaprolactone (PCL) membrane on cell proliferation. *Materials Science and Engineering: C* **2007**, 27 (2), 304-308.
90. Drury, J. L.; Mooney, D. J., Hydrogels for tissue engineering: scaffold design variables and applications. *Biomaterials* **2003**, 24 (24), 4337-4351.

## 5. Publication list

\* Authors contributed equally to this work

1. **Apsite I.**, Stoychev G., Zhang W., Jehnichen D., Xie J., Ionov L. Porous Stimuli-Responsive Self-Folding Electrospun Mats for 4D Biofabrication (2017). *Biomacromolecules*, 18, 3178-3184. <https://doi.org/10.1021/acs.biomac.7b00829>
2. **Apsite I.**, Uribe M. J., Posada F. A., Rosenfeldt S., Salehi S., Ionov L. 4D biofabrication of skeletal muscle microtissues (2019). *Biofabrication*, 12, 2020, 015016. <https://doi.org/10.1088/1758-5090/ab4cc4>
3. **Apsite I.**, Constante G., Dulle M., Vogt L., Caspari A., Boccaccini R. A., Synytska A., Salehi S., Ionov L. 4D Biofabrication of fibrous artificial nerve grafts for neuron regeneration (2020). *Biofabrication*, 12, 2020, 035027. <https://doi.org/10.1088/1758-5090/ab94cf>
4. **Apsite I.\***, Biswas A.\*, Li Y., Ionov L. Microfabrication Using Shape-Transforming Soft Materials (2020). *Advanced Functional Materials*, 1908028. <https://doi.org/10.1002/adfm.201908028>

## 6. Individual contribution to publications and manuscripts

\* Authors contributed equally to this work

1. **Apsite I.**, Stoychev G., Zhang W., Jehnichen D., Xie J., Ionov L. Porous Stimuli-Responsive Self-Folding Electrospun Mats for 4D Biofabrication (2017). *Biomacromolecules*, 18, 3178-3184. <https://doi.org/10.1021/acs.biomac.7b00829>

The concept of research was developed by Georgi Stoychev, Leonid Ionov, and myself. Cell culture studies were carried out by Weizhong Zhang and myself. SAXS and WAXS experiments were carried out by Dieter Jehnichen. Material and sample preparation, DSC, DMA, characterization of responsive properties was done by myself. Prof. Jin Xie provided facilities, equipment and valuable advice for cell culture experiments. The manuscript (text and images) was created by myself and modified by Georgi Stoychev and Prof. Leonid Ionov. Prof. Leonid Ionov supervised the project and contributed to the completion of the manuscript.

2. **Apsite I.**, Uribe M. J., Posada F. A., Rosenfeldt S., Salehi S., Ionov L. 4D biofabrication of skeletal muscle microtissues (2019). *Biofabrication*, 12, 2020, 015016. <https://doi.org/10.1088/1758-5090/ab4cc4>

The concept of research was developed by Sahar Salehi, Leonid Ionov, and myself. DMA experiments were carried out by Juan Manuel Uribe, Andres Fernando Posada, and myself. Cell culture studies were carried out by Sahar Salehi and myself. SAXS and WAXS experiments were carried out by Sabine Rosenfeldt. Material and sample preparation, SEM, DSC, Rheology, and characterization of responsive properties was done by myself. The manuscript (text and images) was created by myself and modified by Sahar Salehi and Prof. Leonid Ionov. Prof. Leonid Ionov supervised the project and contributed to the completion of the manuscript.

3. **Apsite I.**, Constante G., Dulle M., Vogt L., Caspari A., Boccaccini R. A., Synytska A., Salehi S., Ionov L. (2020). *Biofabrication*, 12, 2020, 035027. <https://doi.org/10.1088/1758-5090/ab94cf>

The concept of research was developed by Leonid Ionov, and myself. The concept of cell culture research was developed by Sahar Salehi and myself. DMA, Rheology, real-time degradation and cell culture studies were carried out by Gissela Constante and myself. SAXS and WAXS experiments were carried out by Martin Dulle. Material and sample preparation, SEM, TGA, characterization of responsive properties was done by myself. Aldo Boccaccini and Lena Vogt provided PGS pre-polymer for this research. Zeta potential measurements done by Anja Caspari and Alla Synytska. The manuscript (text and images) was created by myself and modified by Sahar Salehi and Prof. Leonid Ionov. Prof. Leonid Ionov supervised the project and contributed to the completion of the manuscript.

4. **Apsite I.\***, Biswas A.\*, Li Y., Ionov L. Microfabrication Using Shape-Transforming Soft Materials (2020). *Advanced Functional Materials*, 1908028.  
<https://doi.org/10.1002/adfm.201908028>

The concept for the publication was developed by Arpan Biswas, Leonid Ionov and myself. The manuscript (text and figures) was created by Arpan Biswas, Yuki Li, and myself. Prof. Leonid Ionov supervised the project and contributed to the completion of the manuscript.



## Publications

### Part 1. Porous Stimuli-Responsive Self-Folding Electrospun Mats for 4D Biofabrication

**Apsite I.**, Stoychev G., Zhang W., Jehnichen D., Xie J., Ionov L.

Published in *Biomacromolecules*, 18, 3178-3184

(2017)

Reprinted with kind permission from ACS Publications



## Porous Stimuli-Responsive Self-Folding Electrospun Mats for 4D Biofabrication

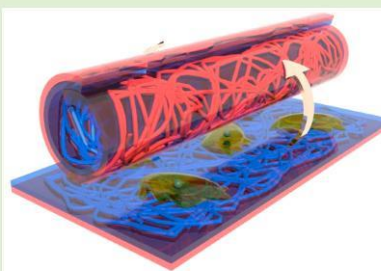
Indra Apsite,<sup>†,‡</sup> Georgi Stoychev,<sup>†,‡</sup> Weizhong Zhang,<sup>§</sup> Dieter Jehnichen,<sup>||</sup> Jin Xie,<sup>§,⊞</sup> and Leonid Ionov<sup>\*,†,‡,⊞,⊠</sup>

<sup>†</sup>College of Family and Consumer Sciences, <sup>‡</sup>College of Engineering, and <sup>§</sup>Department of Chemistry, University of Georgia, Athens, Georgia 30602, United States

<sup>||</sup>Leibniz-Institut für Polymerforschung Dresden e.V., 01069 Dresden, Germany

<sup>⊠</sup>University of Bayreuth, 95447 Bayreuth, Germany

**ABSTRACT:** We report fabrication and characterization of electrospun, porous multi-layer scaffolds based on thermo-responsive polymers polycaprolactone (PCL) and poly(*N*-isopropylacrylamide). We found that the electrospun mats fold into various 3D structures in an aqueous environment at different temperatures. We could determine the mechanism behind different folding behaviors under different conditions by consideration of the properties of the individual polymers. At 37 °C in an aqueous environment, the scaffolds spontaneously rolled into tubular structures with PCL as the inner layer, making them suitable for cell encapsulation. We also demonstrated that the cell adhesion and viability could be improved by coating the polymers with collagen, showing the suitability of this scaffold for several tissue engineering applications.



Tissue engineering is a rapidly expanding field that applies the principles of biology and engineering to develop functional substitutes for tissues and organs.<sup>1</sup> Numerous approaches have been suggested through the years aiming for creating cell-laden 3D bioscaffolds that can sustain cell proliferation and differentiation.<sup>2–6</sup> One of the most important problems is the controlled spatiotemporal encapsulation of the seeded cells inside the artificial 3D structure. Another vital requirement is that the scaffolds exhibit sufficient porosity for further vascularization in order to allow for oxygen and nutrients to reach all cells. Many recent developments target specifically one or another problem. For example, porous scaffolds have been prepared by salt leaching, gas foaming, freeze-drying,<sup>7</sup> electrospinning, and 3D printing, as well as using other approaches.<sup>8,9</sup> In recent years, researchers have also investigated a more convenient method using multiple physically and chemically cross-linked hydrogels for cell encapsulation purposes.<sup>10–14</sup> Although gels have shown really promising properties for cell encapsulation, their mesh size is usually in nanoscale, which restricts cell migration and makes it more applicable to small molecule and enzyme encapsulation.<sup>15</sup> In addition, polymer gels in comparison with a natural extracellular matrix are isotropic, so they can not completely mimic natural conditions in the human body.

Recently, self-folding polymer films have been proposed as an alternative method for the preparation of 3D scaffolds.<sup>16–19</sup> They provide a combination of homogeneous distribution of cells, intrinsic to the hydrogel-based approach, and microporosity, intrinsic to scaffolds.<sup>20</sup> The essence of this method is to create first 2D cellular array and then to let it change its

shape that leads to formation of 3D cellular structures.<sup>21</sup> These films consist of two polymer layers; one of them is stimuli-responsive.<sup>22–24</sup> Although current self-folding films consisting of a hydrogel and a hydrophobic polymer layer have a lot of advantages like homogeneous cell seeding; not only these films have low solvent permeability though the walls that restrain nutrient transport to cell growth but also increase folding time. There are few reports about the fabrication of porous self-folding films using electrospinning.<sup>23</sup> In comparison to hydrogels, electrospun fiber mats have porosity on the scale of micrometers that favors cell adhesion, proliferation, migration, and differentiation.<sup>25</sup> Anisotropic fibrous structure of these bilayers shows close resemblance to natural extracellular matrix. It has been shown that folding of electrospun mats differ from that of polymer films obtained by spin- or dipcoating.<sup>23</sup> Although it appears that self-folding electrospun mats are promising for fabrication of porous 3D cellular structures, their application is restricted by unclearness of folding mechanisms and unavailability of information about their interactions with mammalian cells.

Therefore, in this paper, we reveal mechanisms of actuation of electrospun trilayer mats and investigate their interaction with cells. In our trilayer system, we use electrospun polycaprolactone (PCL) fibers considering biocompatibility of polymer for *in vivo* and *in vitro* studies. In addition PCL is one

Received: June 13, 2017

Revised: August 10, 2017

Published: August 25, 2017

of the most used polymer for different biological applications: scaffolds, drug delivery systems, sutures, and even bone grafts.<sup>26</sup> Second layer of fibers is spun using thermoresponsive poly(*N*-isopropylacrylamide) (PNIPAM). PNIPAM is one of the most studied thermoresponsive polymer.<sup>27</sup> Because of high sensitivity to temperature, this polymer is widely used in biomaterial science.<sup>28</sup> Studies have showed promising results for various tissues: intervertebral discs, adipose, cardiac, and bone.<sup>29–32</sup> We demonstrate in this paper that the trilayer PCL–PNIPAM–PCL mat is able to fold in physiological conditions and it is suitable for encapsulation of cells.

## EXPERIMENTAL SECTION

**Materials.** 4-Hydroxybenzophenone (BPA) (Aldrich), polycaprolactone ( $M_n = 80000$ , Aldrich), rhodamine B (Aldrich), ethyl ether anhydrous (Fisher), acetone (Fisher), *N,N*-dimethylformamide (Acros organics), 1,4-dioxane (Fisher), chloroform (Fisher), thiazolyl blue tetrazolium bromide (Sigma-Aldrich), and 0.1% calf skin collagen in 0.1 M acetic acid (Aldrich) were used as received. *N*-Isopropylacrylamide (NIPAM, Aldrich) was recrystallized from hexane and 2,2'-azobis(2-methyl-propionitrile) (AIBN, Aldrich) was recrystallized from methanol. Murine embryo fibroblast cell line, NIH/3T3, was purchased from ATCC (Manassas, VA).

**Synthesis of P(NIPAM-BPA).** NIPAM (48.5 g), 4-hydroxybenzophenone (1.914 g), and AIBN (0.143 g) were dissolved in 150 mL of dioxane in a 500 mL flask. The solution was purged with nitrogen for 30 min to remove oxygen. The polymerization was carried out at 70 °C overnight under nitrogen atmosphere and constant stirring. The polymer was precipitated in diethyl ether and dried at 60 °C under vacuum.

**Electrospinning.** The electrospinning setup consisted of a multisyringe pump (Fusion 200 Chemyx Inc.), a custom made multiple needle holder with variable distance between the needles, and a Spraybase electrospinning equipment (20 kV voltage controller and rotating drum collector). NORM-JECT 10 mL and Monoject 3 mL syringes were used, and flow rates were adjusted to 0.1 and 0.04 mL/min for the 10 and 3 mL syringes, respectively. Needles with 0.8 mm inner diameter were used for electrospinning. A 18.77 kV voltage was applied to the tip of the needle. Electrospun fibers were collected on grounded drum rotating at 640 rpm. The distance between the needle tip and the collecting drum was 14 cm. Bi- and trilayer systems were obtained by sequential deposition of different polymer solutions (8.5 wt % PCL in chloroform and 35 % PNIPAM in DMF and acetone mixture (1:1)) during electrospinning. The 1:1 DMF/acetone mixture was found to be most suitable for PNIPAM polymer spinning.<sup>33</sup> A total of 1 % of rhodamine B was added to the PCL solution to provide visual contrast between the polymer layers. No rhodamine was added to the PCL solution in the case of samples for the cell proliferation tests. The electrospun polymer mats were pressed together after electrospinning using 20 tons hydraulic press. The microscopic features of the fibers were investigated by field emission scanning electron microscopy (FEI Teneo, FEI Co., Hillsboro, OR).

**Mechanical Properties.** The mechanical properties of electrospun fiber mats were characterized by tensile testing (Instron 4411) and dynamic mechanical analysis (PerkinElmer DMA 8000). Tensile tests were performed at room temperature at 10 mm/min stretching speed. Pressed electrospun samples with dimensions  $120 \times 25 \times 0.5 \text{ mm}^3$  were used.

For the DMA measurements, the dual cantilever tension mode was used. Viscoelastic properties were determined as a function of temperature in the range from 20 to 40 °C and scanning rate  $-2 \text{ K/min}$ . Electrospun pressed samples with  $30 \times 12 \times 0.5 \text{ mm}^3$  dimension were used. In the case of PNIPAM,  $30 \times 9.74 \times 3.49 \text{ mm}^3$  dogbone samples were prepared by melting polymer in mold at 176 °C under 12 ton pressure (Carver hydraulic unit model Nr. 3912).

DSC Differential Scanning Calorimetry was performed on a Mettler Toledo DSC821 measuring module. Samples were prepared by loading 5–10 mg of finely cut polymer pieces in a closed aluminum

crucible. The polymers were scanned in three steps—heating from  $-10$  to  $120 \text{ °C}$ , then cooling down to  $-10 \text{ °C}$ , and then heating to  $120 \text{ °C}$  again. The heating/cooling rate was  $10 \text{ K/min}$  for all samples and all steps.

**X-ray Scattering Investigations.** The X-ray scattering experiments were executed by means of the multirange device Ganesha 300 XL+ (SAXSLAB ApS, Denmark/U.S.A.). We used Cu- $K\alpha$  radiation ( $\mu$ -focus tube 50 kV, 600  $\mu\text{A}$ ; monochromatization with bifocal Göbel mirror). Scattering intensities were accumulated by 2D-detector Pilatus 300 K (pixel size  $172 \times 172 \mu\text{m}^2$ ). Path of rays, sample and detector are completely under vacuum ( $p < 5 \times 10^{-2} \text{ mbar}$ ). For the actual investigations we applied a 2-slit configuration and a beamstop with 2 mm diameter for two scattering ranges with following limits of parameters (Table 1).

**Table 1.** Parameters for SAXS and WAXS

(min–max):	$q \text{ (nm}^{-1}\text{)}$	$d \text{ (nm)}$	$2\Theta \text{ (deg)}$	$l_{\text{sample-det}} \text{ (mm)}$	$t_{\text{acc}} \text{ (s)}$
SAXS	0.1–2.0	125–3.14	0.007–2.8	~1041	7200
WAXS	0.9–24.4	7.0–0.257	1.27–34.8	~101	1800

The experiments were realized in asymmetric transmission (beam perpendicular to sample surface (free-standing)). The primary data were corrected to absorption. Results were presented as 2D scattering patterns  $\lg I(q_x, q_y)$ ; radial profiles  $\lg I(q)$  [orientation neglected]; azimuthal profiles  $I(\varphi)$  [here taken at  $q = 15 \text{ nm}^{-1}$  (WAXS) and  $0.4 \text{ nm}^{-1}$  (SAXS), respectively]. For partially crystalline polymers (here PCL), the lamellae thickness can be estimated from the  $d$ -value (Bragg's law) of the first (strong) scattering maximum in SAXS. The orientation of the morphology (in SAXS) as well as that of crystalline structure (in WAXS) can be characterized using Herman's orientation factor  $f = (3(\cos \varphi)^2 - 1)/2$ . Here,  $\varphi$  denotes the angle between the molecular axis and the local director. The crystallinity was determined according to the peak area method with the crystallinity defined as the ratio of the integral intensity of the crystalline scattering to the total scattering (crystalline + amorphous). The calculations were performed using underground-corrected WAXS curves, in which all available scattering maxima (reflections and amorphous halo inside an appropriate scattering range) will be fitted by means of pseudo-Voigt functions.

**MTT Cell Proliferation Assay.** NIH/3T3 cells were cultured in DMEM containing 10% fetal bovine serum, 100 U/mL penicillin and streptomycin, and 10% nonessential amino acids. Cells were subcultured every 3–4 days once the confluence of cells was 70 %. Thiazolyl blue tetrazolium bromide solution (5 mg/mL) was prepared and sterilized via syringe-filtration through 0.22  $\mu\text{m}$  pore sized filter. Polymer films for MTT cell proliferation assays were cut into proper sizes to fit 24-well plates, and they were sterilized by merging in 70 % ethanol for 6 h for thorough sterilization. Afterward, the ethanol solution was removed, and the films were rinsed 3 times with cold, autoclaved phosphate buffered saline (PBS). Sterile stainless steel rings were added to the wells to prevent films from floating and bending. The polymer films were divided into 3 groups. In Group 1, the film was further coated with collagen before cell seeding. Group 2, NIH/3T3 cells were cultured directly on polymeric film. Group 3 serves as a control where polymeric film was introduced but no cells were applied on polymer mats. Other control groups include cells cultured without adding a film (Group 4) and an empty well filled with incubation medium only (Group 5).

For cell seeding,  $\sim 10^5$  cells/mL were cultured and incubated for 24, 72, or 120 h. For the groups incubated for 120 h, medium was changed on day 3. Standard MTT cell proliferation assay was performed after incubation. Briefly, 50  $\mu\text{L}$  of thiazolyl blue tetrazolium bromide solution was added into each well. The plate was further incubated for 4 h at 37 °C, then the incubation medium was carefully removed. 0.5 mL DMSO was then added into each well. After the reduced formazan products were fully dissolved by gently shaking the plate for 10 min, the purple-colored DMSO solution was transferred into a separate 96-

\* Note: For synthesis of P(NIPAM-BPA) 2 mol % benzophenone acrylate (BPA) was used as cross-linker.

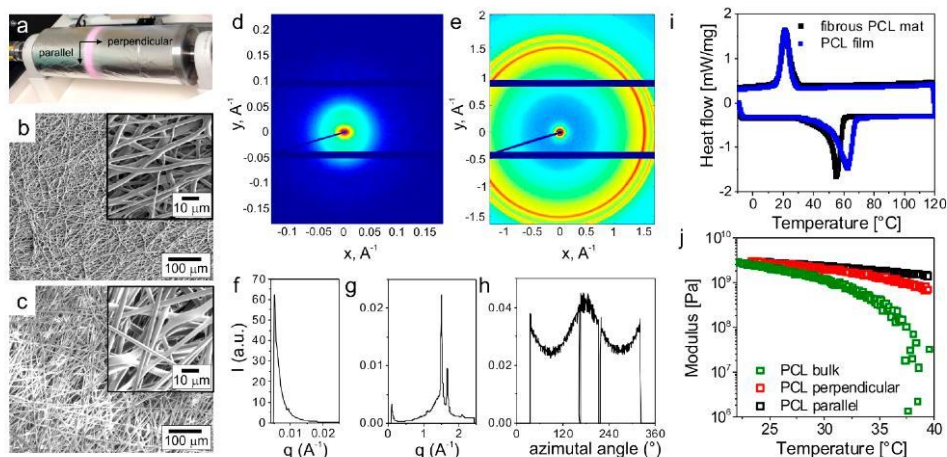


**Figure 1.** Properties of PCL and P(NIPAM-BPA) mats: (a) fabrication of electrospun polymer mats using rotating drum; representative SEM images of PCL (b) and P(NIPAM-BPA) (c) mats; SAXS (d) and WAXS (e) diffractograms of PCL mats; (f, g) radial scattering intensity profiles obtained from SAXS and WAXS; (h) azimuthal profile  $I(\varphi)$  (taken at  $q = 15 \text{ nm}^{-1}$  (WAXS)); (i) DSC and (j) DMA measurements of electrospun mats and PCL film in different directions.

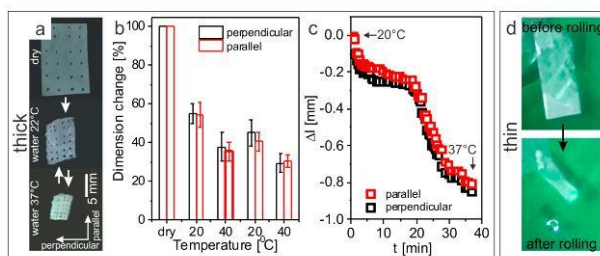


**Figure 2.** Responsive properties of electrospun P(NIPAM-BPA) mats. (a) Photographic snapshots of a thick PNIPAM (thickness  $425 \pm 42 \mu\text{m}$ ) mat in air, floating in water at  $22 \text{ }^\circ\text{C}$  and at  $37 \text{ }^\circ\text{C}$ ; (b) Temperature-dependent swelling and shrinking of thick P(NIPAM-BPA) mats; (c) Swelling kinetics of electrospun PNIPAM mats in water; (d) Folding of thin P(NIPAM-BPA) mats in water at room temperature.

well plate to measure 550 nm absorbance using a microreader ( $N = 5$  per group).

**Live/Dead Assay.** Live/Dead Kit was purchased from Thermo Fisher Scientific and the assay was performed according to the vendor's protocol. Briefly, the stock solutions of the calcein AM and EthD-1 were warmed up to room temperature. Then, a working solution containing  $5 \mu\text{M}$  calcein AM and  $10 \mu\text{M}$  EthD-1 in PBS was prepared. NIH/3T3 cells were preseeded in 24 well plates for 24 h and were rinsed with PBS before incubating with 0.5 mL of the working solution for 30 min. Afterward, fluorescence microscope (FL) images were taken. Live cells that were stained by calcein AM and were imaged through the FITC channel. Dead cells were stained by EthD-1 and were imaged through the TRITC channel. The ratio between live and dead cells were analyzed by counting the numbers of live/dead cells in multiple images ( $n = 5$ ).

## RESULTS AND DISCUSSION

We fabricated P(NIPAM-BPA) (4 mol % BPA) and PCL mats by electrospinning of these polymers on a rotating drum (Figure 1a). P(NIPAM-BPA) fibers were cross-linked during electrospinning via irradiation with 254 nm UV light by exciting benzophenone groups, which generate radicals. PCL fibers were

not cross-linked. The prepared electrospun polymer mats were pressed to make them denser. Here, and further in the text, the direction along the circumference of the electrospinning drum would be denoted as the "parallel" or " $0^\circ$ " direction, while the direction along the cylinder central axis would be called "perpendicular" or " $90^\circ$ " (Figure 1a). The average diameter of P(NIPAM-BPA) and PCL fibers was  $2.3 \pm 0.8 \mu\text{m}$  and  $1.6 \pm 0.7 \mu\text{m}$ , respectively (Figure 1b,c). SEM images of the electrospun mats showed stretched fibers running in all directions, that is, there was no visible preferential fiber orientation in the samples. Dynamic mechanical analysis showed only slight anisotropy in the electrospun mats. There was no difference in the modulus of the samples at room temperature, regardless of the direction of measurement (Figure 1j). At  $40 \text{ }^\circ\text{C}$ , parallel oriented samples demonstrated slightly higher modulus ( $\sim 2\times$  higher) than perpendicularly oriented ones. This difference in mechanical properties in different directions can be explained by preferential orientation of fibers. WAXS/SAXS results support this assumption and show that PCL polymer chains are slightly oriented along the direction of rotation of the drum. The orientation factor for

\* Note: For synthesis of P(NIPAM-BPA) 2 mol % benzophenone acrylate (BPA) was used as cross-linker.

WAXS is 0.06 (Figure 1h). The degree of crystallinity of the electrospun PCL was determined to be around 50%, which is typical for this polymer (Figure 1d–g). Similar degree of crystallinity was obtained from differential scanning calorimetry (DSC) results (Figure 1i). Melting and crystallization temperatures of PCL are about 60 and 20 °C, respectively, as it was revealed by DSC.

Next, we investigated the responsive behavior of individual PCL and P(NIPAM-BPA) mats in aqueous environment at different temperatures. Thick (thickness  $425 \pm 42 \mu\text{m}$ ) and thin (thickness  $105 \pm 4 \mu\text{m}$ ) P(NIPAM-BPA) mats were prepared by electrospinning. It was observed that thick P(NIPAM-BPA) mats shrink when placed in water at room temperature and its length and width decrease down to 55% of the initial value (Figure 2a,b). There was no anisotropy in the contraction of the samples in the parallel and perpendicular directions. Increasing temperature to 40 °C causes further shrinkage of the polymer mat down to 35% of its size in dry state. Repeated cooling–heating cycles of the sample result in its further contraction by an average of 10% (Figure 2b). Thus, swelling and shrinking of P(NIPAM-BPA) mat is isotropic. Moreover, P(NIPAM-BPA) swelling kinetics showed that the swelling rate is equal in all directions (Figure 2c). Thin PNIPAM mats exhibit different behavior. When submerged in water at room temperature, they roll toward the side, which was in contact with the drum during deposition (Figure 2d).

We discovered that PCL mats also demonstrate thermoresponsive properties (Figure 3). In particular, we observed that a

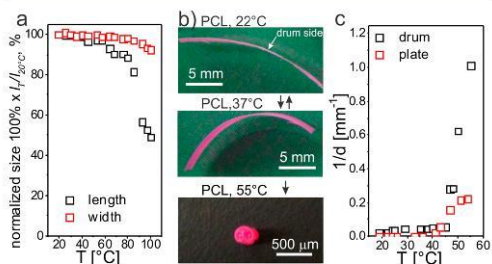


**Figure 3.** Responsive properties of PCL mats. (a) Temperature-induced contraction; (b) Reversible bending in water at 22 and 37 °C as well as irreversible folding at 55 °C; (c) Comparison of radii of curvature for samples with oriented (drum) and random (plate) fibers.

rectangular piece of electrospun PCL mat bends toward its outer side when immersed in water at room temperature (Figure 3b). Increasing the temperature to 37 °C decreased the radius of curvature (Figure 3b). The observed effect was fully reversible between 22 and 37 °C and could be repeated many times. The reason is small changes of volume of PCL upon heating/cooling,<sup>34</sup> which in combination with different density of PCL mat at drum and outer sides cause reversible bending. PCL is relatively stiff at room temperature leading to weak bending. Increasing the temperature lowers the modulus of PCL, augmenting the observed effect. Because temperatures never exceeded the  $T_g$  of PCL, no irreversible changes occur in the sample. However, increasing the temperature to 55 °C, which is around the  $T_g$  for electrospun PCL (see Figure 1i) results in a much stronger and irreversible folding of the PCL mat (Figure 3c). Noteworthy, folding in this case always occurs in the parallel direction. This preferential bending stems from

the slight alignment of the PCL fibers and from the stretched conformation of the macromolecular chains. These stretched chains relax at temperatures above the  $T_g$  of the polymer, and the sample strongly contracts (Figure 3a). In order to test this hypothesis, we prepared a sample by electrospinning on a static collector. In this case, no preferential orientation of the fibers was expected. As expected, weaker folding was observed in this case.

Folding of pure PCL mats at 37 °C is weak and insufficient for cell encapsulation, therefore a P(NIPAM-BPA)-PCL bilayer was prepared (Figure 4a). Such stimuli-responsive polymer

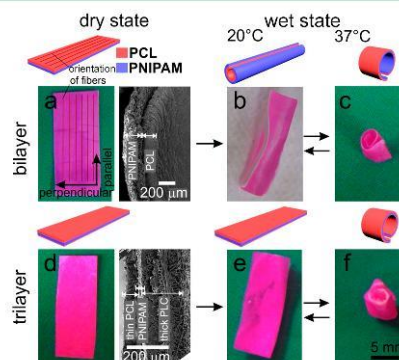


**Figure 4.** Responsive properties of electrospun P(NIPAM-BPA)-PCL bilayer and PCL-P(NIPAM-BPA)-PCL trilayer mats: (a) left, no folding is observed for the bilayer in air at room temperature; right, representative SEM image of a cross-section of the bilayer used to determine the layer thickness; (b) long-side rolling of the bilayer in water at 20 °C; (c) short-side rolling of the bilayer in water at 37 °C; (d) left, PCL-P(NIPAM-BPA)-PCL trilayer mat in air at room temperature—no folding; right, representative SEM image of a cross-section of the trilayer used to determine the layer thickness; (e) trilayer in water at 20 °C, no folding; (f) trilayer in water at 37 °C, short-side rolling.

bilayers have been already shown to undergo significant volume and shape changes suitable for the design of cell-encapsulating structures.<sup>35,36</sup> The PCL layer was electrospun first and P(NIPAM-BPA) was deposited on the top of it. We observed that at room temperature the P(NIPAM-BPA)-PCL electrospun bilayer folds toward PCL side in the perpendicular direction in respect to fibers if the thickness of the P(NIPAM-BPA) layer does not exceed 50  $\mu\text{m}$ . As a result a long tube with PNIPAM as the outer layer is formed (Figure 4b). Increase of the P(NIPAM-BPA) thickness results in its delamination from PCL upon swelling. Folding at 37 °C proceeds according to a different scenario—the bilayer folds in the parallel direction and short scrolls with PCL as the outer layer are formed (Figure 4c). Thus, folding of P(NIPAM-BPA)-PCL bilayer at 37 °C results in the formation of tubes with P(NIPAM-BPA) as the inner surface.

We explain the difference in folding scenarios of P(NIPAM-BPA)-PCL bilayers at room and elevated temperatures by considering the responsive properties of individual polymers. *Room temperature (22 °C)*: Size of PCL remains unchanged and it curls slightly to P(NIPAM-BPA) direction. P(NIPAM-BPA) shrinks slightly and strongly folds along the fibers. *Physiological temperature (37 °C)*: Size of PCL remains almost unchanged

though slight contraction happens to fiber length and it curls in the direction to P(NIPAM-BPA). P(NIPAM-BPA) shrinks strongly that leads to bending of bilayer toward P(NIPAM-BPA) side. Thus, P(NIPAM-BPA) determines the side to which the bilayer folds and PCL determines the direction with respect to fibers.

Folding of bilayer at 37 °C (the preferable temperature for cell proliferation) leads to the formation of tubes with P(NIPAM-BPA) as the inner layer. This is not favorable for cell encapsulation because of their poor adhesion to the swollen P(NIPAM-BPA) and to its limited biocompatibility. In order to form a tube with inner PCL layer, we fabricated a trilayer, which consists of a thick (~400 μm) PCL, thick P(NIPAM-BPA), and thin PCL layers. The thickness of the P(NIPAM-BPA) had to be increased in order to counter the added resistance from the additional PCL layer and to sustain folding. On the other hand, the introduction of a third hydrophobic layer on top of the P(NIPAM-BPA) effectively solved the delamination problem described earlier. The folding of such a trilayer is guided by the behavior of thick PCL and thick P(NIPAM-BPA). The role of the thin PCL is simply to provide proper functionality of the inner surface of the tube. The trilayer does not fold in water at room temperature. The folding at 37 °C follows the scenario of folding of the bilayer: the outer layer is formed by the thick PCL and since P(NIPAM-BPA) is coated by thin PCL layer, the inner layer of the tube is PCL, which provides good adhesion to cells.

Finally, we investigated the impact of self-folding PCL-P(NIPAM-BPA)-PCL trilayer mats on cell adhesion and proliferation. Briefly, we seeded NIH/3T3 cells on a PCL-P(NIPAM-BPA)-PCL film that was either coated or not with collagen, and then examined the cell viability by Live/Dead assay. We observed that NIH/3T3 cells seeded on the collagen coated mats were more likely to express a normal, well spread morphology with high cell surface area (Figure 5a), while cells in the control group without adding collagen tended to exist in spherical shape with low cell surface area (Figure 5b). This suggested that collagen could help facilitate cell adhesion and morphology development, which was also documented by

others.<sup>37</sup> In addition, the ratio between living cells and dead cells were statistically estimated by counting the living cells and dead cells in multiple FL images. For both groups, the ratios were around 1 to 1.5 (Figure 5c). This indicated that the polymeric mats might cast certain effect on the cell viability and normal metabolic activity. Interestingly, we found that the Live/Dead cell ratio of the collagen-added group was slightly higher than the group without collagen. This was considered as a result that collagen-coated surface could help create a more biocompatible environment for cell metabolism and, hence, better protect the cell viability than the naked polymeric surface, which was also evident by the cell morphology difference between the two groups discussed above. We have also investigated viability by MTT assays on days 1, 3, and 5. During our experiments we noticed that our film is giving intensive absorbance signal, so to obtain more reliable results we subtracted signal made by polymer mat from film-containing groups before quantifying viability in relation to cells seeded on plate (Figure 5d). The viability in all film-containing groups was lower than 50% in comparison to cells on plate. Meantime, for all the time points, the viability of collagen-added groups was lower than that without collagen, which seemed contradictory to the Live/Dead assay results. It was known that the MTT assay was designed to measure the cell metabolic activity, which was mainly affected by the cell proliferation rate and viability change. One reason for the low MTT results for all groups was the slow proliferation. For instance, on day 1, the MTT results were around 40–50%, which were roughly consistent with Live/Dead cell ratio results. However, the MTT results on day 3 for film-containing groups dropped to around 10–20% but increased to 20–30% on day 5. Given that all results were obtained by comparing with the blank control and the cells in the blank control seems to have reached the plateau between day 3 and day 5 and slowed down the proliferation rate, the cells attached on the surface of polymeric mats kept proliferating at a slow rate (Figure 5d). Increase in proliferation rate on day 5 could be due to adding new growth media on day 3, thus, making better conditions for groups with and without film. The other reason for the low MTT results would be the viability loss, as we observed it. Interestingly, we found all the MTT results of the collagen-added groups were lower than those without adding collagen. Previously we considered that collagen might help improve the cell viability. Therefore, this MTT result difference was believed as a result of the proliferation effect. Specifically, we suspected that cells cultured with polymeric mats without collagen might more tend more to exist in spherical shapes and proliferate faster than those in the collagen added ones. This phenomenon might be attributed to the 3D folding structures of the mat, the surface property difference, PCL fibers is hydrophobic and with low wettability which could determine cell spherical shape, but combined in multilayer system with P(NIPAM-BPA) hydrogel fibers scaffolds are more hydrophilic that could improve proliferation of cells as growth medium can easily diffuse through fibers. Overall, treatment of trilayer with collagen would allow substantial improvement of cell attachment, protection of cellular viability and normal functions, but maybe slow down the proliferation as free volume between fibers is blocked by collagen, without impeding its folding properties as bending of scaffold edges around metal ring was observed after incubation in 37 °C.

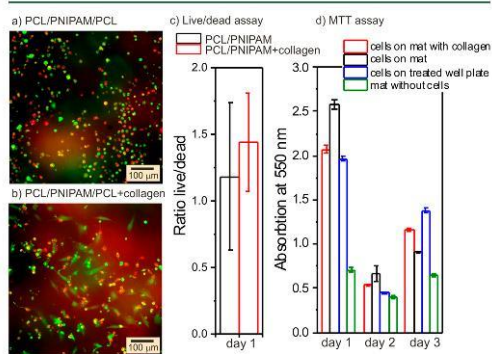


**Figure 5.** Cell proliferation: (a, b) live/dead cell staining after culturing for 24 h on multilayer mat with and without collagen coating; (c) live/dead cell ratio after culturing for 24 h; (d) MTT assay results from two film-containing groups (with and without collagen), cell control group on plate and mat control group, taken after culturing cells for 24, 72, and 120 h.

## CONCLUSIONS

We demonstrated a novel approach for the design of shape-changing biomaterials using porous electrospun polymer multilayers. We demonstrated this approach on the example of mats consisting of thermoresponsive P(NIPAM-BPA) and PCL. These mats demonstrate folding in aqueous environment, which depends on the thickness of the layers and their number. The folding behavior can be tuned in a way that the mats fold in aqueous environment at 37 °C, making them suitable for cell encapsulation and tissue engineering. We demonstrated that treatment of the self-folding polymer with collagen substantially improves cells adhesion and viability. The developed approach opens new perspectives for the structuring of biomaterials and 4D biofabrication.

## AUTHOR INFORMATION

### Corresponding Author

\*E-mail: leonid.ionov@bm.uni-bayreuth.de.

### ORCID

Jin Xie: 0000-0002-8915-6233

Leonid Ionov: 0000-0002-0770-6140

### Author Contributions

The manuscript was written through contributions of all authors. All authors have given approval to the final version of the manuscript.

### Notes

The authors declare no competing financial interest.

## ACKNOWLEDGMENTS

The authors wish to thank Mr. Göbel for assistance in WAXS and SAXS experiments.

## REFERENCES

- (1) Parveen, S.; Krishnakumar, K.; Sahoo, S. K. New Era in Health Care: Tissue Engineering. *J. Stem Cells Regen. Med.* **2006**, *1* (1), 8–24.
- (2) Aubin, H.; Nichol, J. W.; Hutson, C. B.; Bae, H.; Sieminski, A. L.; Cropek, D. M.; Akhyari, P.; Khademhosseini, A. Directed 3D cell alignment and elongation in microengineered hydrogels. *Biomaterials* **2010**, *31* (27), 6941–6951.
- (3) Kolesky, D. B.; Truby, R. L.; Gladman, A.; Busbee, T. A.; Homan, K. A.; Lewis, J. A. 3D bioprinting of vascularized, heterogeneous cell-laden tissue constructs. *Adv. Mater.* **2014**, *26* (19), 3124–3130.
- (4) Taboas, J. M.; Maddox, R. D.; Krebsbach, P. H.; Hollister, S. J. Indirect solid free form fabrication of local and global porous, biomimetic and composite 3D polymer-ceramic scaffolds. *Biomaterials* **2003**, *24* (1), 181–194.
- (5) Ho, M.-H.; Kuo, P.-Y.; Hsieh, H.-J.; Hsien, T.-Y.; Hou, L.-T.; Lai, J.-Y.; Wang, D.-M. Preparation of porous scaffolds by using freeze-extraction and freeze-gelation methods. *Biomaterials* **2004**, *25* (1), 129–138.
- (6) Dhandayuthapani, B.; Yoshida, Y.; Maekawa, T.; Kumar, D. S. Polymeric Scaffolds in Tissue Engineering Application: A Review. *Int. J. Polym. Sci.* **2011**, *2011*, 1.
- (7) Hutmacher, D. W. Scaffold design and fabrication technologies for engineering tissues — state of the art and future perspectives. *J. Biomater. Sci., Polym. Ed.* **2001**, *12* (1), 107–124.
- (8) Hollister, S. J. Porous scaffold design for tissue engineering. *Nat. Mater.* **2005**, *4* (7), 518–524.
- (9) Visser, J.; Melchels, F. P. W.; Jeon, J. E.; van Bussel, E. M.; Kimpston, L. S.; Byrne, H. M.; Dhert, W. J. A.; Dalton, P. D.; Hutmacher, D. W.; Malda, J. Reinforcement of hydrogels using three-dimensionally printed microfibrils. *Nat. Commun.* **2015**, *6*, 6933–6933.
- (10) Fu, Y.; Xu, K. D.; Zheng, X. X.; Giacomini, A. J.; Mix, A. W.; Kao, W. Y. J. 3D cell entrapment in crosslinked thiolated gelatin-poly(ethylene glycol) diacrylate hydrogels. *Biomaterials* **2012**, *33*, 48–58.
- (11) Hoch, E.; Schuh, C.; Hirth, T.; Tovar, G. E. M.; Borchers, K. Stiff gelatin hydrogels can be photo-chemically synthesized from low viscous gelatin solutions using molecularly functionalized gelatin with a high degree of methacrylation. *J. Mater. Sci.: Mater. Med.* **2012**, *23* (11), 2607–2617.
- (12) Nicodemus, G. D.; Bryant, S. J. Cell encapsulation in biodegradable hydrogels for tissue engineering applications. *Tissue Eng., Part B* **2008**, *14* (2), 149–165.
- (13) Sakai, S.; Liu, Y.; Sengoku, M.; Taya, M. Cell-selective encapsulation in hydrogel sheaths via biospecific identification and biochemical cross-linking. *Biomaterials* **2015**, *53*, 494–501.
- (14) Kerscher, P.; Turnbull, I. C.; Hodge, A. J.; Kim, J.; Seliktar, D.; Easley, C. J.; Costa, K. D.; Lipke, E. A. Direct hydrogel encapsulation of pluripotent stem cells enables ontomimetic differentiation and growth of engineered human heart tissues. *Biomaterials* **2016**, *83*, 383–395.
- (15) Murayama, S.; Ishizuka, F.; Takagi, K.; Inoda, H.; Sano, A.; Santa, T.; Kato, M. Small Mesh Size Hydrogel for Functional Photocontrol of Encapsulated Enzymes and Small Probe Molecules. *Anal. Chem.* **2012**, *84* (3), 1374–1379.
- (16) Malachowski, K.; Jamal, M.; Jin, Q.; Polat, B.; Morris, C. J.; Gracias, D. H. Self-Folding Single Cell Grippers. *Nano Lett.* **2014**, *14* (7), 4164–4170.
- (17) Silverberg, J. L.; Na, J.-H.; Evans, A. A.; Liu, B.; Hull, T. C.; Santangelo, C.; Christian, D.; Lang, R. J.; Hayward, R. C.; Cohen, I. Origami structures with a critical transition to bistability arising from hidden degrees of freedom. *Nat. Mater.* **2015**, *14* (4), 389–393.
- (18) Thérien-Aubin, H.; Wu, Z. L.; Nie, Z.; Kumacheva, E. Multiple Shape Transformations of Composite Hydrogel Sheets. *J. Am. Chem. Soc.* **2013**, *135* (12), 4834–4839.
- (19) Stoychev, G.; Turcaud, S.; Dunlop, J. W. C.; Ionov, L. Hierarchical multi-step folding of polymer bilayers. *Adv. Funct. Mater.* **2013**, *23* (18), 2295–2300.
- (20) Zakharchenko, S.; Pureskiy, N.; Stoychev, G.; Waurisch, C.; Hickey, S. G.; Eychmuller, A.; Sommer, J.-U.; Ionov, L. Stimuli-responsive hierarchically self-assembled 3D porous polymer-based structures with aligned pores. *J. Mater. Chem. B* **2013**, *1* (13), 1786–1793.
- (21) Ionov, L. Soft microorigami: self-folding polymer films. *Soft Matter* **2011**, *7* (15), 6786–6791.
- (22) Ionov, L. Polymeric Actuators. *Langmuir* **2015**, *31* (18), 5015–5024.
- (23) Jiang, S.; Liu, F.; Lerch, A.; Ionov, L.; Agarwal, S. Unusual and Superfast Temperature-Triggered Actuators. *Adv. Mater.* **2015**, *27* (33), 4865–4870.
- (24) Zakharchenko, S.; Sperling, E.; Ionov, L. Fully Biodegradable Self-Rolled Polymer Tubes: A Candidate for Tissue Engineering Scaffolds. *Biomacromolecules* **2011**, *12* (6), 2211–2215.
- (25) Wang, X.; Ding, B.; Li, B. Research: Biomimetic electrospun nanofibrous structures for tissue engineering. *Mater. Today* **2013**, *16*, 229–241.
- (26) Kweon, H.; Yoo, M. K.; Park, I. K.; Kim, T. H.; Lee, H. C.; Lee, H.-S.; Oh, J.-S.; Akaik, T.; Cho, C.-S. A novel degradable polycaprolactone networks for tissue engineering. *Biomaterials* **2003**, *24* (5), 801–808.
- (27) Sharma, Y.; Tiwari, A.; Hattori, S.; Terada, D.; Sharma, A. K.; Ramalingam, M.; Kobayashi, H. Fabrication of conducting electrospun nanofibers scaffold for three-dimensional cells culture. *Int. J. Biol. Macromol.* **2012**, *51* (4), 627–631.
- (28) Cooperstein, M. A.; Canavan, H. E. Assessment of cytotoxicity of (N-isopropyl acrylamide) and Poly(N-isopropyl acrylamide)-coated surfaces. *Biointerphases* **2013**, *8* (1), 1–12.
- (29) Tan, H.; Ramirez, C. M.; Miljkovic, N.; Li, H.; Rubin, J. P.; Marra, K. G. Thermosensitive injectable hyaluronic acid hydrogel for adipose tissue engineering. *Biomaterials* **2009**, *30* (36), 6844–6853.
- (30) Yu, Y.; Zhang, H.; Sun, H.; Xing, D. D.; Yao, F. L. Nano-hydroxyapatite formation via co-precipitation with chitosan-g-poly(N-

isopropylacrylamide) in coil and globule states for tissue engineering application. *Front. Chem. Sci. Eng.* **2013**, *7* (4), 388–400.

(31) Li, Z.; Guo, X.; Matsushita, S.; Guan, J. Differentiation of cardiosphere-derived cells into a mature cardiac lineage using biodegradable poly(N-isopropylacrylamide) hydrogels. *Biomaterials* **2011**, *32* (12), 3220–3232.

(32) Sivashanmugam, A.; Arun Kumar, R.; Vishnu Priya, M.; Nair, S. V.; Jayakumar, R. An overview of injectable polymeric hydrogels for tissue engineering. *Eur. Polym. J.* **2015**, *72*, 543–565.

(33) Rockwood, D. N.; Chase, D. B.; Akins, R. E., Jr; Rabolt, J. F. Characterization of electrospun poly(N-isopropyl acrylamide) fibers. *Polymer* **2008**, *49* (18), 4025–4032.

(34) Ionov, L.; Stoychev, G.; Jehnichen, D.; Sommer, J. U. Reversibly Actuating Solid Janus Polymeric Fibers. *ACS Appl. Mater. Interfaces* **2017**, *9* (5), 4873–4881.

(35) Stoychev, G.; Pureskiy, N.; Ionov, L. Self-folding all-polymer thermoresponsive microcapsules. *Soft Matter* **2011**, *7*, 3277–3279.

(36) Zakharchenko, S.; Pureskiy, N.; Stoychev, G.; Stamm, M.; Ionov, L. Temperature controlled encapsulation and release using partially biodegradable thermo-magneto-sensitive self-rolling tubes. *Soft Matter* **2010**, *6* (12), 2633–2636.

(37) He, W.; Ma, Z.; Yong, T.; Teo, W. E.; Ramakrishna, S. Fabrication of collagen-coated biodegradable polymer nanofiber mesh and its potential for endothelial cells growth. *Biomaterials* **2005**, *26* (36), 7606–7615.



Part 2. 4D biofabrication of skeletal muscle microtissues

**Apsite I.**, Uribe M. J., Posada F. A., Rosenfeldt S., Salehi S., Ionov L.

Published in *Biofabrication*, 12, 2020, 015016

(2019)

Reproduced under the terms and conditions of the Creative Commons 'CC BY 3.0'



## Biofabrication



PAPER

### 4D biofabrication of skeletal muscle microtissues

OPEN ACCESS

Indra Apsite<sup>1</sup>, Juan Manuel Uribe<sup>1</sup>, Andrés Fernando Posada<sup>1</sup> , Sabine Rosenfeldt<sup>2</sup>, Sahar Salehi<sup>3,4</sup>  and Leonid Ionov<sup>1,4</sup> RECEIVED  
6 June 2019REVISED  
17 September 2019ACCEPTED FOR PUBLICATION  
10 October 2019PUBLISHED  
11 December 2019

Original content from this work may be used under the terms of the [Creative Commons Attribution 3.0 licence](https://creativecommons.org/licenses/by/4.0/).

Any further distribution of this work must maintain attribution to the author(s) and the title of the work, journal citation and DOI.



<sup>1</sup> Faculty of Engineering Sciences and Bavarian Polymer Institute, University of Bayreuth, Ludwig Thoma Str. 36A, 95447 Bayreuth, Germany

<sup>2</sup> Department of Physical Chemistry I, Faculty of Biology, Chemistry & Earth Sciences and Bavarian Polymer Institute, University of Bayreuth, Universitätsstraße 30, 95447 Bayreuth, Germany

<sup>3</sup> Department of Biomaterials, University of Bayreuth, Prof.-Rüdiger-Bormann Str. 1, 95447 Bayreuth, Germany

<sup>4</sup> Authors to whom any correspondence should be addressed.

E-mail: [sahar.salehi@bm.uni-bayreuth.de](mailto:sahar.salehi@bm.uni-bayreuth.de) and [leonid.ionov@uni-bayreuth.de](mailto:leonid.ionov@uni-bayreuth.de)

**Keywords:** electrospinning, self-folding, biofabrication, skeletal muscle

Supplementary material for this article is available [online](#)

#### Abstract

Skeletal muscle is one of the most abundant tissues in the body. Although it has a relatively good regeneration capacity, it cannot heal in the case of disease or severe damage. Many current tissue engineering strategies fall short due to the complex structure of skeletal muscle. Biofabrication techniques have emerged as a popular set of methods for increasing the complexity of tissue-like constructs. In this paper, 4D biofabrication technique is introduced for fabrication of the skeletal muscle microtissues. To this end, a bilayer scaffold consisting of a layer of anisotropic methacrylated alginate fibers (AA-MA) and aligned polycaprolactone (PCL) fibers were fabricated using electrospinning and later induced to self-fold to encapsulate myoblasts. Bilayer mats undergo shape-transformation in an aqueous buffer, a process that depends on their overall thickness, the thickness of each layer and the geometry of the mat. Proper selection of these parameters allowed fabrication of scroll-like tubes encapsulating myoblasts. The myoblasts were shown to align along the axis of the anisotropic PCL fibers and further differentiated into aligned myotubes that contracted under electrical stimulation. Overall the significance of this approach is in the fabrication of hollow tubular constructs that can be further developed for the formation of a vascularized and functional muscle.

#### 1. Introduction

Growing population, increasing lifespan and an aging of society has led to a growing need for donor organs and organ replacement. However, limited availability of donor tissues, as well as the high risk of immune rejection of the transplant raise a great need for development of new methods for tissue engineering [1]. One of the most important tasks in tissue engineering is the replacement of damaged or lost skeletal muscle. An average adult male is made up of ca. 40% of skeletal muscle, making skeletal muscle the most abundant tissue in the body [2]. Skeletal muscle has a complex structure and is formed with bundles of parallel, packed and organized fibers [3]. Even though skeletal muscle shows a high capacity of self-repair, it is unable to regenerate in the case of severe damage or disease, such as tumor ablation and volume loss

injuries (VML) [4, 5]. One big challenge in engineering of functional skeletal muscle tissues is the formation of highly aligned muscle fibers similar to the native structure. Due to this, skeletal muscle is considered especially important for further development of tissue-replacement strategies.

Multiple attempts have been undertaken to engineer 2D structures mimicking the natural morphology of skeletal muscle tissue and using diverse techniques which are based on (i) patterned substrates, and (ii) mechanical/electrical stimulation [6–8]. In the case of chemically/topographically patterned substrates (quasi 2D objects), cells form a continuous layer on a patterned surface (cell density is comparable to that in natural tissue) and tend to align according to the pattern [9, 10]. This approach allows fabrication of relatively thin aligned cell sheets. However, scaling-up to highly organized and orientated cells in a thick

multilayer structure using this method is not trivial. The second strategy consists of the use of hydrogels with encapsulated myoblasts (3D objects) and their exposure to oscillating/constant mechanical deformation or pulsing electrical stimulation [11, 12]. Common cell density used in this approach is ca.  $10^6$ – $10^7$  cell  $\text{ml}^{-1}$  [8, 13]. Higher initial cell density might change the stability of the hydrogel and make it brittle [14], while the fabrication of tissues with a high cell density and supporting the maturation and functionality of these cells is still a challenge.

In this paper, we introduce 4D biofabrication [15, 16] to address current challenges in fabrication of skeletal muscle tissues. 4D biofabrication comprises a variety of fabrication technologies and assumes that the desired structure/shape/morphology is achievable by a shape-transformation of preliminary fabricated 3D elements. Importantly, the shape-transformation should occur in a controlled manner by applying an external stimulus such as swelling in aqueous media, pH or temperature changes [15, 17]. In our approach, we utilize a shape-changing polymer bilayer consisting of stimuli-responsive, biodegradable methacrylated alginate anisotropic fibers (AA-MA, outer layer of self-folded tube) and aligned, biodegradable electrospun polycaprolactone nanofibers (PCL, inner layer of self-folded tube). This construct has a number of advantages over shape-changing layers previously used for 4D biofabrication [16, 18–20]. In contrast to widely used thermo-responsive (meth-) acrylamides [18, 20–22] and unstructured poly(ethylene glycol) (PEG) based scaffolds [16, 23], a bottom AA-MA layer is simultaneously, both sensitive to signal compatible cells with a presence of  $\text{Ca}^{2+}$  ions, and is biodegradable [24–26]. Furthermore, we observed that the AA-MA fibers swelled as expected for a thin layer of hydrogel. The aligned PCL is biodegradable and the electrospun fibers were shown to guide both shape-transformation and cell orientation [27–34], which cannot be provided by isotropic hydrogels and unstructured solid polymers. Moreover, the porosity of an electrospun layer allows for the diffusion of oxygen and nutrition to cells [18, 35], which is usually hindered by used solid polymer layers [16, 19, 36]. There have been extensive studies on cell alignment on various 2D substrates like ribbons and electrospun fibers [5, 30], though in this study we describe self-folding material with the ability to align cells during their growth that has not been discussed before. We show the ability to fine-tune formed self-folded tubular structure diameters in a significantly wide range (0.1–70 mm), which makes this material suitable for single micrometer size muscle fiber and large muscle bundle formation. In this study, first, we cultured mouse myoblast cells on such a fibrous bilayer mat (figures 1(a), (b)). Mats roll and form tubular multilayer structure with a channel inside (figure 1(c)). Finally, myotubes are formed inside the rolled structure after differentiation

(figure 1(d)). This process results in the formation of a continuous cell construct inside a rolled fibrous scroll-like tube (figure 1(d)).

## 2. Materials and methods

### 2.1. Materials

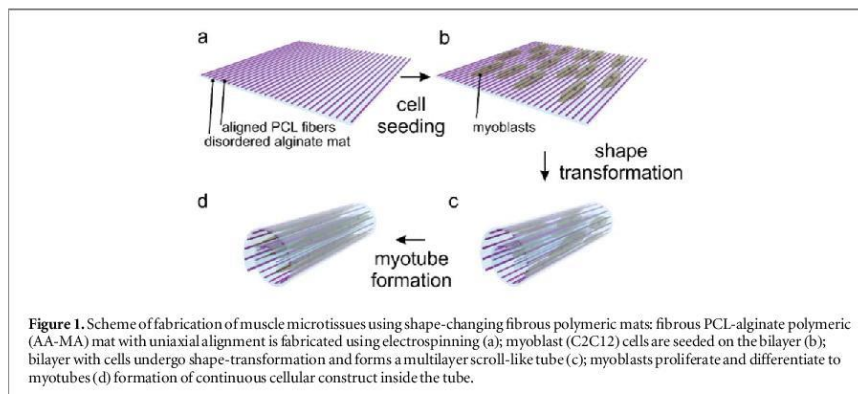
Polycaprolactone (PCL) ( $M_n = 80\,000$  g  $\text{mol}^{-1}$ , Aldrich), Pluronic<sup>®</sup> F-127 (Aldrich), Chloroform anhydrous (Aldrich), Triethanolamine (TEA) (Merk), 1-vinyl-2-pyrrolidinone (VP) (Aldrich), Eosin Y (EY) (Aldrich), Methacrylic anhydride (MA) (Aldrich), Ethanol (EtOH) (Aldrich), Sodium alginate (AA) (Roth), Poly(ethylene oxide) (PEO) [ $MW\ 1\,000\,000$  g  $\text{mol}^{-1}$ ] (Polysciences Inc.), Sodium hydroxide (NaOH) (Aldrich), Ethylenediaminetetraacetic acid (EDTA) (Aldrich), Calcium chloride dehydrate (Aldrich), Dulbecco's phosphate buffered saline (PBS) (Aldrich), Calcein AM (Thermo Fisher Scientific), Ethidium homodimer (EthD-1) (Thermo Fisher Scientific), anti-myosin antibody (Thermo Fisher Scientific), goat anti rabbit IgG 488 (Thermo Fisher Scientific), 4',6-diamidino-2-phenylindole (DAPI) (Thermo Fisher Scientific), Triton X-100 (Aldrich), Albumin Fraction V (BSA) (Roth), MEM-non-essential amino acid solution (MEM-NEAA) (gibco), MEM essential amino acid (gibco), Phalloidin Dylight<sup>™</sup> 488 (Thermo Fisher Scientific), Dulbecco's Modified Eagle Medium (DMEM) (Merk), T-butyl alcohol (Aldrich), Horse Serum (gibco), Penicillin Streptomycin (Pen/Strep) (gibco), Fetal Bovine Serum (FBS) (Merck), GlutaMax (gibco), 4-(2-hydroxyethyl)-1-piperazineethanesulfonic acid (HEPES) (Carl Roth), murine C2C12 myoblasts (passage number less than 7) were purchased from ATCC (Manassas, VA).

### 2.2. Synthesis of methacrylated alginate (AA-MA)

The methacrylate groups in alginate were introduced using the procedure described before [37]. A 20-fold excess of methacrylic anhydride was added dropwise to 2% alginate solution. The reaction pH was constantly adjusted to pH 8 using 5 M NaOH. The mixture was incubated at 4 °C for 24 h using constant stirring at 800 rpm. AA-MA was precipitated and washed in ethanol to remove the remaining methacrylic acid and anhydride. Clean substance was air dried for further use.

### 2.3. Electrospinning

The electrospinning setup consists of a custom-made multi-syringe pump, a needle holder with a variable distance between the needles and an electrospinning equipment (30 kV voltage controller, two conductive bars and a rotating drum as collectors). Omnifix<sup>®</sup> 3 and 5 ml syringes were used, and flow rates were adjusted to 0.02  $\text{ml min}^{-1}$ . Needles with 0.8 mm inner diameter were used and 15 kV voltage was applied to the tip of the needle, whereas 5 kV voltage was added to collector. Electrospun fibers were collected either



on the rotating drum (640 rpm) or between two conductive bars (distance between bars 4 cm). The distance between the needle tip and collectors was kept constant at 15 cm. Bilayer systems were produced by sequential deposition of different polymer solutions during electrospinning. The PCL solution in chloroform with 8.5 wt% concentration was electrospun to obtain PCL fibers. Alginate fibers were electrospun using 3 wt% AA-MA solution containing 10  $\mu$ l of 0.5% EY in VP and 200  $\mu$ l of 0.5 M TEA. The spinning solution was also mixed with 5 wt% PEO and 30 wt% Pluronic F127 with weight ratio 70/30/2 and stirred overnight [25].

#### 2.4. Scanning electron microscopy (SEM)

Structure and microscopic features of the fibers were investigated by field emission scanning electron microscopy (FE-SEM) (FEI Teneo, FEI Co., Hillsboro, OR and Carl Zeiss Microscopy GmbH, Germany). Fully dried samples were covered with  $\sim$ 10 nm gold, to ensure conductivity.

#### 2.5. Dynamical mechanical analysis (DMA)

The mechanical properties of electrospun fiber mats were characterized by dynamic mechanical analysis (Anton Paar MCR 702 TwinDrive, Austria). Samples with dimensions 50  $\times$  10  $\times$  0.8 mm<sup>3</sup> were prepared and dual cantilever tension mode was used for the measurement. During the measurement, static (150 mN) and dynamic force (130 mN) was added to the sample. Frequency was kept constant during the measurement (1 Hz). The temperature range used during the measurement was from 20  $^{\circ}$ C to 37  $^{\circ}$ C and a scanning rate of 2  $^{\circ}$ C min<sup>-1</sup> was used to characterize the viscoelastic properties.

#### 2.6. Differential scanning calorimetry (DSC)

DSC was performed on a Mettler Toledo DSC3 (USA). Samples were prepared by loading 5–10 mg of finely cut PCL mat pieces in a closed aluminum crucible. The polymers were scanned in three steps: (1) heating

from  $-10$   $^{\circ}$ C to 120  $^{\circ}$ C, (2) cooling down to  $-10$   $^{\circ}$ C, and (3) heating to 120  $^{\circ}$ C again. For all samples, the heating/cooling rate was 10 K min<sup>-1</sup>.

#### 2.7. Small-angle x-ray scattering (SAXS)

All small-angle x-ray scattering (SAXS) data were measured using the SAXS system 'Double Ganesha AIR' (SAXSLAB, Denmark). The x-ray source of this laboratory-based system was a rotating anode (copper, MicoMax 007HF, Rigaku Corporation, Japan). The data were recorded by a position sensitive detector (PILATUS 300 K, Dectris). To cover the range of scattering vectors between 0.002–1  $\text{\AA}^{-1}$ , different detector positions were used. The measurements were done in parallel and with a perpendicular geometry of the beam to the bilayer mat at room temperature.

#### 2.8. Rheology

Rheological properties of non-crosslinked 3% AA-MA solution were measured using Rheometer AR G2 (TA instruments, USA). Cone-plate geometry with a size of 20 mm was used in oscillatory mode. Solution complex viscosity, depending on the temperature, was measured using a temperature range from 20  $^{\circ}$ C to 40  $^{\circ}$ C, shear rate was kept constant at 3.34 1/s (calculated theoretical shear rate in electrospinning needle). Storage and loss modulus depending angular frequency was measured using frequency sweep measurements, where angular frequency varied from 0.1 to 100 Hz at 10% strain.

#### 2.9. Cell culture studies

C2C12 mouse muscle cells (passage number <7) were cultured on the PCL aligned fibers and bilayer PCL/AA-MA fibrous scaffold. First, fibrous scaffolds were fixed in the cell crown (Scaffdex CellCrown<sup>TM</sup> inserts) and after washing with 70% ethanol and PBS, were sterilized using UV light for 30 min. To enhance the cell adhesion on PCL fibers, the PCL side of the bilayer and PCL scaffolds were coated with sterilized FNC solution (fibronectin, collagen, albumin cocktail

solution, Thermo Fisher) for 30 s. Following the coating of scaffolds, a cell suspension with a density of  $10^5$  cell  $\text{ml}^{-1}$  was seeded on top and incubated for 30 min for initial attachment of the cells. The growth medium of C2C12 cells containing DMEM, 10 v/v% FBS serum, 1% Pen/Strep, 4 mM Glutamin and 20 mM HEPES were added to samples and the cell viability as well as their alignment was monitored at different time points of 1, 3, 5, and 7 days after the culture.

Myoblast cells, cultured on both bilayer and pure PCL fibrous scaffolds, after 7 days of culture, were moved to a differentiation medium containing DMEM, 2 v/v% Horse serum, 1% Pen/Strep, 4 mM Glutamin and 20 mM HEPES. The differentiated cells and myosin expression were evaluated by immunostainings on day 4 and 7 after differentiation and cells were stimulated electrically to evaluate their functionality on day 7.

#### 2.9.1. Live/dead assay

The viability of the muscle cells cultured on bilayers, as well as PCL fibers, were measured using Live-Dead assay. A staining solution containing 1  $\mu\text{l}$  of Calcein AM (Thermo Fisher) and 4  $\mu\text{l}$  of Ethidium EthD-1 (Thermo Fisher) was prepared in 2 ml PBS and samples were covered with staining solution and incubated for 20 min at room temperature before imaging using a fluorescence microscope (Leica DMi8, Germany). The cell viability was analyzed at different time points, such as 1, 3 and 7 days after the culture by counting the number of live and dead cells in ten images.

#### 2.9.2. Staining of actin filament and nucleus

To quantify the alignment of the muscle cells, cultured on bilayers as well as PCL fibers, the actin filaments and nuclei were stained using DAPI (Thermo Fisher) and Phalloidin Dylight™ 488 (Thermo Fisher). The staining solution containing an initial concentration of 500  $\mu\text{l}$  0.1 mg  $\text{ml}^{-1}$  DAPI and 250  $\mu\text{l}$  Phalloidin in 10 ml PBS, was prepared according to the number of samples to stain the actin and nuclei of the cells. Firstly, the samples after 1, 3 and 7 days in culture were washed with PBS and then fixed using 3.7% formaldehyde solution for 15 min at room temperature. After fixation of cells, the sample was washed with PBS and the cell membranes were permeabilized with 0.1% Triton solution for 5 min at room temperature. Next, samples were washed with PBS, and fully covered with staining solution. After 30 min of incubation samples were washed with PBS and imaged using a fluorescence microscope. To investigate the cell alignment, morphological changes of nuclei were analyzed. Image J and an orientation plug-in was used to analyze ten images taken from different samples. Nuclei orientation angles of  $<10^\circ$  to fibers were considered as aligned.

#### 2.9.3. Myosin heavy chain staining

To investigate the formation of myotubes and the expression of the myosin heavy chains on day 4 and 7 after incubation in the differentiation medium, samples were stained using the immunostaining protocol in the following. Firstly, samples were fixed and cell membranes were permeabilized as described previously for actin staining. Then 5% BSA in PBS blocking solution was added and incubated at 37 °C for 15–30 min. Solution was aspirated and samples were washed with PBS. Next, primary antibody MY32 (Thermo Fisher) 1000x diluted in BSA 0.1% was added and incubated overnight at 4 °C. Samples were further washed with PBS and then staining solution of a secondary antibody (goat anti mouse IgG 488, Thermo Fisher), and DAPI in 1000x dilution in BSA 0.1% was added. Samples were covered from light and incubated at 37 °C for 1 h. After incubation and washing steps with PBS the images were taken using a fluorescent microscope. The images taken from different samples and different time points were analyzed using Image J software and by evaluating the myotube length, aspect ratio and counting the number of nuclei in the formed myotubes. To get more representative results, ten images of different places on samples were used.

#### 2.9.4. Electrical stimulation

Differentiated muscle cells grown on fibrous bilayer scaffolds after 7 days of differentiation were stimulated using a custom-made electrical stimulation device to evaluate the functionality of the myotubes. Briefly, cell seeded electrospun mesh were taped in 60 mm culture dishes with silicone adhesive tape and after 7 days of differentiation, they were stimulated electrically using a self-made stimulation dish which was made of two parallel platinum electrodes. The stimulation dish was sterilized each time prior using under the UV light for 15 min and platinum electrodes were placed perpendicular to the fiber direction and subjected to previously optimized continuous square electrical pulses (4–5 V, frequency: 1 Hz, duration: 1 ms) [38]. A stimulation medium was prepared adding 1% MEM-non-essential amino acid (gibco) and 2% MEM essential amino acid (gibco) to the differentiation medium. The contraction of muscle cells was captured using time-lapse imaging.

#### 2.9.5. Cell imaging using SEM

To investigate the cell spreading and their morphology after adhesion on fabricated bilayers, samples were fixed, dehydrated and analyzed using SEM. Alcohol concentration gradient (50%, 70%, 80%, 90%, 100% of EtOH) was used to gradually remove water from the samples. Then, samples were covered with a mixture of EtOH and tert-butyl alcohol (1:1 v/v) for 5 min at room temperature. Next, samples were dipped in pure 100% tert-butyl alcohol. To freeze tert-butanol, samples were put in a  $-80$  °C freezer for 1 h. Lyophilizer was used to dry the samples completely. When samples

were fully dried, they were prepared for SEM imaging as mentioned before in the section SEM.

### 2.10. Statistical analysis

Obtained data were shown as the mean  $\pm$  standard deviation (SD) (three replicates were used). A student's test and one-way analysis of variance (ANOVA) followed by Tukey's multiple comparison tests were performed to analyze differences between each two experimental groups. A value of  $p < 0.05$  was considered as statistically significant.

## 3. Results and discussion

We used electrospinning to prepare polycaprolactone (PCL)—methacrylated alginate (AA-MA) bilayer mats. It is essential that PCL fibers are uniaxially aligned to, (i) provide orientation cues to cells, and to (ii) guide shape-transformation of the bilayer resulting in the formation of a tube. Orientation of AA-MA fibers was not crucial as they were not used as the cell substrate and, due to extensive swelling, no longer had distinctive structural cues for cells to follow. PCL fibrous mats with aligned fibers were fabricated as a first layer by electrospinning, where two different collectors such as a rotating drum and parallel bars were used. We found that the diameter of PCL fibers varies slightly with the method of deposition and was  $\sim 2.0 \pm 2.0 \mu\text{m}$  and  $1.6 \pm 1.1 \mu\text{m}$ , when a rotating drum and parallel bars collector were used, respectively (figures 2(a)–(b), S1(a)–(d) are available online at [stacks.iop.org/BF/12/015016/mmedia](https://stacks.iop.org/BF/12/015016/mmedia)). AA-MA mats with random orientation of fibers were deposited on top of preliminary prepared PCL mats. The spinning solution of the AA-MA fibers contained Eosin Y and Triethanolamine (TEA) as photoinitiator and crosslinking agent for photocrosslinking under green light (wavelength: 532 nm). We also prepared individual PCL and AA-MA mats for characterization of their individual properties.

It was determined that the parallel bars collector resulted in a higher degree of alignment of PCL fibers (60% of all fibers had  $<10^\circ$  fiber orientation angle) compared to the drum collector (40%). On the other hand, the rotating drum allowed fabrication of a thicker fiber mat ( $500 \mu\text{m}$ ) in comparison with the parallel bar ( $100 \mu\text{m}$ ) (figure 2(c)). We observed that the degree of fiber alignment in mats produced by both methods decreased with increasing spinning time and the thickness of mat, which was caused by fiber thickening and entanglement [39]. Small and wide angle x-ray scattering measurements confirmed uniaxial orientation of polymer chains and lamellas. At low scattering vectors  $q$  the SAXS signal scales with  $q^{-4}$  as expected for a 3D object as the mat. The strong anisotropy of the signal in that range proves the preferred orientation of the fibres inside the mat. A shoulder around  $0.05 \text{ \AA}^{-1}$  is visible in the 1D data,

corresponding to a correlation length of about 14 nm, if the mat is measured in parallel beam direction this feature is seen in the 2D image as spots on opposite sites. As a result of the preparation method, the peakedness of the shoulder is most pronounced in parallel geometry as a consequence of the better orientation in the equatorial plane (thinnest dimension) of the mat. The preferred orientation of the fibres itself is reflected by the lozenge-like shape at lowest  $q$ . The degree of crystallinity of electrospun PCL fibers was of about 40% as it was revealed by Differential Scanning Calorimetry (DSC) (figure S2(a)).

Dynamic mechanical analysis (DMA) revealed the anisotropic mechanical properties of PCL mats—there is a significant difference of elastic modulus in different directions (figure 2(d)). Elastic modulus measured for longitudinal orientation of fibers was 20.7 MPa and it was significantly higher than that measured for transverse orientation ( $E = 6.3 \text{ MPa}$ ). The higher value of longitudinal modulus can be explained by the fact that the stretching of the oriented fiber requires larger force than the separation of individual fibers. We separately investigated swelling properties of freestanding AA-MA mat. It results that the swelling degree of polymer mat decreases with increasing concentration of  $\text{Ca}^{2+}$  ions (figure 2(f)). Interestingly, while the thickness of photocrosslinked AA-MA mats strongly depends on concentration of  $\text{Ca}^{2+}$  ions (range 300%–1300%) (figure 2(f)), the lateral width changes are almost independent of concentration of  $\text{Ca}^{2+}$  ions and are in the range 10%–15% (figure S2(d)).

The PCL-alginate bilayers demonstrated shape-transformation behavior in an aqueous environment (water, PBS, water with different  $\text{Ca}^{2+}$  ion concentration) as they started to roll and form tubular scroll-like structures. Eventually, the diameter of these tubes and the direction of folding of bilayers depend on both: (i) the orientation of PCL fibers with respect to the main axis of a polymer mat, and (ii) the concentration of  $\text{Ca}^{2+}$  ions (figure 3). We observed that bilayers roll and form tubes in an aqueous environment with low  $\text{Ca}^{2+}$  ions concentration. PCL and AA-MA mats formed the inner and outer surfaces of the tubes, respectively (figure 3(a)). Increased concentration of  $\text{Ca}^{2+}$  ions resulted in unrolling of the bilayers due to the decreased swelling degree of alginate in different concentrations of  $\text{Ca}^{2+}$  ions solution ( $0.00145\text{--}0.08 \text{ mol l}^{-1}$ , figure 3(b)). Interestingly, we observed a change of direction of folding of bilayer towards AA-MA side at a certain  $\text{Ca}^{2+}$  ions concentration ( $\sim 0.08 \text{ mol l}^{-1}$  for samples with PCL/AA-MA thickness ratio 0.5–6). In this case, the bilayers flexed such that the PCL layer was under tension, or, in other words, there was convex flexure of the PCL side (figures 3(c)–(e)). The mechanism behind this bending is likely the relaxation of stretched PCL fibers [18]; during electrospinning the PCL fibers are stretched and therefore they relax and slightly bend towards the

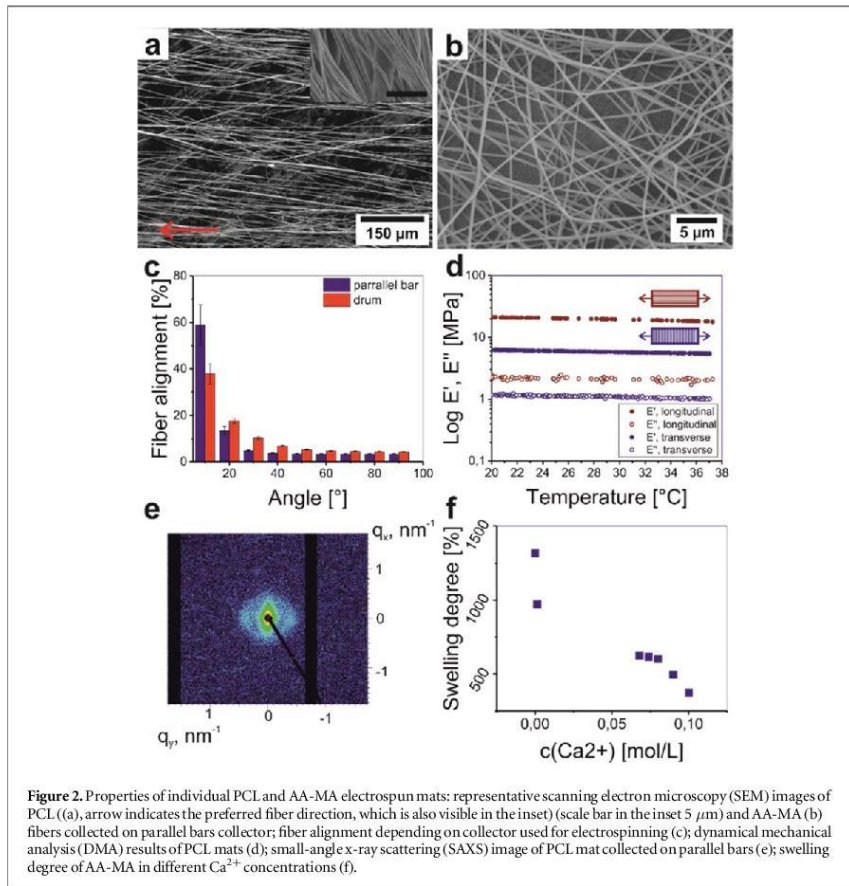


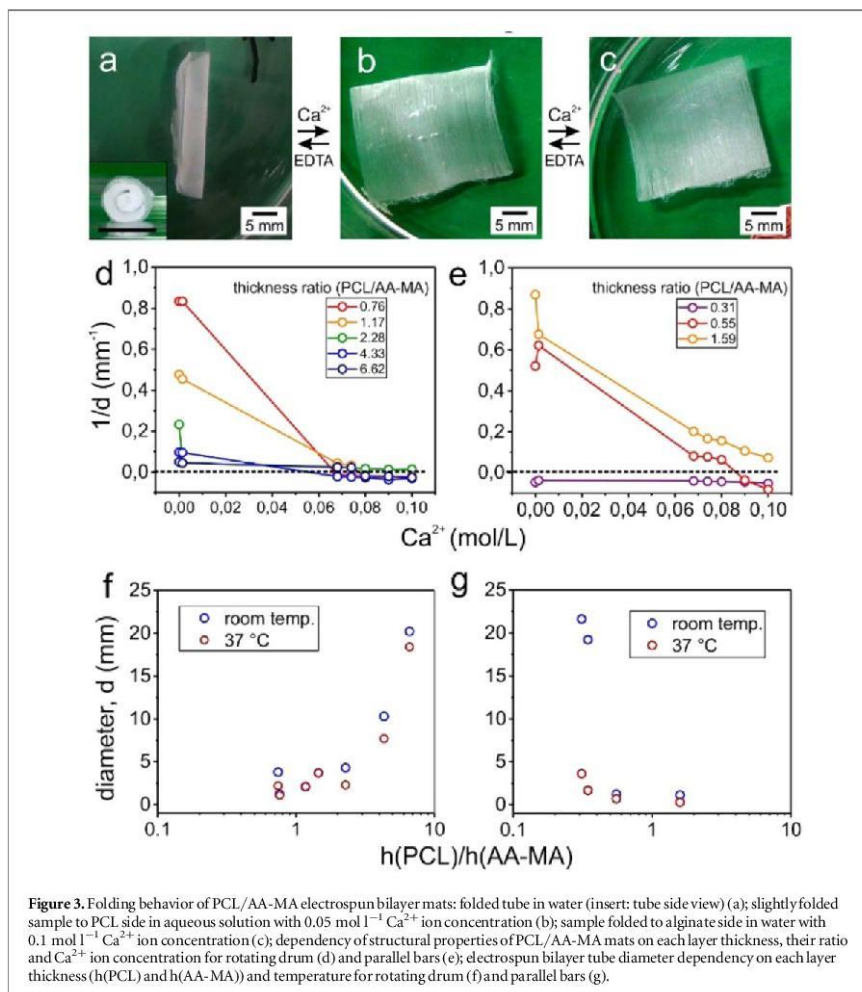
**Figure 2.** Properties of individual PCL and AA-MA electrospun mats: representative scanning electron microscopy (SEM) images of PCL (a), arrow indicates the preferred fiber direction, which is also visible in the inset (scale bar in the inset 5  $\mu\text{m}$ ) and AA-MA (b) fibers collected on parallel bars collector; fiber alignment depending on collector used for electrospinning (c); dynamical mechanical analysis (DMA) results of PCL mats (d); small-angle x-ray scattering (SAXS) image of PCL mat collected on parallel bars (e); swelling degree of AA-MA in different  $\text{Ca}^{2+}$  concentrations (f).

AA-MA side as soon as they are removed from the collectors (dry state). Likewise, after the addition of  $\text{Ca}^{2+}$  ions solution (wet state) the relaxation behavior of PCL fibers restrict the swelling of AA-MA fibers and bend the bilayer towards the alginate side.

The ratio between thickness of PCL and AA-MA mats as well as the temperature of aqueous environment also affects the tube diameter. As it is shown in figures 3(d)–(e), increase of the thickness of PCL mat first resulted in decrease of tube diameter. Symmetric bilayer mats (1:1 thickness ratio of PCL and AA-MA,  $h(\text{PCL})/h(\text{AA-MA})$ ) form tubes with minimal diameters. Further, an increase of the thickness of PCL mat resulted in the increase of the diameter of the tubes (figures 3(d)–(e)). Qualitatively, this behavior can be explained by considering intrinsic properties of the materials. In a thin PCL mat (ratio PCL/AA-MA  $< 0.3$ ), PCL layer is not stiff enough to resist against the swelling of alginate layers, therefore, the tube diameter is large. Thicker PCL layer ( $0.3 < \text{ratio PCL/AA-MA} < 2$ ) is able to sufficiently restrict the

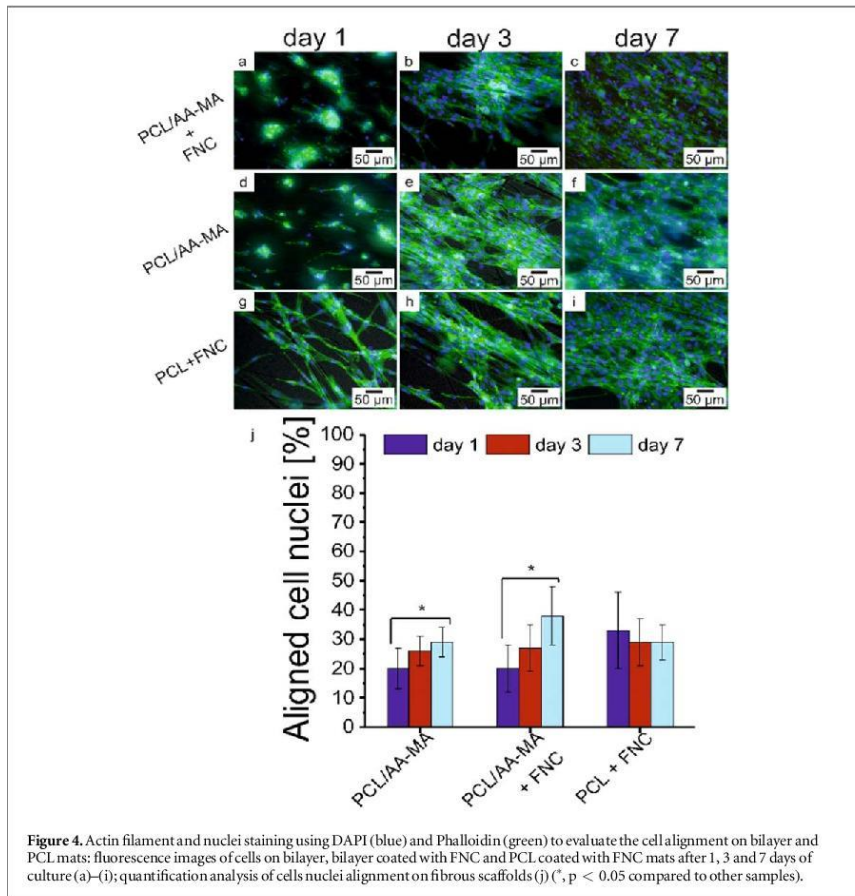
swelling of AA-MA mat to reduce the diameter of the resulted tube. However, a very thick layer of PCL (ratio PCL/AA-MA  $> 2$ ), in opposition, showed stiffer behavior and a swollen layer of AA-MA was not able to deform or bend the bilayer. Further, temperature was shown to have an effect on the tube diameter: generally, the diameter of tubes formed at higher temperature (37  $^{\circ}\text{C}$ ) was slightly smaller than those formed at room temperature (figures 3(f)–(g)) due to the softening and relaxation of PCL at higher temperatures [18]. Therefore, the variation caused by temperature changes on tube diameters is more profound when the AA-MA layer is thicker than the PCL layer. Consequently, we can conclude that PCL/AA-MA bilayer electrospun mats are able to form tubes in an aqueous environment and the diameter of these tubes can be precisely controlled by varying the thickness of the layers, the concentration of  $\text{Ca}^{2+}$  ions and the temperature.

The folding scenario of bilayer mats depends also on their shape and total thickness (figures S3–5). In



terms of shapes, we examined rectangular, square and circular mats, and in terms of thickness we measured thin (thickness  $\leq 100 \mu\text{m}$ ) and thick (thickness  $\geq 500 \mu\text{m}$ ) mats. Thin rectangular bilayer mats ( $\leq 100 \mu\text{m}$ ) were always rolled perpendicular with respect to the orientation direction of fibers (figures S4(a)–(d)). Square mats also fold crosswise with respect to direction orientation of fibers (figures S4(e)–(f)). Their folding starts from two opposite sides and results in fibers being perpendicular to the main axis of the formed tube (figure S3). Interestingly, the circular mat started to fold predominately from one side and the folding was always parallel with respect to the main axis of orientation and the direction of fibers. In other words, the resulted tubes had fibers oriented along the main axis of the tube (figures S4(g)–(h)).

Folding of thicker samples ( $\geq 500 \mu\text{m}$ ) also depends on their shape and thickness (figure S5). Similar to the folding scenario of thin circular mats, thick circular mats form tubes by having PCL fibers oriented along its length (figure S5(c)). Rectangular mats folded predominantly such that fibers in the formed tube are oriented along the axis of the tube (figures S5(b), (d)). In case of square shaped mats, the folding began at opposite corners of the mat, which resulted in a small-angle twisting in respect to the length of the tube (figure S5(a)). One can assume that there are four factors that can effect a scenario of folding of rectangular and square bilayers: (i) mechanical anisotropy determined by orientation of PCL fibers, (ii) shape/edge effects, (iii) thickness and (iv) environmental conditions (temperature, ion concentration).

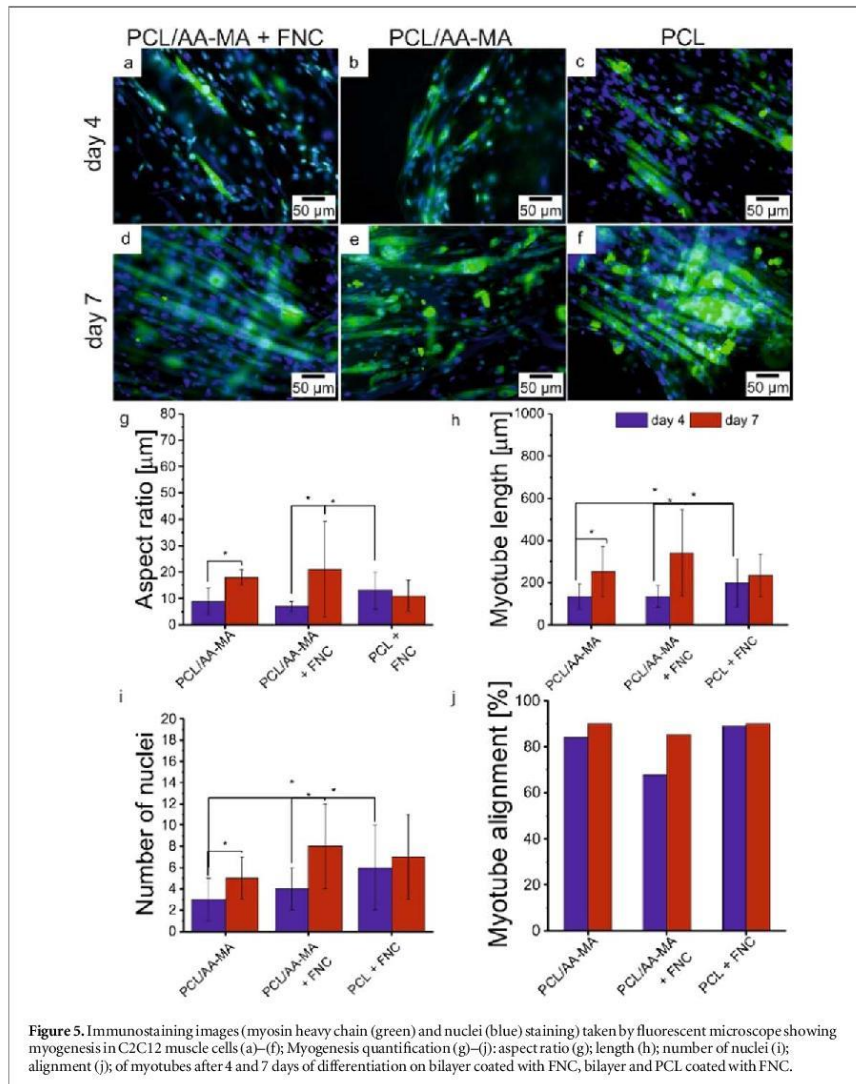


Due to the full symmetrical shape, folding of circular mats shall not be influenced by shape/edge effects, therefore, the circular shape is most promising for the fabrication of tubes with parallel orientation of fibers.

To study the formation of muscle microtissue on electrospun mats, we used thin ( $<100 \mu\text{m}$ ) PCL/AA-MA bilayer mats prepared using parallel bars cut into the shape of circles and seeded with mouse myoblasts (C2C12) on the PCL side of the bilayer (oriented fibers). This system was used due to 20% higher alignment of PCL fibers, and a smaller formed tube diameter which is closer to natural muscle fiber diameter ( $100 \mu\text{m}$ ) [40]. The cell adhesion to hydrophobic PCL layer was improved by its treatment with fibronectin, collagen, and albumin (FNC) solution. Previously, we showed the effect of FNC protein coating to improve the adhesion of cells on the surface of hydrophobic materials such as PCL [31]. Non-coated bilayer and PCL mats were used as controls. During experiments, we have observed no cell adhesion on the alginate side of the bilayer which can also clearly show that PCL

fibers are the side for adhering and aligning the cells. As mentioned above, our porous PCL/AA-MA bilayer mats form tubes due to the swelling of alginate material and self-folding behavior. Therefore, to control the cell seeding and to facilitate the imaging process for future steps, samples were fixed in cell culture crowns to avoid instant tube formation. However, as a result of self-folding, cultured cells were able to be trapped inside the non-transparent 3D structure and formed a cell layer within the construct without any disruption of self-folded structure, as is shown in the electrical stimulation section (figure 6(c)).

Cells cultured on bilayers as well as PCL aligned fiber mats showed a high viability above 90% independently, whether mats were treated with FNC or not. As it was shown in (figure S6–9), myoblast cells on non-coated (aligned) PCL fibers, did not adhere with homogenous distribution and rather formed clusters. Moreover, after 7 days of culture those clusters did not show alignment on fibers and stayed with a round morphology. However, on FNC coated fibers, cells



were able to adhere and spread (figure S13). Therefore, bilayers were treated with FNC in all further experiments to promote cell adhesion.

In addition, we observed that thickness of AA-MA and PCL layers affected the cell growth and viability. On the bilayer mats with 20  $\mu\text{m}$  thick PCL and 60  $\mu\text{m}$  thick AA-MA, cells tended to make a cluster and spread weakly (figure S10). In fact, on such a bilayer with thicker AA-MA layer and thinner PCL layers, more cells are in contact with swollen AA-MA fibers, which do not offer any chemical groups to adhere to (figures S7 and 11).

Cell alignment on fibrous mats, which was analyzed after staining of actin filament and nuclei, using

DAPI and phalloidin, also confirmed the dependency of cells behavior on thickness of alginate layer and surface treatment with FNC. As mentioned above, the presence of an AA-MA layer in the bilayer mat resulted in the lower degree of cell alignment one day after the cell seeding independently, whether it was coated with FNC or not. However, this poor alignment was significantly improved after a week of culture (figures 4, S11–14). Accordingly, we cultured the cells on PCL control samples (coated and non-coated) and observed the treatment of PCL mats with FNC allowed substantial increase of degree of cell alignment even one day after culture. After seven days, all samples showed comparable cell alignment  $\sim 30\%$  of the cells

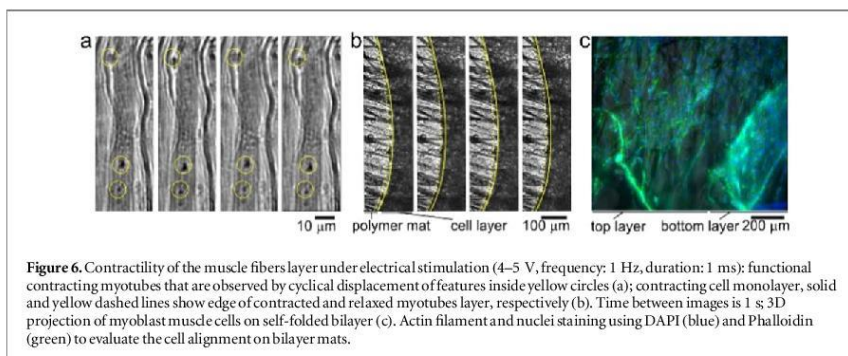


**Figure 6.** Contractility of the muscle fibers layer under electrical stimulation (4–5 V, frequency: 1 Hz, duration: 1 ms): functional contracting myotubes that are observed by cyclical displacement of features inside yellow circles (a); contracting cell monolayer, solid and yellow dashed lines show edge of contracted and relaxed myotubes layer, respectively (b). Time between images is 1 s; 3D projection of myoblast muscle cells on self-folded bilayer (c). Actin filament and nuclei staining using DAPI (blue) and Phalloidin (green) to evaluate the cell alignment on bilayer mats.

were aligned with the fibers. This was also confirmed by SEM micrographs, where we could see the formation of monolayer of muscle cells on bilayer after seven days of culture (figure S15). As it was mentioned, lower initial cell alignment on bilayer mats and weak cell adhesion on thin bilayers can be explained by the influence of alginate. In fact, alginate is a polysaccharide that does not contain any chemical groups promoting cell adhesion. FNC most probably was not adsorbed by this hydrophilic hydrogel but provided a thin protein coating to cells for the initial cell attachment.

After 7 days of culture, the medium was exchanged with one containing a lower serum content (2% horse serum) to enhance the differentiation and fusion of myoblasts cells to myotubes. To prove the formation of muscle tissue bundles, the myogenesis was monitored using immunostaining and quantified within one week of differentiation on the fibrous mats. We observed generation of small myotubes and fusion of myoblasts after 4 days of differentiation (150 μm length and number of nuclei lower than 5) (figures 5(h), (i), S16–18). They continued to enlarge and mature within 7 days up to 350 μm length and number of nuclei higher than 8 on FNC-coated PCL/AA-MA bilayer mat. In the first 4 days of differentiation, we observed faster myotube formation on PCL mats compared to bilayers, and cells grew in width rather than length, resulting in a slight decrease of their aspect ratio. Myotube formation was likely delayed by alginate, which does not promote cell adhesion. We observed the formation of continuous layer of muscle fibers on the surface of bilayer and PCL mats after 7 days of differentiation.

The functionality and contractility of the muscle cell layer formed on the fibrous self-folding bilayer was tested after 7 days of differentiation by electrical stimulation (14 days total in culture). We observed that the mature myotubes, which are oriented along fibers contract synchronously with the applied pulses (figure 6, video S19–21). Moreover, we observed that a continuous muscle fiber layer, which was delaminated

from a bilayer mat upon its manual unfolding, contracts as whole under electrical stimulation. This implied that there was a formation of functional, aligned skeletal muscle microtissue (thickness ~20 μm) inside the self-rolled fibrous PCL/AA-MA bilayer mat.

#### 4. Conclusions

Using a 4D biofabrication approach, we were able to produce functional skeletal muscle microtissues. PCL/AA-MA electrospun bilayer mats with uniaxial alignment of PCL fibers were able to undergo programmed shape-transformation and to form multilayer scroll-like tubular constructs, where the fibers were aligned in parallel with the tube's axis. These longitudinally aligned fibers were able to guide the alignment of myoblasts and to allow the fabrication of a continuous structure of aligned myotubes inside the self-rolled multilayer construct, which are able to contract responding to electrical stimulation.

This new approach allows fabrication of important building blocks for tissue engineering—aligned 3D skeletal muscle fiber bundles with tubular structure. This hollow tubular construct can be further developed for formation of vascularized tissue to deliver oxygen and nutrition to the cells inside the rolled construct, eventually maturing into a piece of tissue to be implanted into the body.

#### Acknowledgments

This work was supported by DFG (Grant N. IO 68/11-1; IO 68/14-1; SA 3575/1-1; Project N 326998133—SFB/TRR225 (subproject B03)). We would further like to thank Prof. Minko and Prof. Scheibel for providing us with electrospinning equipment and lab facilities, and Elise DeSimone for paper revisions.

## ORCID iDs

Andrés Fernando Posada  <https://orcid.org/0000-0002-0032-2224>

Sahar Salehi  <https://orcid.org/0000-0002-6740-4195>

Leonid Ionov  <https://orcid.org/0000-0002-0770-6140>

## References

- [1] Berthiaume F, Maguire TJ and Yarmush M L 2011 Tissue engineering and regenerative medicine: history, progress, and challenges *Annual Review of Chemical and Biomolecular Engineering* **2** 403–30
- [2] Marieb E N and Hoehn K 2010 *Human Anatomy & Physiology* (San Francisco, CA: Benjamin Cummings)
- [3] Ostrovidov S, Shi X, Sadeghian R B, Salehi S, Fujie T, Bae H, Ramalingam M and Khademhosseini A 2015 Stem cell differentiation toward the myogenic lineage for muscle tissue regeneration: a focus on muscular dystrophy *Stem Cell Reviews and Reports* **11** 866–84
- [4] Almada A E and Wagers A J 2016 Molecular circuitry of stem cell fate in skeletal muscle regeneration, ageing and disease *Nat. Rev. Mol. Cell Biol.* **17** 267
- [5] Salehi S, Ostrovidov S, Ebrahimi M, Sadeghian R B, Liang X, Nakajima K, Bae H, Fujie T and Khademhosseini A 2017 Development of flexible cell-loaded ultrathin ribbons for minimally invasive delivery of skeletal muscle cells *ACS Biomaterials Science & Engineering* **3** 579–89
- [6] Chen S, Nakamoto T, Kawazoe N and Chen G 2015 Engineering multi-layered skeletal muscle tissue by using 3D microgrooved collagen scaffolds *Biomaterials* **73** 23–31
- [7] Wang L, Wu Y, Guo B and Ma P X 2015 Nanofiber yarn/hydrogel core-shell scaffolds mimicking native skeletal muscle tissue for guiding 3D myoblast alignment, elongation, and differentiation *ACS Nano* **9** 9167–79
- [8] Kang H-W, Lee S J, Ko I K, Kengla C, Yoo J J and Atala A 2016 A 3D bioprinting system to produce human-scale tissue constructs with structural integrity *Nat. Biotechnol.* **34** 312
- [9] Yim E K F, Reano R M, Pang S W, Yee A F, Chen C S and Leong K W 2005 Nanopattern-induced changes in morphology and motility of smooth muscle cells *Biomaterials* **26** 5405–13
- [10] Zhao Y, Zeng H, Nam J and Agarwal S 2009 Fabrication of skeletal muscle constructs by topographic activation of cell alignment *Bioelectrochem.* **102** 624–31
- [11] Powell C A, Smiley B L, Mills J and Vandenburgh H H 2002 Mechanical stimulation improves tissue-engineered human skeletal muscle *American Journal of Physiology-Cell Physiology* **283** C1557–65
- [12] Nagamine K, Sato H, Kai H, Kaji H, Kanzaki M and Nishizawa M 2018 Contractile skeletal muscle cells cultured with a conducting soft wire for effective, selective stimulation *Sci. Rep.* **8** 2253
- [13] Tasoglu S and Demirci U 2013 Bioprinting for stem cell research *Trends Biotechnol.* **31** 10–9
- [14] Mauk R L, Seyhan S L, Ateshian G A and Hung C T 2002 Influence of seeding density and dynamic deformational loading on the developing structure/function relationships of chondrocyte-seeded agarose hydrogels *Ann. Biomed. Eng.* **30** 1046–56
- [15] Kirillova A, Maxson R, Stoychev G, Gomillion C T and Ionov L 2017 4D biofabrication using shape-morphing hydrogels *Adv. Mater.* **29** 1703443
- [16] Vannozzi L, Yasa I C, Ceylan H, Mencassi A, Ricotti L and Sitti M 2018 Self-folded hydrogel tubes for implantable muscular tissue scaffolds *Macromol. Biosci.* **18** 1700377
- [17] Ionov L 2018 4D biofabrication: materials, methods, and applications *Adv. Healthcare Mater.* **7** 1800412
- [18] Apsite I, Stoychev G, Zhang W, Jehnichen D, Xie J and Ionov L 2017 Porous stimuli-responsive self-folding electrospun mats for 4D biofabrication *Biomacromolecules* **18** 3178–84
- [19] Stroganov V, Pant J, Stoychev G, Janke A, Jehnichen D, Fery A, Handa H and Ionov L 2018 4D biofabrication: 3D cell patterning using shape-changing films *Adv. Funct. Mater.* **28** 1706248
- [20] Pedron S, van Lierop S, Horstman P, Penterman R, Broer D J and Peeters E 2011 Stimuli responsive delivery vehicles for cardiac microtissue transplantation *Adv. Funct. Mater.* **21** 1624–30
- [21] Stoychev G, Turcaud S, Dunlop J W C and Ionov L 2013 Hierarchical multi-step folding of polymer bilayers *Adv. Funct. Mater.* **23** 2295–300
- [22] Fernandes R and Gracias D H 2012 Self-folding polymeric containers for encapsulation and delivery of drugs *Adv. Drug Del. Rev.* **64** 1579–89
- [23] Randall C L, Kalinin Y V, Jamal M, Shah A and Gracias D H 2011 Self-folding immunoprotective cell encapsulation devices *Nanomed. Nanotechnol. Biol. Med.* **7** 686–9
- [24] Bhattarai N and Zhang M 2007 *Controlled Synthesis and Structural Stability of Alginate-based Nanofibers* **18** 45601
- [25] Bonino C A, Krebs M D, Saquing C D, Jeong S I, Shearer K L, Alsberg E and Khan S A 2011 Electrospinning alginate-based nanofibers: from blends to crosslinked low molecular weight alginate-only systems *Carbohydr. Polym.* **85** 111–9
- [26] Muggli D S, Burkoth A K, Keyser S A, Lee H R and Anseth K S 1998 Reaction behavior of biodegradable, photo-cross-linkable polyanhydrides *Macromolecules* **31** 4120–5
- [27] Jiang S, Liu F, Lerch A, Ionov L and Agarwal S 2015 Unusual and superfast temperature-triggered actuators *Adv. Mater.* **27** 4865–70
- [28] Peng L, Zhu J and Agarwal S 2017 Self-rolled porous hollow tubes made up of biodegradable polymers *Macromol. Rapid Commun.* **38** 1700034
- [29] Liu L, Ghaemi A, Gekle S and Agarwal S 2016 One-component dual actuation: poly(NIPAM) can actuate to stable 3D forms with reversible size change *Adv. Mater.* **28** 9792–6
- [30] Ostrovidov S et al 2017 Gelatin-polyaniline composite nanofibers enhanced excitation-contraction coupling system maturation in myotubes *ACS Applied Materials & Interfaces* **9** 42444–58
- [31] Salehi S, Czugala M, Stafiej P, Fathi M, Bahners T, Gutmann J S, Singer B B and Fuchsluger T A 2017 Poly(glycerol sebacate)-poly( $\epsilon$ -caprolactone) blend nanofibrous scaffold as intrinsic bio- and immunocompatible system for corneal repair *Acta Biomater.* **50** 370–80
- [32] Liu W, Thomopoulos S and Xia Y 2012 Electrospun nanofibers for regenerative medicine *Adv. Healthcare Mater.* **1** 10–25
- [33] Schnell E, Klinkhammer K, Balzer S, Brook G, Klee D, Dalton P and Mey J 2007 *Guidance of Glial Cell Migration and Axonal Growth on Electrospun Nanofibers of Poly- $\epsilon$ -caprolactone and a Collagen/poly- $\epsilon$ -Caprolactone Blend* **28** 3012–25
- [34] Chen T, Bakhshi H, Liu L, Ji J and Agarwal S 2018 Combining 3D printing with electrospinning for rapid response and enhanced designability of hydrogel actuators *Adv. Funct. Mater.* **28** 1800514
- [35] Cheng S, Jin Y, Wang N, Cao F, Zhang W, Bai W, Zheng W and Jiang X 2017 Self-adjusting, polymeric multilayered roll that can keep the shapes of the blood vessel scaffolds during biodegradation *Adv. Mater.* **29** 1700171
- [36] Zakharchenko S and Ionov L 2015 Anisotropic liquid microcapsules from biomimetic self-folding polymer films *ACS Applied Materials & Interfaces* **7** 12367–72
- [37] Smeds K A, Pfister-Serres A, Miki D, Dastgheib K, Inoue M, Hatchell D L and Grinstaff M W 2001 Photocrosslinkable polysaccharides for *in situ* hydrogel formation *J. Biomed. Mater. Res.* **55** 254–5
- [38] Banan Sadeghian R, Ebrahimi M and Salehi S 2018 Electrical stimulation of microengineered skeletal muscle tissue: effect of stimulus parameters on myotube contractility and maturation *J. Tissue Eng. Regen. Med.* **12** 912–22
- [39] Katta P, Alessandro M, Ramsier R D and Chase G G 2004 Continuous electrospinning of aligned polymer nanofibers onto a wire drum collector *Nano Lett.* **4** 2215–8
- [40] Mescher A L 2015 *Junqueira's Basic Histology: Text and Atlas* 14 edn (New York: McGraw-Hill)

# Supporting Information

## 4D Biofabrication of Skeletal Muscle Microtissues

*Indra Apsite<sup>1</sup>, Juan Manuel Uribe<sup>1</sup>, Andrés Fernando Posada<sup>1</sup>, Sabine Rosenfeldt<sup>2</sup>, Sahar Salehi<sup>3\*</sup>, Leonid Ionov<sup>1\*</sup>*

<sup>1</sup> Faculty of Engineering Sciences and Bavarian Polymer Institute, University of Bayreuth,  
Ludwig Thoma Str. 36A, 95447 Bayreuth, Germany

<sup>2</sup> Department of Physical Chemistry I, Faculty of Biology, Chemistry & Earth Sciences and  
Bavarian Polymer Institute, University of Bayreuth, Universitätsstraße 30, 95447 Bayreuth,  
Germany

<sup>3</sup> Chair of Biomaterials, University of Bayreuth, Karolinenreuther Str. 50, 95448 Bayreuth,  
Germany

E-mail: [leonid.ionov@uni-bayreuth.de](mailto:leonid.ionov@uni-bayreuth.de) and [sahar.salehi@bm.uni-bayreuth.de](mailto:sahar.salehi@bm.uni-bayreuth.de)

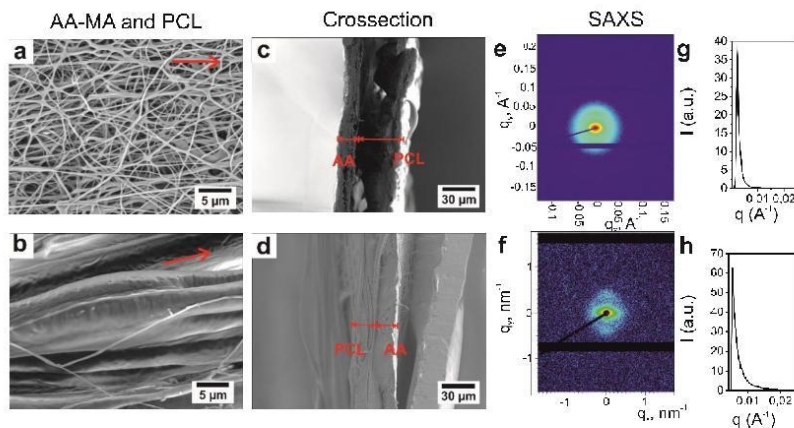


Figure S1. Characteristics of AA-MA (top row) and PCL (bottom row) mats. SEM image of AA-MA (a) and PCL (b) mat collected using drum; The red arrows indicate the preferred directions of the fibers. SEM cross-section of drum and parallel bar electrospun bilayers (c,d); 2D SAXS (e,f) and 1D SAXS patterns (g,h) of the mats showing the preferred orientation of the fibers.

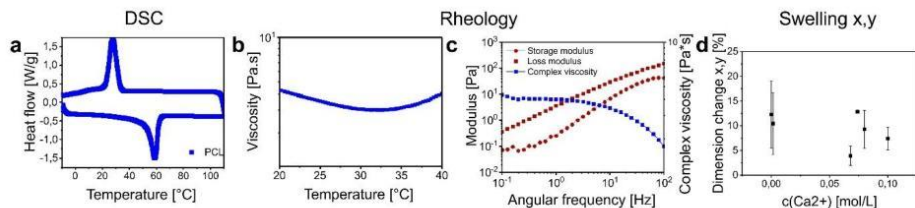


Figure S2. DSC measurement of electrospun PCL fibers using parallel bar method (a); Rheology measurements of noncrosslinked alginate hydrogel (b,c); longitudinal (x) and transverse (y) swelling degree of the AA-MA mat (d).

Movie S3. Folding of rectangular shaped PCL/AA-MA bilayer.

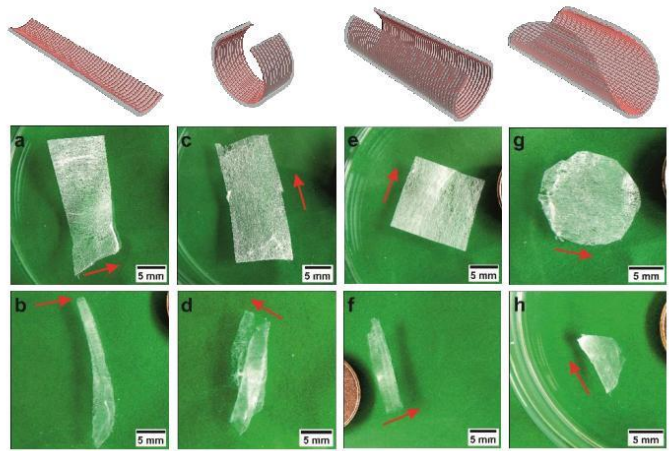


Figure S4. PCL/AA-MA bilayer mat with thickness  $\leq 100 \mu\text{m}$  folding behavior: folding of thin rectangular sample with transverse fiber alignment (a,b), folding of thin rectangular sample with longitudinal fiber alignment (c,d), folding of square shaped sample (e,f) and folding of circle shaped sample (g,h).

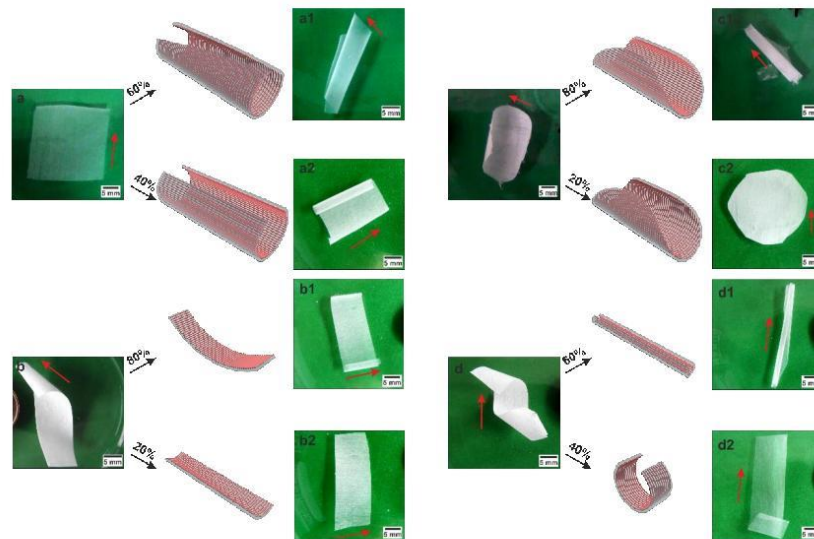


Figure S5. PCL/AA-MA bilayer mat with thickness  $\geq 500 \mu\text{m}$  folding behavior in percentage of probability following certain folding scenario: two folding scenarios of square shaped sample (a1-2), folding of thin rectangular sample with transverse fiber alignment (b1-2), folding of circular shaped sample (c1-2), folding of thin rectangular sample with longitudinal fiber alignment (d1-2).

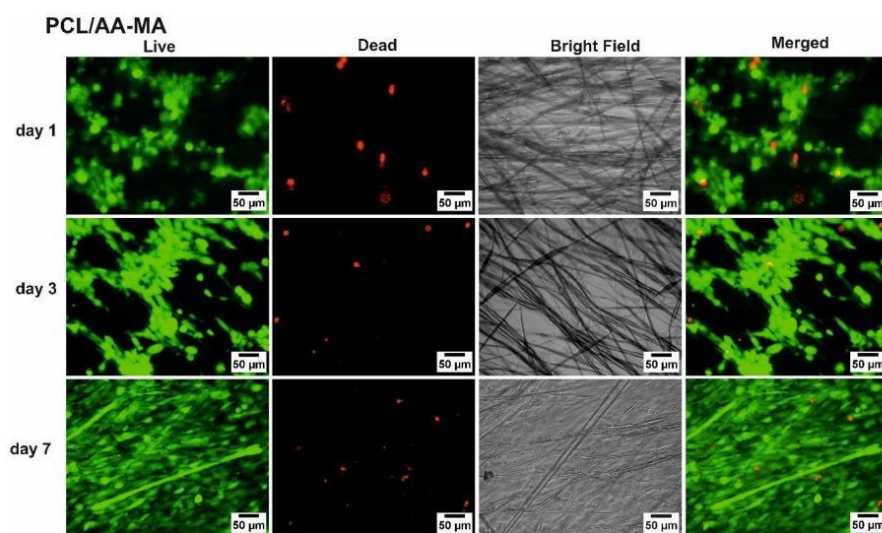


Figure S6. C2C12 mouse myoblast cell viability during 7 days of culture on PCL/AA-MA bilayer in growth culture medium (thin AA-MA layer) using live/dead assay. Green and red channels represent live and dead cells, respectively.

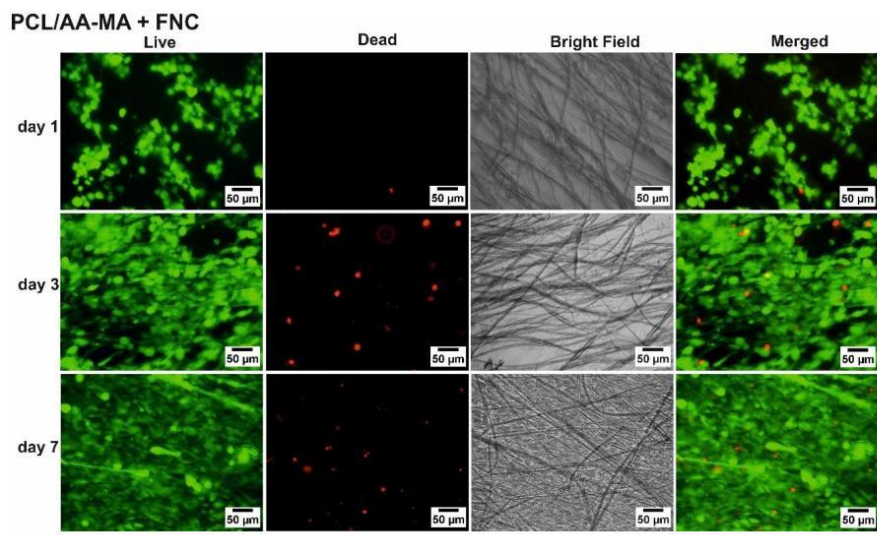


Figure S7. C2C12 mouse myoblast cell viability during 7 days of culture on PCL/AA-MA bilayer with FNC coating in growth culture medium using live/dead assay. Green and red channels represent live and dead cells, respectively.

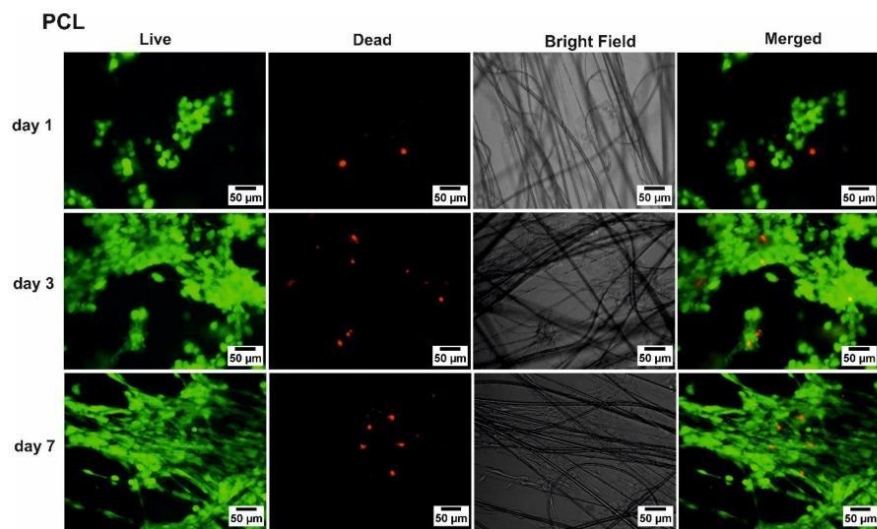


Figure S8. C2C12 mouse myoblast cell viability during 7 days of culture on PCL in growth culture medium using live/dead assay. Green and red channels represent live and dead cells, respectively.

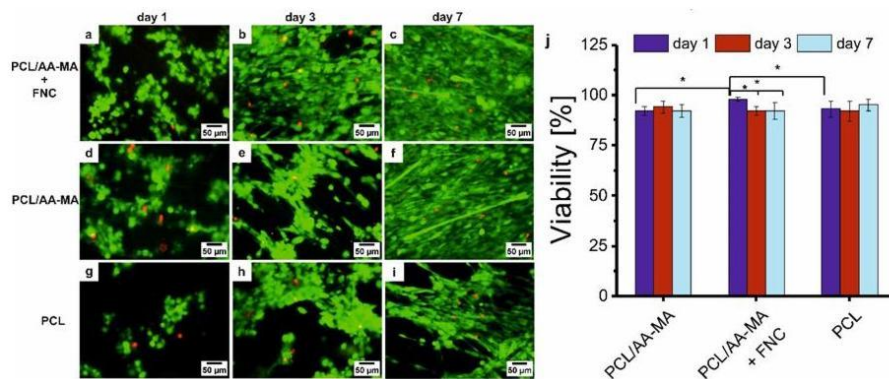


Figure S9. C2C12 mouse myoblast cell viability during 7 days of culture in growth culture medium using live/dead assay: fluorescent microscope images of cells on bilayer with FNC coating, bilayer and PCL mats (a-i); quantification analysis of the cell viability (\*,  $p < 0.05$  compared to other samples)(j). Green and red channels represent live and dead cells, respectively.

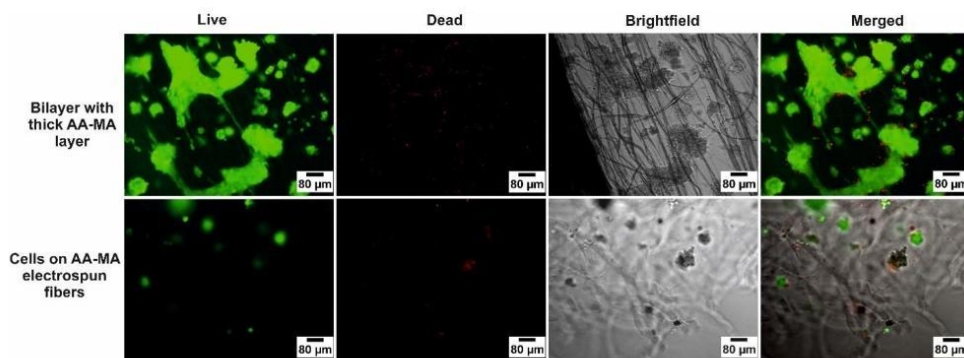


Figure S10. Live/dead staining of C2C12 mouse myoblast cell viability on bilayer with thick AA-MA layer and on AA-MA fibers after 3 days in growth culture medium ( $88\pm 5\%$  viability). Green and red channels represent live and dead cells, respectively.

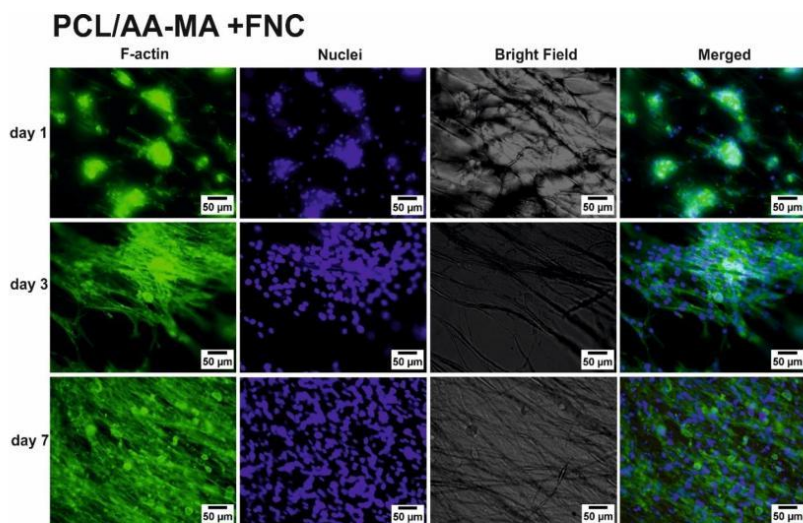


Figure S11. Actin filament and nuclei staining using DAPI (Blue) and Phalloidin (Green) to evaluate the cell alignment on bilayer mats coated with FNC after 1, 3 and 7 days in growth culture medium.

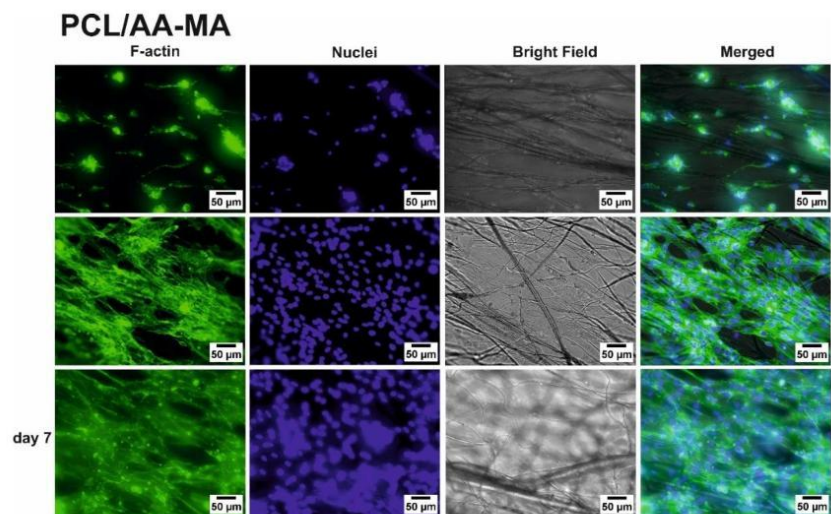


Figure S12. Actin filament and nuclei staining using DAPI (Blue) and Phalloidin (Green) to evaluate the cell alignment on bilayer mats without FNC coating after 1, 3 and 7 days in growth culture medium.

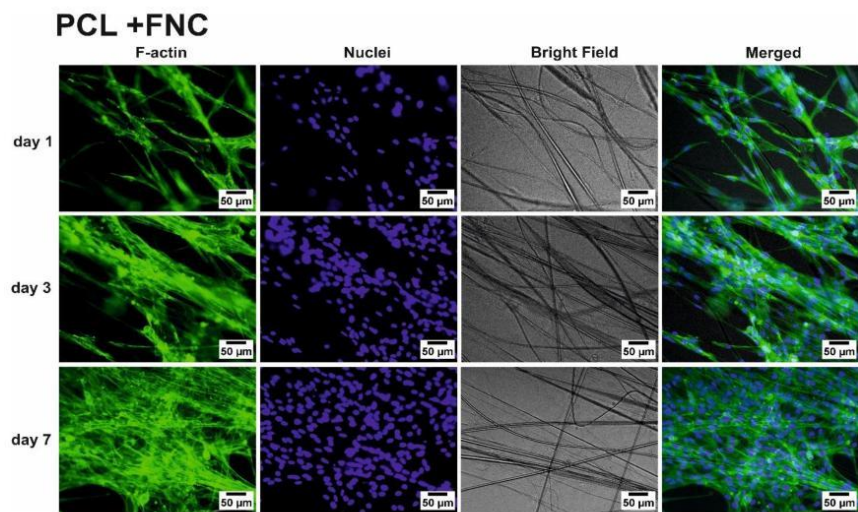


Figure S13. Actin filament and nuclei staining using DAPI (Blue) and Phalloidin (Green) to evaluate the cell alignment on PCL mats with FNC coating after 1, 3 and 7 days in growth culture medium.

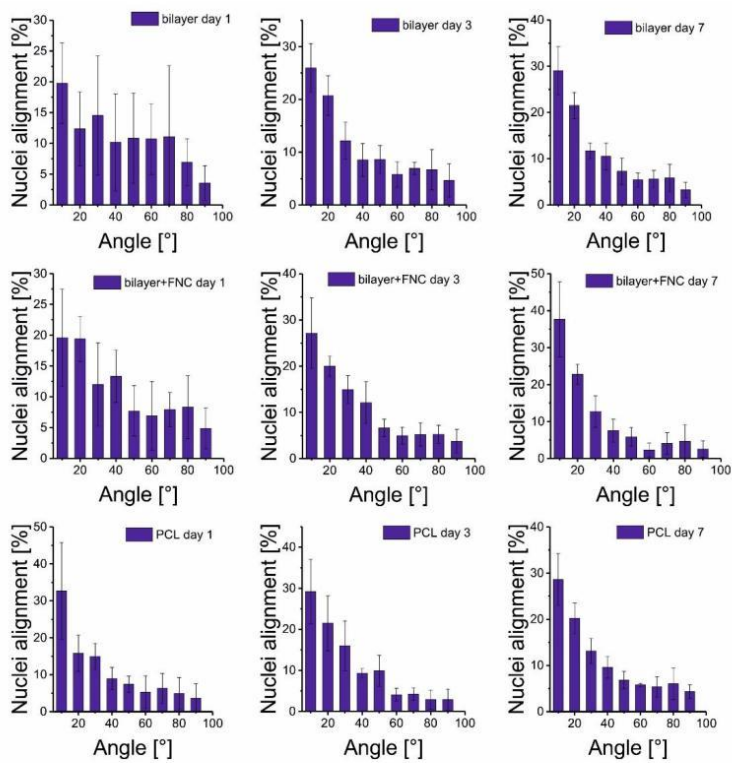


Figure S14. C2C12 mouse myoblast cell nuclei alignment on bilayer, bilayer coated with FNC and PCL coated with FNC after 1, 3 and 7 days in culture in growth culture medium.

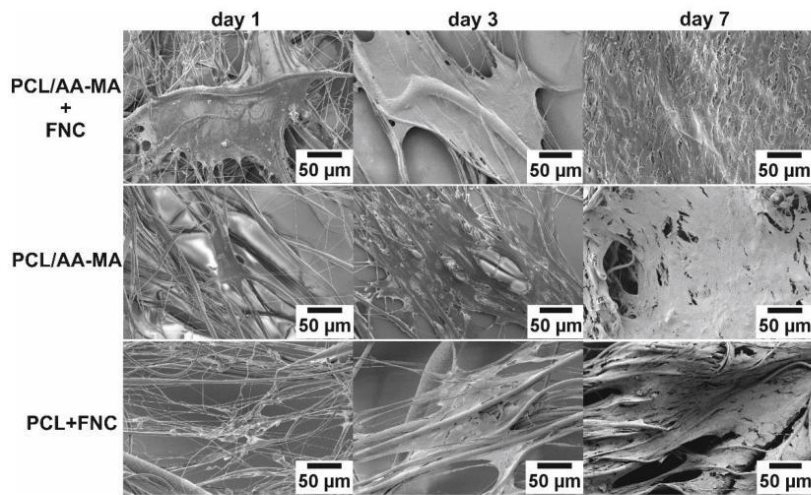


Figure S15. SEM images of C2C12 mouse myoblast cell on bilayer with FNC coating, bilayer and PCL with FNC coating after 1, 3 and 7 day in growth culture medium.

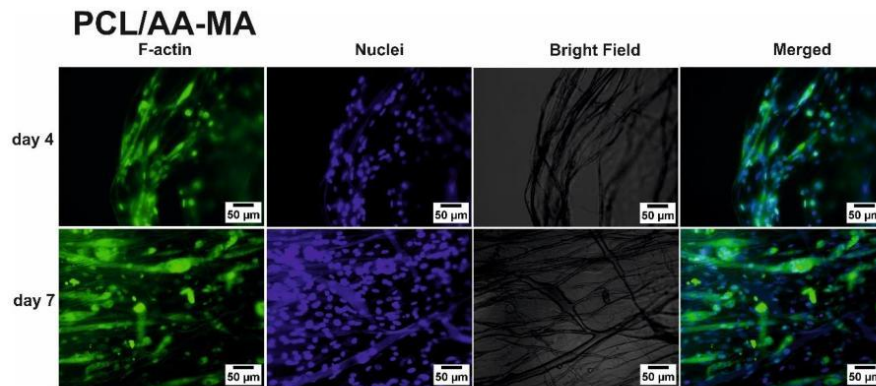


Figure S16. Immunostaining images (myosin heavy chain (Green) and nuclei (Blue) staining) taken by fluorescent microscope showing myogenesis in C2C12 muscle cells on bilayer mats without FNC coating after differentiation for 4 and 7 days in differentiation medium.

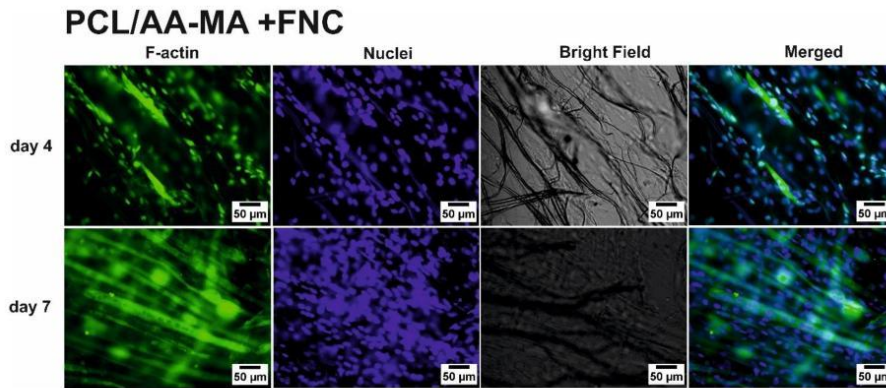


Figure S17. Immunostaining images (myosin heavy chain (Green) and nuclei (Blue) staining) taken by fluorescent microscope showing myogenesis in C2C12 muscle cells on bilayer mats with FNC coating after differentiation for 4 and 7 days in differentiation medium.

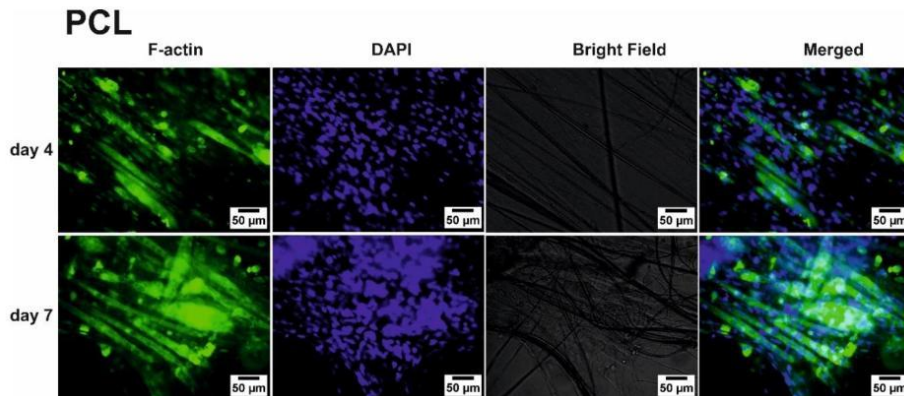


Figure S18. Immunostaining images (myosin heavy chain (Green) and nuclei (Blue) staining) taken by fluorescent microscope showing myogenesis in C2C12 muscle cells on PCL mats without FNC coating after differentiation for 4 and 7 days in differentiation medium.

Movie S19. Electrical stimulation of myotubes on bilayer.

Movie S20. Electrical stimulation of myotubes on bilayer.

Movie S21. Electrical stimulation of functional myotube layer on bilayer.

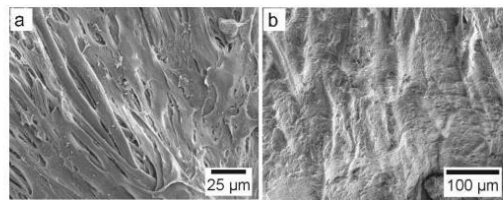


Figure S22. SEM image of myotubes (a) and muscle cell monolayer on bilayer after electrical stimulation (b).



Part 3. 4D Biofabrication of fibrous artificial nerve graft for neuron regeneration

**Apsite I.**, Constante G., Dulle M., Vogt L., Caspari A., Boccaccini R. A., Synytska A.,  
Salehi S., Ionov L.

Published in *Biofabrication* 12, 2020, 035027

(2020)

Reproduced under the terms and conditions of the Creative Commons CC BY 4.0



# Biofabrication



## PAPER

### OPEN ACCESS

RECEIVED  
12 March 2020

REVISED  
27 April 2020

ACCEPTED FOR PUBLICATION  
20 May 2020

PUBLISHED  
29 June 2020

Original content from this work may be used under the terms of the Creative Commons Attribution 4.0 licence.

Any further distribution of this work must maintain attribution to the author(s) and the title of the work, journal citation and DOI.



## 4D Biofabrication of fibrous artificial nerve graft for neuron regeneration

Indra Apsite<sup>1</sup>, Gissela Constante<sup>1</sup>, Martin Dulle<sup>2</sup> , Lena Vogt<sup>3</sup>, Anja Caspari<sup>4</sup>, Aldo R Boccaccini<sup>5</sup> , Alla Synytska<sup>4</sup> , Sahar Salehi<sup>5</sup> and Leonid Ionov<sup>1,6</sup>

<sup>1</sup> Faculty of Engineering Sciences and Bavarian Polymer Institute, University of Bayreuth, Ludwig Thoma Str. 36A, 95447, Bayreuth, Germany

<sup>2</sup> Forschungszentrum Jülich GmbH JCNS-1/IBI-8: Neutron Scattering and Biological Matter, 52425, Jülich, Germany

<sup>3</sup> Institute of Biomaterials, Department of Materials Science and Engineering, University of Erlangen-Nuremberg, Cauerstraße 6, 91058, Erlangen, Germany

<sup>4</sup> Leibniz Institute of Polymer Research Dresden e.V., Hohe Str. 6, 01069, Dresden, Germany

<sup>5</sup> Department of Biomaterials, University of Bayreuth, Prof.-Rüdiger-Bormann Str. 1, 95447, Bayreuth, Germany

<sup>6</sup> Author to whom any correspondence should be addressed.

E-mail: [leonid.ionov@uni-bayreuth.de](mailto:leonid.ionov@uni-bayreuth.de)

**Keywords:** electrospinning, self-folding, nerve guide conduits, 4D biofabrication, neuron cells

Supplementary material for this article is available [online](#)

### Abstract

In this paper, we describe the application of the 4D biofabrication approach for the fabrication of artificial nerve graft. Bilayer scaffolds consisting of uniaxially aligned polycaprolactone-poly(glycerol sebacate) (PCL-PGS) and randomly aligned methacrylated hyaluronic acid (HA-MA) fibers were fabricated using electrospinning and further used for the culture of PC-12 neuron cells. Tubular structures form instantly after immersion of fibrous bilayer in an aqueous buffer and the diameter of obtained tubes can be controlled by changing bilayer parameters such as the thickness of each layer, overall bilayer thickness, and medium counterion concentration. Designed scaffolds showed a self-folded scroll-like structure with high stability after four weeks of real-time degradation. The significance of this research is in the fabrication of tuneable tubular nerve guide conduits that can simplify the current existing clinical treatment of neural injuries.

### 1. Introduction

More than a million people each year are affected by peripheral nerve injuries, which can lead to the reduction of motor function, sensory perception, and in severe cases even death [1, 2]. Neural injuries, in general, can be caused by physical trauma, accident or genetics [3–5]. One of the biggest challenges in the treatment of nerve injuries is to bridge both endings of the ruptured nerve without causing inflammation or fibrosis, and this is especially important for neural defects with a large gap [6]. Autografts are used in clinical practice to oppose nerve ends. Although this technique has shown promising outcomes for nerve injury repair, it requires suitable donor material [7, 8]. Therefore, tissue engineering approach and usage of implantable hollow nerve guide conduits (NGCs) have been introduced as an attractive alternative; however, until now, NGCs have been

used only for small defect repair [9]. Various tissue engineering and biofabrication approaches including bioprinting, micropatterning, self-assembly, and electrospinning have been used to solve this issue by providing 3D scaffolds that could support and guide neurons during regeneration [10–15]. Various approaches have been explored to develop tubular structures as conduits with specific topographies and anisotropic morphology to guide nerve growth [3, 14–20]. 3D bioprinting of cell-laden hydrogels is one of the most used and promising methods for the fabrication of NGCs in the latest years. This approach allows homogenous cell distribution [21]. Nevertheless, there are several limitations of 3D printing such as the low resolution of printing of a tubular structure [22], narrow NGCs wall thickness to ensure waste product and nutrient permeability [23], and high shear forces during direct printing of NGCs [24].

Another shortcoming of tubular NGCs is the complex fixation of endings of the ruptured nerves. As a solution to this problem, 4D biofabrication is expected to allow wrapping and fixing of the endings of a ruptured nerve with a shape-morphing material. 4D biofabrication is based on the fabrication of complex 3D structures out of simple 2D and 3D objects by their shape transformation in a response to external stimuli [25, 26]. Therefore, 4D biofabrication can offer a number of advantages that are not accessible using conventional 3D fabrication techniques. Furthermore, it shows great potential in mimicking human tissues with tubular and anisotropic structures such as blood vessels [27–30], muscle fibers [31–33], and neural tissues [15, 34–38]. Self-folding materials have shown the potential to encapsulate cells, guide the differentiation of neuron cells, and neurites outgrowth using various fillers [15, 36, 39]. Recently, the possibility of fabrication of the NGCs was demonstrated with the example of a self-folding bilayer of non-porous solid chitosan film and electrospun spider silk fibers. The inner part of the tubular constructs were filled with a collagen cryogel [15]. It can be expected that the non-porosity of the chitosan layer can negatively affect the transport of nutrition to the inner part of the formed tube.

In this study, we introduce an advanced structural design—porous and completely electrospun self-folding bilayer as a potential NGC. The electrospun self-folding bilayers are unique materials because of their ability to offer a remarkable combination of fiber guided shape transformation [40–42], extra-fast actuation [43, 44], high permeability [27, 33, 45], and cell growth and alignment [33]. We show that biodegradable electrospun bilayer made of polycaprolactone-poly(glycerol sebacate) (PCL-PGS) and methacrylated hyaluronic acid (HA-MA) forms stable scroll-like tubular structures where the inner layer with aligned fibers provides the contact guidance to cells to form unidirectional neurites outgrowth. In advantage to all previously used shape-changing layers (alginate hydrogel-polycaprolactone fibers [33], chitosan film with silk fibers [15], alginate and hyaluronic acid hydrogels films [28], poly(N-isopropyl acrylamide)-based bilayers [46], and gelatine hydrogel/polycaprolactone film [47]), the system presented in this paper offers a unique combination of important advantages such as improved biocompatibility, suitable structural and mechanical anisotropy, adjusted mechanical properties, porosity, biodegradability, and the possibility to tune shape-transformation behaviour. In particular, in this research, we have proven that NGCs can be fabricated within a wide range of diameters (0.1–40 mm) that should allow personalized fabrication of NGCs which closely fit damaged and ruptured nerve stumps and could solve the existing problem of NGCs with over- and undersized diameters [48]. All main polymers (PCL, PGS, and HA), used

in this study to fabricate NGCs, are Food and Drug Administration (FDA) approved, biodegradable and biocompatible polymers, that in the latest years, have shown high potential for soft tissue engineering [49–53]. Moreover, we, for the first time, present a study on the degradation rate of shape-changing materials.

## 2. Materials and methods

### 2.1. Materials

Glycerol (BioXtra,  $\geq 99\%$  (GC), Product number G6279, Merck KGaA), Sebacic acid (99%, Product number V001987, Merck KGaA), Polycaprolactone (PCL) ( $M_n = 80\,000\text{ g mol}^{-1}$ , Product number 440 744, Merck KGaA), Hyaluronic acid sodium salt (MW 1–2 Million Da, Product number YH05852, Carbosynth), a Poly(ethylene oxide) (PEO) (MW 1 000 000  $\text{g mol}^{-1}$ , Product number 21 295, Polysciences Inc.), Pluronic® F-127 (Product number P2443, Merck KGaA), 2-Hydroxy-4'-(2-hydroxyethoxy)-2-methylpropiophenone (Irgacure D2959) (Merck KGaA), Chloroform anhydrous (Merck KGaA), Methacrylic anhydride (MA) (Merck KGaA), Ethanol 99% (EtOH) (Merck KGaA), Sodium hydroxide (NaOH) (Merck KGaA), Ethylenediaminetetraacetic acid (EDTA) (Merck KGaA), Calcium chloride dehydrate (Merck KGaA), Potassium chloride (BioXtra,  $\geq 99.0\%$ , Merck KGaA), Hydrochloric acid (ACS reagent, 37%, Merck KGaA), Potassium hydroxide (BioXtra,  $\geq 85\%$  KOH basis, Merck KGaA) Dulbecco's phosphate buffered saline (DPBS) (Merck KGaA), Roswell Park Memorial Institute (RPMI) 1640 Medium (gibco), Dulbecco's Modified Eagle Medium (DMEM) low glucose (Merck), Horse Serum (gibco), Penicillin Streptomycin (Pen/Strep) (gibco), Fetal Bovine Serum (FBS) (Merck), GlutaMax (gibco), 4-(2-hydroxyethyl)-1-piperazineethanesulfonic acid (HEPES) (Carl Roth), Gentamycin (Merck KGaA), Albumin Fraction V (BSA) (Roth), Collagen IV (Product number AB756P, Merck KGaA), Calcein AM (Thermo Fisher Scientific), Ethidium homodimer (EthD-1) (Thermo Fisher Scientific), alamarBlue™ HS Cell Viability Reagent (Thermo Fisher Scientific), Nerve growth factor (NGF), Rb pAb to beta III tubulin (abcam 18 207), Alexa fluor goat anti rabbit IgG 488 (Thermo Fisher Scientific), 4',6-diamidino-2-phenylindole (DAPI) (Thermo Fisher Scientific), Triton X-100 (Merck KGaA). The PC-12 cell line derived from a transplantable rat pheochromocytoma were purchased from ATCC (Manassas, VA) (ATCC® CRL-1721™)

### 2.2. Synthesis of mildly cross-linked PGS

To synthesize mildly cross-linked PGS, the described procedure by Jaafar *et al* was used [54]. Briefly, glycerol and sebacic acid were mixed in ratio 1:1 at 120 °C under nitrogen flow for 24 h. The obtained prepolymer after this reaction was moved to a vacuum oven and mildly cross-linked for 24 h. The yield of the synthesis was above 80% [55]. The chemical nature

of mildly cross-linked PGS was assessed via Fourier transform infrared attenuated total reflectance spectroscopy (ATR-FTIR) (IRAffinity-1S, Shimadzu Corporation, Kyōto, Japan). Therefore, 40 spectral scans were averaged across the spectral range of 4000 to 400  $\text{cm}^{-1}$  with a resolution of 4  $\text{cm}^{-1}$ . The measurement was performed at room temperature. The data was visualized via Origin (OriginLab, Northampton, MA, USA).

The chemical nature of synthesized PGS was confirmed by FTIR spectroscopy. PGS prepolymer before crosslinking showed all characteristic IR bonds of PGS: 2927  $\text{cm}^{-1}$  ( $\text{CH}_2$  stretching-asymmetric), 2852  $\text{cm}^{-1}$  ( $\text{CH}_2$  stretching-symmetric), 1298  $\text{cm}^{-1}$  (C-O and C-C stretching in the crystalline phase), 1732  $\text{cm}^{-1}$  (carbonyl stretching), 1224  $\text{cm}^{-1}$  (C-O-C stretching asymmetric), 3431  $\text{cm}^{-1}$  (hydroxyl stretching) (figure S1 (available online at [stacks.iop.org/BF/12/035027/mmedia](https://stacks.iop.org/BF/12/035027/mmedia))). These characteristics are in accordance with previous research [49, 56, 57].

### 2.3. Synthesis of methacrylated hyaluronic acid (HA-MA)

The methacrylate groups were introduced in HA acid using the procedure described by Smeds *et al* [58]. A 20-fold excess of methacrylic anhydride regarding to HA acid was added dropwise to a 2% HA solution. Reaction pH was constantly adjusted to pH 8 using 5M NaOH. The mixture was incubated at 4 °C for 24 h using constant stirring at 800 rpm. To clean HA-MA from impurities, the dialysis process was started against the Milli-Q water for a week at 37 °C. In this case, the dialysis tubes (Spectra/Por) with a molecular weight cut-off (MWCO) of 12 000–14 000 Da and a pore diameter of 25 Å was used, and the solution after one week of dialysis was freeze-dried using Freezone 2.5 (USA) for 48 h. The yield of synthesis was 84 %.

### 2.4. Electrospinning

A custom-made electrospinning device with a multi-syringe pump and high voltage source was used for fiber spinning. Omnifix® 1, 3 and 6 ml syringes were used, and flow rates were adjusted to 0.2  $\text{ml h}^{-1}$  and 0.36  $\text{ml h}^{-1}$  for PCL-PGS and HA-MA solutions, respectively. Needles with 0.8 mm inner diameter were used, and 15 kV and 28 kV were applied to the tip of the needle for the spinning of the PCL-PGS and HA-MA solutions, respectively. Electrospun fibers were collected on a custom-made rotating four-bar grounded collector (500 rpm), with a 4 cm distance between the bars. The distance between the needle tip and collectors was kept constant 15 and 28 cm for PCL-PGS and HA-MA fibers, respectively. Bilayer systems were produced by the sequential deposition of different polymer solutions during electrospinning. 8.5 wt% PCL solution in chloroform was used for PCL fiber preparation. Whereas for PCL-PGS fibers various solutions with wt%

from 8%–13% were prepared in chloroform, where the ratio between PGS and PCL was varied from 1:1 till 1:4. For the fabrication of hyaluronic acid fibers, 2 wt% solution of HA-MA was mixed with 10% (w/v) Irgacure D29590 solution to reach the concentration of 99.9% hyaluronic acid and 0.1% (w/v) photo crosslinker. To increase the spinnability, 5 wt% PEO and 20 wt% Pluronic F127 solutions were added to the HA-MA solution. For the final electrospinning solution, the weight ratio of each solution was 44/38/18 (HA-MA/PEO/Pluronic F127)[59]. The electrospun HA-MA fibers were photo-crosslinked under UV light (VL-215, 8 W  $\text{cm}^{-2}$ ) with 254 nm wavelength for 15 min with a distance of 2 cm.

### 2.5. Scanning electron microscopy (SEM)

The fiber morphologies were investigated using a field emission scanning electron microscopy (FE-SEM) (FEI Teneo, FEI Co., Hillsboro, OR, and Carl Zeiss Microscopy GmbH, Germany) and Apreo SEM (Thermo Fisher Scientific, USA). Fully dried samples were covered with ~10 nm gold or 1.3 nm platinum to ensure the electrical conductivity.

### 2.6. Dynamical mechanical analysis (DMA)

The mechanical properties of electrospun fiber mats were characterized by dynamic mechanical analysis (Anton Paar MCR 702 TwinDrive, Austria). Samples with dimensions 50 × 10 × 0.8  $\text{mm}^3$  were prepared and dual cantilever tension mode was used for the measurement. During measurement, static (60 mN) and dynamic forces (50 mN) were applied. The frequency (1 Hz) was kept constant during the measurement. The temperature range used during the measurement was varied from 20 to 37 °C with a scanning rate of 2 °C  $\text{min}^{-1}$  to characterize the viscoelastic properties of the materials.

### 2.7. Thermogravimetric analysis (TGA)

Degradation of the PCL and PCL-PGS fibers was studied using a temperature ramp applied by Mettler Toledo TGA 2 STAR System (USA) from 25 °C to 600 °C at a heating rate of 20 °C  $\text{min}^{-1}$  under nitrogen atmosphere.

### 2.8. Differential scanning calorimetry (DSC)

The thermal behaviour of the PCL, PCL-PGS electrospun fibers, and mildly cross-linked PGS was studied using DSC (Mettler Toledo DSC3, USA). Samples were prepared by loading 5–27 mg of finely cut PCL, PCL-PGS electrospun fibers, and mildly cross-linked PGS in a closed aluminum crucible. The polymers were scanned in three steps: (1) heating from –10 °C to 120 °C, (2) cooling down to –10 °C, and (3) heating to 120 °C again. For all samples, the heating/cooling rate was 10 K  $\text{min}^{-1}$ .

### 2.9. Zeta potential measurements

Zeta potential was measured using the streaming potential measurement mode of Electrokinetic Analyzer EKA (Anton Paar, Austria).  $10 \times 20$  mm sample size,  $150 \text{ ml min}^{-1}$  flow rate, 250 mbar max. pressure was used during measurements. KCl,  $c = 10^{-3} \text{ mol l}^{-1}$  was used as a measuring solution. Titration in acidic and alkaline range was done using HCl or KOH solutions with  $c = 0.1 \text{ mol l}^{-1}$ .

### 2.10. Small-angle x-ray scattering (SAXS)

The scattering patterns were recorded using the SAXS system 'Ganesh-Air' from (SAXSLAB/XENOCs, France). The x-ray source of the laboratory-based system was a D2-MetalJet (Excillum, Sweden) with a liquid metal anode operating at 70 kV and 3.57 mA with Ga-K $\alpha$  radiation (wavelength  $\lambda = 0.13414 \text{ nm}$ ) providing a very small beam ( $<100 \mu\text{m}$ ). The beam was slightly focused with a focal length of 55 cm using a specially made x-Ray optics (Xenocs) to provide a very small and intense beam at the sample position. Two pairs of scatter less slits were used to adjust the beam size depending on the detector distance. For the covered  $q$  range of  $0.08 \text{ nm}^{-1}$  to  $22 \text{ nm}^{-1}$ , two detector distances were used. The electrospun fibers were fixed on a metal frame with scotch tape and directly put in the x-ray beam. The empty camera was used for background subtraction including transmission correction. As the exact thickness of the samples was not measured, the data was not presented on an absolute scale. Azimuthal averages of the low  $q$  part ( $0.13$  to  $0.3 \text{ nm}^{-1}$ ) corresponding to the fiber orientation, the mid  $q$  part ( $0.3$  to  $0.6 \text{ nm}^{-1}$ ) corresponding to the oriented internal crystalline domains perpendicular to the fiber direction and the high  $q$  part ( $14$  to  $15 \text{ nm}^{-1}$ ) were used for the order parameter analysis. The  $q$  ranges from the radially averaged profiles were chosen to cover the whole peak as seen on the 2D detector image. The order parameter  $S = \frac{3\cos^2\chi - 1}{2}$  for all extracted peaks was obtained with the Kratky method by directly fitting the azimuthally averaged scattering profiles [60, 61] which was described more in detail in the supporting info.

### 2.11. Rheology

The rheological behaviour of a 2% HA-MA electrospinning solution was measured using MCR 702 (Anton Paar, Graz, Austria). Plate-plate geometry with a diameter of 25 mm was used. The complex viscosity, storage, and loss modulus of the polymer solution were evaluated by performing a frequency sweep measurements from  $50^\circ\text{C}$  to  $100^\circ\text{C}$  and varying from 0.1 to 100 Hz. Shear rate was kept constant to  $3 \text{ s}^{-1}$  (calculated theoretical shear rate in electrospinning needle).

### 2.12. Real-time degradation test

The degradation rate of the materials was tested at various time points such as 1, 2, 3, and 4 weeks in

DPBS solution at  $37^\circ\text{C}$ . DPBS solution pH was kept constant at pH 7 during all degradation. Samples were weighted after freeze-drying at each time point.

### 2.13. Contact angle measurements

The surface hydrophobicity of PCL and PCL-PGS films was analyzed using a commercial contact angle meter KRÜSS Drop Shape Analyzer DSA25E (Germany). Films were carefully cast and dried on silicon wafers to form a thin layer for measurements. Sessile drop measurements were done to measure the contact angle ( $\Theta$ ). The selected probe liquid was Milli-Q water with a volume of  $2 \mu\text{l}$  and a rate of  $2.67 \mu\text{l s}^{-1}$ . All the measurements were made at room temperature.

### 2.14. Cell culture studies

PC-12 cells (with a passage number less than 7) were cultured on the PCL, PCL-PGS aligned fibers, HA-MA random fibers, and bilayer PCL-PGS/HA-MA fibrous scaffold. To analyze the cell behaviour on the bilayers, two sets of experiments were performed. In one set fibrous scaffolds (bi- and mono-layer) were fixed in the crowns (Scaffdex CellCrown™ inserts) for a better visualizing of the cells in the 3D constructs. In the second set, freestanding bilayer scaffolds were used to study the self-folding and entrapping the cell suspension within the formed tubes. Scaffolds were sterilized using 70% ethanol for 1 h and UV light under the clean bench for 30 min. To increase the adhesion of the PC-12 cells on the PCL-PGS side of the bilayer, as well as the monolayer control samples (PCL and PCL-PGS fibers), the surface of the fibers were coated with sterilized 20% collagen type IV solution in DPBS for 30 s. The following  $30\,000 \text{ cells cm}^{-2}$  and  $10\,000 \text{ cells cm}^{-2}$  were seeded on scaffolds for cell viability, adhesion, and differentiation test, respectively. The growth medium of PC-12 cells was prepared based on the cultural method suggested by ATCC® CRL-1721™ and it was composed of RPMI 1640, 10 v/v % horse serum, 5 v/v % FBS serum, 2 mM glutamine. The culture medium was refreshed every three days.

#### 2.14.1. Live/dead assay

Viability of the neuronal cells on fibrous scaffolds (PCL, PCL-PGS aligned fibers, HA-MA random fibers, and bilayer PCL-PGS/HA-MA fibrous scaffold) was measured using Live-Dead assay at 4 and 7 d after the culture. Staining solution containing  $1 \mu\text{l}$  of Calcein AM and  $4 \mu\text{l}$  of Ethidium EthD-1 was prepared in 2 ml DPBS and samples were covered with staining solution and incubated for 20 min at room temperature before imaging using fluorescence microscopy (Nikon Ti2, Japan). The cell viability was analyzed by measuring the area of live and dead cells in 10 random images.

#### 2.14.2. Cell metabolic activity

The proliferation rate of the PC-12 cells cultured on various fiber mats was measured using Alamar Blue assay after 4 and 7 d of culture. According to the manufacturer protocol, 10% of Alamar Blue reagent was added to the samples with 500  $\mu\text{l}$  of cell culture growth medium and incubated for 165 min at 37 °C. 24-well plates were carefully rocked back and forth every 30 min to avoid the gradient formation. After the incubation time, the supernatant collected from each sample was kept on ice in the dark condition to stop the reaction. 100  $\mu\text{l}$  of the aliquots were transferred to 96-well plate to measure the fluorescence using a plate reader (BertholdTech TriStar2S, Germany) (535 nm of excitation wavelength and 590 nm of emission wavelength). As positive control completely reduced Alamar Blue was used and as negative control 10% Alamar Blue in growth media without cells.

#### 2.15. Cell differentiation

To investigate the cell differentiation, 10 000 cells  $\text{cm}^{-2}$  were cultured on the collagen-coated samples and after two days of culture growth medium was exchanged by differentiation medium containing DMEM with low glucose, horse serum, Glutamine, Penicillin/Streptomycin, HEPES and 100  $\text{ng ml}^{-1}$  NGF. The differentiation medium was refreshed every two days. After 7 d of differentiation, the following immunostaining protocol was performed to visualize the behaviour and morphological changes of the cells. First, the samples were washed twice with DPBS and then fixed using 3.7% formaldehyde solution for 15 min in room temperature. After the fixation of cells, the samples were washed two times with DPBS and the cell membranes were permeabilized with 0.1 v/v % Triton solution for 5 min at room temperature. Then, 5 wt.% BSA in DPBS blocking solution was added and incubated at 37 °C for 15–30 min. The solution was aspirated and samples were washed twice with DPBS. Next, primary antibody Anti-beta III Tubulin 500x diluted in 0.1 wt.% BSA was added and incubated overnight at 4 °C. Samples were further washed twice with DPBS and then secondary antibody (goat anti-mouse IgG 488) and DAPI in 1000x dilution in 0.1 wt.% BSA was added and incubated in dark at 37 °C for 1 h. After removing the staining solution samples were washed again with DPBS two times and images were taken using a fluorescent microscope.

#### 2.16. Statistical analysis

Obtained data were shown as the mean  $\pm$  standard deviation (SD) (3–5 replicates were used). Student's t-test and one-way analysis of variance (ANOVA) followed by Tukey's multiple comparison tests were performed to analyze differences between every two experimental groups. A value of  $p < 0.05$  was considered statistically significant.

### 3. Results and discussion

In this work, we decided to use PCL-PGS/HA-MA bilayer electrospun mats. The top layer is formed by uniaxial aligned PCL-PGS fibers; the bottom layer is formed by disordered HA-MA fibers. This structure has certain advantages to previously used electrospun PCL-alginate bilayer. In particular, we replaced alginate, which has a negative effect on cell viability [33], by hyaluronic acid, which is a natural component of the extracellular matrix. PCL is a semicrystalline polymer with elastic modulus in the order of hundreds of megapascals that is much higher than that of soft tissue. PGS is expected to soften PCL by lowering the elastic modulus. Considering the aimed application of the bilayer mats, the upper layer must provide guidance for the neural cells that is achieved by generating of uniaxially aligned fibers. The orientation of the bottom layer is however not important for cell alignment. Having both layers highly porous is also very important for providing diffusion of nutrition and oxygen to cells. The pore size shall be smaller than the size of the cells to avoid cell migration inside the tube. Therefore, electrospinning was used to produce the bilayers.

The electrospinning technique was used for the fabrication of PCL-PGS/HA-MA bilayer scaffolds with uniaxially aligned PCL-PGS fibers. PCL-PGS solution in chloroform was electrospun first and HA-MA was electrospun on the top of the PCL-PGS electrospun mat. We have used specially designed four-bar rotating collector to achieve a high degree of orientation of produced fibers (figures 1(a) and (b)) [33, 62, 63]. Separate PCL-PGS and HA-MA mats were also prepared by electrospinning and were used as reference material.

Each component of the bilayer was characterized first. DSC measurement showed that pure mildly cross-linked PGS is semi-crystalline and has two melting temperatures measured at 7 and 37 °C ( $T_m$ ) that agrees with previously reported data [56] (figures 1(c), S2–3). Based on the DSC analysis, the crystallinity of mildly cross-linked PGS after cooling to 0 °C and warming to room temperature was measured to be about 20 %. The crystallization point of PGS is around 0 °C meaning that PGS after evaporation of the remaining solvent (glycerol) is amorphous as solvent plays the role of plasticizer, which reduced melting/crystallization temperatures of the polymer [64, 65]. Whereas melting ( $T_m$ ) and crystallization ( $T_c$ ) temperatures of PCL fibers were measured to be 60 °C and 25 °C, respectively meaning that the PCL fibers are solid. The degree of crystallinity of PCL is ca 50% as it was revealed by DSC (figures 1(c), S3). Interestingly, PCL-PGS electrospun fibers showed two melting points at 45 and 60 °C, which confirmed the presence of both polymers PGS and PCL, respectively, in the electrospun fibers and their partial miscibility. We believe that 45 °C could be the

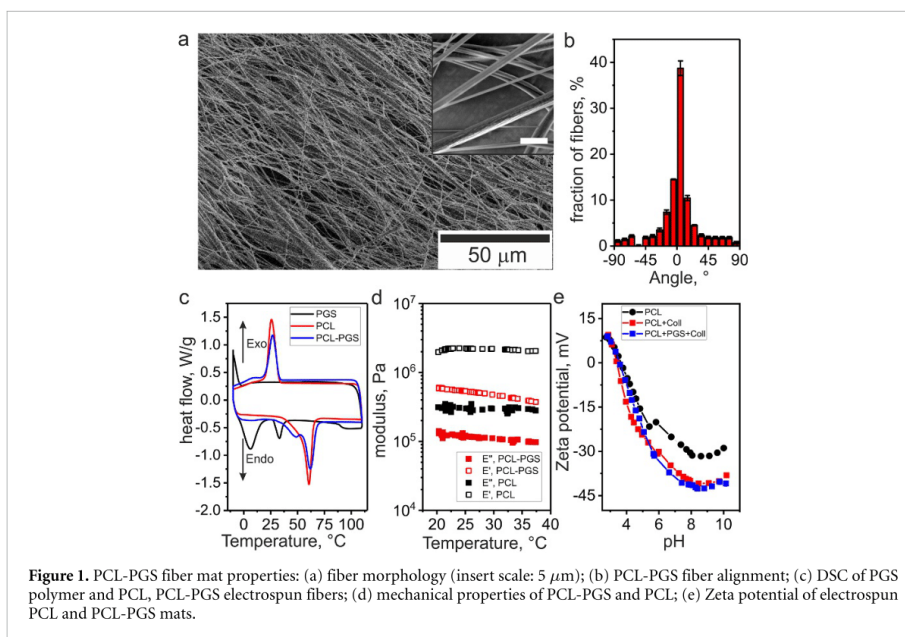


**Figure 1.** PCL-PGS fiber mat properties: (a) fiber morphology (insert scale: 5  $\mu\text{m}$ ); (b) PCL-PGS fiber alignment; (c) DSC of PGS polymer and PCL, PCL-PGS electrospun fibers; (d) mechanical properties of PCL-PGS and PCL; (e) Zeta potential of electrospun PCL and PCL-PGS mats.

melting point of sebacic acid, in which one carboxylic group reacted with glycerol. We did not observe separate crystallization of PGS at around 0 °C. These results agreed with previous reports [56].

Contact angle measurement revealed that hydrophobicity of uniform cast PCL films decreased with the addition of PGS in the structure—contact angle decreases from 77° for pure PCL down to 45° for PCL-PGS blends with 50 wt.% of PGS content. Pure mildly cross-linked PGS showed hydrophilic properties with a water contact angle of about 35° (figure S4). Casted polymer films were used for contact angle measurements to avoid surface influence and increase the reproducibility.

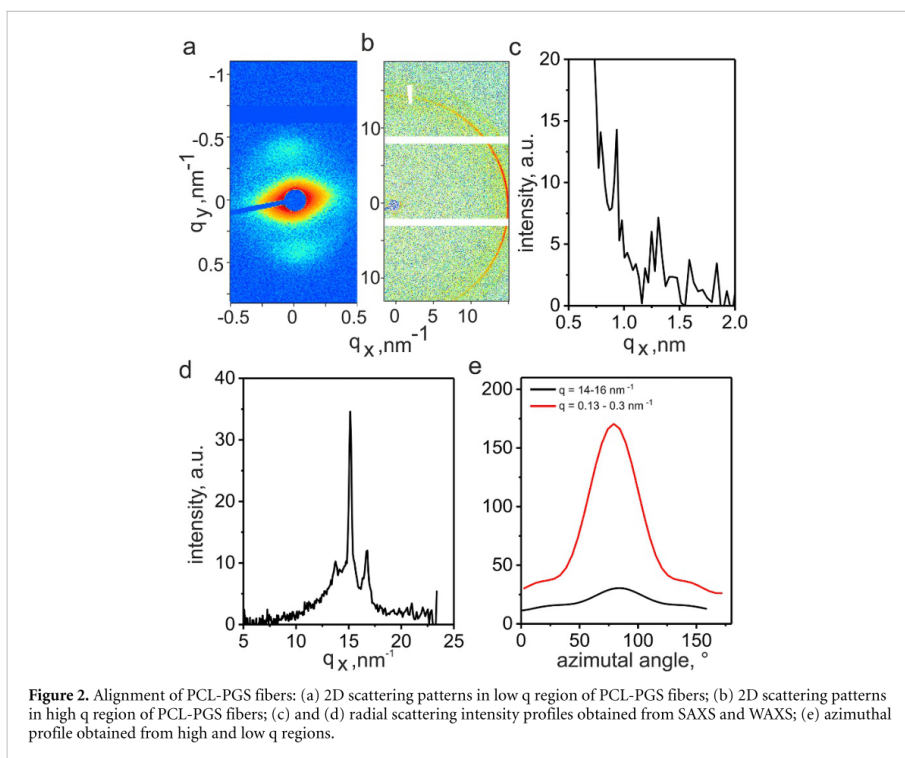
The presence of PGS in PCL changed its charge—PCL-PGS fibers demonstrate more negative zeta potential than PCL fibers do (figure 1(e)). The reason for this difference could be the presence of a large number of terminal carboxylic groups in PGS. Adsorption of collagen increased slightly negative value of the zeta potential of PGS-PCL fibers.

We explored the effect of ratio between PCL and PGS on the properties of produced nanofibers and found out that PCL-PGS blends with 75% and 80% of PCL content formed the most uniform and bead free fibers with fiber diameter  $\sim 0.6 \pm 0.2 \mu\text{m}$  (figures 1(a) and S5). Moreover, a blend of 75% PCL and 25% PGS showed favorable hydrophobicity (64°). Thus, this composition was used in further experiments.

It was found that the presence of PGS in PCL fibers substantially affects the mechanical properties of fibers. In particular, PCL-PGS fibers with 75% PCL content showed 3 times lower storage modulus

(0.6 MPa) than that of pure electrospun PCL fibers (1.9 MPa). Considering that 25% of PGS decreased storage modulus by 3 times, we speculate that PGS and PCL are partially miscible and PGS acts as a plasticizer. It is known that the mechanical properties of polymers should mimic that of the natural tissues. Here in agreement with previous studies, it is proved that PGS can affect the mechanical properties of the PCL [49]. However, the elastic modulus of the PCL-PGS fibrous mat is still two orders magnitudes higher than the modulus of the natural neural tissue (0.1–10 kPa [66]) (figure 1(d)). On the other hand, it was previously reported that NGCs made of cross-linked urethane-doped polyester with a similar modulus (0.64 MPa) was shown a good cell response *in vivo* for the peripheral nerve regeneration [67]. This allows us to assume that the mechanical properties of our mats might not have a negative effect on cells. Moreover, it is worth to mention that the storage modulus 0.6 MPa of the PCL-PGS electrospun fibers is lower than that of the natural collagen type I fibrils (1.1 MPa) [68].

SAXS and wide angle x-ray scattering (WAXS) were used to elucidate the structure of aligned PCL-PGS fibers (figure 2). Obtained results showed that PCL-PGS fibers are semi-crystalline as evidenced by the typical (110) and (200) reflections of the PCL crystals. The degree of crystallinity was measured around 50% that is similar to that obtained from DSC results. There were also two reflexes at  $q = 0.15$  perpendicular to the fiber direction which correspond to the long period of lamellar stacks ( $d = 15 \text{ nm}$ ). Both SAXS and WAXS measurements confirmed the



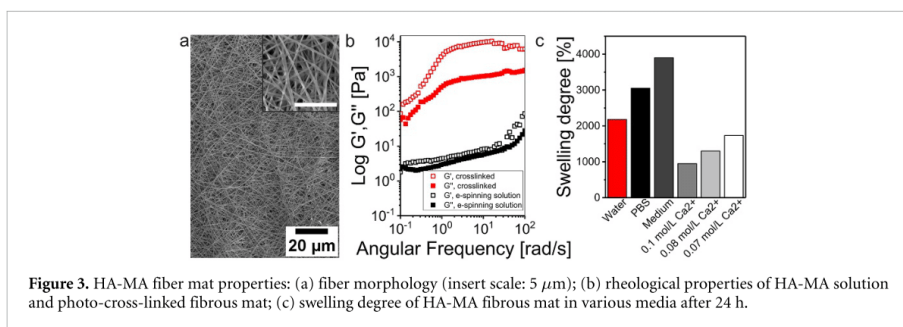
high degree of orientation of polymer chains and crystalline lamellas. We obtained the following values of order parameters from analysis of peak widths at different  $q$ :  $S = 0.45$  ( $q = 0.13\text{--}0.3\text{ nm}^{-1}$ );  $S = 0.25$  ( $q = 0.3\text{--}0.6\text{ nm}^{-1}$ );  $S = 0.22$  ( $q = 14\text{--}16\text{ nm}^{-1}$ ). These values, however, show an underestimated degree of orientation for polymer chains and crystalline lamellas in the fiber structures as fibers themselves were not perfectly uniaxially aligned in the macro-scale (figure 1(b)).

The second component in the bilayer is a layer of randomly oriented HA-MA fibers with a diameter of around  $0.2 \pm 0.1\ \mu\text{m}$  (figure 3(a)). HA-MA, similar to the methacrylated alginate (AA-MA) from our previous work [33], was electrospun after the addition of PEO ( $10^6\text{ g mol}^{-1}$ ) as a polymer chain extender for fiber formation and Pluronic F127 to reduce the surface tension of water. The polymer chain extender is forming hydrogen bonds between natural and synthetic polymers that allow the reduction of solution viscosity and increase the stability of the hydrogel. These crosslinks ensure entanglements between hydrogel chains during electrospinning.

The storage modulus of the HA-MA aqueous spinning solution was about 2 Pa at 0.1 Hz and 50 Pa at 100 Hz. Storage modulus increased to ca 100 Pa (0.1 Hz) and  $10^4$  (100 Hz) after irradiation with a UV light that indicated on crosslinking of the polymer.

Decrease of storage modulus with a decrease of frequency indicated the existence of temporary physical crosslinks with relaxation time approximately one second, which contributes to the rigidity of hydrogels at high frequency.

We found out that the swelling degree of cross-linked electrospun HA-MA mats depends on the counterion concentration and pH of the media: a swelling degree was measured ca 2000% in pure water, 3000% in 0.1 M DPBS and 4000% in cell culture medium (figure 3(c)). This variation in swelling degrees could be attributed to the difference in composition of the media such as the presence of specific ions and compounds [28, 33, 69]. We observed the variation of the ion content of the media also affected the swelling degree where an increase of  $\text{Ca}^{2+}$  ion concentration in solution from 0 to  $0.1\text{ mol l}^{-1}$ , resulted in a decrease of swelling degree of HA-MA by 50%. Similar swelling changes were observed with a change of the medium from water, DPBS to cell growth medium with low counterion content. It has been discussed before that swelling of hyaluronic hydrogels is not just dependent on ion strength but as well on the pH of the medium [70]. Our results showed the highest swelling degree was measured in cell culture media with pH 7.58, next in DPBS with pH 7.37 and finally, the lowest swelling was measured in deionized water with pH 6.79. In conclusion, HA



swelling degree increases in media with higher pH, which agrees to previously reported research [70].

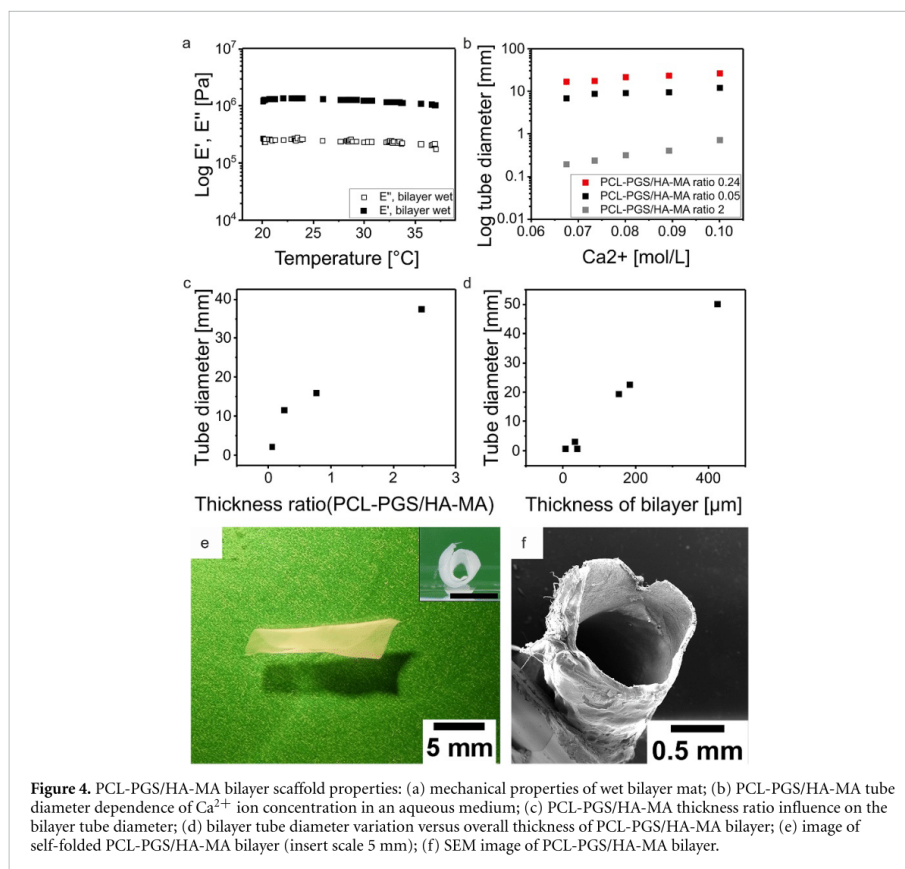
Next, we prepared the bilayer electrospun mats based on aligned PCL-PGS fibers and disordered HA-MA fibers. The improved hydrophilicity of the PCL-PGS layer and low thickness of each layer improved the integration of both layers in the designed bilayer system and no delamination of layers was observed during all experiments. The thickness of the mats varied in the range between 70 and 200  $\mu\text{m}$ . Mats possess high porosity (95%) that is valuable for the fast exchange of nutrients, oxygen, and waste products in the tissue engineering applications. The storage modulus of the bilayer in the wet state (1.2 MPa) was lower compared to the dry state (3.4 MPa) that can be attributed to the swelling of HA-MA fibrous mat. Indeed, swollen HA-MA is very soft and does not contribute to the rigidity of bilayer. The measured value of the storage modulus of the bilayer in the wet state (1.2 MPa) was slightly higher than that of the PCL-PGS mat (0.6 MPa). This discrepancy can be explained by the difficulty of measurements of the thickness of the mats due to their compressibility.

The PCL-PGS/HA-MA bilayer demonstrated shape-transformation behaviour in an aqueous environment (cell culture medium, DPBS, and water), which means as soon as the bilayer film is immersed in aqueous media, it started to roll and formed a hollow tubular scroll-like structure (Movie S1). To investigate the shape-transformation of PCL-PGS/HA-MA bilayer systems, we studied the effects of various factors on the tube inner diameter formed after the self-folding. In particular, the concentration of  $\text{Ca}^{2+}$  ions in the aqueous media, the ratio between the thickness of each layer, and the overall thickness of the bilayer were varied and the inner diameter of the resulted tubes was measured (figures 4(b)–(e)). We found out that the self-folded bilayer mat unfolds with the increasing calcium ion concentration in the medium. This process was reversible and a decrease of concentration of  $\text{Ca}^{2+}$  ions led to the refolding of the unfolded bilayer. This behaviour is in agreement with our previous study with AA-MA [33]. The folding/unfolding of bilayer upon changes of the

concentration of  $\text{Ca}^{2+}$  ions is due to the changes in the swelling degree of HA-MA as was discussed previously (figure 4(b)). It was observed that the tubular self-folded structure was formed after 10 s of immersion in water, and then the sample was moved to the solution with higher calcium ion content, it unfolded within 27 s. The sample was folded again within 40 s after immersion in the cell culture medium with low calcium ion content. We can conclude the bilayer systems can undergo reversible folding in less than 1 min.

The increase of the ratio between the thickness of the hydrophobic PCL-PGS layer and the hydrophilic HA-MA layer also resulted in an increase of inner tube diameter, which correlates with the prediction of the Timoshenko equation [71]. In fact, Timoshenko equation predicts that the higher the ratio of thicknesses of the hydrophobic (PCL-PGS) layer versus the hydrophilic (HA-MA) layer is, the larger the bilayer tube diameter will be. This dependence can be explained by the restricted swelling of the hydrophilic polymer (HA-MA) by more rigid hydrophobic polymer (PCL-PGS) (figure 4(c)). An increase in the overall thickness of the bilayer also resulted in the increase of the diameter of the tube that also correlates with the Timoshenko equation. Circular shape bilayers were used for folding to set the fiber alignment along the long axis of the tubular construct [33].

The degradability of the bilayers as well as the control materials such as PCL, PCL-PGS, and HA-MA electrospun mats were studied for 4 weeks in DPBS solution at 37  $^{\circ}\text{C}$ . We have observed cavities on the surface of ‘as prepared’ electrospun PCL fibers (figure 5(a)), which are due to the usage of highly volatile solvents such as chloroform in electrospinning [72, 73]. After 4 weeks of incubation of PCL fibers in DPBS buffer, the area of these cavities on the fibers has increased from 8%–40% (figures 5(a), (e), (j), and S7). In contrast to pure PCL fibers, ‘as prepared’ PCL-PGS fibers did not have cavities on their surface before the degradation test. However, we observed the formation of cavities on the surface of PCL-PGS fibers after 2 weeks of degradation. Moreover, the morphology of PCL-PGS fibers changed during degradation and



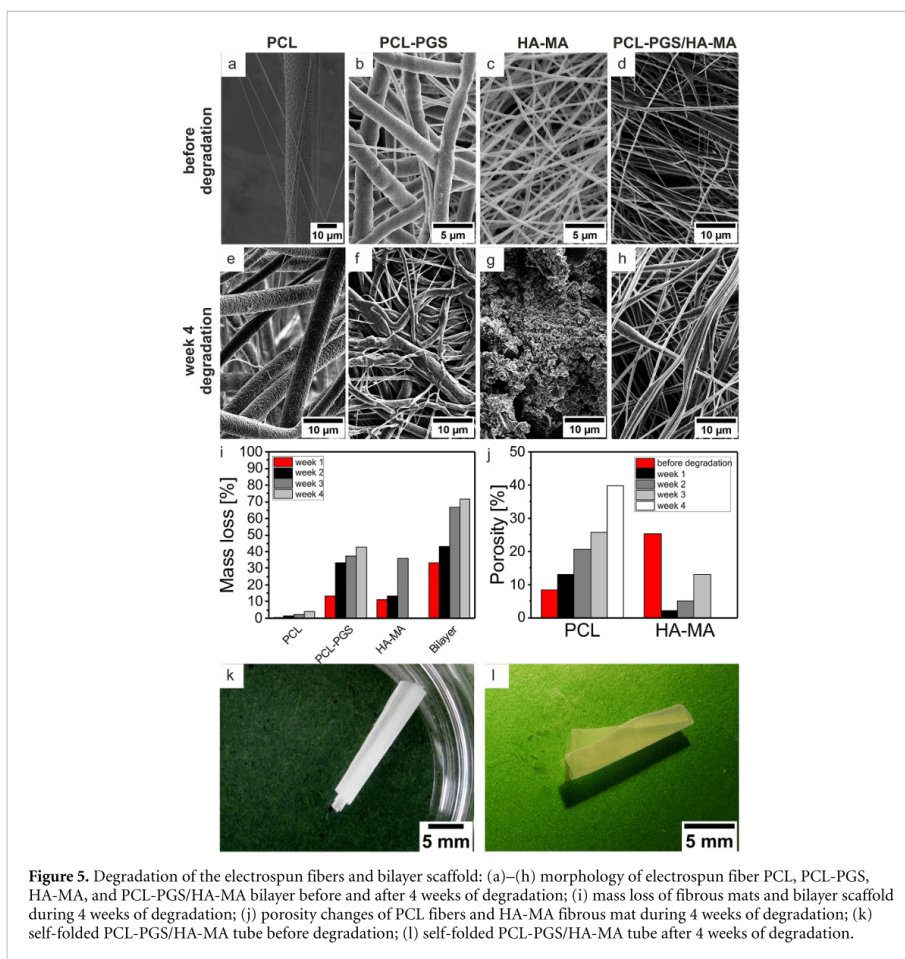
fused fibers with a dense fibrous network were formed (figures 5(b), (f), and S7). In our opinion, these pores on the ‘as prepared’ PCL-PGS fibers were not visible before the degradation test as they are filled by PGS. PGS is initially liquid at room temperature (crystallization point  $0\text{ }^{\circ}\text{C}$ ) and we believe that it fills the cavities during electrospinning. On the other hand, it is known that the degradation rate of polymers depends on their structure and mobility of the polymer chains; therefore, highly crystalline polymers like PCL degrade slower, while liquid amorphous polymers like PGS degrade faster. Therefore, we believe that PGS degrades first resulting in disclosing of cavities, which were hidden and filled with PGS polymer after fiber spinning.

Electrospun HA-MA fibers also showed significant morphological changes after one week of incubation in DPBS solution during the degradation test. Swollen HA-MA fibrous mat did not show any fibrous structure. Instead, a dense hydrogel layer was observed, which gradually degraded and became more porous until only a few polymer particles were remained (figures 4(c), (g), (j), and S7). The fast degradation rate of the HA-MA layer can be explained

by its nature—hydrogel is a highly swollen substance and the polymer chains are mobile.

Similar degradation behavior of the HA-MA layer was observed in bilayers. After 1 week of degradation, the HA-MA fibers formed a film on the top of the PCL-PGS fibers (figure S7). After 2 and 3 weeks of degradation, the remaining of HA-MA and PGS coating was completely removed from the PCL fibers and the porous PCL fibers were remained after 4 weeks of degradation (figures 5(d), (h), and S7).

The morphological changes explained above during the degradation test were also confirmed by the mass loss measurements for each fibrous mat and bilayers (figure 5(i)). Pure PCL fibers showed negligible mass loss ( $< 5\%$ ) that correlates with the absence of morphological changes. The addition of 25% of PGS to PCL made it more degradable—up to 40% of its mass was lost after 4 weeks of degradation. It is notable that while a fraction of PGS in the blend is 25%, 40% of entire fibrous mesh was degraded meaning that PCL also contributes to the degradation. Indeed, our previous experiments showed that PCL and PGS are partially miscible that results in



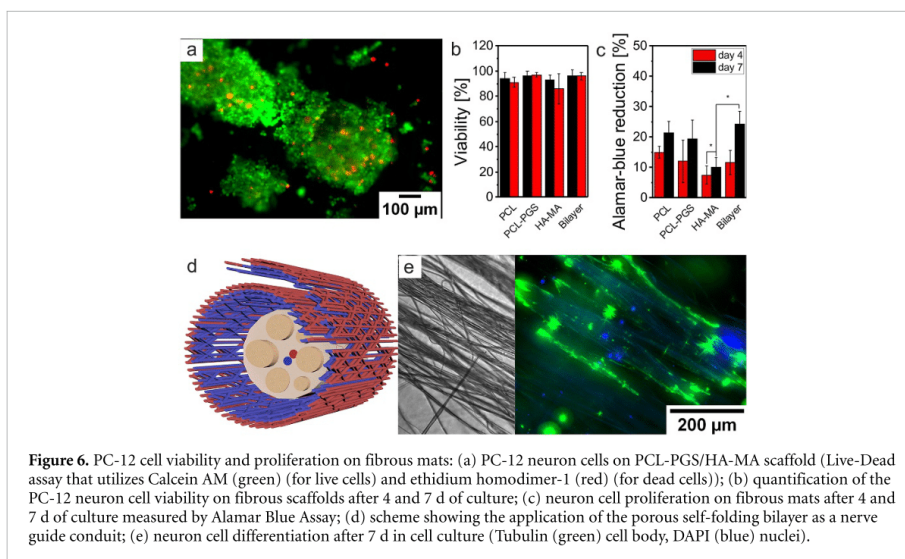
plasticization that can increase the degradation rate of PCL.

The degradation rate of HA-MA fibers was also measured. However, due to the high swelling and mass loss, we first removed the mat from the DPBS solution and freeze-dried it each time prior to measuring its remaining mass. Interestingly, the degradation rate of HA-MA was slightly lower than that of PCL-PGS that can be attributed to the error of measurements—freeze-dried polymer could contain a small amount of salt from the buffer that increases the mass of the polymer. Furthermore, the HA-MA mat has completely disintegrated in pieces, which could not be collected and mass loss could not be measured in week 4.

At last, the weight loss of the bilayer was measured by about 70%, which is due to the nearly complete degradation of PGS and HA-MA fibers after 4 weeks of incubation in the DPBS solution. Despite the massive degradation of the materials, the rolled

tubes after 4 weeks of degradation remained stable and only tube diameter had increased up to 3 times (figures 5(k), (l)).

Finally, we investigated the interaction of the neuronal cells PC-12 in contact with the PCL-PGS/HA-MA bilayer in the form of the mat and self-rolled tubes. Two sets of samples were used for cell culture—fixed bilayers in cell culture crowns and free-standing bilayers. To avoid the full folding of free-standing bilayers, initially small volume of the cell suspension was placed on the scaffold and after the adhesion of cells, the additional culture medium was added. First, PC-12 neuron cells were cultured on the top of the unfolded bilayer and the viability and the proliferation rate of the cells were measured after 4 and 7 d of culture using live-dead and Alamar blue assay. Due to the weak adhesion of the PC-12 cells, the surface of the scaffolds, as well as the flasks, which were used for culturing the cells, was coated with collagen solution (collagen type IV diluted 1:5 in DPBS),



which has shown good adhesion of PC-12 cells and improved expression of proteins, important for PC-12 cell growth and differentiation [74, 75]. After 4 d of culture, neuronal cells showed good adhesion and high viability (93%–96%) in contact with all of the fibrous mats as well as the bilayer (figures 6(a), (b), and S8–13). After a week of culture, the viability was measured 86%–97%, however, the cell adhesion on HA-MA fibers was significantly lower, which can be explained by the fast degradation behaviour of the materials (figure S8).

Interestingly, the lowest cell proliferation was measured on HA-MA mats after 7 d of culture (figure 6(c)), which is in agreement with previous studies using polysaccharides for the PC-12 cell culture [76]. Cell proliferation on pure PCL mat, PCL-PGS mat, and bilayer was nearly the same. It worth mentioning that lower proliferation of cells on HA-MA mat is not affecting the suitability of the bilayer as the cells are initially cultured on the aligned PCL-PGS fibrous mats and the cell interaction to this side of the bilayer will play a role in the formation of the cell layer. This fact was confirmed by cell proliferation studies presented in figures 6(c) and (e).

After differentiation of the cells for 7 d in contact with medium containing  $100 \text{ ng ml}^{-1}$  of NGF, we observed that neuron cells were spread and elongated in the direction of fibers and started to form neurites, which was immunostained using beta III Tubulin and shown with a green color in figure 6(e). This observation can indicate the feasibility of shape-changing PCL-PGS/HA-MA bilayer fibrous mats as an NGC for neural tissue regeneration (figure 6(d)).

#### 4. Conclusions

In this paper, we reported the 4D fabrication and potential application of the shape-transforming fibrous mats as NGCs. This approach was based on the fabrication of electrospun bilayer composed of disordered HA-MA fibers and aligned PCL-PGS fibers. The bilayers were able to roll and form tubular structures in aqueous media. The diameter of the tube could be precisely controlled by varying the concentration of calcium ions, the ratio between the thickness of the layers and the total thickness of the bilayer. By blending PCL with PGS, we significantly improved the softness and degradation rate of the electrospun scaffold forming a substrate with closer properties to the soft tissues. Our designed scaffolds showed high biocompatibility and degradability (70% of mass loss after 4 weeks of degradation). Formed tubular constructs out of bilayer mat showed good stability even after 4 weeks of degradation and the scroll-like shape stayed stable. Neural cells cultured on bilayers showed high adhesion, viability, and proliferation after 7 d of culture.

#### Acknowledgments

This work was supported by DFG (Grant No. IO 68/17-1, IO 68/14-1; SA 3575/1-1; SY—125/6-3; Project No. 326998133—SFB/TRR225 (subproject B03)). We would further like to thank Professor Scheibel for allowing us to use DSC, TGA, and SEM equipment to conduct this research.

## ORCID iDs

Martin Dulle  <https://orcid.org/0000-0001-5699-7530>

Aldo R Boccaccini  <https://orcid.org/0000-0002-7377-2955>

Alla Synytska  <https://orcid.org/0000-0002-0643-7524>

Sahar Salehi  <https://orcid.org/0000-0002-6740-4195>

Leonid Ionov  <https://orcid.org/0000-0002-0770-6140>

## References

- [1] Daly W, Yao L, Zeugolis D, Windebank A and Pandit A 2012 A biomaterials approach to peripheral nerve regeneration: bridging the peripheral nerve gap and enhancing functional recovery *J. R. Soc. Interface* **9** 202–21
- [2] Xie J, MacEwan M R, Schwartz A G and Xia Y 2010 Electrospun nanofibers for neural tissue engineering *Nanoscale* **2** 35–44
- [3] Wu Y, Wang L, Hu T, Ma P X and Guo B 2018 Conductive micropatterned polyurethane films as tissue engineering scaffolds for Schwann cells and PC12 cells *J. Colloid Interface Sci.* **518** 252–62
- [4] Taylor C A, Braza D, Rice J B and Dillingham T 2008 The incidence of peripheral nerve injury in extremity trauma *Am. J. Phys. Med. Rehabil.* **87** 381–5
- [5] Noble J, Munro C A, Prasad V S S V and Midha R 1998 Analysis of upper and lower extremity peripheral nerve injuries in a population of patients with multiple injuries *J. Trauma Acute Care Surg.* **45** 116–22
- [6] Bellamkonda R V 2006 Peripheral nerve regeneration: an opinion on channels, scaffolds and anisotropy *Biomaterials* **27** 3515–8
- [7] Hallgren A, Björkman A, Chemnitz A and Dahlin L B 2013 Subjective outcome related to donor site morbidity after sural nerve graft harvesting: a survey in 41 patients *BMC Surg.* **13** 39
- [8] Ijpmma F F A, Nicolai J-P A and Meek M F 2006 Sural nerve donor-site morbidity: thirty-four years of follow-up *Ann. Plast. Surg.* **57** 391–5
- [9] Blitterswijk C A V, Moroni L, Rouwkema J, Siddappa R and Sohier J 2008 *Tissue Eng.* ed C V Blitterswijk et al (New York: Academic) pp xii–xxxvi
- [10] Burnstine-Townley A, Eshel Y and Amdursky N 2019 Conductive scaffolds for cardiac and neuronal tissue engineering: governing factors and mechanisms *Adv. Funct. Mater.* **30** 1901369
- [11] Edri R et al 2019 Personalized hydrogels for engineering diverse fully autologous tissue implants *Adv. Mater.* **31** 1803895
- [12] Sarker M D, Naghieh S, McInnes A D, Ning L, Schreyer D J and Chen X 2019 Bio-fabrication of peptide-modified alginate scaffolds: printability, mechanical stability and neurite outgrowth assessments *Bioprinting* **14** e00045
- [13] Morelli S, Piscioneri A, Salerno S, Chen -C-C, Chew C H, Giorno L, Drioli E and De Bartolo L 2017 Microtube array membrane bioreactor promotes neuronal differentiation and orientation *Biofabrication* **9** 025018
- [14] Pawar K, Welzel G, Haynl C, Schuster S and Scheibel T 2019 Recombinant spider silk and collagen-based nerve guidance conduits support neuronal cell differentiation and functionality in vitro *ACS Appl. Bio Mater.* **2** 4872–80
- [15] Aigner T B, Haynl C, Salehi S, O'Connor A and Scheibel T 2020 Nerve guidance conduit design based on self-rolling tubes *Mater. Today Bio* **5** 100042
- [16] Li Y, Huang G, Zhang X, Wang L, Du Y, Lu T J and Xu F 2014 Engineering cell alignment in vitro *Biotechnol. Adv.* **32** 347–65
- [17] Kim J I, Hwang T I, Lee J C, Park C H and Kim C S 2020 Regulating electrical cue and mechanotransduction in topological gradient structure modulated piezoelectric scaffolds to predict neural cell response *Adv. Funct. Mater.* **30** 1907330
- [18] Simitzi C, Stratakis E, Fotakis C, Athanassakis I and Ranella A 2015 Microconical silicon structures influence NGF-induced PC12 cell morphology *J. Tissue Eng. Regen. Med.* **9** 424–34
- [19] Golafshan N, Kharaziha M, Fathi M, Larson Benjamin L, Giatsidis G and Masoumi N 2018 Anisotropic architecture and electrical stimulation enhance neuron cell behaviour on a tough graphene embedded PVA: alginate fibrous scaffold *RSC Adv.* **8** 6381–9
- [20] Wieringa P A, Gonçalves de Pinho A R, Micera S, van Wezel R J A and Moroni L 2018 Biomimetic architectures for peripheral nerve repair: a review of biofabrication strategies *Adv. Healthc. Mater.* **7** 1701164
- [21] Knowlton S, Anand S, Shah T and Tasoglu S 2018 Bioprinting for neural tissue engineering *Trends Neurosci.* **41** 31–46
- [22] Dixon A R, Jariwala S H, Bilis Z, Loverde J R, Pasquina P F and Alvarez L M 2018 Bridging the gap in peripheral nerve repair with 3D printed and bioprinted conduits *Biomaterials* **186** 44–63
- [23] Hu Y et al 2016 3D-engineering of cellularized conduits for peripheral nerve regeneration *Sci. Rep.* **6** 32184
- [24] Heinrich M A et al 2019 3D bioprinting: from benches to translational applications *Small* **15** 1805510
- [25] Ionov L 2018 4D biofabrication: materials, methods, and applications *Adv. Healthc. Mater.* **7** 1800412
- [26] Sydney Gladman A, Matsumoto E A, Nuzzo R G, Mahadevan L and Lewis J A 2016 Biomimetic 4D printing *Nat. Mater.* **15** 413
- [27] Apsite I, Stoychev G, Zhang W, Jehnichen D, Xie J and Ionov L 2017 Porous stimuli-responsive self-folding electrospun mats for 4D biofabrication *Biomacromolecules* **18** 3178–84
- [28] Kirillova A, Maxson R, Stoychev G, Gomillion C T and Ionov L 2017 4D biofabrication using shape-morphing hydrogels *Adv. Mater.* **29** 1703443
- [29] Stroganov V, Pant J, Stoychev G, Janke A, Jehnichen D, Fery A, Handa H and Ionov L 2018 4D biofabrication: 3D cell patterning using shape-changing films *Adv. Funct. Mater.* **28** 1706248
- [30] Zakharchenko S, Pureskiy N, Stoychev G, Stamm M and Ionov L 2010 Temperature controlled encapsulation and release using partially biodegradable thermo-magneto-sensitive self-rolling tubes *Soft Matter* **6** 2633–6
- [31] Vannozzi L, Yasa I C, Ceylan H, Menciasci A, Ricotti L and Sitti M 2018 Self-folded hydrogel tubes for implantable muscular tissue scaffolds *Macromol. Biosci.* **18** 1700377
- [32] Yeo M, Lee H and Kim G H 2016 Combining a micro/nano-hierarchical scaffold with cell-printing of myoblasts induces cell alignment and differentiation favorable to skeletal muscle tissue regeneration *Biofabrication* **8** 035021
- [33] Apsite I, Uribe J M, Posada A F, Rosenfeldt S, Salehi S and Ionov L 2019 4D biofabrication of skeletal muscle microtissues *Biofabrication* **12** 015016
- [34] Sakai K, Teshima T F, Nakashima H and Ueno Y 2019 Graphene-based neuron encapsulation with controlled axonal outgrowth *Nanoscale* **11** 13249–59
- [35] Li J and Shi R 2007 Fabrication of patterned multi-walled poly-L-lactic acid conduits for nerve regeneration *J. Neurosci. Methods* **165** 257–64
- [36] Froeter P, Huang Y, Cangellaris O V, Huang W, Dent E W, Gillette M U, Williams J C and Li X 2014 Toward intelligent synthetic neural circuits: directing and accelerating neuron cell growth by self-rolled-up silicon nitride microtube array *ACS Nano* **8** 11108–17
- [37] Schulze S, Huang G, Krause M, Aubyn D, Quiñones V A B, Schmidt C K, Mei Y and Schmidt O G 2010 Morphological

- differentiation of neurons on microtopographic substrates fabricated by rolled-up nanotechnology *Adv. Eng. Mater.* **12** B558–B64
- [38] Yeh C-W, Wang L-W, Wu H-C, Hsieh Y-K, Wang J, Chen M-H and Wang T-W 2017 Development of biomimetic micro-patterned device incorporated with neurotrophic gradient and supportive Schwann cells for the applications in neural tissue engineering *Biofabrication* **9** 015024
- [39] Teshima T F, Nakashima H, Ueno Y, Sasaki S, Henderson C S and Tsukada S 2017 Cell assembly in self-foldable multi-layered soft micro-rolls *Sci. Rep.* **7** 17376
- [40] Liu L, Bakhshi H, Jiang S, Schmalz H and Agarwal S 2018 Composite polymeric membranes with directionally embedded fibers for controlled dual actuation *Macromol. Rapid Commun.* **39** 1800082
- [41] Liu L, Ghaemi A, Gekle S and Agarwal S 2016 One-component dual actuation: poly(NIPAM) can actuate to stable 3D forms with reversible size change *Adv. Mater.* **28** 9792–6
- [42] Peng L, Zhu J and Agarwal S 2017 Self-rolled porous hollow tubes made up of biodegradable polymers *Macromol. Rapid Commun.* **38** 1700034
- [43] Jiang S, Liu F, Lerch A, Ionov L and Agarwal S 2015 Unusual and superfast temperature-triggered actuators *Adv. Mater.* **27** 4865–70
- [44] Chen T, Bakhshi H, Liu L, Ji J and Agarwal S 2018 Combining 3D printing with electrospinning for rapid response and enhanced designability of hydrogel actuators *Adv. Funct. Mater.* **28** 1800514
- [45] Chen C, Tang J, Gu Y, Liu L, Liu X, Deng L, Martins C, Sarmento B, Cui W and Chen L 2019 Bioinspired hydrogel electrospun fibers for spinal cord regeneration *Adv. Funct. Mater.* **29** 1806899
- [46] Stoychev G, Turcaud S, Dunlop J W C and Ionov L 2013 Hierarchical multi-step folding of polymer bilayers *Adv. Funct. Mater.* **23** 2295–300
- [47] Stroganov V, Zakharchenko S, Sperling E, Meyer A K, Schmidt O G and Ionov L 2014 Biodegradable self-folding polymer films with controlled thermo-triggered folding *Adv. Funct. Mater.* **24** 4357–63
- [48] Isaacs J and Browne T 2014 Overcoming short gaps in peripheral nerve repair: conduits and human acellular nerve allograft *Hand* **9** 131–7
- [49] Salehi S, Bahnert T, Gutmann J S, Gao S L, Mäder E and Fuchsluger T A 2014 Characterization of structural, mechanical and nano-mechanical properties of electrospun PGS/PCL fibers *RSC Adv.* **4** 16951–7
- [50] Salehi S, Fathi M, Javanmard S H, Bahnert T, Gutmann J S, Ergün S, Steuhl K P and Fuchsluger T A 2014 Generation of PGS/PCL blend nanofibrous scaffolds mimicking corneal stroma structure *Macromol. Mater. Eng.* **299** 455–69
- [51] Rai R et al 2013 Biomimetic poly(glycerol sebacate) (PGS) membranes for cardiac patch application *Mater. Sci. Eng.: C* **33** 3677–87
- [52] Masoumi N et al 2014 Electrospun PGS:PCL microfibers align human valvular interstitial cells and provide tunable scaffold anisotropy *Adv. Health. Mater.* **3** 929–39
- [53] Salehi S, Czugala M, Stafiej P, Fathi M, Bahnert T, Gutmann J S, Singer B B and Fuchsluger T A 2017 Poly (glycerol sebacate)-poly ( $\epsilon$ -caprolactone) blend nanofibrous scaffold as intrinsic bio- and immunocompatible system for corneal repair *Acta. Biomater.* **50** 370–80
- [54] Jaafar I H, Ammar M M, Jedlicka S S, Pearson R A and Coulter J P 2010 Spectroscopic evaluation, thermal, and thermomechanical characterization of poly(glycerol-sebacate) with variations in curing temperatures and durations *J. Mater. Sci.* **45** 2525–9
- [55] Kim M, Hwang M, Kim J-H and Chung D 2014 Biodegradable and elastomeric poly(glycerol sebacate) as a coating material for nitinol bare stent *Biomed. Res. Int.* **2014** 956952
- [56] Gaharwar A K, Nikkhah M, Sant S and Khademhosseini A 2014 Anisotropic poly (glycerol sebacate)-poly ( $\epsilon$ -caprolactone) electrospun fibers promote endothelial cell guidance *Biofabrication* **7** 015001
- [57] Liang S, Cook W D and Chen Q 2012 Physical characterization of poly(glycerol sebacate)/Bioglass® composites *Polym. Int.* **61** 17–22
- [58] Smeds K A, Pfister-Serres A, Miki D, Dastgheib K, Inoue M, Hatchell D L and Grinstaff M W 2001 Photocrosslinkable polysaccharides for in situ hydrogel formation *J. Biomed. Mater. Res.* **55** 254–5
- [59] Bonino C A, Krebs M D, Saquing C D, Jeong S I, K L S, Alsberg E and Khan S A 2011 Electrospinning alginate-based nanofibers: from blends to crosslinked low molecular weight alginate-only systems *Carbohydr. Polym.* **85** 111–19
- [60] Sims M T, Abbott L C, Richardson R M, Goodby J W and Moore J N 2019 Considerations in the determination of orientational order parameters from X-ray scattering experiments *Liq. Cryst.* **46** 11–24
- [61] Biehl R 2019 Jscatter, a program for evaluation and analysis of experimental data *PLoS One* **14** e0218789
- [62] Tan G Z and Zhou Y 2018 Tunable 3D nanofiber architecture of polycaprolactone by divergence electrospinning for potential tissue engineering applications *Nano-Micro Lett.* **10** 73
- [63] Kim J I, Hwang T I, Aguilar L E, Park C H and Kim C S 2016 A controlled design of aligned and random nanofibers for 3D bi-functionalized nerve conduits fabricated via a novel electrospinning set-up *Sci. Rep.* **6** 23761
- [64] Vieira M G A, da Silva M A, Dos Santos L O and Beppu M M 2011 Natural-based plasticizers and biopolymer films: A review *Eur. Polym. J.* **47** 254–63
- [65] Mohsin M, Hossin A and Haik Y 2011 Thermal and mechanical properties of poly(vinyl alcohol) plasticized with glycerol *J. Appl. Polym. Sci.* **122** 3102–9
- [66] Moore S W, Roca-Cusachs P and Sheetz M P 2010 Stretchy proteins on stretchy substrates: the important elements of integrin-mediated rigidity sensing *Dev. Cell* **19** 194–206
- [67] Tran R T, Choy W M, Cao H, Qattan I, Chiao J-C, Ip W Y, Yeung K W K and Yang J 2014 Fabrication and characterization of biomimetic multichanneled crosslinked-urethane-doped polyester tissue engineered nerve guides *J. Biomed. Mater. Res. A* **102** 2793–804
- [68] Jansen K A, Licup A J, Sharma A, Rens R, MacKintosh F C and Koenderink G H 2018 The role of network architecture in collagen mechanics *Biophys. J.* **114** 2665–78
- [69] DeSimone E, Schacht K and Scheibel T 2016 Cations influence the cross-linking of hydrogels made of recombinant, polyanionic spider silk proteins *Mater. Lett.* **183** 101–4
- [70] Shah C B and Barnett S M 1992 Swelling behavior of hyaluronic acid gels *J. Appl. Polym. Sci.* **45** 293–8
- [71] Timoshenko S 1925 Analysis of bi-metal thermostats *J. Opt. Soc. Am.* **11** 233–55
- [72] Fashandi H and Karimi M 2012 Pore formation in polystyrene fiber by superimposing temperature and relative humidity of electrospinning atmosphere *Polymer* **53** 5832–49
- [73] Megelski S, Stephens J S, Chase D B and Rabolt J F 2002 Micro- and nanostructured surface morphology on electrospun polymer fibers *Macromolecules* **35** 8456–66
- [74] Tomaselli K J, Damsky C H and Reichardt L F 1987 Interactions of a neuronal cell line (PC12) with laminin, collagen IV, and fibronectin: identification of integrin-related glycoproteins involved in attachment and process outgrowth *J. Cell Biol.* **105** 2347–58
- [75] Paralkar V M, Weeks B S, Yu Y M, Kleinman H K and Reddi A H 1992 Recombinant human bone morphogenetic protein 2B stimulates PC12 cell differentiation: potentiation and binding to type IV collagen *J. Cell Biol.* **119** 1721–8
- [76] Hu M H, Yang K-C, Sun Y H, Chen Y C, Yang S H and Lin F-H 2017 In situ forming oxidised hyaluronic acid/adipic acid dihydrazide hydrogel for prevention of epidural fibrosis after laminectomy *Eur. Cell Mater.* **34** 307–20

# Supporting Information

## 4D Biofabrication of fibrous artificial nerve graft for neuron regeneration

*Indra Apsite<sup>1</sup>, Gissela Constante<sup>1</sup>, Martin Dulle<sup>2</sup>, Lena Vogt<sup>3</sup>, Anja Caspari<sup>4</sup>, Aldo R.  
Boccaccini<sup>3</sup>, Alla Synytska<sup>4</sup>, Sahar Salehi<sup>5</sup>, Leonid Ionov<sup>1\*</sup>*

<sup>1</sup> Faculty of Engineering Sciences and Bavarian Polymer Institute, University of Bayreuth,  
Ludwig Thoma Str. 36A, 95447 Bayreuth, Germany

<sup>2</sup> Forschungszentrum Jülich GmbH Jülich Centre for Neutron Science (JCNS-1) and Institute for  
Complex Systems (ICS-1), 52425 Jülich, Germany

<sup>3</sup> Institute of Biomaterials, Department of Materials Science and Engineering, University of  
Erlangen-Nuremberg, Cauerstraße 6, 91058 Erlangen, Germany

<sup>4</sup> Leibniz Institute of Polymer Research Dresden e.V., Hohe Str. 6, 01069 Dresden, Germany

<sup>5</sup> Department of Biomaterials, University of Bayreuth, Prof.-Rüdiger-Bormann Str. 1, 95447  
Bayreuth, Germany

E-mail: leonid.ionov@uni-bayreuth.de

### TGA measurements:

We found that the presence of PGS in the structure of PCL-PGS electrospun fibers results in decreases of initial degradation temperature. TGA measurements showed that pure PCL electrospun fibers have initial degradation temperature  $\sim 390$  °C, whereas PCL-PGS electrospun fibers degrade at about 330 °C (Figure S1). The initial degradation temperature for pure PGS pre-polymer has been reported to be about 300 °C<sup>1</sup>. To conclude, PCL and PCL-PGS fibers are thermally stable, although this stability can be reduced by increasing the PGS content in the blend as PGS shows lower stability than PCL.

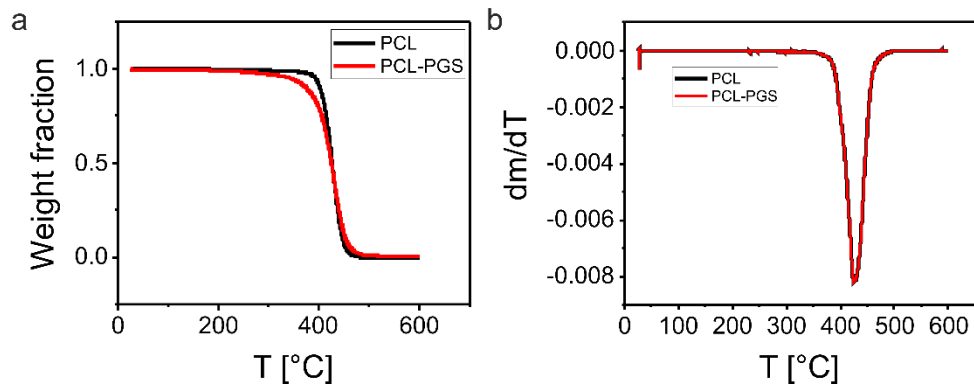


Figure S1. Thermogravimetric analysis of PCL and PCL-PGS fibers: a) weight fraction; b) dm/dT

### DSC measurements:

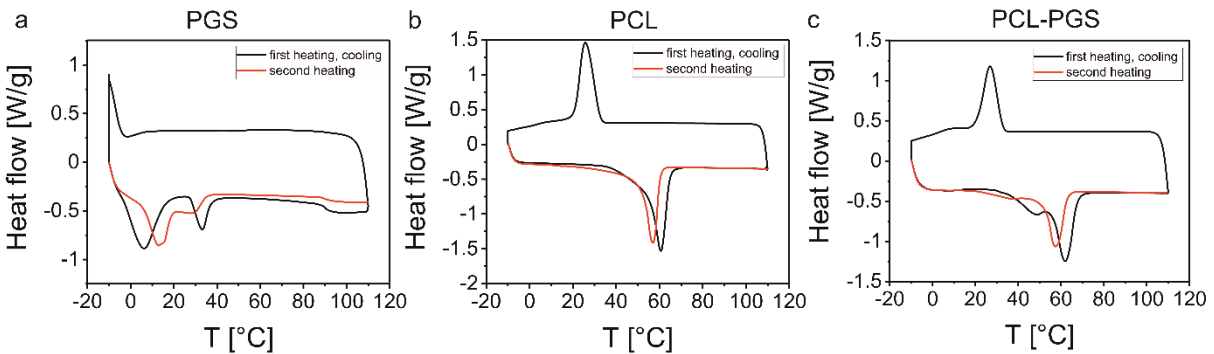


Figure S2. Differential scanning calorimetry: a) PGS pre-polymer; b) electrospun PCL fibers; c) electrospun PCL-PGS fibers

### Contact angle measurements:

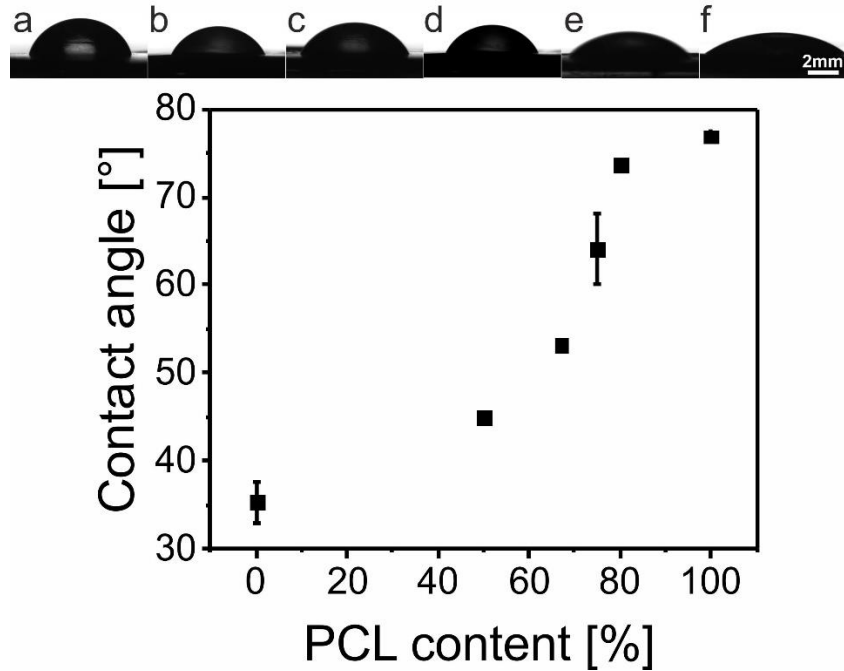
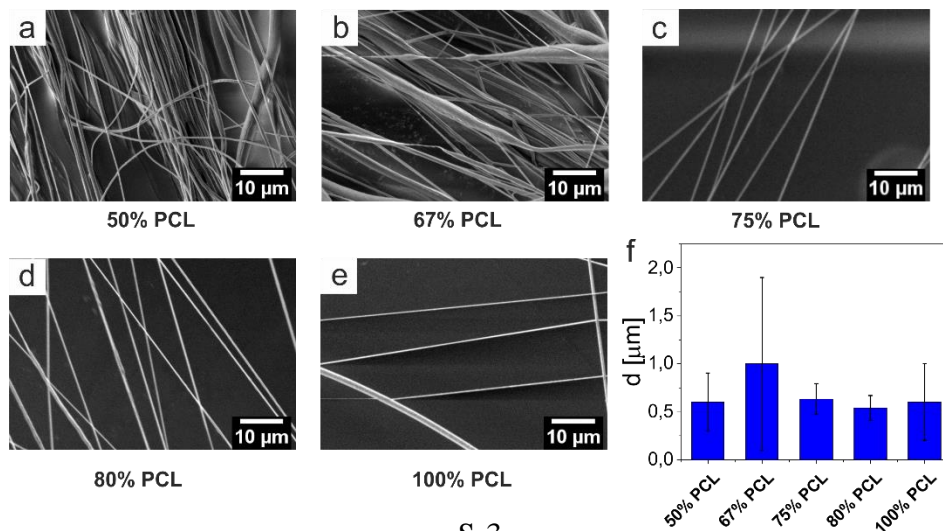


Figure S3. PCL-PGS film hydrophobicity depending on the PCL content in the blend. Liquid drop image on PCL (a), PCL-PGS blend containing 80 % PCL (b), PCL-PGS blend containing 75 % PCL (c), PCL-PGS blend containing 67 % PCL (d), PCL-PGS blend containing 50 % PCL (e), PGS pre-polymer (f).

### Fiber diameter analysis:



S-3

Figure S4. Electrospinning of PCL-PGS fibers: a) electrospun fibers from PCL-PGS blend containing 50 % PCL; b) electrospun fibers from PCL-PGS blend containing 67 % PCL; c) electrospun fibers from PCL-PGS blend containing 75 % PCL; d) electrospun fibers from PCL-PGS blend containing 80 % PCL; e) electrospun PCL fibers; f) electrospun fiber diameters depending on PCL content in the PCL-PGS blend

**DMA measurements:**

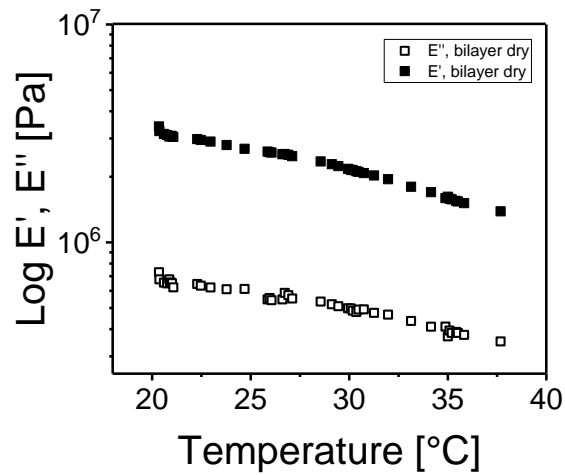


Figure S5. DMA of dry PCL-PGS/HA-MA bilayer

**Biodegradation analysis:**

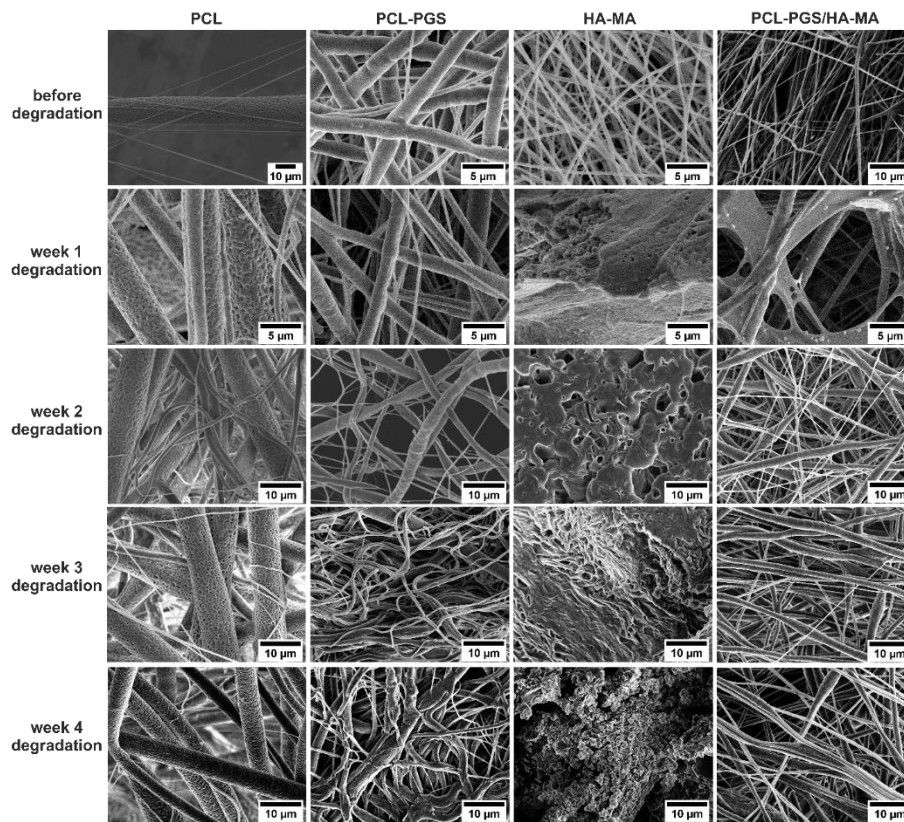


Figure S6. Morphology of fibrous mats after 1, 2, 3 and 4 weeks of degradation in PBS solution at 37 °C.

**Cell culture studies:**

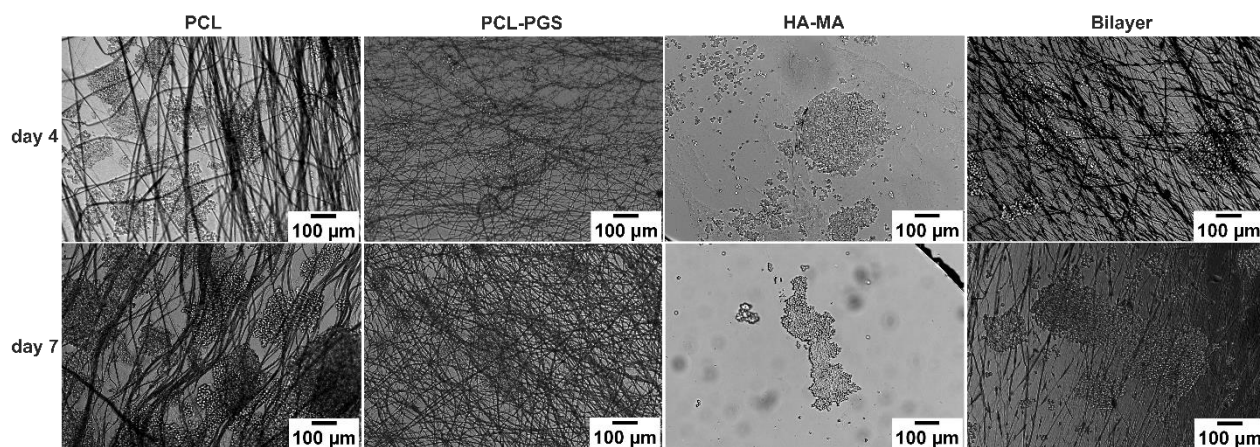


Figure S7. Microscopy snapshots of cells on fibrous mats after 4 and 7 days in culture.

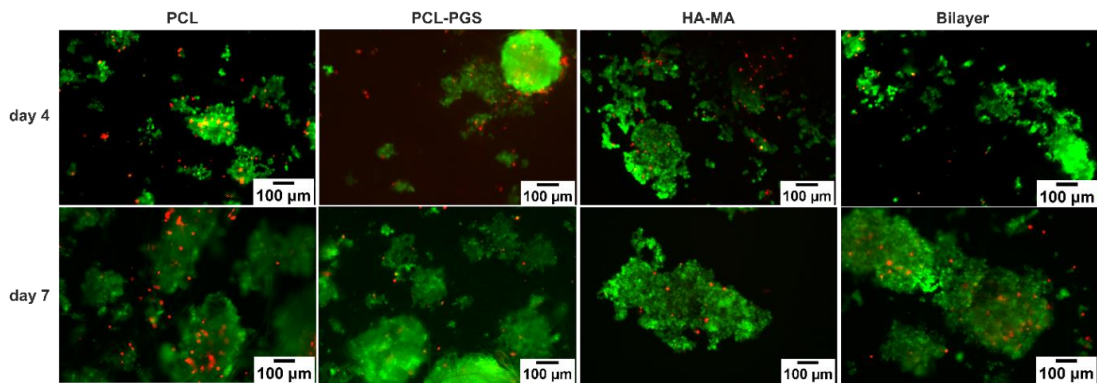


Figure S8. Viability of PC-12 neuron cells (Live/Dead assay) on fibrous scaffolds after 4 and 7 days in culture. Red - dead cells; green - live cells.

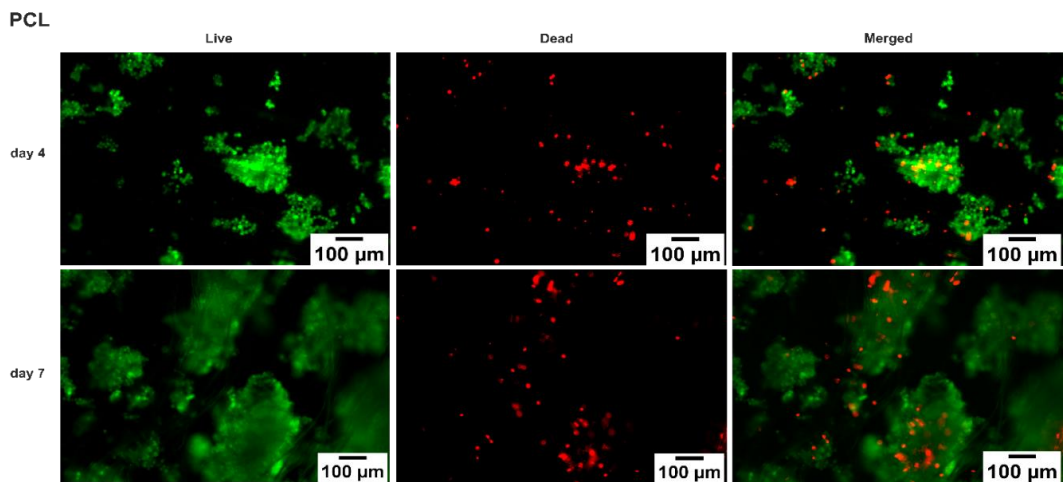


Figure S9. PC-12 neuron cell viability on PCL fibers after 4 and 7 days in culture. Live/dead assay: green - live cells; red - dead cells.

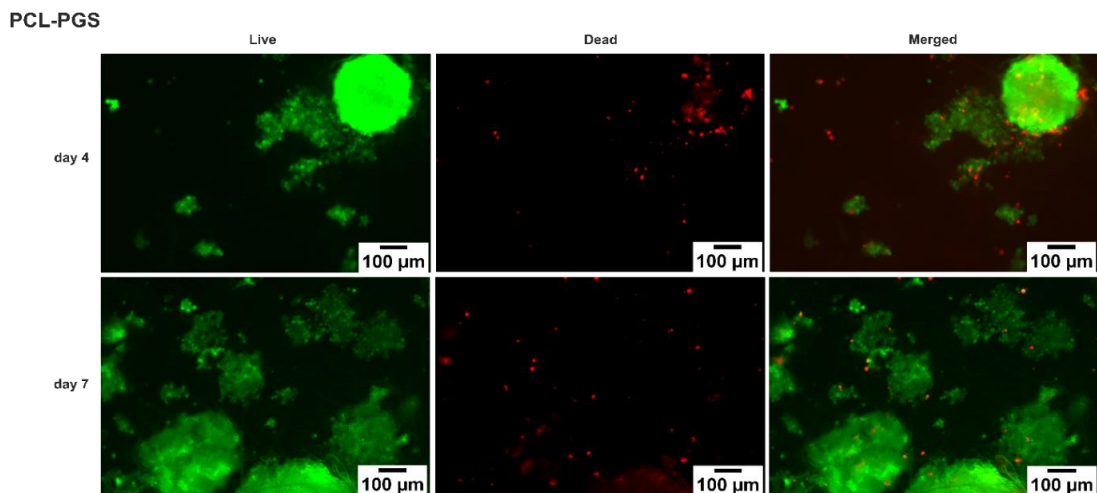


Figure S10. PC-12 neuron cell viability on PCL-PGS fibers after 4 and 7 days in culture. Live/dead assay: green - live cells; red - dead cells.

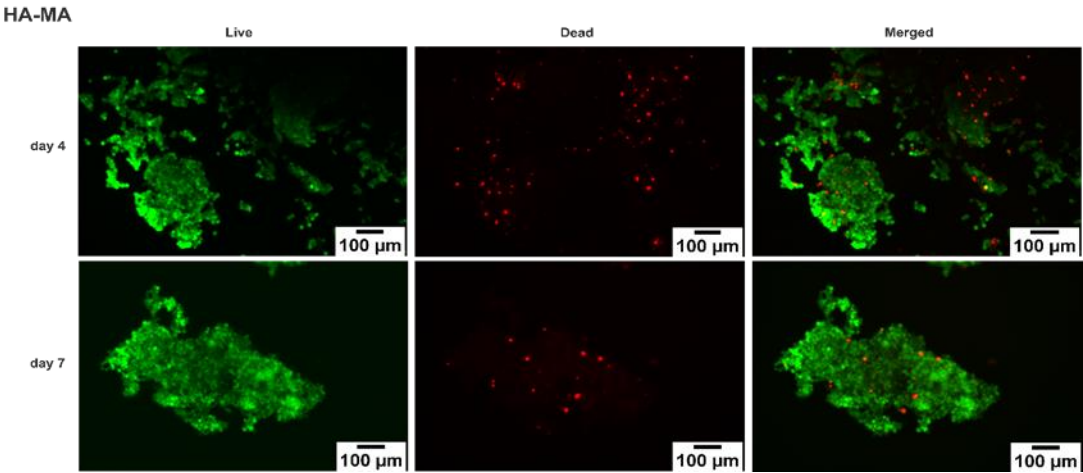


Figure S11. PC-12 neuron cell viability on HA-MA fibers after 4 and 7 days in culture. Live/dead assay: green cells - live; red - dead cells.

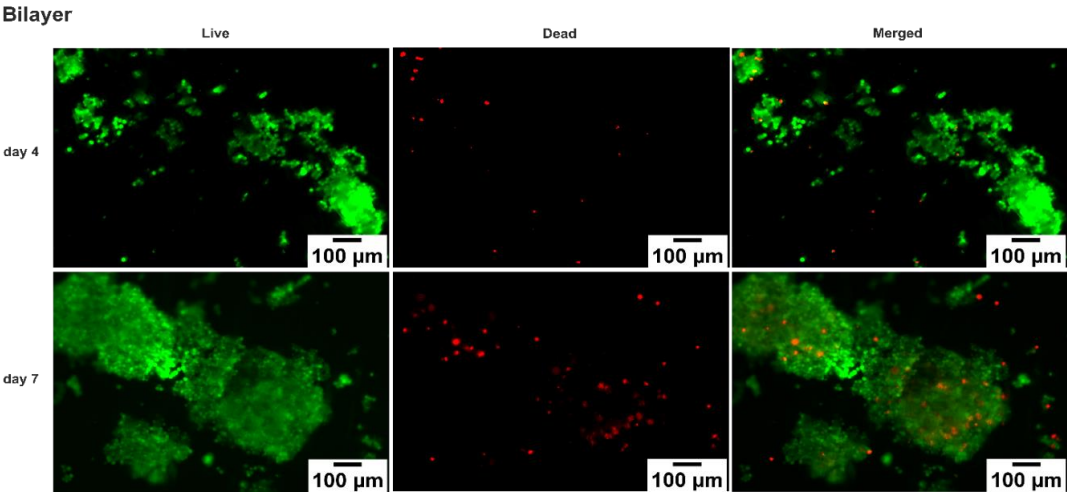


Figure S12. PC-12 neuron cell viability on PCL-PGS/HA-MA bilayer scaffold after 4 and 7 days in culture. Live/dead assay: green - live cells; red - dead cells.

## SAXS analysis:

### Determination of orientational order parameter from SAXS measurements:

Here an exemplary procedure for the fitting and calculation of the orientational order parameter starting from the raw data is given. The same procedure was used for all three parameters. We used Kratky method for result analysis, which is described in detail by Sims et al.<sup>2</sup>

It has the distinct advantage that a fit to the scattering data directly gives the parameters to describe the orientation distribution function of the scattering object in the examined  $q$ -region. The orientation distribution function is called  $f(\beta)$  with  $\beta$  being the angle between the principle axis of a rod or fiber or crystalline domain and the average orientation of all principle axes. This distribution function is described as a sum of the even Legendre polynomials  $P_L(\cos\beta)$  in its expanded form:

$$f(\beta) = \sum_{n=0}^{\infty} f_{2n} \cos^{2n} \beta$$

(1)

The coefficients  $f_{2n}$  can be determined by fitting the experimental data, with the following equation

$$I(a) = f_0 + \frac{1}{2} f_2 \cos^2 a + \frac{3}{8} f_4 \cos^4 a + \frac{5}{16} f_6 \cos^6 a \dots$$

(2)

With  $a$  being the azimuthal angle in radians. These coefficients are then used to obtain the order parameter  $S$  via

$$\langle \cos^2 \beta \rangle = \frac{\sum_{n=0}^{\infty} \frac{f_{2n}}{2n+3}}{\sum_{n=0}^{\infty} \frac{f_{2n}}{2n+1}}$$

(3)

$$S = 1/2 (3\langle \cos^2 \beta \rangle - 1)$$

(4)

The function  $I(a)$  that is used for fitting is extracted in the following way.

The background subtracted from the 2D image of the sample is radially averaged. From this radial average, the position of the peak corresponding to the oriented part of the sample and  $q$  is determined. The whole width of this peak ( $0.3\text{-}0.6 \text{ nm}^{-1}$ ) is used for the azimuthal average along  $q$  to get a plot  $I(a)$  vs  $a$ . This plot is fitted with equation 2 and the coefficients are used to calculate  $S$  via equations 3 and 4.

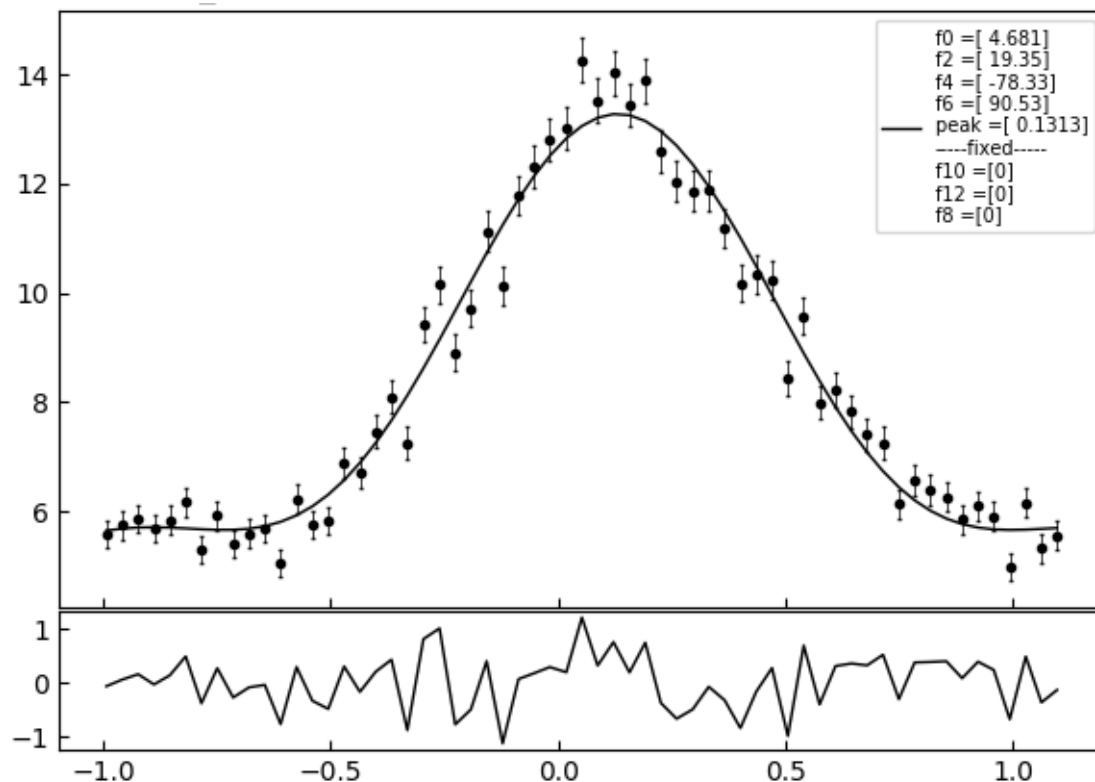


Figure S13. Fit of equation 2 to the azimuthal average over one of the peaks corresponding to the spacing of the crystalline domains within the fibres

## **Movies:**

Movie S1. Self-folding of PCL-PGS/HA-MA fibers

Movie S2. Bilayer self-folding in various mediums

## **References:**

1. Gaharwar, A. K.; Patel, A.; Dolatshahi-Pirouz, A.; Zhang, H.; Rangarajan, K.; Iviglia, G.; Shin, S.-R.; Hussain, M. A.; Khademhosseini, A., Elastomeric nanocomposite scaffolds made from poly(glycerol sebacate) chemically crosslinked with carbon nanotubes. *Biomaterials Science* **2015**, *3* (1), 46-58.
2. Sims, M. T.; Abbott, L. C.; Richardson, R. M.; Goodby, J. W.; Moore, J. N., Considerations in the determination of orientational order parameters from X-ray scattering experiments. *Liq. Cryst.* **2019**, *46* (1), 11-24.



## Part 4. Microfabrication Using Shape-Transforming Soft Materials

**Apsite I.**, Biswas A., Li Y., Ionov L.

Published in *Advanced Functional Materials*, 1908028

(2020)

Reproduced under the terms and conditions of the Creative Commons ‘CC BY 4.0’



# Microfabrication Using Shape-Transforming Soft Materials

Indra Apsite, Arpan Biswas, Yuqi Li, and Leonid Ionov\*

The fabrication of hollow and multicomponent micro-objects with complex inner structures using state-of-the-art subtractive, formative, and additive manufacturing technologies is challenging. Controlled shape transformation offers a very elegant solution to this challenge. While shape transformations on macroscale can be achieved using either manual or automatic manipulation, shape transformations on microscale can better be realized using shape-changing polymers such as hydrogels, shape-memory polymers, liquid crystalline elastomers, and others. This review discusses the properties of different classes of shape-changing materials, the principle of shape transformation, possibilities to achieve complex shape transformation, as well as applications of shape-changing materials in microfabrication and other fields.

## 1. Introduction

The development of methods for fabrication is important for every aspect of our life: from building of houses, assembling of cars to microelectronic devices. There is broad pallet of methods for fabrication of macroscopic object including subtractive manufacturing (lathe, cutting, milling), additive manufacturing (3D printing), and formative manufacturing (molding). Some of these methods are computerized that allows programmable fabrication of very complex parts. While most of these methods provide acceptable quality at a reasonable price of macroscopic objects, attempts to downscale them and to increase resolution results in a tremendous increase in costs. In particular, the milling machine (subtractive manufacturing) is efficient for the fabrication of centimeter larger objects, and the size of the drill determines the resolution. Fabrication of millimeter and submillimeter objects requires very fine drills and very expensive

I. Apsite, Dr. A. Biswas, Dr. Y. Li, Prof. L. Ionov  
Faculty of Engineering Science  
Department of Biofabrication  
University of Bayreuth  
Ludwig Thoma Str. 36A, 95447 Bayreuth, Germany  
E-mail: Leonid.Ionov@uni-bayreuth.de

Dr. Y. Li  
College of Materials Science and Engineering  
Guilin University of Technology  
Jiangnan Str. 12, 541004 Guilin, China  
Prof. L. Ionov  
Bavarian Polymer Institute  
Universitätsstr. 30, 95440 Bayreuth, Germany

 The ORCID identification number(s) for the author(s) of this article can be found under <https://doi.org/10.1002/adfm.201908028>.

© 2020 The Authors. Published by WILEY-VCH Verlag GmbH & Co. KGaA, Weinheim. This is an open access article under the terms of the Creative Commons Attribution License, which permits use, distribution and reproduction in any medium, provided the original work is properly cited.

DOI: 10.1002/adfm.201908028

machines to control them. The same can be applied for 3D printing. Different 3D printing methods like fused deposition modeling (FDM; extrude thermoplastic filaments above its melts temperature) and laser sintering are very successful for the fabrication of centimeter-large objects; they fail when are used for fabrication of the submillimeter and microsized object.<sup>[1,2]</sup> Stereolithography allows 10 μm resolution but is limited for the use of certain materials and has difficulties with the fabrication of hollow objects. Two-photon polymerization allows unprecedented resolution, but it is limited for very specific substances and is very expensive and

slow.<sup>[3]</sup> Molding may be considered as the cheapest technology for fabrication of small elements if one does not consider that molds have to be fabricated firsthand by some other techniques. Fabrication of hollow objects and multicomponent objects with complex inner structure is even more challenging.

One possibility for the fabrication of complex shapes is the use of controlled shape transformation. The most brilliant example of the applicability of controlled shape transformation for the fabrication of complex shapes is the Japanese art of paper folding—Origami. While folding of macroscopic objects can be done either manually or by using special machines, folding of micro-objects is not trivial—the machines, which allow micro-manipulation, are expensive and allow low throughput. One suitable solution is to use special materials, which are capable of controlled shape transformation. All these materials possess different mechanical and actuation properties that make them more suitable for some and less suitable for other applications (Table 1). This review discusses basic principles of design of such materials, their mechanical and actuation properties, principles of complex shape transformation, and application of shape transformation in the field of microfabrication and others.

## 2. Shape Changing Materials

Shape changing polymers are smart polymeric materials that are capable of changing their shapes in the presence of certain external stimuli.<sup>[4]</sup> All shape-changing polymers have several features, which allow their reversible shape-transformation. First, they must be able to demonstrate elastic deformation that is commonly provided by the presence of crosslinking points. Namely, crosslinking points are responsible for the reversibility of deformation. These crosslinking points can be either covalent or physical bonds such as crystallites, glassy-hard domains, H-bond, ionic interactions, etc. and molecular switches, which are sensitive external stimuli. Based on these, some polymeric

building blocks have been recognized which are appropriate for demonstrating shape-changing behavior (Figure 1). Covalently connected polymer frameworks are the most common example of shape-changing polymers in which switching segments are connected via covalent bonds and produce net points (Netpoint is typically the connection point of the polymer chains which helps in determining the permanent shape of shape-changing polymers) (Figure 1a). In some shape-changing polymers, the covalently connected frameworks have some side chains attached to the main chain, which can form a segregated phase, as observed in (Figure 1b). Sometimes the reversible bonding between two side chains also helps in showing shape-changing behavior (Figure 1c). The triblock copolymers with multiphase morphologies (Figure 1d) or some copolymers with liquid crystal elastomer as a switching segment also belong to this class (Figure 1e). Furthermore, the physical interactions like dipole–dipole interactions, hydrogen bonding or ion rich domains are also capable of producing net point for showing shape-changing behavior (Figure 1f).<sup>[5,6]</sup> Apart from these molecular architectures, sometimes processing and capillary phenomenon also plays some role in producing shape-changing behavior in polymers. Elastic deformation is also observed for semicrystalline and glassy polymers at low deformation degree.

Second, polymer chains must be in the state when they are mobile or undergo a transition between mobile and immobile states. Thus, polymers can demonstrate shape-changing properties either above their glass transition/melting point or at a temperature close to it. Third, shape-changing polymers must be sensitive to stimuli that are provided by the presence of certain chemical groups or additives, which are sensitive to pH, ionic strength, light, electromagnetic field, magnetic field, etc.<sup>[7]</sup> Meanwhile, all polymers demonstrate sensitivity to temperature when the temperature is varied around glass transition/melting. In this part of the review, the principles or mechanisms which are responsible for triggering the shape-changing behaviors in different classes of polymers will be discussed thoroughly.

### 2.1. Relaxation Phenomena (Shape-Memory Polymer)

Shape memory behavior is an entropic phenomenon, and it is associated with the relaxation behavior of the polymer chains or segments.<sup>[8,9]</sup> Many mechanisms have been proposed to describe the shape memory behavior of polymers considering the relaxation behavior of polymeric segments. Typically, shape memory polymers (SMPs) consist of switching segments that are capable of reversible phase transformation at a transition temperature (glass transition or melting temperature transition) and shape determining segments or net points that prevent the permanent deformation.<sup>[10–12]</sup> In initial shape, the polymer chains remain in a coiled state which is the low energy state (highest entropy), and any macroscopic deformation above the transition temperature (glass or melting) keeping the network structure intact would cause conformational changes of polymer chains along with enhancement in the energy state (Figure 2a).<sup>[8]</sup> The freezing of that conformation below the transition temperature allows the system to maintain its high energy state. Further, heating above transition temperature helps the molecular chains to recover their permanent configuration utilizing the entropic energy.



**Indra Apsite** received her Bachelor's and Master's degree in chemistry from the University of Latvia (Riga) in 2013 and 2015, respectively. She is currently a Ph.D. candidate at University of Bayreuth (Germany) under the supervision of Prof. Leonid Ionov, and her current research focuses on fibrous shape-morphing materials as a substrate for biofabrication and tissue engineering of skeletal muscle and nerve tissues.



**Arpan Biswas** is currently working as a research associate at the Faculty of Engineering Science, Biofabrication, University of Bayreuth. He received his Ph.D. from IIT (BHU) in 2018 and completed his M.Sc. from West Bengal State University, West Bengal. His research interests include designing and 3D printing of smart stimuli-responsive polymers for biomedical applications.



**Leonid Ionov** is a professor for biofabrication at the University of Bayreuth. He graduated in chemistry in 1999 from Lomonosov Moscow State University and completed his Ph.D. in 2005 as well as habilitation in 2015 at Dresden University of Technology. After that he worked at the University of Georgia as a faculty member. His main research activities are focused on 3D printing and bioprinting as well as on shape-changing polymers.

So, the storage and release of entropic energy through conformational changes is the driving force for executing the shape memory behavior in polymers. The relaxation behavior or viscoelastic property of the molecular chains of SMPs also contributes to the molecular mechanism of shape memory behavior. Hence, the thermoviscoelastic model is perfect to describe the shape-memory phenomena in polymers. Initially, different thermoviscoelastic models have been proposed considering stress relaxation as a simple phenomenon,<sup>[13–15]</sup> and it is very easy to describe such simple relaxation behavior only by one Maxwell or Kelvin–Voigt element. However, in a real case, the

**Table 1.** Mechanical and actuation properties of various shape-changing materials.

Materials	Young's modulus [MPa]	Tensile/actuation stress [MPa]	Elongation at break/actuation strain [%]	Actuation time	Recovery ratio [%]	Lifting weights [times]	Work density [ $\text{J g}^{-1}$ ]	Ref.
Hydrogels	0.008–5.6	0.01–8.3	150–1500	10–600 s	90–99	25–60	N/A	[61–68]
Shape memory polymer	0.82–349	8.9–24.3	130–1240	10–1500 s	81–99.3	600–3500	N/A	[69–75]
Dielectric elastomer	0.03–5	0.1–4	4.5–215	1.0 ms–1.0 s	N/A	1.0–16.7	0.03–0.15	[25,76–80]
Liquid crystal elastomers	2.0–177.8	0.038–25	120–475	1.0–1200 s	85–99	250–5680	N/A	[81–86]

relaxation phenomenon is very complex for polymers because of their complicated structure, and it requires multiple parameters to describe. For example, Mulliken and Boyce proposed a model considering two Maxwell branches to describe  $\alpha$  and  $\beta$

transitions in polymers due to different strain rates.<sup>[16]</sup> Further, Zhao et al. reported that the isothermal crystallization behavior with the time of a polymeric network is the responsible factor for triple/multiple shape-memory behaviors in polymers.<sup>[17]</sup> The isothermal crystallization generally consists of primary and secondary crystallization. In primary crystallization, the crystals are formed through nucleation of the amorphous chains of the polymers without any intervention on the confinement of the crystals while the secondary crystals grow in the part of the amorphous regions which are already interfaced by the primary crystals. (Figure 2b) Usually, the secondary crystals are thinner (low melting temperature) as compared to primary crystals (high melting temperature), and when this thickness difference becomes significant, it produces distinct melting endotherms. These multiple melting endotherms help the polymer to show triple or multiple shape-memory effect.<sup>[18]</sup> The energy released during the melting of the crystals helps the polymeric materials to regain its permanent shape. Behl et al. reported temperature-sensitive polymer actuation considering the broad melting temperature range of a semicrystalline polymer network.<sup>[19]</sup> According to them, crystallites with different melting temperatures act as bricks as well as temperature-responsive volume changing units. The crystallites with a lower melting temperature are responsible for reversible actuation while the crystallites with a high melting temperature act as a skeleton forming domains. (Figure 2c) The macroscopic shape actuation of semicrystalline polymers is only possible if the domains are aligned in the matrix and are connected covalently. A “spring model” is proposed by Biswas et al., considering the molecular flipping of some crystalline parts to demonstrate the molecular mechanism of reversible bidirectional shape memory behavior.<sup>[20]</sup> In this model, the soft segments (blue color) of the polymer are sandwiched between hard segments (red color) and some hard segments are also distributed within the soft segment part in the presence of strong interaction. (Figure 2d) Now, above the transition temperature, the distributed hard segment starts to move toward the consolidated hard segments along with the coiling of the liquid soft segment that again redistributed within the soft segments during cooling. Thus, reversible flipping of the tiny hard segments with heating–cooling cycles at the molecular level helps to trigger reversible shape memory behavior in polymers macroscopic levels.

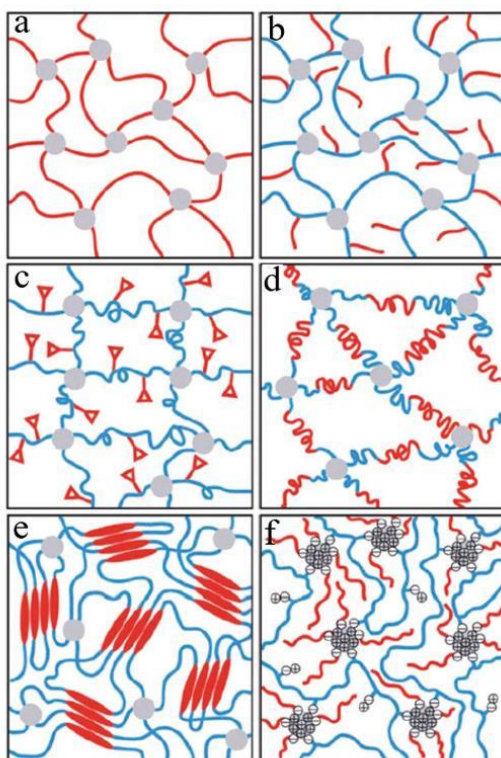


**Figure 1.** Examples of some typical molecular architecture which are suitable for showing shape-changing behavior: a) The covalent bonds between the switching segments (red color) produces net points (gray color); b) the side chain acts as switching segment in this case; c) the reversible bonding between the functional group (red color) acts as molecular switches; d) ABA triblock system acts as the switching segments and produces the net point at junction; e) the organized mesogens in liquid crystal elastomers acts as the switching domains; f) the physical interaction like dipole–dipole interactions, H-bonding, etc. produces the net point. Reproduced with permission.<sup>[15,6]</sup> Copyright 2013, Royal Society of Chemistry.

## 2.2. Dielectric Elastomer

Dielectric elastomers are another kind of shape-changing polymers, whose actuation is based on relaxation. Dielectric

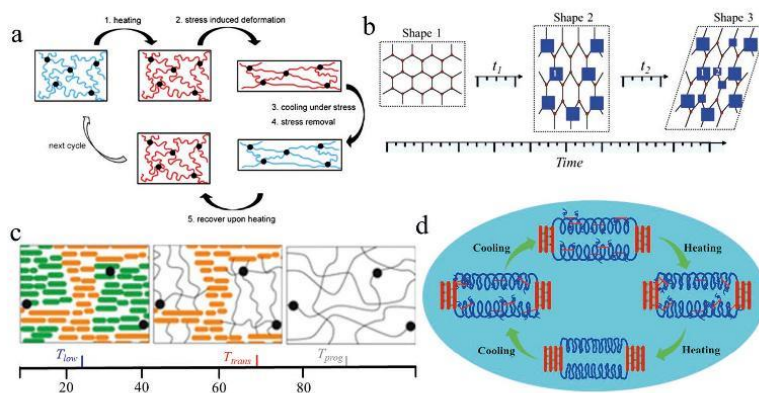


**Figure 2.** Relaxation as a driving force in shape memory behavior: a) the molecular mechanism of shape memory behavior in a chemically crosslinked polymer moiety. The stored energy in the molecular backbone after fixing the deformed shape through cooling provides sufficient energy during the recovery process, Reproduced with permission.<sup>[8]</sup> Copyright 2015, Elsevier; b) time depended crystallization in the amorphous part of the polymer chain responsible for the triple shape memory behavior, Reproduced with permission.<sup>[17]</sup> Copyright 2015, Elsevier; c) in this model, the crystallites are like bricks and reversible melting and crystallization of some bricks with a low melting temperature with temperature cycles triggering reversible shape memory actuation, Reproduced with permission.<sup>[19]</sup> Copyright 2013, United State National Academy of Science; d) in this spring model, reversible flipping of some tiny crystallites along with the actuation domain triggering the reversible shape-changing behavior. Adapted with permission.<sup>[20]</sup> Copyright 2016, American Chemical Society.

elastomers are placed between two compliant electrodes and acts as a compliant capacitor model. The application of voltage to the electrodes placed on the opposite side of the elastomer creates opposite net charges, which form stress (Maxwell stress) in the elastomer film due to electrostatic attraction (coulombic attraction). This so-called Maxwell stress triggers the thinning of the dielectric elastomer which is further compensated by the expansion in the plane of elastomer (Figure 3a). This expansion strain is sufficient enough to activate the shape-changing behavior in the dielectric elastomer.<sup>[21]</sup> However, the uniform electric field throughout elastomer restricts the switching of the elastomer to a new shape, but the presence of a passive layer can introduce the bending actuation in the material. According to the compliant capacitor model, the actuators can show either in-plane expansion,<sup>[21]</sup> liner actuation,<sup>[22,23]</sup> or bending.<sup>[24]</sup> The stress and strain produced by the parallel plate actuation are equal in both perpendicular direction ( $\sigma_x = \sigma_y = -1/2\sigma_z$ ),<sup>[25]</sup> which is not desired all the time, and to overcome this limitation different strategies have been considered. For example, the attachment of a passive layer with the flexible dielectric elastomer and the electrode on both sides helps in converting the voltage induced linear expansion into a flexural actuation.<sup>[24]</sup> Figure 3b shows different bending behavior of the bilayer structure consisting of a dielectric elastomer (active layer) and fibers (passive layer), with varying fiber configuration. In another approach, Hajiesmaili and Clarke demonstrated that the shape morphing of dielectric elastomers can be manipulated by varying the spatial distribution of the electric field using an internal mesoarchitecture of the electrodes.<sup>[26]</sup> The actuation of a strip into a torus structure with positive curvature (outer part of the torus) or negative curvature (inner part of the torus) can be achieved by changing the width of the electrode gradually from bottom to top, as observed in Figure 3c. The strip with decreasing electrode's width from bottom to top (11 to 1 mm) results in torus structure with

positive curvature while strip with increasing electrode's width results in torus structure with negative curvature.

### 2.3. Volume Change (Swelling Hydrogels)

Shape changing hydrogels are water-swollen crosslinked frameworks, which are capable of reversible swelling/deswelling with changes in environmental water contact due to change of affinity of polymer chains toward the water.<sup>[27,28]</sup> The degree of swelling of any hydrogels is directly associated with crosslinking density and molar free energy of mixing which is again the function of interchain interactions, solvents, and entropy of mixing (Flory–Rehner Theory). So, if the average molar mass of the connecting moieties between two adjacent network nodes is  $\overline{M}_c$ , the crosslinking density ( $\nu_c$ ) of the crosslinked polymeric network can be calculated using the Flory–Rehner equation (Equation (1))<sup>[6]</sup>

$$\nu_c = \frac{\ln(1-\phi_2) + \phi_2 + \phi_2^2 \chi_{12}}{V_1 \left[ \left( \frac{\phi_2}{2} \right) - \phi_2^{1/3} \right]} = \frac{\rho}{\overline{M}_c} \quad (1)$$

where,  $\chi_{12}$  is responsible for Flory solvent–polymer interaction,  $\rho$  is the density of the network,  $V_1$  is the molar volume of the solvent and the  $\phi_2$  is the volume fraction of the polymer in the swollen state ( $\phi_2 = V_d/V_{sw}$ ;  $V_d$  is the volume in the dry state, and  $V_{sw}$  is the volume in the swollen state).

For hydrogels with a constant crosslinking density, the entropic and energetic components can be influenced by the temperature and solvent quality, which again associated with temperature, pH, and other parameters. So, the degree of swelling of hydrogels can be influenced by the temperature, pH and other parameters.<sup>[29]</sup> Hydrophobic interactions play an important role in the molecular mechanism of shape-changing

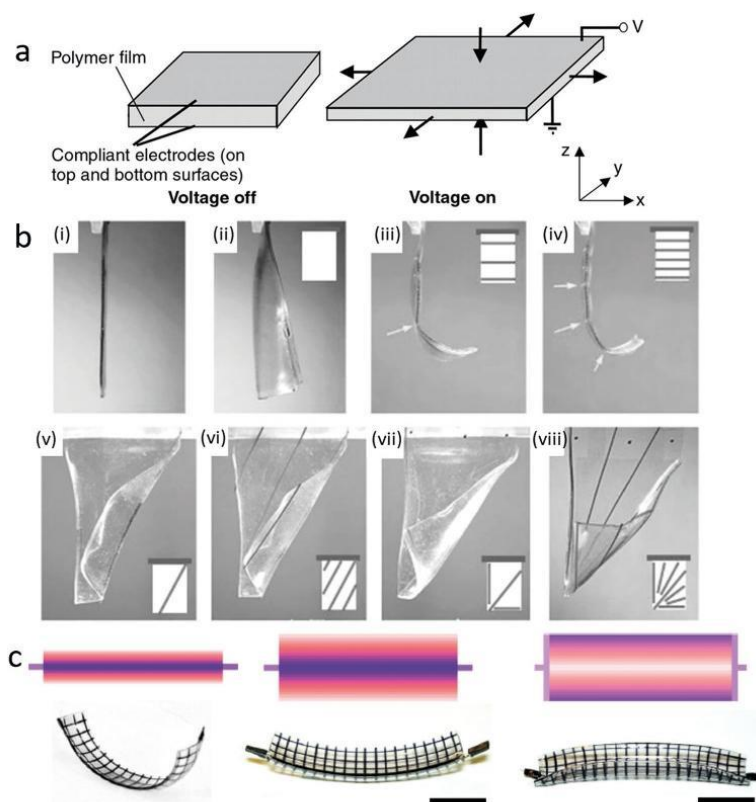


**Figure 3.** The actuation of dielectric elastomers: a) The linear expansion of the dielectric elastomer due to the production of electrostatic force in the presence of compliant electrodes on the elastomer film, Reproduced with permission.<sup>[21]</sup> Copyright 2000, American Association for the Advancement of Science; b) the actuation of a bilayer structure of dielectric elastomer and fibers. i) The side view of the bilayer, ii) the actuation without fibers, iii, iv) side of bending of the bending actuation of the bilayer in presence of different number of fibers, v–viii) the bending behavior with varying number and arrangement of the fibers in the bilayer structure, Reproduced with permission.<sup>[24]</sup> Copyright 2015, Wiley-VCH.; c) demonstration of morphing behavior of a dielectric elastomer with the width of the electrode. The flat sheet of the elastomer produces torus structure with positive curvature when the width of the electrodes decreases from bottom to top. However, the reverse phenomenon takes place when the width of the electrodes increases gradually from bottom to top. The scale bar is 20 mm. Reproduced under the terms and conditions of the Creative Commons CC BY 4.0 license.<sup>[24]</sup> Copyright 2019, The Authors, published by Springer Nature.

hydrogels. The cooling induced segregation of polymer chains in a hydrophilic medium in the presence of hydrophobic interaction and further heating induced dissociation of aggregations of the polymer chains collectively triggering the shape-changing behavior in some temperature-sensitive shape-changing hydrogels.<sup>[30]</sup> (Figure 4a) The hydrophobic interaction provides additional crosslinking, which helps in fixing the temporary shapes. Further, the loss of this additional crosslinking at elevated temperature provides sufficient energy to recover the permanent shape. Apart from thermal stimulation, sometimes the complexation between the metal ion and organic moiety can also trigger the shape-changing behavior in hydrogels.<sup>[31,32]</sup> The additional crosslinking provided by the complexation between the metal ion and organic moiety helps in obtaining the temporary shape in shape-changing hydrogels. Further, the changing

in the oxidation state of the metal ion in the presence of external stimuli triggers the shape recovery process through the elimination of the additional crosslinking. (Figure 4b) In some cases, reversible supramolecular interactions such as host–guest interactions, red-ox interaction or antigen–antibody interactions triggering the shape fixing process producing some additional crosslinking in the hydrogel. Again, the elimination of that crosslinkings in the presence of pH or antigen stimuli helps in recovering the permanent shapes, as observed in Figure 4c.<sup>[33–36]</sup>

#### 2.4. Nonuniform Strain (Liquid Crystal Elastomer)

Anisotropic shape changing in response to an external stimulus is a widespread phenomenon in liquid crystal elastomers

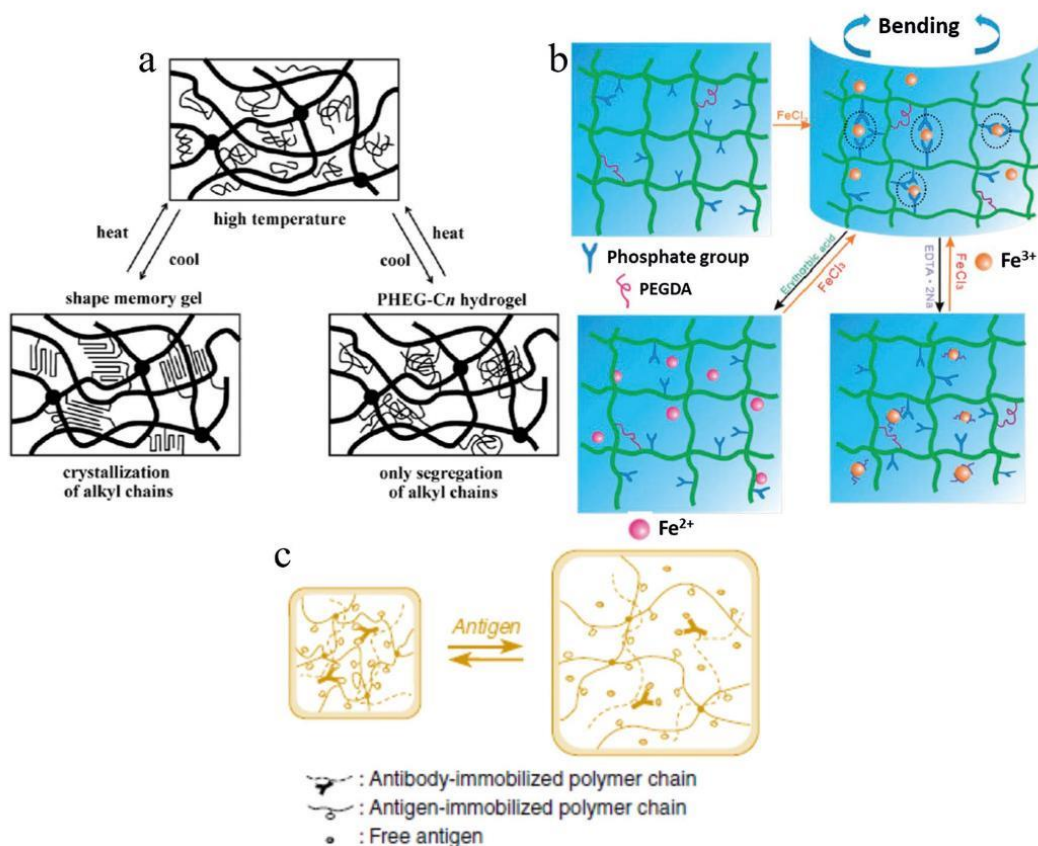


**Figure 4.** The different shape-changing mechanism in hydrogels: a) The hydrophobic interaction induced aggregation of side chains of polymers, triggering the shape-changing behavior in hydrogels, Reproduced with permission.<sup>[39]</sup> Copyright 2012, Elsevier. b) The change in the degree of crosslinking due to the change in the oxidation state of the metal ion in presence of stimulus, triggering shape-changing phenomenon, Adapted with permission.<sup>[31]</sup> Copyright 2014, Royal Society of Chemistry; c) according to this molecular model, the antigen-induced change in the crosslinking density responsible for the reversible actuation in hydrogel; Reproduced with permission.<sup>[36]</sup> Copyright 1999, Springer Nature.

(LCEs). LCEs belong to a unique class of materials with properties of elastomers (entropic elasticity) as well as liquids crystals (self-organization).<sup>[37,38]</sup> LCEs are capable of remembering their previous state after phase transformation in the presence of stimuli, which enable them to contract and expand reversibly.<sup>[39–41]</sup> In the presence of the weakly crosslinked network, liquid crystal elastomers represent a state in between solids and liquids. Further, they have long-range orientational ordering due to the mesogenic moieties. Hence, under applied stress, a curvature elasticity along with deformation of this order is observed in liquid crystal elastomers. The combination of these two physical properties in a material help in emerging a qualitatively new state of matter in which the mesogenic polymer chains are capable of continuous orientational ordering because of the high molecular mobility of the polymer chains. Further, the mobile nature of the axis of orientational

symmetry breaking allows it to respond against applied elastic strains, and the whole system behaves like a Cosserat medium in which internal torques are permissible, and therefore, elastic stress may be nonsymmetric.<sup>[42]</sup> According to the molecular model of nonuniform deformations within the elastic limit of LCEs, developed by Trentjev et al., the free energy of deformations is a function of large nonsymmetric affine strains in the rubbery network and gradient of curvature deformations in the director field. Further, the elastic constants for the nonuniform directors in the presence of elastic strain depends on the polymer step length anisotropy.<sup>[42]</sup> Again, de Gennes et al. suggested a strong uniaxial deformation in LCEs without any significant change in volume, in response to a decrease in temperature across the isotropic to liquid crystal transition, is due to the change in the orientational order of liquid crystals.<sup>[43]</sup> Later, Finkelmann and Kundler reported that the nematic to

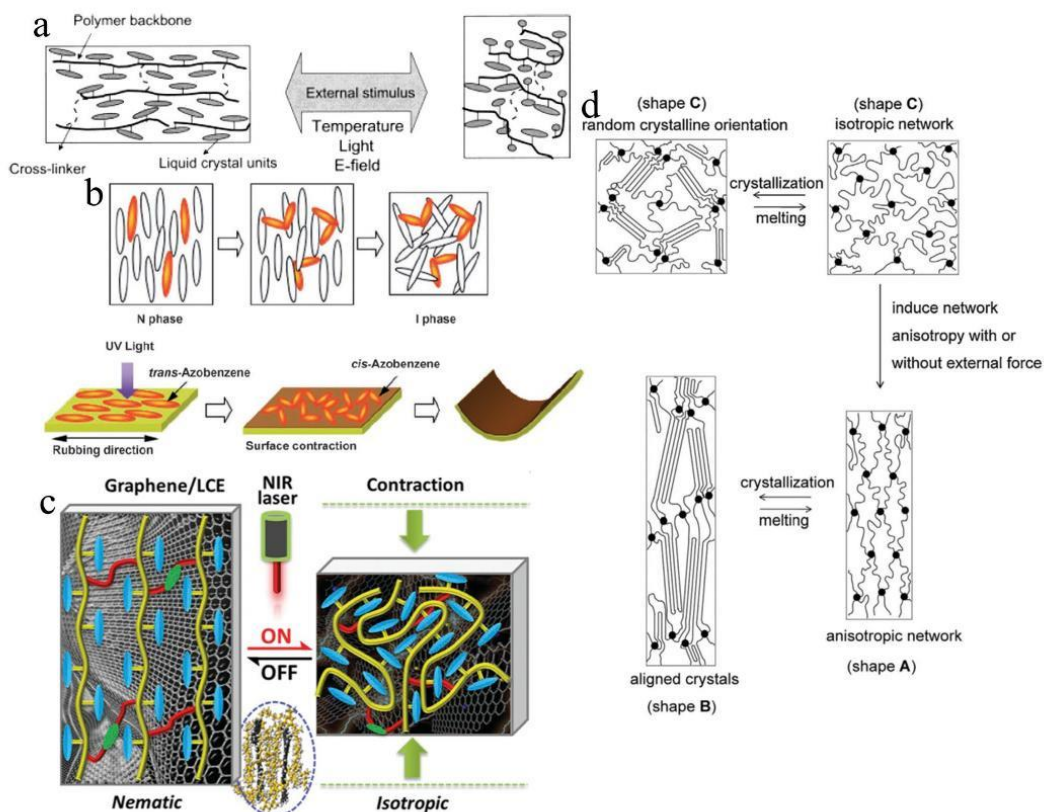


**Figure 5.** Nonuniform strain-induced shape-changing behavior: a) The processing induced (electrospinning) organization of the liquid crystal mesogens provides sufficient energy for showing shape actuation through anisotropic strain recovery, Reproduced with permission.<sup>[41]</sup> Copyright 2003, American Chemical Society; b) the photoisomerization of the surface liquid crystal domains of the LCEs due to limited absorption of light results self-folding of the shape through nonuniform strain recovery, Reproduced with permission.<sup>[49]</sup> Copyright 2006, Wiley-VCH; c) the photothermal property of graphene and hot stretching induced self-organization combined to trigger the shape-changing phenomenon, Reproduced with permission.<sup>[47]</sup> Copyright 2015, Wiley-VCH; d) the stretching induced organization of the molecular sheets improves the crystallization behavior of the materials, which trigger the anisotropic reversible shape-changing behavior in conventional polymers. Reproduced with permission.<sup>[8]</sup> Copyright 2015, Elsevier.

isotropic phase transition in LCEs is the driving force behind the temperature-induced spontaneous deformation along the director axis.<sup>[40]</sup> Naciri et al. prepared LCEs fibers with the side-on attachment of the liquid crystal mesogens. (Figure 5a) The processing induced alignment of the mesogen groups along the axis of the fiber allow the anisotropic contraction of the fiber along the fiber axis in the presence of external stimuli through the disorganization of the mesogenic groups.<sup>[41]</sup> Pei et al. reported the actuation behavior of liquid crystal elastomers with transferable crosslinking. The actuation process follows an alternative mechanism for mechanical relaxation. LCEs produce high alignment of liquid crystals instead of external stress relaxation through the creep of nonliquid crystal temporary framework with transferable links.<sup>[44]</sup> Ikeda et al. reported photo-induced 3D anisotropic deformation in LCEs

(Figure 5b) containing the azobenzene derivatives as liquid crystal mesogens and swollen in a solvent or heated above the glass transition temperature.<sup>[45]</sup> The azobenzene groups are sensitive to light and show photoresponsive *cis-trans* isomerization on exposure to light, which causes a significant change in length.<sup>[46]</sup> The limited absorption of light allowing only the surface mesogens to show photo isomerization which leads to the bending or 3D deformation in the developed materials. Further, a near-infrared spectroscopy responsive reversible mechanical actuation is achieved in graphene/LCE nanocomposite, where the graphene acts as photoactive constituents.<sup>[47]</sup> The in situ UV photopolymerization along with concurrent hot stretching organizes of the liquid crystal mesogens, and the extensive interactions between the graphene and mesogens allow the graphene sheets to distribute uniformly in the matrix. Now, the

photothermal effect of graphene along with the high self-organization of the mesogens collectively trigger the photoresponsive reversible actuation phenomenon in nanocomposite (Figure 5c) and entropy driven elasticity is the driving force behind this large reversible deformation in the reported LCE which is one of the advantages of this material over other conventional polymeric materials.<sup>[48]</sup>

Apart from LCEs, some conventional polymers are also able to show anisotropic shape-changing behavior. Lendlein's group reported a thermoresponsive reversible bidirectional shape-changing phenomenon in a block copolymer made of polycaprolactone (PCL) and poly( $\omega$ -pentadecalactone) (PPD) building blocks<sup>[50]</sup> and proposed a molecular mechanism that triggers the reversible shape-changing phenomenon (Figure 5d). Shape C is the permanent shape of the polymer in which the polymer chains are randomly oriented. The programming through uniaxial deformation changed the conformation of both the crystalline domains (PCL and PPD), as observed in shape A. Further, the heating-cooling cycles allow only the PCL domain to melt or crystallize while the PPD domain remains unchanged and produce the network anisotropy for PCL domain without external force. Overall, the programming induced conformational anisotropy deforms the PPD domain, and the constrain produced by the deformed PPD domain helps the PCL domain to be in oriented conformation.<sup>[51]</sup> The crystallization induced elongation and melting induced contraction of the length with heating-cooling cycles along the programming axis produces the reversible shape-changing behavior in this material.

## 2.5. Surface Tension

Surface tension or the capillary force becomes a very relevant and dominating driving force for showing shape-changing behavior in soft materials or materials with small dimensions as surface force starts to dominate over the bulk force of gravity at a smaller level.<sup>[52]</sup> Sometimes, this surface force is so strong that it destroys the thin structure of micro or nanoscale devices.<sup>[53]</sup> There are many reports in which the capillary action or surface tension functions as the driving force for shape-changing behavior or arranging and adjusting the 2D rigid objects at the surface of the water.<sup>[54]</sup> To understand the relative importance of surface energy with respect to bulk elasticity, a liquid droplet with surface tension  $\gamma$  is considered over an ideal smooth and uniform solid surface.<sup>[55]</sup> (Figure 6a) After deposition, the droplet makes an angle  $\theta$  with the surface of a rigid substrate, which is classically adjusted through a balance among all surface forces at the interaction line. If the typical extent of deformation at the pinched region is  $\delta$ , then it can be defined by Equation (2)<sup>[56]</sup>

$$\delta \sim \frac{\gamma}{E} \sin \theta \quad (2)$$

where,  $E$  is the elastic modulus of the material, and  $\gamma \sin \theta$  is the vertical component of surface tension, which helps in deforming the substrate by pulling the substrate.<sup>[57]</sup> Further, consider an elastic plate (length  $L$ , width  $w$ , and thickness  $h$ ) coated with a thin liquid layer with surface tension  $\gamma$ . The contact of this plate with a rigid cylinder (radius  $R$ ) coated with same liquid layer

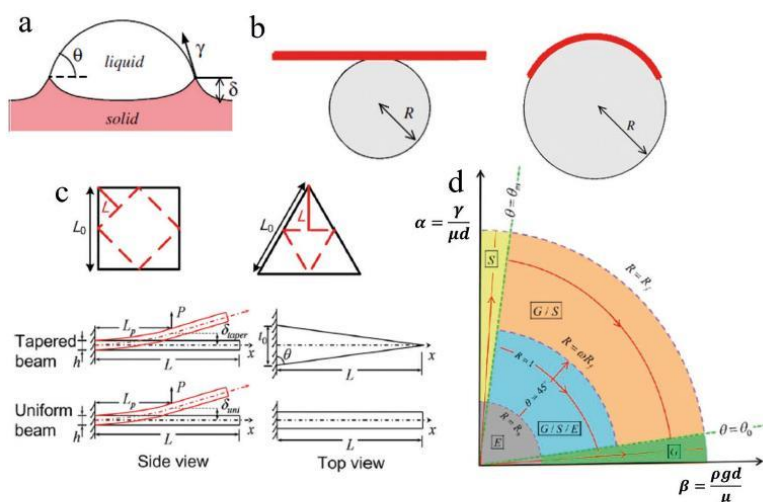


**Figure 6.** Surface tension as the driving force in shape-changing behavior: a) Model describing surface deformation at the solid-liquid interface due to surface tension, Reproduced with permission.<sup>[55]</sup> Copyright 2008, American Chemical Society; b) the model helps in optimizing different responsible factors for bending of an elastic plate (red color) in contact with any cylinder (both coated with a thin layer of liquid), Reproduced with permission.<sup>[58]</sup> Copyright 2010, Institute of Physics Publishing; c) according to this model, the self-folding is driven by the capillary interactions at the triple junction; the symmetric red dash line denotes the bending point in both square and trigonal schematic models, Reproduced with permission.<sup>[59]</sup> Copyright 2009, United State National Academy of Science; d) the deformation map describing the role of elasticity ( $E$ ), gravity ( $G$ ), surface tension ( $S$ ) in defining the shape of a soft material. Reproduced with permission.<sup>[60]</sup> Copyright 2013, American Chemical Society.

leads to the wrapping of the cylinder by the plate (Figure 6b) which results in enhancement not only in the surface energy by  $2\gamma wL$  but also in the elastic energy by  $BwL/2R^2$ ; where  $B$  is the bending modulus of the elastic plate and  $B = Eh^3/12(1 - \nu^2)$ ,  $E$  and  $\nu$  are the elastic modulus and Poisson ratio of the materials. Hence, the wrapping is only possible if the radius of the cylinder  $R > \frac{\sqrt{B/\gamma}}{2}$ ; where  $\sqrt{B/\gamma} = L_{EC}$  (elasto-capillary length).

So, the characteristic length of the flexible plate should be less than the radius of the rigid cylinder for spontaneous wrapping.<sup>[58]</sup> Guo et al. reported the self-folding behavior of thin-film single crystal silicon and proposed a mechanics model identifying the responsible parameter.<sup>[59]</sup> According to this model, the folding behavior of the thin film is driven by the capillary interaction at the triple junction. Figure 6c shows that the thin sheets are like tapered cantilever beam and the capillary force works on the beam at a particular position ( $L_p$ ) with an extent of  $\gamma t$  where  $t$  is the width of the beam or length of the contact line at  $L_p$  and this capillary force should be enough to overcome the bending resistance of the beam for self-folding of the thin films. A deformation map is proposed by Xu et al. to understand the influence of different parameters on the surface tension drove shape-changing behavior and to optimize difference influencing factors for successful folding.<sup>[60]</sup> The map is prepared using polar coordinate system and considering two extreme conditions; i) in which the deformation is exclusively driven by the surface tension and the overall strain due to the surface tension is in the order of  $\alpha = \gamma/\mu d$ ,  $\mu$  is the shear modulus and  $d$  is the length of the axis, and ii) in which the gravity is the dominating factor and average strain is in the order of  $\beta = \rho g d/\mu$  where the  $\rho$  is the mass density and  $g$  is the gravitational force. (Figure 6d) The map is divided into five region depending on the role of the elasticity ( $E$ ), gravity ( $G$ ), and surface tension ( $S$ ) in defining the shape of the material.

### 3. Principles of Complex Shape Transformation

The shape-changing behavior of polymeric materials can be precisely programmed by their geometry and structure. Here, we discuss how different kinds of complex actuations are realized in different shape-changing materials.<sup>[87]</sup>

The folding behavior of a material can be defined as deformation of a material keeping the in-surface distance between the two distinct points of the material without self-intersections.<sup>[88]</sup> The folding is a sharp curvature of the material, which results due to the deformation of the material along a crease and produces a narrow hinge area with sharp angles.<sup>[89,90]</sup> Folding can be achieved in a material utilizing the stress mismatch between the active and passive layers.<sup>[91-93]</sup> For example, the hinge printed with active materials (shape-changing material) and other parts printed with inactive materials results in folding in the presence of the appropriate stimulus. The 4D printed structure developed by Tibbitts folds into a precisely truncated octahedron in the presence of water stimuli.<sup>[94]</sup>

Bending can be defined as the disseminated deformation in the material throughout the deflected area resulting in curvature in the material.<sup>[89,95]</sup> Bending can be achieved by attaching two materials with different degrees of swelling or shrinking

behavior. The bilayer structure will bend to keep equal strain at the interface of the bilayer on activation by the stimuli.<sup>[93]</sup> Zhang et al. fabricated a lightweight 3D composite structure that remains flat on heating due to the release of internal strain but starts to bend on cooling to room temperature.<sup>[96]</sup> There is some basic difference between folding and bending, such as folding results due to localized deformation while bending happens due to global deformation in the material.<sup>[97]</sup> Further, in the presence of continuously applied force during bending, the shape changing results rolling deformation in the material. The main difference between bending and rolling is rolling consists of multiple gradients while bending consists of only two gradients.

Twisting behavior can be achieved in a material by using in-plane stretching. The combination of two anisotropic active layers of a similar kind with stretching direction perpendicular to each other results in self-twisting in the bilayer structure. Shape changing material with a small width is favorable for showing twisting behavior.<sup>[98]</sup> The printing of fibers with certain angle results twisting in shape.<sup>[96]</sup>

Helixing can be characterized by the smooth distortion of the material in space, which results in a three-dimension curvature.<sup>[92]</sup> Helixing deformation can be achieved in a bilayer structure through the uniaxial stretching or shrinking of the active layer with a nonzero angle between the axis of stretching and the axis of bilayer structure.<sup>[99]</sup> The basic difference between twisting and helixing is that the axis of twist is centered in twist shape while helixing possesses multiple axes.

The buckling deformation can be achieved by the application of compressive stress above a critical value, which results in sudden sideways failure in a flat structural membrane.<sup>[100]</sup> The compressive stress can be generated through the in-plane organization of different active and passive elements. Menan et al. discussed four different ways, such as material tessellation, in-plane material gradients, nonhomogeneous exposure to stimuli and application mechanical stress, to generate buckling deformation.

Curving can be defined as the deviation in the geometry of an object from its plane or flat shape. This type of shape-changing behavior can be achieved through the unequal stress generation in between the active and passive layer. The different degrees of swelling of two layers in the presence of stimuli can produce unequal stress in the material.<sup>[94]</sup> Further, the stress gradient could be generated by the application of varying intensity of the stimuli along with the thickness of the material.<sup>[101]</sup>

The topographical changes can produce distorted or uneven shape in the material, which is quite similar to the physical properties of ground terrain. The surface topography can be defined as the local deviation of a surface from its flat plane. The concentric circles in the presence of suitable stimuli produce mountain and valley-like features.<sup>[102]</sup> Further, it can also be realized under compressive loading.<sup>[94]</sup>

The unequal swelling/shrinking behavior of a bilayer structure with similar stiffness and layer thickness results in wave or curling shape in response to an appropriate stimulus.<sup>[94,103]</sup> The basic difference between waving and curling is the consistency of the wave after distortion. Further, curling possesses irregular curves while waving consists of more symmetric curves. The wave shape can be tuned by changing the position and

materials of each layer. The trilayer structure developed by Wu et al. consists of an active layer of SMP and two passive layers. The heating induced activation of SMP of the trilayer structure results in a wave shape.<sup>[93]</sup>

### 3.1. Complex Deformation of Stress Relaxation-Based Shape-Changing Polymers (Shape Memory Polymers)

Complex shape changing in SMPs is highly associated with the complex programming of the permanent shape of the SMPs into temporary shape, and different kinds of stimuli can play an important role in executing this complex shape-changing phenomenon.<sup>[104,105]</sup> Thus, complex actuation in shape-memory polymers can be achieved without structuring but by their deformation. This not only increases the versatility of programming as well as helps in predicting the pathway.

Exposure to the whole sample to conditions when which polymer chains become mobile results in simultaneous actuation of all parts of a sample—it simply returns to its initial shape. Sequential folding can be achieved when samples are exposed to localized stimuli such as light. Indeed, heating of sample with laser light allows site-specific shape transformation, which is determined by the permanent shape. For example, the photothermal or magnetothermal effect of nanoparticles or dyes can play an important role in the production of heat in the presence of light or magnetic field.<sup>[106,107]</sup> The more advance complex programming can be achieved using the light of different wavelengths, which produces heat after absorbing light selectively by some special dyes.<sup>[108,109]</sup> Liu et al. developed a simple method to show complex shape changing in a prestrained polymer sheet. They printed ink using a desktop printer onto the polymer sheet, and irradiation with light allows the printed zone to produce heat which triggers the gradient shrinking of the polymer chains across the thickness of the polymer sheet. This shrinkage causes the polymer sheet to fold immediately.<sup>[106]</sup> Similarly, sequential folding can be achieved by printing different color ink over the polystyrene sheet and then irradiate the polymer sheet with LED light of particular color to trigger the folding process. **Figure 7a** shows the sequential folding of a nested box on exposing to red and green light, respectively, on which red and green ink is printed with a desktop printer. The folding of the nested box taking place due to the photothermal effect produced by the inks printed over it.<sup>[108]</sup>

Another way to achieve complex deformation of shape-memory polymers is to use a multicomponent object. For example, the electromechanical or thermos-mechanical shape changing can be achieved after programming the composite utilizing its broad glass transition temperature.<sup>[110]</sup> This composite acts like an ion polymer–metal composite and the transportation of ions and water molecules along with the electrostatic force under the influence of applied voltage, trigger the electromechanical shape-changing phenomenon in this composite. Simultaneous application of temperature and electric stimulus helps the composite material to show very complex shape transformation behavior, as observed in **Figure 7b**. The temperature triggers the twisting and bending while the electric field activates the oscillation. Tolley et al. reported a complex shape-changing phenomenon of shape memory polymer

composite under uniform heating.<sup>[111]</sup> The polymer composite is fabricated by putting the prestrained SMP in between two papers, as observed in **Figure 7c**. The heat-induced contraction of the SMP resulting bending in the laminate structure, perpendicular to the axis  $p$  and toward the gap until the two sides of the upper layer come in contact, fighting against the force of gravity at the free end. Although multilayer shape memory polymers have some advantages like good and easily tunable elastic properties, although their fabrication is still time-consuming and complex in nature. To overcome this issue, Jin et al. developed a crystalline shape memory polymer with thermo and photoreversible bonding to produce complex shape actuation.<sup>[112]</sup> In this case, two different responsibilities are assigned to two different reversible bonding. The network anisotropy and location of actuation are generated through the activation of photoreversible bonding in a spatial-selective manner while shape-memory behavior is controlled by the thermoreversible bonding. The combination of the effects of these two different type of reversible bonding triggers complex shape transformation, from simple 2D films to 3D structures (**Figure 7d**).

### 3.2. Complex Deformation of Shape-Changing Polymers with Volume Change (Hydrogels)

In most cases, the hydrogels and other volume changing polymers exhibit shape-changing behavior because of their isotropic volume expansion and contraction in response to a stimulus. Complex shape changing such as bending, twisting, and folding can be achieved by inhomogeneous expansion or contraction of the material in different directions.<sup>[113]</sup> At the end, the way how shape-transformation occurs depends on the structure of hydrogel. For example, the bending behavior can be produced through the introduction of bilayers of two different polymeric materials with different expansion co-efficient while the twisting behavior can be achieved using bilayers of different materials with gradually changing thickness ratio between two layers. Twisting is achieved when the ratio between the thickness of parts with different swelling properties changes gradually along with the sample.

More complex actuation can be achieved when several bilayer elements are combined with each other and with nonactuating parts. Small bilayer connected to nonactuating elements can be used to introduce sharp edges. The curvature of the edge is determined by parameters of the bilayer, and the bending angle also depends on the size of the bilayer. **Figure 8a** shows that the attachment of the bilayer structure in the structure of film triggers the formation of hinge shapes. The bilayer structure is patterned using noncontact photolithography of the hydrogel which is composed of *N*-isopropyl-acrylamide (NIPAm), acrylic acid (AAc), and poly-ethylene oxide diacrylate (PEODA). The “Venus Flytrap” shape reversible closes and opens with changing the pH due to different degrees of swelling of the two different layers.<sup>[114]</sup> Similarly, patterned polymer film with areas of different swelling magnitude results in similar phenomena.

Bilayers can bend in one direction that restricts possibilities for microfabrication. Hayward and co-workers have proposed a very interesting solution to this problem—they have fabricated

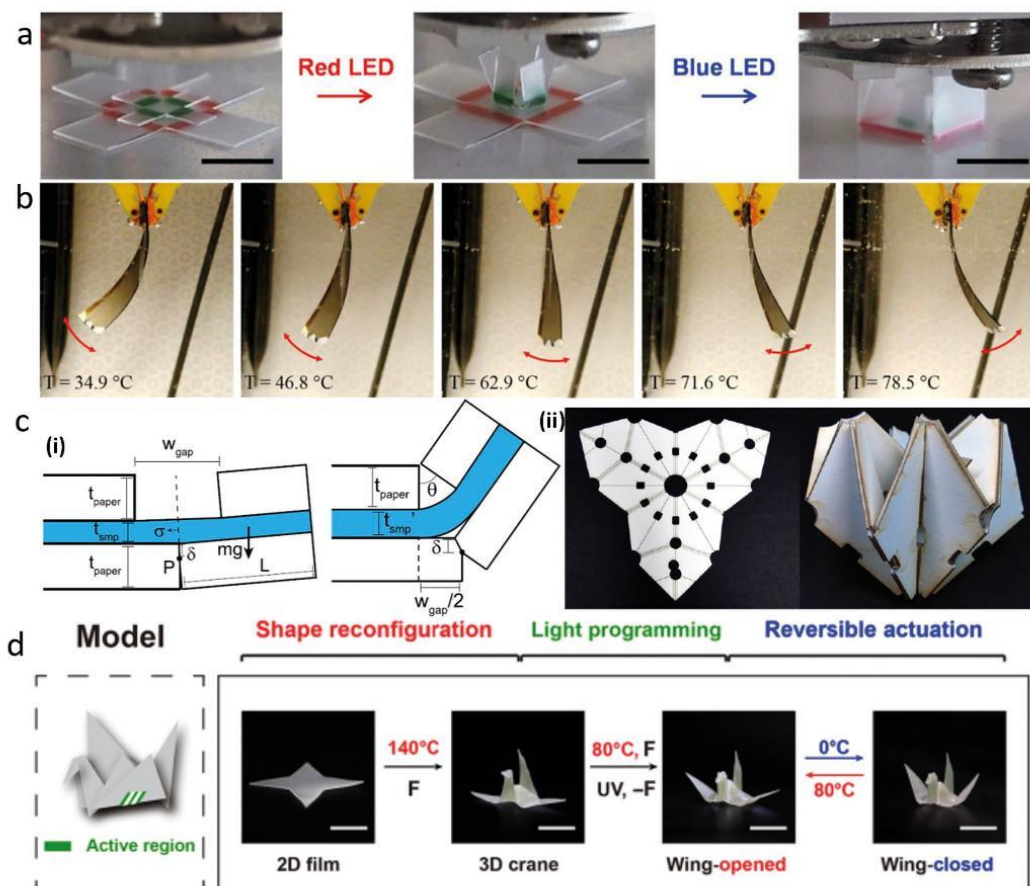


**Figure 7.** Complex shape-changing behavior of shape memory polymer through stress relaxation: a) The sequential shape-changing behavior of a SMP coated with different dyes, which activate the shape-changing behavior using photothermal effect, Reproduced with permission.<sup>[108]</sup> Copyright 2017, American Association for the Advancement of Science; b) the oscillation of the shape of a multiple SMP-metal composite is observed in presence of constant electric field (a sinusoid AC voltage of 3.7 V initial amplitude and 1 Hz frequency) and with varying temperature, Reproduced under the terms and conditions of the Creative Commons CC by 4.0 license.<sup>[110]</sup> Copyright 2016, Springer Nature; c) the active layer of SMP sandwich between two inactive layers of paper folds perpendicular to the  $p$  until the sides of the two-layer touches with each other i). The self-folding behavior of a trilayer structure due to the contraction of SMP layer on activation ii), Reproduced with permission<sup>[111]</sup> Copyright 2014, Institute of Physics Publishing; d) the thermo and photo reversible bonding triggers the complex 2D to 3D shape transformation in a SMP. Reproduced with permission.<sup>[112]</sup> Copyright 2018, American Association for the Advancement of Science.

trilayer structure when the top and bottom layers do not swell, and the middle layer is a stimuli-responsive hydrogel. Bending to one or another side can be achieved when either top or passive bottom layers are missing. The patterned sheet developed by Hayward and his co-worker using pendent benzophenone containing poly(*N*-isopropyl acrylamide) copolymers showing self-actuating behavior on changing temperature (Figure 8b). The heating (49 °C) induced deswelling, recover the flat shape while cooling (22 °C) induced swelling helps to obtain the initial hybrid shape.<sup>[115]</sup> Figure 8c describes the folding behavior of the trilayers structure in which the active hydrogel layer is

sandwiched in between two passive layers, and the small gaps in the upper or lower side help the trilayer structure to bend in one or other side. The photo-crosslinkable trilayer pattern structure developed by Na et al. shows reversible complex shape-changing behavior utilizing temperature-dependent swelling/deswelling behavior of the active hydrogel layer.<sup>[116]</sup> Another way of achieving folding behavior is to use the swelling pathways, which are determined by the shape of the film, as observed in Figure 8d. In which, a six-ray star-like bilayer structure of poly(*N*-isopropyl acrylamide-co-acrylic acid) (P(NIPAM-AA) and poly-(methyl methacrylate) (PMMA) shows complex

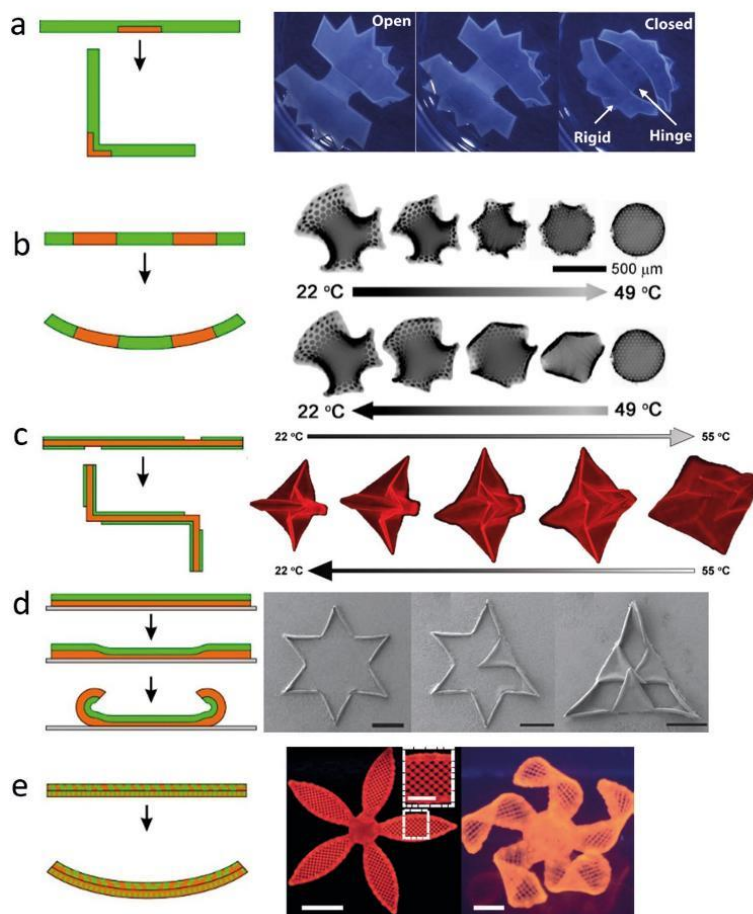


**Figure 8.** Various strategies to introduce complex shape changing in polymers by using structure: a) pattern bilayer: reversible actuation of “Venus Flytrap” shape of bilayer hydrogel of poly (*N*-isopropylacrylamide-co-acrylic acid)/poly(ethylene oxide) diacrylate (NIPAM-AAc/PEODA) with pH change, Reproduced with permission.<sup>[114]</sup> Copyright 2010, Elsevier; b) patterned film: reversible shape-changing behavior of hydrogel of pendent benzophenone containing poly(*N*-isopropyl acrylamide) copolymers. The heating induced deswelling helps to get the flat structure while cooling induced swelling produces the initial structure, Reproduced with permission.<sup>[115]</sup> Copyright 2012, American Association for the Advancement of Science; c) the heating leads to deswelling and cooling induced swelling of photo crosslinkable trilayer pattern structure triggers the reversible self-folding phenomenon, Reproduced with permission.<sup>[116]</sup> Copyright 2015, Wiley-VCH; d) self-folding behavior of a star shape bilayer structure through the edge activation, Reproduced with permission.<sup>[117]</sup> Copyright 2013, Wiley-VCH; e) the complex changing behavior due to anisotropic swelling behavior of composite. Reproduced with permission.<sup>[95]</sup> Copyright 2016, Springer Nature.

multistep folding through edge activation.<sup>[117]</sup> Further, the introduction of anisotropic volume expansion using either fibers or platelets can produce complex shape changing in a material (Figure 8e).<sup>[118]</sup> Gladman et al. reported the complex shape-changing behavior of a polymer composite due to anisotropic swelling behavior. The processing induced alignment of the cellulose fibrils controls the swelling of the composite and results in complex 3D morphologies in the presence of the stimulus.<sup>[95]</sup> The extent of bending depends on the elastic modulus, swelling ratio, thickness ratio of the layers ( $m = a_{\text{bottom}}/a_{\text{top}}$ ), and the

total thickness of the bilayer ( $h = a_{\text{top}} + a_{\text{bottom}}$ ). The mean and Gaussian curvatures scale, respectively

$$H = c_1 \frac{\alpha_{\parallel} - \alpha_{\perp}}{h} \frac{\sin^2 \theta}{c_2 - c_3 \cos 2\theta + m^4 \cos 4\theta} \quad \text{and} \quad (3)$$

$$G = c_4 \frac{(\alpha_{\parallel} - \alpha_{\perp})^2}{h^2} \frac{\sin^2 \theta}{c_5 - c_6 \cos 2\theta + m^4 \cos 4\theta}$$

where, the  $c_1, c_2, c_3, \dots$  etc. are the elastic constants that are assigned by their swollen equilibrium value. Hence, there are

variety of possibilities to produce complex shape-changing behavior in hydrogel-based systems.

### 3.3. Complex Deformation of Shape-Changing Polymers with the Nonuniform Strain (Liquid Crystal Elastomers)

Complex shape-changing behavior in liquid crystal elastomers can be attained either through in-depth or/in-plane variation of molecular orientation<sup>[119–124]</sup> or by using photoresponsive mesogens, which are capable of deforming upon irradiation with light.<sup>[125,126]</sup> Hence, folding in liquid crystal elastomers can be controlled by organized irradiation with light and by controlling the distribution of molecular directors. van Oosten et al. reported complex shape-changing behavior in an LCE containing two different dyes (A3MA and DR1A).<sup>[119]</sup> It is explored that the self-organization and anisotropic orientation of mesogens controlling complex folding. According to Figure 9a(i), a gradual change in the orientation of the mesogen units with the thickness of the materials, a parallel orientation in the top

to a perpendicular orientation at the bottom with respect to the substrate at bottom. This type of splayed molecular orientation is controlling not only the folding direction but also the axis of folding of the film. Different complex folding is achieved using varying compositions of the two dyes and using the light of different wavelengths and different compositions. (Figure 9a(ii)) In the dark, no folding is observed, but in the presence of ultraviolet light, the yellow part responsible for A3MA dye starts bending. At the same time, the red part responsible for DR1A dye remains unbent. Again, in the presence of visible light, the reverse phenomenon is observed; the red part starts bending while the yellow part remains unbent. Finally, in the presence of both UV and visible light, a flap bending throughout the length is observed because of the simultaneous absorption of light by the DR1A at 360 nm and A3AM at 440 nm. So, the switching between these four states in the presence of different light generates cilia motion. Haan et al. introduced complex shape-changing behavior in LCEs through the developed of series 3D patterned structure of liquid crystal units. In the presence of appropriate stimuli such as pH or temperature, an

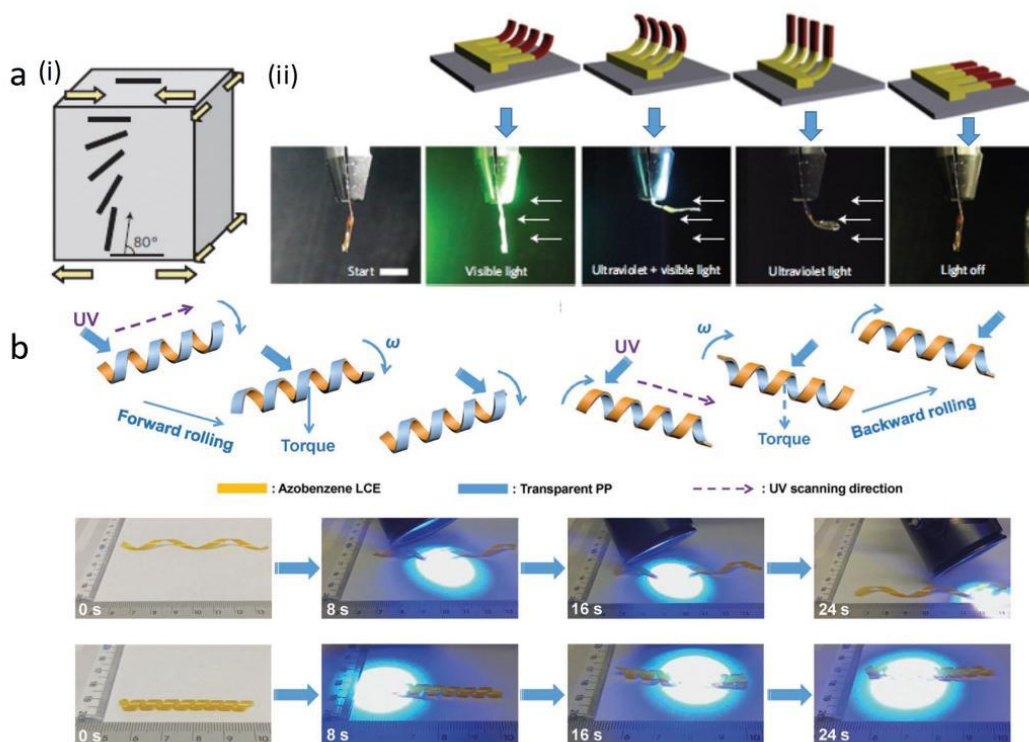


**Figure 9.** Complex shape changing due to nonuniform strain: a) The orientation of the liquid crystal units gradually changes from top to bottom in the LCE film i); The extent of bending of the film in the presence of different wavelength of light. The A3AM dye-containing yellow part bends in the presence of ultraviolet rays while the DR1A containing the red part of the film bends in the presence of visible light. A cilia motion is observed in the film on the simultaneous application of a different source of light ii), Reproduced with permission.<sup>[119]</sup> Copyright 2009, Springer Nature; b) forward and backward rolling motion of a spring-like motor, made of LCE inner side and outer side, respectively, due to the torque produced by structured irradiation with UV-light. Reproduced with permission.<sup>[125]</sup> Copyright 2017, Wiley-VCH.

accordion-like deformation can be achieved in a striped shape selecting the appropriate composition of the reactive mesogen mixture. A large deformation can be achieved through this type of out of plane shape changing by contracting a monodomain sample with the uniform nematic director.<sup>[124]</sup> A novel strategy has been introduced by Lu et al. to improve complex shape-changing behavior in LCEs by enhancing the photoinduced mechanical force.<sup>[125]</sup> The basic idea is to store the mechanical energy in the polymer backbone through deformation (such as stretching or twisting) and use that stored energy during the light-induced shape transformation. The irradiation with light not only produces mechanical force through the direct light to mechanical energy conversion upon *cis-trans* photo isomerization of the azobenzene liquid crystal unit as well as activate the release of the prestored deformation energy. The combination of these two forces helps in producing wheels or spring-like motors, as observed in Figure 9b. The motion in a spring-like motor is generated through the production of UV light-induced torque, while forward or backward direction of the motion depends on the processing of the bilayer structure of BOPP and LCE. When the LCE layer is in the upper side of the ribbon backward movement takes place while it is in the inner side of the ribbon reverse movement takes place.

#### 4. Application of Shape-Transforming Soft Materials

Depending on shape-transforming material type, the principle of transformation and stimuli, these materials can be used in various fields like smart textiles, tissue engineering, soft robotics, microfluidics, sensors, drug delivery, optical devices, and electronic devices (Figure 10). All applications can be divided into several groups. Mechanical actuators and soft robotic systems belong to the first group and relay of both amplitudes of deformation and force generated during deformation (described by stroke-force dependence). Some applications utilize shape transformation to affect other properties. Examples of such applications are lenses (focal length is changed) and smart textiles (appearance and heat exchanges are changed). The third group of applications utilizes shape transformation to generate shapes, which otherwise are not possible or difficult to achieve. An example of such kind of application is tissue engineering.

##### 4.1. Stroke-Force Dependence

###### 4.1.1. Soft Robotics

Soft robotics is one of the fastest-growing fields of application for shape-transforming materials. In comparison to metal-based hard materials, soft materials offer multifunctionality and reconfigurability.<sup>[127]</sup> The use of soft materials in robotics, allow us to access small inaccessible regions, to manipulate delicate objects, and to have safe interactions with robotic design system.<sup>[128]</sup> Shape transforming soft materials are even more interesting for soft robotics applications than other soft materials, due to their shape change there is limited need for hydraulic or pneumatic pumps to actuate and induce the motion in the system. Shape transforming materials have

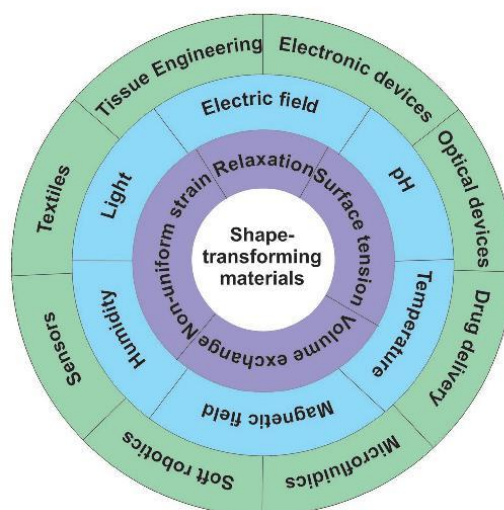
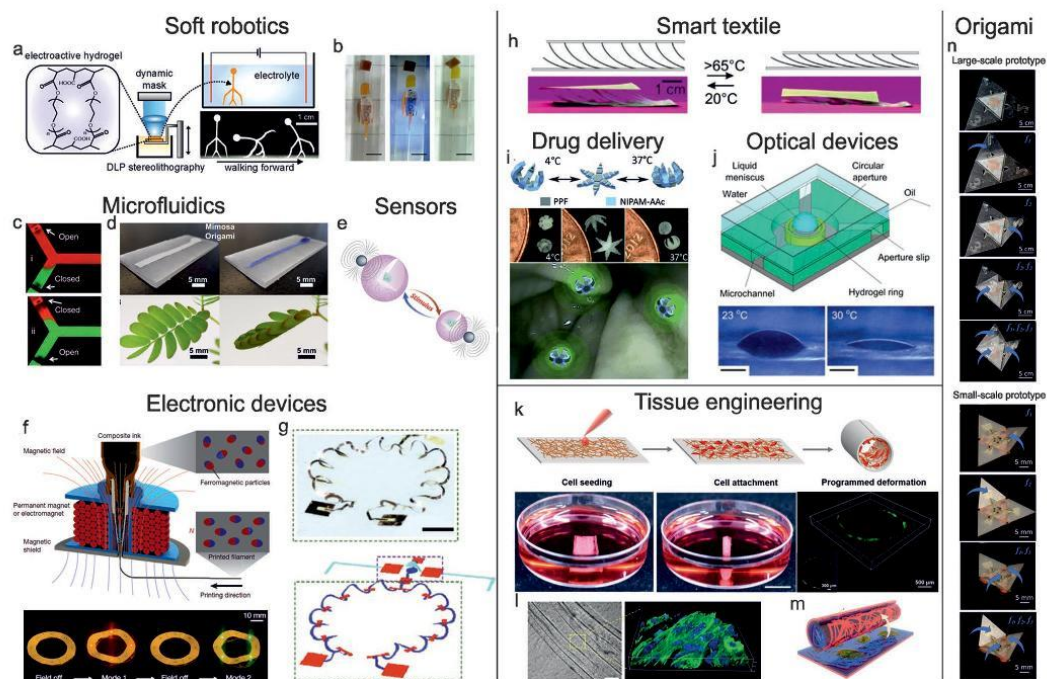


Figure 10. Scheme showing the shape-transforming soft material principle of transformation, stimuli, and applications.

showed that with proper design they can achieve such bio-inspired locomotions as walking, jumping and swimming, which are solely based on their shape-changing characteristics.<sup>[129]</sup> As an example, Han et al. designed electroactive hydrogels that by changing the electric field was able to grip and transport objects and do bidirectional locomotion<sup>[130]</sup> (Figure 11a). By using digital light processing (DLP) based micro 3D printing technique, they were able to get various size 3D structures with high resolution, fast actuation and ease control. These kinds of hydrogels have the potential to be used as actuating material for artificial muscle design and soft robotics. Though there is one problem with this kind of soft robot, the electric field is required. One option to solve this issue and prepare wireless actuator that is controlled by using light. Huang et al. described light driven liquid-crystal soft robotic system where UV light and white light works as “power and signal lines”<sup>[131]</sup> (Figure 11b). Liquid crystal film was able to achieve shape transformation with light due to azobenzene molecules that are included in the film, with UV irradiation azobenzene molecules switch from *cis* to *trans* isomer that changes the length of molecule and induces bending of the film. The prepared soft robot was able to swim in water and carry loads. Light driven soft robots have potential to be used in micro machines and robotics.

###### 4.1.2. Microfluidics

Fluid manipulation in channels with dimensions of tens of micrometers is called microfluidics; this field is constantly growing as it could improve various fields: chemical synthesis, biological analysis, optics, information technology, etc.<sup>[132]</sup> Microfluidic devices by itself is usually small in scale, whereas their



**Figure 11.** Overview of different application of shape-transforming soft materials: a) 3D printed electroactive hydrogel soft robotic manipulation and locomotion. Adapted with permission.<sup>[130]</sup> Copyright 2018, American Chemical Society; b) miniaturized swimming soft robot controlled by remote light signals. Scale bar 3 mm. Adapted with permission.<sup>[131]</sup> Reproduced under the terms and conditions of the Creative Commons CC BY 4.0 license.<sup>[131]</sup> Copyright 2015, Springer Nature; c) microfluidic actuators based on temperature-responsive PNIPAM hydrogels. Adapted with permission.<sup>[133]</sup> Adapted under the terms and conditions of the Creative Commons CC BY 4.0 License.<sup>[133]</sup> Copyright 2018, Springer Nature; d) Mimosa origami: self-organization of a rectangular-shaped Janus bilayer. Adapted with permission.<sup>[134]</sup> Copyright 2016, American Association for the Advancement of Science; e) hybrid sensor with temperature-responsive PNIPAM hydrogel as a spacing transducer. Adapted with permission.<sup>[138]</sup> Reproduced under the terms and conditions of the Creative Commons CC BY 4.0 license.<sup>[138]</sup> Copyright 2018, Springer Nature; f) 3D printed soft materials with programmed ferromagnetic domains. Adapted with permission.<sup>[139]</sup> Copyright 2018, Springer Nature; g) 3D morphable mesostructures for microelectronic devices. Adapted with permission.<sup>[140]</sup> Copyright 2018, Springer Nature; h) structures with switchable thickness based on Janus fibers for smart textile application. Adapted with permission.<sup>[144]</sup> Copyright 2017, American Chemical Society; i) stimuli-responsive theragripers for chemomechanical-controlled drug release. Adapted with permission.<sup>[150]</sup> Copyright 2014, Wiley-VCH; j) smart optical lenses with tunable focal lengths based on PNIPAM hydrogel. Adapted with permission.<sup>[153]</sup> Copyright 2006, Springer Nature; k) shape morphing scaffolds for 3D endothelialization, photographs showing the temporary planar shapes (25 °C) and the permanent shapes (37 °C). Scale bar 1 cm., 3D tubular organization of HUVECs on the bilayer in permanent tubular shape (green color, stained by Calcein AM) cultured. Adapted with permission.<sup>[158]</sup> Copyright 2018, Wiley-VCH; l) bright-field image taken after 10 d of incubation of C2C12 cells in the internal part of the PEGDA tube and the 3D reconstructed confocal image of the partially aligned cells. Green and blue colors represent the cytoskeleton and cell nuclei, respectively. Adapted with permission.<sup>[159]</sup> Copyright 2018, Wiley-VCH; m) 4D biofabrication of porous tubular PCL/PNIPAM scaffolds. Adapted with permission.<sup>[160]</sup> Copyright 2017, American Chemical Society; n) Wireless folding of multijoint robots. Adapted with permission.<sup>[163]</sup> Copyright 2017, The American Association for the Advancement of Science.

equipment that is required to control the device could be large (pumps, valves, mixing units). Due to shape-changing properties and force that is generated during actuation, shape-transforming materials are well suited for valve preparation in microfluidic channels. For example, recently D'Eramo has shown the potential to use temperature-responsive hydrogel as poly(*N*-isopropylacrylamide) (PNIPAM) for microfluidic valves<sup>[133]</sup> (Figure 11c). At 40 °C (above LCST), PNIPAM hydrogel shrinks, but in the room temperature, hydrogel swells, closing the valve in this case. They have prepared 780 microcages, were able to open and close in 250 and 600 ms, respectively. They were able to

use these cages for single-cell handling and the nuclear acid amplification test (NAAT), which proves systems functionality for microfluidics. Another interesting approach is to fabricate stimuli-responsive microchannels that can be open and closed, used for bulb mixing, and can form U, T- junctions described by Wong et al.<sup>[134]</sup> (Figure 11d). They prepared electrospun Janus bilayers from polyvinyl chloride (PVC) and PCL, which mimicked *Mimosa pudica* opening and closing. They showed the possible design of complex microchannel fabrication and as well they were able to achieve high flow rates (4.7  $\mu\text{L s}^{-1}$ ) that are two orders of magnitude higher than traditional wicking-based

devices. These both approaches show the future possibility to fully design microfluidic device from fast, responsive shape transforming soft materials.

#### 4.1.3. Sensors

Fast response time, various stimuli, and macroscopic shape change are assets of shape transforming soft materials that make them attractive for sensor development. Shape transforming materials like hydrogels can respond to stimuli like temperature, pH, specific ions, and chemicals, which makes them suitable for sensing. Usually, atomic force microscope (AFM) cantilevers are used to make hydrogel-based sensors; one side of the cantilever is covered with hydrogel layer, and AFM cantilever bends accordingly to the swelling state of hydrogel.<sup>[135–137]</sup> The bending of the cantilever can be detected by a change in reflection of the laser beam of the cantilever surface. This kind of sensing method is simple and easy to use; any AFM device can be used for this method. Zhang et al. described more advance sensing by using stimuli-responsive hydrogel as a spacing transducer in-between nanodiamond and magnetic nanoparticles<sup>[138]</sup> (Figure 11e). The use of nanodiamond center-based magnetometry provides the ability to use the system for quantum biosensing, but unfortunately, they are unable to sense parameters like pressure and temperature and can be influenced by parameters like pH and nonmagnetic biomolecules. As a solution to these problems, they use hydrogel that fully covers nanodiamond, and then they docked magnetic nanoparticles on top of the hydrogel shell. Due to hydrogel swelling and shrinking, there is a sharp variation in the separation distance of diamond and nanoparticles, which makes a change in the magnetic field, and these changes can be detected easily by nanodiamond center. The hybrid sensor showed reversibility and stability for more than one week and higher sensibility than nanodiamond alone in the same conditions. With proper design and this hybrid system can be used for sensing other physiological parameters: pH, enzymes, sugar, and other types of nonmagnetic biomolecules.

#### 4.1.4. Electronic Devices

Shape transforming soft materials can be used in electronic devices because of their ability to change the form as well generate the force as mentioned before. For example, Kim et al. have designed 3D printed soft materials that contain programmed ferromagnetic domains that were able to exhibit electric functions<sup>[139]</sup> (Figure 11f). These ferromagnetic domains were printed using composite ink of magnetizable particles, fumed silica particles, and rated silicone rubber matrix. During 3D printing, they applied a magnetic field to the dispensing nozzle to align the magnetic particle in ferromagnetic domains. When the magnetic field is applied to the printed substrate, it induces torques on the embedded ferromagnetic particles forming stresses that lead to macroscale material response. To test designed structure ability to be used as flexible electronics, they added components like PDMS insulator, conductive silver ink, magnetic ink, and two-color LEDs. By changing magnetic field direction, they were

able to switch on red or green LED, depending on magnetic particle arrangement in the ferromagnetic domain. This platform can be further examined with various elastomer and hydrogel matrices as well as the change of magnetic particles. Rodgers and their group have been working on various shape-transforming electronic devices.<sup>[140–142]</sup> Their latest research describes microelectronic devices that can be actuated by multistable buckling mechanics<sup>[140]</sup> (Figure 11g). Prepared mesostructures could be reconfigured in three to four different states, showing their versatility. To show the potential of using these shape transforming materials for electronic devices, they integrated silicon n-channel metal-oxide-semiconductor field-effect transistors (n-MOSFET) and  $\mu$ -LEDs on top of 3D mesostructure. To show potential for wireless communication of these microelectronic devices, they used passive radiofrequency circuits and concealable antennas.

## 4.2. Shape Transformation Affect Material Properties

### 4.2.1. Smart Textiles

Smart textile is a promising application for shape memory polymers (SMPs). Smart textiles can be designed by using single actuating SMPs fibers that are incorporated in textiles; this single fiber actuates with the change of humidity and/or temperature, which leads to shrinking and folding of the whole textile. This concept has been shown by designer Leenders using a hairdryer and incorporating nitinol fiber inside of textile, with increase and decrease of the temperature sleeves of textile can be rolled up or down.<sup>[143]</sup>

As another option, we described the method of producing non-crosslinked shape-transforming Janus fibers for smart textile applications.<sup>[144]</sup> 3D printing and melt-spinning were used to obtain Janus fibers consisting of fusible PCL as first polymer and acrylonitrile butadiene styrene (ABS) or polylactide (PLA) as the second polymer. ABS and PLA were chosen as the second polymer because of their high softening point (Figure 11h). This Janus fiber model was able to show reversible actuation due to the contraction of PCL polymer in the presence of entanglements during crystallization and relaxation of stressed nonfusible side during melting. Design fibers demonstrate various advantages in comparison to existing smart fibers like fast actuation rate, reversible actuation, actuation temperature range from 0–70 °C, and high plasticity for repair when the fiber is deformed or broken.

### 4.2.2. Drug Delivery

The main challenge of drug delivery is to transfer the necessary concentration of drugs to the intended site of action. As high doses are necessary in most cases, there is a high risk of potential side effects and reduced efficiency when the drug is absorbed in various parts of the human body and cannot reach the intended site.<sup>[128,145–147]</sup> As a solution to this problem, scientists are working on multiple systems that could reach the intended site in a controlled manner and could release drugs based on specific environmental cues.<sup>[148]</sup> Shape transforming

soft materials can be used for drug encapsulation and can be controlled by adding or removing stimuli, thus being a good model for targeted drug delivery. Nevertheless, drug release depends on the surface to volume ratio, which makes changes of the surface to volume ratio during swelling of stimuli-responsive material especially interesting for drug delivery.<sup>[7,149]</sup> Gracias and his group have designed stimuli-responsive theragrippers for chemomechanical-controlled release of fluorescent dyes and commercial drugs like mesalamine and doxorubicin<sup>[150]</sup> (Figure 11i). They used photolithography to design theragrippers that consisted of rigid poly(propylene fumarate) segments and stimuli-responsive poly(N-isopropylacrylamide-co-acrylic acid) hinges. Due to thermos-responsive hinges, gripper closes above 32 °C temperature allowing it to grip onto tissue when it reaches body temperature from a cold state. Theragrippers showed improved site-specific delivery and time-tunable drug release, making it suitable for applicability in the gastrointestinal tract.

#### 4.2.3. Optical Devices

Micro lenses with tunable focal length can be designed using stimuli-responsive hydrogels. In this case, focal length depends on particle size, which changes with the swelling degree of hydrogel after external stimuli are added to the system.<sup>[29,151,152]</sup> Another approach describes water–oil interface liquid micro lenses that are mounted on a ring formed by macroscopic stimuli-responsive hydrogel<sup>[153]</sup> (Figure 11j). When appropriate stimuli were added to the system, the hydrogel ring underneath the aperture expanded or shrunk. The actuation of hydrogel induces volume change of water droplet in the middle of the ring. Variations of the volume enclosed by the ring and volume of the water droplet generate pressure difference across the water–oil interface that regulates the geometry of the liquid meniscus. These lenses showed a fast response rate and did not require a complicated external control system.

### 4.3. Shape Generation During Transformation

#### 4.3.1. Tissue Engineering

While the world's populations are increasing and aging, scientists have focused on tissue engineering field to solve the challenge of organ and tissue shortage and provide a new treatment for patients.<sup>[7,128,154]</sup> Using tissue-engineering techniques, we can replace, preserve and regenerate different tissues and organs.<sup>[128,154,155]</sup> Material ability to transform its shape is promising for the field of tissue engineering; because of dynamic shape change, we would be able to achieve less invasive surgical procedures.<sup>[156]</sup> Shape-transforming soft materials can be used for various tissue regeneration as cardiac, bone, skeletal, vascular and endothelial.<sup>[7,157]</sup>

An important feature for shape transformation soft materials is their easy and reversible transformation from flat 2D sheet to the 3D tubular structure. This approach is crucial for tubular human tissue formation like skeletal muscle bundles, ves-

sels, and arteries, osteons, axons, etc. For example, Zhao et al. described shape morphing scaffolds for 3D endothelialization, where they co-electrospun functional polycaprolactone (PCL) and methacrylated gelatin (GelMA) layer on top of biocompatible shaping SMPs film for better cell adhesion<sup>[158]</sup> (Figure 11k). Endothelial cells showed high seeding efficiency and cell viability on shape morphing constructs that were able to perform shape transformation in physiological temperature. These tubular structures showed potential for small diameter vascular graft formation with improved endothelialization. Similarly Vannozzi et al.<sup>[159]</sup> (Figure 11l), showed the potential of using poly(ethylene glycol) diacrylate (PEGDA) bilayers for implantable fascicle-like muscle cell fabrication. Two different molecular weight PEGDA was used to achieve and control folding behavior, based on each layer thickness. Cardiac and muscle cells exhibited high cell viability and preserved their contractile function. As well, electrospun bilayers with no supportive layer had showed potential to be used in tissue engineering for cell encapsulation. Apsite et al. designed multilayer electrospun mesh system consisting of PCL and PNIPAM, that can self-fold in physiological conditions and sustain cell viability<sup>[160]</sup> (Figure 11m).

#### 4.3.2. Shape-Transforming Origami

Term Origami is used to describe folding paper art coming from Japan, where a 2D flat sheet is folded in various complex 3D structures like crane, rhino, and various other animals. Following simple axioms and theorems it is possible to fold any soft or rigid material, which makes this principle more attractive to industrial applications as solar panels, space telescopes, stents for medical purposes, high tech origami, grocery bags, vacuumatics, programmable matter folding.<sup>[161]</sup> Shape transforming has been widely used for development of foldable devices. R. Wood and his group have developed wireless multijoint folding robots based on shape memory polymer origami-based foldable robot that was able to self-fold, actuate and even degrade in acetone or water.<sup>[162]</sup> Origami robot was thermally activated and due to cubic neodymium magnet that was incorporated in polystyrene robot, they were able to control direction of locomotion using magnetic field. These kinds of origami-based complex 3D structures can be in future used in vivo. In most recent research, they prepared device that was based on electromagnetic power transmission and resonance selectivity<sup>[163]</sup> (Figure 11n). They achieve folding using magnetically active shape memory alloy (SMA) actuator as the electrical load, which does not require any physical contact and allows to actuate each SMA individually or in groups. The advantage of this method is that you can prepare robotic systems small weight like 0.8 g and still have high energy density.

## 5. Summary and Outlook

There is considerable progress in the development of materials with shape-changing properties as well as in understanding and programming of shape transformation that allows a broad variety in shapes. The controlled shape transformation can be

utilized for diverse applications including soft robotics, microfluidics, sensory, electronic devices, smart textiles, drug delivery, optical devices, tissue engineering. In spite of significant prepared progress in all these areas, properties of available materials are not always optimal from point of view of particular applications. For example, shape transformation requires high mobility of polymer chains and is observed above melting/glass transition point. Moreover, reversibility of actuation requires crosslinking of polymers. In other words, polymers have properties of elastomer in the state when they actuate. Elastic modulus of elastomer depends on crosslinking density and typically is in the order of megapascals. Crosslinking density is even lower in swollen elastomers (gels), and therefore, they are even softer. The force generated during the actuation of shape-changing polymers is roughly elastic modulus multiplied by actuation amplitude. This force is usually much lower than the force generated by hard motors/actuators. Therefore, shape-changing polymers are unable to compete with classic motor-based actuators in conventional robotics. On the other hand, due to their softness, shape-changing polymers have distinct advantages in the “soft” applications such as soft robotics, tissue engineering, flexible optics, where “hard” actuators cannot be applied. Moreover, due to their softness, shape-changing polymers allow considerable amplitude of shape transformation at lower absorbed energy. Although basic principles of application of shape-changing polymers in these fields have been successfully demonstrated, their practical application is still problematic because each of these “soft” applications put new requirements for properties of materials. For example, optical devices may require either high transparency of polymers or their special optical properties. Bio-related applications like tissue engineering and drug delivery require biocompatible and biodegradable shape-changing polymers, which are also able to change their shape at the conditions acceptable for living matter. Thus, the first open problem is the precise tailoring of the properties of shape-changing polymers.

The second problem is the weakness of the materials. Shape transformation is often accompanied by considerable local deformations, which may lead to rupture of materials. Therefore, the development of self-healing shape-changing materials can be one of the future directions of development. Although the task may look simple because there are many approaches for the design of self-healing materials, the real solution for this problem is difficult. In fact, the self-healing of cracks is commonly based on the interdiffusion of chain segments and the reversibility of bonds. Both these processes assume plastic deformation of materials, i.e., actuator will undergo not pure elastic but visco-elastic deformation and reversibility of actuation will not be complete.

The third big challenge in the field of microfabrication using controlled shape transformation is miniaturization. Fabrication of micrometer—size shape-changing structures is a multistep procedure, which is very expensive and requires the use of sophisticated equipment. Recently, 3D printing became very popular for fabrication shape-changing structures that have even led to the development of the new area in 3D printing—4D printing. There are several most widely used 3D printing techniques, but no one of them allows the fabrication of microstructures at low costs. Indeed, fused deposition modeling (FDM) printing allows fabrication of multicomponent structures,

but its resolution is ca 100–200  $\mu\text{m}$ . Stereolithography allows a much better resolution, which is ca 10  $\mu\text{m}$ , it can hardly be used for fabrication of multicomponent objects as it requires a constant exchange of photopolymer. Ink-jet printing and similar drop-based technologies allow high resolution but operate with low viscosity liquids such as oligomer/monomer solution, which have to be photopolymerized afterward. Melt electrospinning writing is a very interesting method for the fabrication of very fine structures from viscous polymer melts. This method is however based on the deposition of continuous fibers and fabrication of dots and discrete elements not possible. All this means that currently a combination of different 3D printing methods is needed for microfabrication of shape-changing structures.

Forth challenge related to microfabrication is the precise programming of shape transformation. There are brilliant works<sup>[164,165]</sup> demonstrating impressive possibilities to program the folding, there are still unsolved problems related to stability, reversibility, and possibilities to reprogram the folding. For example, there is no report about a shape-changing material which allows full flexibility of folding when (i) the same film can be folded and unfolded in a variety of ways and (ii) there is a possibility to decide if folding is reversible or irreversible, that must allow fixation of folded structures. The reason for these effects is the intrinsic properties of individual shape-changing materials. As an illustration, the hydrogel-based shape-changing film can fold in various ways depending on their structure. On the other hand, as soon as stimuli are removed the shape of folded objects changes. The same happens when the hydrogel layer dries.

In summary, the microfabrication using shape-changing polymers is a rapidly developing field, and many new excellent works are published on this topic each day. Despite this, there are still many problems to be solved before microfabrication using shape-changing polymers became real technology.

## Acknowledgements

I.A. and A.B. contributed equally to this work. L.I. is thankful to DFG (grants IO 68/10-1 and 68/11-1) for financial support.

## Conflict of Interest

The authors declare no conflict of interest.

## Keywords

applications, principles, shape-changing materials

Received: September 28, 2019

Revised: November 18, 2019

Published online:

- [1] S. Ford, T. Minshall, *Addit. Manuf.* **2019**, *25*, 131.
- [2] T. D. Ngo, A. Kashani, G. Imbalzano, K. T. Q. Nguyen, D. Hui, *Composites, Part B* **2018**, *143*, 172.
- [3] Y. Zhou, *J. Biomed. Sci.* **2017**, *24*, 80.

- [4] A. Lendlein, S. Kelch, *Angew. Chem., Int. Ed.* **2002**, *41*, 2034.  
 [5] Q. Zhao, M. Behl, A. Lendlein, *Soft Matter* **2013**, *9*, 1744.  
 [6] M. Behl, J. Zotzmann, A. Lendlein, *Adv. Polym. Sci.* **2010**, *226*, 1.  
 [7] A. Kirillova, L. Ionov, *J. Mater. Chem. B* **2019**, *7*, 1597.  
 [8] Q. Zhao, H. J. Qi, T. Xie, *Prog. Polym. Sci.* **2015**, *49–50*, 79.  
 [9] A. Biswas, A. P. Singh, D. Rana, V. K. Aswal, P. Maiti, *Nanoscale* **2018**, *10*, 9917.  
 [10] J. Dong, R. A. Weiss, *Macromolecules* **2011**, *44*, 8871.  
 [11] R. Dolog, R. A. Weiss, *Macromolecules* **2013**, *46*, 7845.  
 [12] A. Biswas, V. K. Aswal, P. Maiti, *J. Colloid Interface Sci.* **2019**, *556*, 147.  
 [13] H. Tobushi, N. Ito, K. Takata, S. Hayashi, *Mater. Sci. Forum* **2000**, *327–328*, 343.  
 [14] H. Tobushi, T. Hashimoto, S. Hayashi, E. Yamada, *J. Intell. Mater. Syst. Struct.* **1997**, *8*, 711.  
 [15] T. D. Nguyen, H. J. Qi, F. Castro, K. N. Long, *J. Mech. Phys. Solids* **2008**, *56*, 2792.  
 [16] A. D. Mulliken, M. C. Boyce, *Int. J. Solids Struct.* **2006**, *43*, 1331.  
 [17] J. Zhou, Q. X. Li, S. A. Turner, V. S. Ashby, S. S. Sheiko, *Polymer* **2015**, *72*, 464.  
 [18] C. A. Avila-Orta, F. J. Medellin-Rodriguez, Z. G. Wang, D. Navarro-Rodriguez, B. S. Hsiao, F. J. Yeh, *Polymer* **2003**, *44*, 1527.  
 [19] M. Behl, K. Kratz, U. Noechel, T. Sauter, A. Lendlein, *Proc. Natl. Acad. Sci. USA* **2013**, *110*, 12555.  
 [20] A. Biswas, V. K. Aswal, P. U. Sastry, D. Rana, P. Maiti, *Macromolecules* **2016**, *49*, 4889.  
 [21] R. Pelrine, R. Kornbluh, Q. B. Pei, J. Joseph, *Science* **2000**, *287*, 836.  
 [22] F. Carpi, D. De Rossi, *Mater. Sci. Eng., C* **2004**, *24*, 555.  
 [23] F. Carpi, C. Salaris, D. De Rossi, *Smart Mater. Struct.* **2007**, *16*, S300.  
 [24] S. Shian, K. Bertoldi, D. R. Clarke, *Adv. Mater.* **2015**, *27*, 6814.  
 [25] S. Shian, R. M. Diebold, D. R. Clarke, *Opt. Express* **2013**, *21*, 8669.  
 [26] E. Hajiesmaili, D. R. Clarke, *Nat. Commun.* **2019**, *10*, 183.  
 [27] Y. Osada, A. Matsuda, *Nature* **1995**, *376*, 219.  
 [28] C. C. Wang, W. M. Huang, Z. Ding, Y. Zhao, H. Purnawali, *Compos. Sci. Technol.* **2012**, *72*, 1178.  
 [29] L. Ionov, *Mater. Today* **2014**, *17*, 494.  
 [30] K. Inomata, T. Terahama, R. Sekoguchi, T. Ito, H. Sugimoto, E. Nakanishi, *Polymer* **2012**, *53*, 3281.  
 [31] A. Yasin, H. Z. Li, Z. Lu, S. U. Rehman, M. Siddiq, H. Y. Yang, *Soft Matter* **2014**, *10*, 972.  
 [32] R. D. Harris, J. T. Auletta, S. A. M. Motlagh, M. J. Lawless, N. M. Perri, S. Saxena, L. M. Weiland, D. H. Waldeck, W. W. Clark, T. Y. Meyer, *ACS Macro Lett.* **2013**, *2*, 1095.  
 [33] X.-J. Han, Z.-Q. Dong, M.-M. Fan, Y. Liu, J.-H. Li, Y.-F. Wang, Q.-J. Yuan, B.-J. Li, S. Zhang, *Macromol. Rapid Commun.* **2012**, *33*, 1055.  
 [34] O. Peters, H. Ritter, *Angew. Chem., Int. Ed.* **2013**, *52*, 8961.  
 [35] Z.-Q. Dong, Y. Cao, Q.-J. Yuan, Y.-F. Wang, J.-H. Li, B.-J. Li, S. Zhang, *Macromol. Rapid Commun.* **2013**, *34*, 867.  
 [36] T. Miyata, N. Asami, T. Urugami, *Nature* **1999**, *399*, 766.  
 [37] H. R. Brand, H. Pleiner, P. Martinoty, *Soft Matter* **2006**, *2*, 182.  
 [38] X. J. Wang, *Prog. Polym. Sci.* **1997**, *22*, 735.  
 [39] D. L. Thomsen, P. Keller, J. Naciri, R. Pink, H. Jeon, D. Shenoy, B. R. Ratna, *Macromolecules* **2001**, *34*, 5868.  
 [40] I. Kundler, H. Finkelmann, *Macromol. Chem. Phys.* **1998**, *199*, 677.  
 [41] J. Naciri, A. Srinivasan, H. Jeon, N. Nikolov, P. Keller, B. R. Ratna, *Macromolecules* **2003**, *36*, 8499.  
 [42] E. M. Terentjev, M. Warner, G. C. Verwey, *J. Phys. II* **1996**, *6*, 1049.  
 [43] P.-G. De Gennes, M. Hébert, R. Kant, *Macromol. Symp.* **1997**, *113*, 39.  
 [44] Z. Pei, Y. Yang, Q. Chen, E. M. Terentjev, Y. Wei, Y. Ji, *Nat. Mater.* **2014**, *13*, 36.  
 [45] T. Ikeda, M. Nakano, Y. Yu, O. Tsutsumi, A. Kanazawa, *Adv. Mater.* **2003**, *15*, 201.  
 [46] M.-H. Li, P. Keller, B. Li, X. Wang, M. Brunet, *Adv. Mater.* **2003**, *15*, 569.  
 [47] Y. Yang, W. Zhan, R. Peng, C. He, X. Pang, D. Shi, T. Jiang, Z. Lin, *Adv. Mater.* **2015**, *27*, 6376.  
 [48] C. Ohm, M. Brehmer, R. Zentel, *Adv. Mater.* **2010**, *22*, 3366.  
 [49] Y. L. Yu, T. Ikeda, *Angew. Chem., Int. Ed.* **2006**, *45*, 5416.  
 [50] M. Behl, K. Kratz, J. Zotzmann, U. Nöchel, A. Lendlein, *Adv. Mater.* **2013**, *25*, 4466.  
 [51] F. Zou, S. Chen, *Mater. Today: Proc.* **2019**, *16*, 1548.  
 [52] M. Boncheva, D. A. Bruzewicz, G. M. Whitesides, *Pure Appl. Chem.* **2003**, *75*, 621.  
 [53] N. Chakrapani, B. Wei, A. Carrillo, P. M. Ajayan, R. S. Kane, *Proc. Natl. Acad. Sci. USA* **2004**, *101*, 4009.  
 [54] N. Bowden, I. S. Choi, B. A. Grzybowski, G. M. Whitesides, *J. Am. Chem. Soc.* **1999**, *121*, 5373.  
 [55] R. Pericet-Cámara, A. Best, H.-J. Butt, E. Bonaccorso, *Langmuir* **2008**, *24*, 10565.  
 [56] A. I. Rusanov, *J. Colloid Interface Sci.* **1978**, *63*, 330.  
 [57] G. R. Lester, *J. Colloid Sci.* **1961**, *16*, 315.  
 [58] B. Roman, J. Bico, *J. Phys.: Condens. Matter.* **2010**, *22*, 493101.  
 [59] X. Guo, H. Li, B. Yeop Ahn, E. B. Duoss, K. J. Hsia, J. A. Lewis, R. G. Nuzzo, *Proc. Natl. Acad. Sci. USA* **2009**, *106*, 20149.  
 [60] X. Xu, A. Jagota, S. Peng, D. Luo, M. Wu, C.-Y. Hui, *Langmuir* **2013**, *29*, 8665.  
 [61] Y. Zhang, Y. Li, W. Liu, *Adv. Funct. Mater.* **2015**, *25*, 471.  
 [62] M. Balk, M. Behl, A. Lendlein, *Smart Mater. Struct.* **2019**, *28*, 055026.  
 [63] Y. C. Zhang, J. X. Liao, T. Wang, W. X. Sun, Z. Tong, *Adv. Funct. Mater.* **2018**, *28*, 1707245.  
 [64] J. Odent, T. J. Wallin, W. Pan, K. Kruemplestaedter, R. F. Shepherd, E. P. Giannelis, *Adv. Funct. Mater.* **2017**, *27*, 1701807.  
 [65] H. Guo, C. Mussault, A. Marcellan, D. Hourdet, N. Sanson, *Macromol. Rapid Commun.* **2017**, *38*, 1700287.  
 [66] R. Luo, J. Wu, N.-D. Dinh, C.-H. Chen, *Biomicrofluidics* **2015**, *25*, 7272.  
 [67] Y. Yang, Y. Tan, X. Wang, W. An, S. Xu, W. Liao, Y. Wang, *ACS Appl. Mater. Interfaces* **2018**, *10*, 7688.  
 [68] T. Wang, J. Huang, Y. Yang, E. Zhang, W. Sun, Z. Tong, *ACS Appl. Mater. Interfaces* **2015**, *7*, 23423.  
 [69] Y. Zhou, J. Tan, D. Chong, X. Wan, J. Zhang, *Adv. Funct. Mater.* **2019**, *29*, 1901202.  
 [70] N. Van Herck, F. E. Du Prez, *Macromolecules* **2018**, *51*, 3405.  
 [71] A. Melocchi, N. Inverardi, M. Uboldi, F. Baldi, A. Maroni, S. Pandini, F. Briatico-Vangosa, L. Zema, A. Gazzaniga, *Int. J. Pharm.* **2019**, *559*, 299.  
 [72] T. Chatterjee, P. Dey, G. B. Nando, K. Naskar, *Polymer* **2015**, *78*, 180.  
 [73] K. J. Wang, X. X. Zhu, *ACS Biomater. Sci. Eng.* **2018**, *4*, 3099.  
 [74] Y. T. Yao, T. Y. Zhou, J. J. Wang, Z. H. Li, H. B. Lu, Y. J. Liu, J. S. Leng, *Composites, Part A* **2016**, *90*, 502.  
 [75] J. Zotzmann, M. Behl, D. Hofmann, A. Lendlein, *Adv. Mater.* **2010**, *22*, 3424.  
 [76] R. Pelrine, R. Kornbluh, Q. B. Pei, J. Joseph, *Science* **2000**, *287*, 836.  
 [77] F. Carpi, D. De Rossi, *Mater. Sci. Eng., C* **2004**, *24*, 555.  
 [78] F. Carpi, C. Salaris, D. D. Rossi, *Smart Mater. Struct.* **2007**, *16*, S300.  
 [79] H. Imamura, K. Kadooka, M. Taya, *Soft Matter* **2017**, *13*, 3440.  
 [80] T.-G. La, G.-K. Lau, L.-L. Shiau, A. W. Y. Tan, *Proc. SPIE* **2014**, *9056*, 90560X.  
 [81] D. J. Roach, C. Yuan, X. Kuang, V. C. F. Li, P. Blake, M. L. Romero, I. Hammel, K. Yu, H. J. Qi, *ACS Appl. Mater. Interfaces* **2019**, *11*, 19514.  
 [82] A. Kotikian, R. L. Truby, J. W. Boley, T. J. White, J. A. Lewis, *Adv. Mater.* **2018**, *30*, 1706164.  
 [83] L. Yu, H. Shahsavan, G. Rivers, C. Zhang, P. X. Si, B. X. Zhao, *Adv. Funct. Mater.* **2018**, *28*, 1802809.  
 [84] B. T. Michal, B. M. McKenzie, S. E. Felder, S. J. Rowan, *Macromolecules* **2015**, *48*, 3239.

- [85] W. Wu, L. M. Yao, T. S. Yang, R. Y. Yin, F. Y. Li, Y. L. Yu, *J. Am. Chem. Soc.* **2011**, *133*, 15810.
- [86] L. Liu, M.-H. Liu, L.-L. Deng, B.-P. Lin, H. Yang, *J. Am. Chem. Soc.* **2017**, *139*, 11333.
- [87] L. Ionov, *Macromol. Chem. Phys.* **2013**, *214*, 1178.
- [88] E. D. Demaine, *Discrete and Computational Geometry*, Springer, Heidelberg **2001**.
- [89] C. Lauff, T. W. Simpson, M. Frecker, Z. Ounaies, S. Ahmed, P. von Lockette, R. Strzelec, R. Sheridan, J.-M. Lien, presented at ASME 2014 Int. Design Engineering Technical Conf. and Computers and Information in Engineering Conf., Buffalo, NY, August **2014**.
- [90] J. Ryu, M. D'Amato, X. Cui, K. N. Long, H. J. Qi, M. L. Dunn, *Appl. Phys. Lett.* **2012**, *100*, 161908.
- [91] Q. Ge, C. K. Dunn, H. J. Qi, M. L. Dunn, *Smart Mater. Struct.* **2014**, *23*, 094007.
- [92] L. Ionov, *Polym. Rev.* **2013**, *53*, 92.
- [93] J. T. Wu, C. Yuan, Z. Ding, M. Isakov, Y. Q. Mao, T. J. Wang, M. L. Dunn, H. J. Qi, *Sci. Rep.* **2016**, *6*, 24224.
- [94] S. Tibbitts, *Archit. Des.* **2014**, *84*, 116.
- [95] A. S. Gladman, E. A. Matsumoto, R. G. Nuzzo, L. Mahadevan, J. A. Lewis, *Nat. Mater.* **2016**, *15*, 413.
- [96] Q. Zhang, K. Zhang, G. Hu, *Sci. Rep.* **2016**, *6*, 22431.
- [97] J. Ryu, M. D'Amato, X. D. Cui, K. N. Long, H. J. Qi, M. L. Dunn, *Appl. Phys. Lett.* **2012**, *100*, 161908.
- [98] S. Armon, H. Aharoni, M. Moshe, E. Sharon, *Soft Matter* **2014**, *10*, 2733.
- [99] S. Janbaz, R. Hedayati, A. A. Zadpoor, *Mater. Horiz.* **2016**, *3*, 536.
- [100] T. van Manen, S. Janbaz, A. A. Zadpoor, *Mater. Today* **2018**, *21*, 144.
- [101] Z. Zhao, J. Wu, X. Mu, H. Chen, H. J. Qi, D. Fang, *Sci. Adv.* **2017**, *3*, e1602326.
- [102] G. F. Hu, A. R. Damanpack, M. Bodaghi, W. H. Liao, *Smart Mater. Struct.* **2017**, *26*, 125023.
- [103] P. Cendula, S. Kiravittaya, Y. F. Mei, C. Deneke, O. G. Schmidt, *Phys. Rev. B* **2009**, *79*, 085429.
- [104] R. Mohr, K. Kratz, T. Weigel, M. Lucka-Gabor, M. Moneke, A. Lendlein, *Proc. Natl. Acad. Sci. USA* **2006**, *103*, 3540.
- [105] H. Y. Jiang, S. Kelch, A. Lendlein, *Adv. Mater.* **2006**, *18*, 1471.
- [106] Y. Liu, J. K. Boyles, J. Genzer, M. D. Dickey, *Soft Matter* **2012**, *8*, 1764.
- [107] A. M. Schmidt, *Macromol. Rapid Commun.* **2006**, *27*, 1168.
- [108] Y. Liu, B. Shaw, M. D. Dickey, J. Genzer, *Sci. Adv.* **2017**, *3*, e1602417.
- [109] D. Habault, H. Zhang, Y. Zhao, *Chem. Soc. Rev.* **2013**, *42*, 7244.
- [110] Q. Shen, S. Trabia, T. Stalbaum, V. Palmre, K. Kim, I.-K. Oh, *Sci. Rep.* **2016**, *6*, 24462.
- [111] M. T. Tolley, S. M. Felton, S. Miyashita, D. Aukes, D. Rus, R. J. Wood, *Smart Mater. Struct.* **2014**, *23*, 094006.
- [112] B. Jin, H. Song, R. Jiang, J. Song, Q. Zhao, T. Xie, *Sci. Adv.* **2018**, *4*, eaao3865.
- [113] T. G. Leong, A. M. Zarafshar, D. H. Gracias, *Small* **2010**, *6*, 792.
- [114] N. Bassik, B. T. Abebe, K. E. Laffin, D. H. Gracias, *Polymer* **2010**, *51*, 6093.
- [115] J. Kim, J. A. Hanna, M. Byun, C. D. Santangelo, R. C. Hayward, *Science* **2012**, *335*, 1201.
- [116] J.-H. Na, A. A. Evans, J. Bae, M. C. Chiappelli, C. D. Santangelo, R. J. Lang, T. C. Hull, R. C. Hayward, *Adv. Mater.* **2015**, *27*, 79.
- [117] G. Stoychev, S. Turcaud, J. W. C. Dunlop, L. Ionov, *Adv. Funct. Mater.* **2013**, *23*, 2295.
- [118] R. M. Erb, J. S. Sander, R. Grisch, A. R. Studart, *Nat. Commun.* **2013**, *4*, 1712.
- [119] C. L. van Oosten, C. W. M. Bastiaansen, D. J. Broer, *Nat. Mater.* **2009**, *8*, 677.
- [120] M. Camacho-Lopez, H. Finkelmann, P. Palffy-Muhoray, M. Shelley, *Nat. Mater.* **2004**, *3*, 307.
- [121] L. T. de Haan, C. Sánchez-Somolinos, C. M. W. Bastiaansen, A. P. H. J. Schenning, D. J. Broer, *Angew. Chem., Int. Ed.* **2012**, *51*, 12469.
- [122] Y. Sawa, F. Ye, K. Urayama, T. Takigawa, V. Gimenez-Pinto, R. L. B. Selinger, J. V. Selinger, *Proc. Natl. Acad. Sci. USA* **2011**, *108*, 6364.
- [123] K. M. Lee, T. J. Bunning, T. J. White, *Adv. Mater.* **2012**, *24*, 2839.
- [124] L. T. de Haan, V. Gimenez-Pinto, A. Konya, T.-S. Nguyen, J. M. N. Verjans, C. Sánchez-Somolinos, J. V. Selinger, R. L. B. Selinger, D. J. Broer, A. P. H. J. Schenning, *Adv. Funct. Mater.* **2014**, *24*, 1251.
- [125] X. Lu, S. Guo, X. Tong, H. Xia, Y. Zhao, *Adv. Mater.* **2017**, *29*, 1606467.
- [126] S. Palagi, A. G. Mark, S. Y. Reigh, K. Melde, T. Qiu, H. Zeng, C. Parmeggiani, D. Martella, A. Sanchez-Castillo, N. Kapernaum, F. Giesselmann, D. S. Wiersma, E. Lauga, P. Fischer, *Nat. Mater.* **2016**, *15*, 647.
- [127] G. Stoychev, A. Kirillova, L. Ionov, *Adv. Opt. Mater.* **2019**, *7*, 1900067.
- [128] O. Erol, A. Pantula, W. Liu, D. H. Gracias, *Adv. Mater. Technol.* **2019**, *4*, 1900043.
- [129] H. Cui, Q. Zhao, Y. Wang, X. Du, *Chem. - Asian J.* **2019**, *14*, 2369.
- [130] D. Han, C. Farino, C. Yang, T. Scott, D. Browe, W. Choi, J. W. Freeman, H. Lee, *ACS Appl. Mater. Interfaces* **2018**, *10*, 17512.
- [131] C. Huang, J.-a. Lv, X. Tian, Y. Wang, Y. Yu, J. Liu, *Sci. Rep.* **2015**, *5*, 17414.
- [132] G. M. Whitesides, *Nature* **2006**, *442*, 368.
- [133] L. D'Eramo, B. Chollet, M. Leman, E. Martwong, M. Li, H. Geisler, J. Dupire, M. Kerdraon, C. Vergne, F. Monti, Y. Tran, P. Tabeing, *Microsyst. Nanoeng.* **2018**, *4*, 17069.
- [134] W. S. Y. Wong, M. Li, D. R. Nisbet, V. S. J. Craig, Z. Wang, A. Tricoli, *Sci. Adv.* **2016**, *2*, e1600417.
- [135] L. Ionov, *Langmuir* **2015**, *31*, 5015.
- [136] R. Bashir, J. Z. Hilt, O. Elibol, A. Gupta, N. A. Peppas, *Appl. Phys. Lett.* **2002**, *81*, 3091.
- [137] J. Z. Hilt, A. K. Gupta, R. Bashir, N. A. Peppas, *Biomed. Micro-devices* **2003**, *5*, 177.
- [138] T. Zhang, G.-Q. Liu, W.-H. Leong, C.-F. Liu, M.-H. Kwok, T. Ngai, R.-B. Liu, Q. Li, *Nat. Commun.* **2018**, *9*, 3188.
- [139] Y. Kim, H. Yuk, R. Zhao, S. A. Chester, X. Zhao, *Nature* **2018**, *558*, 274.
- [140] H. Fu, K. Nan, W. Bai, W. Huang, K. Bai, L. Lu, C. Zhou, Y. Liu, F. Liu, J. Wang, M. Han, Z. Yan, H. Luan, Y. Zhang, Y. Zhang, J. Zhao, X. Cheng, M. Li, J. W. Lee, Y. Liu, D. Fang, X. Li, Y. Huang, Y. Zhang, J. A. Rogers, *Nat. Mater.* **2018**, *17*, 268.
- [141] Z. Yan, M. Han, Y. Shi, A. Badea, Y. Yang, A. Kulkarni, E. Hanson, M. E. Kandel, X. Wen, F. Zhang, Y. Luo, Q. Lin, H. Zhang, X. Guo, Y. Huang, K. Nan, S. Jia, A. W. Oraham, M. B. Mevis, J. Lim, X. Guo, M. Gao, W. Ryu, K. J. Yu, B. G. Nicolau, A. Petronico, S. S. Rubakhin, J. Lou, P. M. Ajayan, K. Thornton, G. Popescu, D. Fang, J. V. Sweedler, P. V. Braun, H. Zhang, R. G. Nuzzo, Y. Huang, Y. Zhang, J. A. Rogers, *Proc. Natl. Acad. Sci. USA* **2017**, *114*, E9455.
- [142] C. Yu, Z. Duan, P. Yuan, Y. Li, Y. Su, X. Zhang, Y. Pan, L. L. Dai, R. G. Nuzzo, Y. Huang, H. Jiang, J. A. Rogers, *Adv. Mater.* **2013**, *25*, 1541.
- [143] M. Leenders, Shape Memory Textile Jacket, <https://www.youtube.com/watch?v=EikQOrLyc-A> (accessed: December 2019).
- [144] L. Ionov, G. Stoychev, D. Jehnichen, J. U. Sommer, *ACS Appl. Mater. Interfaces* **2017**, *9*, 4873.
- [145] S. Mitravotri, P. A. Burke, R. Langer, *Nat. Rev. Drug Discovery* **2014**, *13*, 655.
- [146] A. S. Hoffman, *J. Controlled Release* **2008**, *132*, 153.
- [147] J. Li, D. J. Mooney, *Nat. Rev. Mater.* **2016**, *1*, 16071.

- [148] S. Fusco, M. S. Sakar, S. Kennedy, C. Peters, R. Bottani, F. Starsich, A. Mao, G. A. Sotiriou, S. Pané, S. E. Pratsinis, D. Mooney, B. J. Nelson, *Adv. Mater.* **2014**, *26*, 952.
- [149] Y. Wang, Y. Miao, J. Zhang, J. P. Wu, T. B. Kirk, J. Xu, D. Ma, W. Xue, *Mater. Sci. Eng., C* **2018**, *84*, 44.
- [150] K. Malachowski, J. Breger, H. R. Kwag, M. O. Wang, J. P. Fisher, F. M. Selaru, D. H. Gracias, *Angew. Chem., Int. Ed.* **2014**, *53*, 8045.
- [151] J. Kim, M. J. Serpe, L. A. Lyon, *J. Am. Chem. Soc.* **2004**, *126*, 9512.
- [152] J. Kim, N. Singh, L. A. Lyon, *Angew. Chem., Int. Ed.* **2006**, *45*, 1446.
- [153] L. Dong, A. K. Agarwal, D. J. Beebe, H. Jiang, *Nature* **2006**, *442*, 551.
- [154] J. L. Drury, D. J. Mooney, *Biomaterials* **2003**, *24*, 4337.
- [155] L. E. Niklason, J. Gao, W. M. Abbott, K. K. Hirschi, S. Houser, R. Marini, R. Langer, *Science* **1999**, *284*, 489.
- [156] S. Miao, H. Cui, M. Nowicki, S.-J. Lee, J. Almeida, X. Zhou, W. Zhu, X. Yao, F. Masood, M. W. Plesniak, M. Mohiuddin, L. G. Zhang, *Biofabrication* **2018**, *10*, 035007.
- [157] L. Ionov, *Adv. Healthcare Mater.* **2018**, *7*, 1800412.
- [158] Q. Zhao, J. Wang, H. Cui, H. Chen, Y. Wang, X. Du, *Adv. Funct. Mater.* **2018**, *28*, 1801027.
- [159] L. Vannozzi, I. C. Yasa, H. Ceylan, A. Menciassi, L. Ricotti, M. Sitti, *Macromol. Biosci.* **2018**, *18*, 1700377.
- [160] I. Apsite, G. Stoychev, W. Zhang, D. Jehnichen, J. Xie, L. Ionov, *Biomacromolecules* **2017**, *18*, 3178.
- [161] L. J. Fei, D. Sujan, *Conf. Proc. IEEE Eng. Med. Biol. Soc.* **2013**, *7*, 229.
- [162] S. Miyashita, S. Guitron, M. Ludersdorfer, C. R. Sung, D. Rus, *IEEE Int. Conf. on Robotics and Automation (ICRA)*, IEEE, Piscataway, NJ **2015**, pp. 1490–1496.
- [163] M. Boyvat, J.-S. Koh, R. J. Wood, *Sci. Rob.* **2017**, *2*, eaan1544.
- [164] J. L. Silverberg, J.-H. Na, A. A. Evans, B. Liu, T. C. Hull, C. D. Santangelo, R. J. Lang, R. C. Hayward, I. Cohen, *Nat. Mater.* **2015**, *14*, 389.
- [165] J. L. Silverberg, A. A. Evans, L. McLeod, R. C. Hayward, T. Hull, C. D. Santangelo, I. Cohen, *Science* **2014**, *345*, 647.



## Supporting Information

### Polymer synthesis and product characterization

#### Synthesis of benzophenone acrylate (BPA)

4-Hydroxybenzophenone (20 g, 0.1009 mol), N,N-diisopropylethylamine (19.3 ml, 0.1110 mol) and 80 ml of anhydrous methylene chloride was added into 500 ml two-necked round-bottom flask fitted with a magnetic stirrer, a thermometer, and an addition funnel with anhydrous acryloyl chloride (9.02 ml, 0.1110 mol) solution in 20 ml of methylene chloride. The acryloyl chloride solution was added dropwise into the flask under cooling (0-5°C) for ca. 3 hours. Then methylene chloride was removed by rotary evaporation. The residues were washed with 80 ml of 20% HCl, and afterwards with 80 ml of saturated solution of sodium hydrocarbonate. After washing, obtained residue was dried over anhydrous sodium sulfate. The solution was passed through a silica gel column using chloroform as the eluent. Chloroform was removed by a rotary evaporator. Finally, 24.44g (95% of yielding) of BPA was obtained. <sup>1</sup>H NMR (CDCl<sub>3</sub>, 500 MHz): 6.01 (dd, J<sub>1</sub> ¼ 10.40, J<sub>2</sub> ¼ 1.26, 1H), 6.28 (dd, J<sub>1</sub> ¼ 10.40, J<sub>3</sub> ¼ 17.34, 1H), 6.60 (dd, J<sub>3</sub> ¼ 17.34, J<sub>2</sub> ¼ 1.26, 1H), 7.20 (m, 2H), 7.43 (m, 2H), 7.54 (m, 1H), 7.74 (m, 2H), 7.81 (m, 2H).

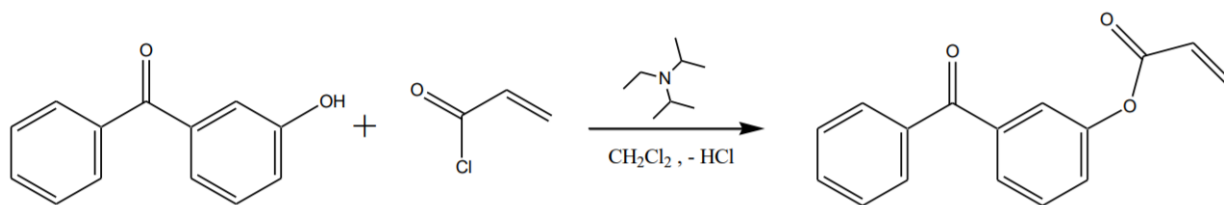


Figure S1. Synthesis of benzophenone acrylate.

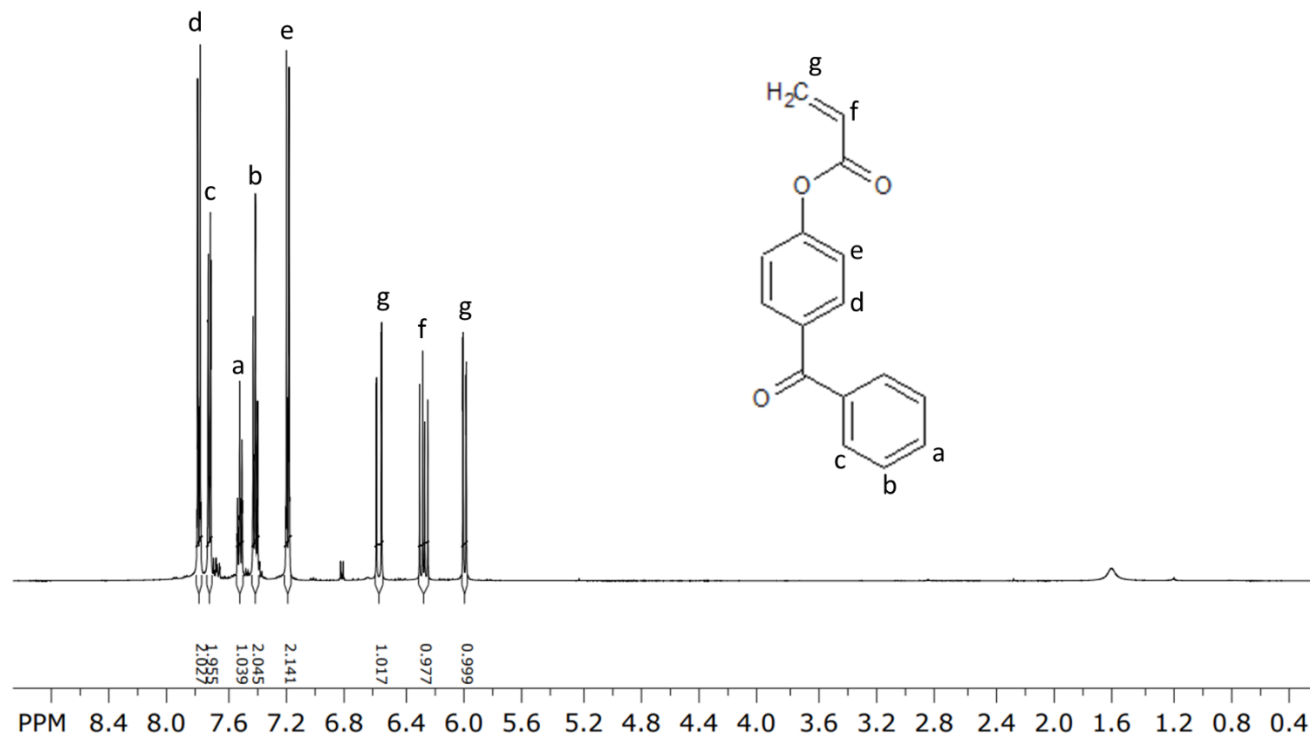


Figure S2.  $^1\text{H-NMR}$  spectrum of obtained benzophenone acrylate

#### Synthesis of poly(N-isopropylacrylamide)-benzophenone acrylate (P(NIPAM-BPA))

N-isopropylacrylamide (NIPAM, 48.5 g), BPA (1.914 g, 2 mol %), 2,2'-azobis(2-methylpropionitrile) (AIBN, 0.143 g) were added in 500 ml round-bottom flask with a magnetic stirrer for the synthesis of P(NIPAM-BPA). As a solvent 150 ml of ethanol were added and then everything was stirred for 5 min until all components were fully dissolved. The flask was closed with a rubber septum and nitrogen was purged through synthesis solution. After purging the solution was set in a pre-heated oil bath ( $T=70^\circ\text{C}$ ). The reaction was carried out for 12 h. Then the solution was poured in diethyl ether under vigorous stirring to precipitate the polymer. Precipitated polymer was filtered through 100 ml ceramic filter (pore size 4) and dried in vacuum oven at  $40^\circ\text{C}$  for 6 h.  $^1\text{H NMR}$  ( $\text{CDCl}_3$ , 500 MHz): 1.05 (t, 3H), 1.46 (d, 2H), 1.97 (s, 1H), 3.85 (s, 1H), 7.14 (m, 1H).

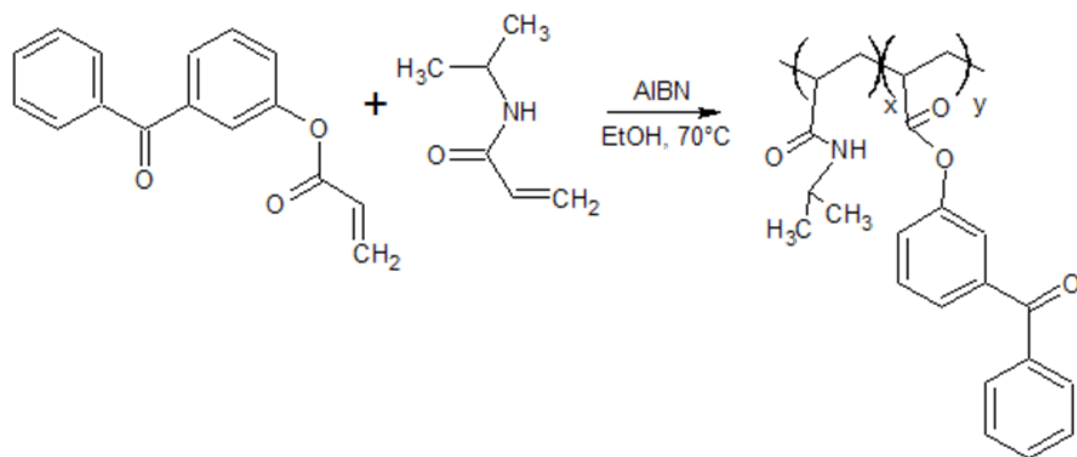


Figure S3. Synthesis of P(NIPAM-BPA)

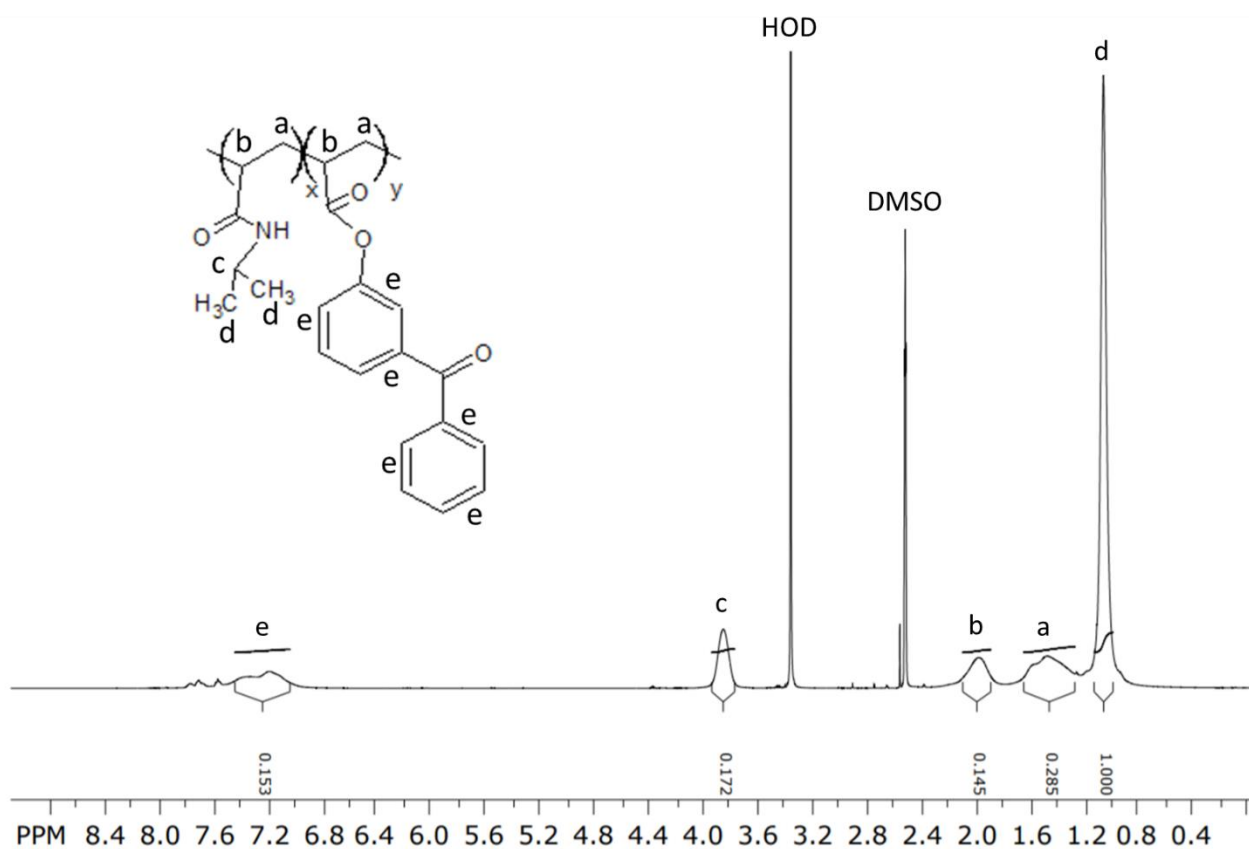


Figure S4. <sup>1</sup>H-NMR spectrum of synthesized P(NIPAM-BPA)

## Synthesis of methacrylated alginate and hyaluronic acid

20-fold excess of methacrylic anhydride was added dropwise to 2 % alginate solution. During the reaction, the solution was kept at pH 8 by adding 5 M NaOH dropwise. The mixture was incubated at 4 °C for 24 h using constant stirring at 800 rpm. Synthesized methacrylated alginate was precipitated and washed in ethanol. The clean substance was dried using freeze drying.

To investigate the methacrylation of alginate, proton NMR was performed for alginate as a reference and methacrylated alginate. <sup>1</sup>H-NMR showed peaks from 4.57 to 4.97 ppm that are characteristic for C-5 alternating blocks and guluronic acid anomeric proton in alginate structure. The peaks presented in the spectra for AA-MA determined the presence of methylene groups at 6.11 and 5.65 ppm and methyl groups between around 1.7 ppm that corresponds to the reaction of methacrylation. The degree of methacrylation of alginate was calculated from <sup>1</sup>H-NMR spectra based on the ratio of the integrals for the area of the methyl and methylene peaks. The resulting methacrylation was close to 74 %.

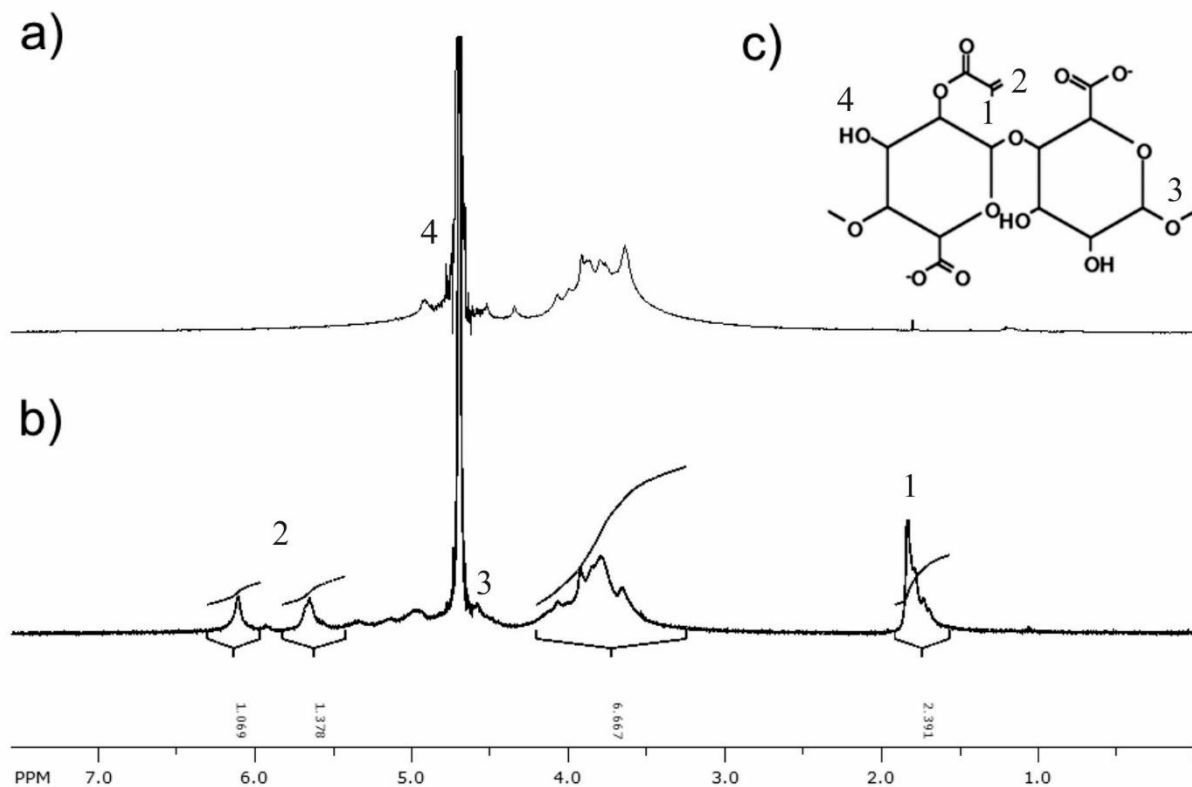


Figure S5. <sup>1</sup>H-NMR spectrum of a) non-modified alginate, b) methacrylated alginate; and c) chemical structure of methacrylated alginate monomer

Methacrylation of hyaluronic acid was done following the same protocol as for alginate. To investigate the degree of methacrylation  $^1\text{H-NMR}$  of hyaluronic acid and synthesis product was performed. Similar as for alginate, typical hyaluronic acid describing peaks around 3.76 to 4.49 were observed, that showed protons located in C-5 alternating blocks. HA-MA spectra revealed peaks around 5.37 and 5.68 that described methylene protons from methacrylation, as well as the peak around 1.99 that describes methyl protons. Based on integrals of methyl and methylene peaks, the calculated degree of methacrylation of hyaluronic acid was 33 %.

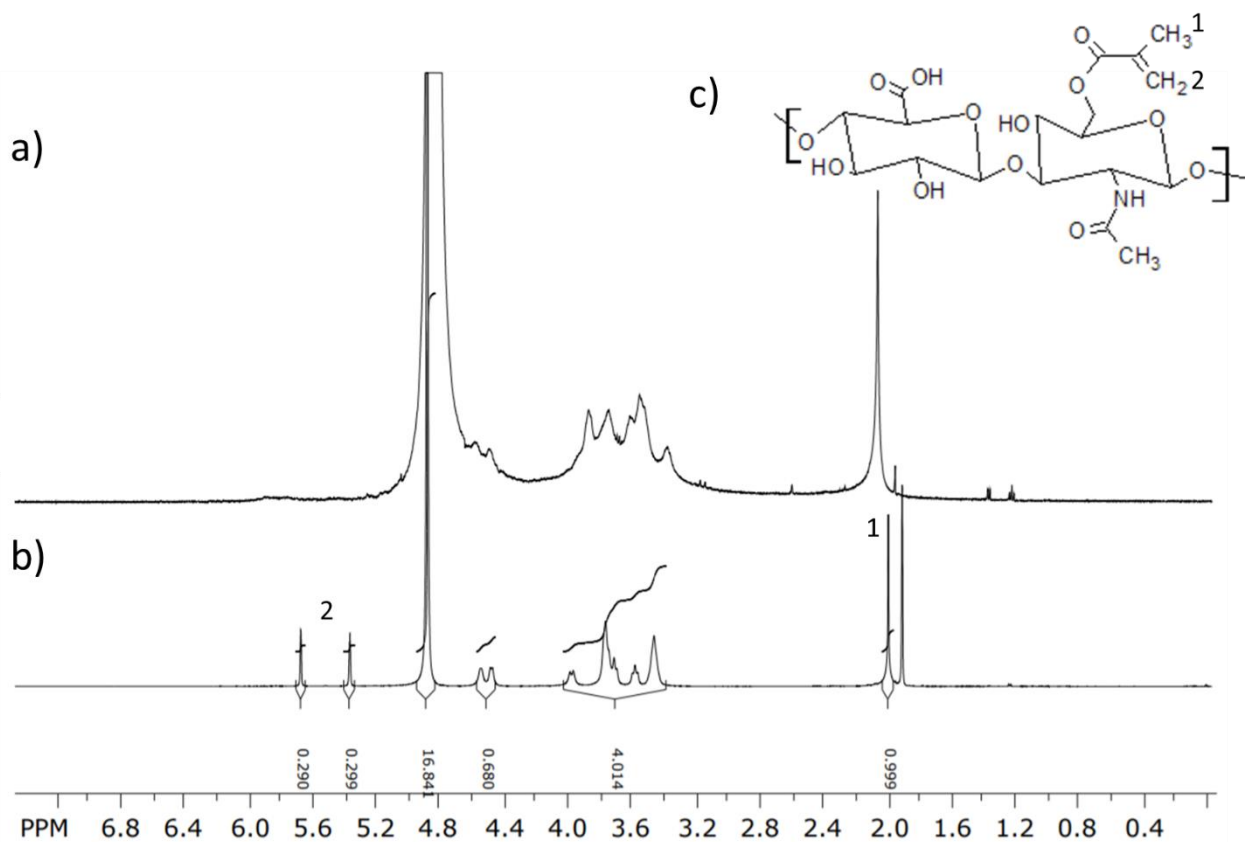


Figure S6.  $^1\text{H-NMR}$  spectrum of a) non-modified hyaluronic acid, b) methacrylated hyaluronic acid; and c) chemical structure of methacrylated hyaluronic monomer



## Acknowledgments

Foremost, I would like to thank my supervisor Prof. Leonid Ionov for giving me the opportunity to work in his group, advising and supporting me throughout all this process. I would also like to thank my PhD committee members Prof. Thomas Scheibel and Prof. Schmidt who gave me valuable advice during my Ph.D.

I also would like to thank all my colleagues and Ionov lab members who helped me during my time in the group: Ivan Raguzin, Georgi Stoychev, Vladislav Stroganov, Alina Kirillova, Juan Manuel Uribe, Andres Fernando Posada, Arpan Biswas, Katharina Bauer, Amit Shukla and Gissela Constante.

Thanks to all collaborators who made it possible to conduct necessary experiments for publications: Weizhong Zhang and Prof Jin Xie, Prof. Dieter Janichen, Dr. Sabine Rosenfeldt, Dr. Martin Dulle, Lena Vogt and Prof. Aldo R. Boccaccini, Anja Caspari and Dr. habil. Alla Synytska. I would like to say special thanks to Dr. Sahar Salehi for supervising me during cell culture in the early and late hours of the day. Additionally, I would like to express my gratitude to Dr. Elise Liensdorf for always finding time to revise my work. As well I would like to say special thanks to Prof. Minko and his group and to Prof. Scheibel and his group for providing our group with equipment and support while our lab was not established and the move was postponed.

Last but not least, I would like to thank my family and my fiancée Maxime Vinzio for never-ending support during all this time.



## (Eidesstattliche) Versicherungen und Erklärungen

(§ 9 Satz 2 Nr. 3 PromO BayNAT)

*Hiermit versichere ich eidesstattlich, dass ich die Arbeit selbstständig verfasst und keine anderen als die von mir angegebenen Quellen und Hilfsmittel benutzt habe (vgl. Art. 64 Abs. 1 Satz 6 BayHSchG).*

(§ 9 Satz 2 Nr. 3 PromO BayNAT)

*Hiermit erkläre ich, dass ich die Dissertation nicht bereits zur Erlangung eines akademischen Grades eingereicht habe und dass ich nicht bereits diese oder eine gleichartige Doktorprüfung endgültig nicht bestanden habe.*

(§ 9 Satz 2 Nr. 4 PromO BayNAT)

*Hiermit erkläre ich, dass ich Hilfe von gewerblichen Promotionsberatern bzw. -vermittlern oder ähnlichen Dienstleistern weder bisher in Anspruch genommen habe noch künftig in Anspruch nehmen werde.*

(§ 9 Satz 2 Nr. 7 PromO BayNAT)

*Hiermit erkläre ich mein Einverständnis, dass die elektronische Fassung meiner Dissertation unter Wahrung meiner Urheberrechte und des Datenschutzes einer gesonderten Überprüfung unterzogen werden kann.*

(§ 9 Satz 2 Nr. 8 PromO BayNAT)

*Hiermit erkläre ich mein Einverständnis, dass bei Verdacht wissenschaftlichen Fehlverhaltens Ermittlungen durch universitätsinterne Organe der wissenschaftlichen Selbstkontrolle stattfinden können.*

.....  
Ort, Datum, Unterschrift